

# LASER-INDUCED SURFACE STRUCTURING

FOR ELECTRON CLOUD MITIGATION IN PARTICLE ACCELERATORS

---

## DISSERTATION

for the award of the academic degree  
doctor rerum naturalium  
Dr. rer. nat.

accepted by:

Faculty of Physics and Earth Science Systems  
of the University of Leipzig

submitted by:

M.Sc. Elena Bez

born on 14/08/1994  
in Münsingen, Germany

---

assessors:

Prof. Dr. André Anders  
University of Leipzig  
Institute for Surface Engineering (IOM)

Prof. Dr. Isabel Montero Herrero  
Institute of Materials Science of Madrid

date of award:

28/10/2024





# Abstract

The formation of electron clouds by secondary electron multiplication in the beam pipes of particle accelerators can lead to reduced performance during operation. Surface roughening using ultrashort pulse lasers efficiently reduces the secondary electron yield (SEY) of a surface. In this study, a solution for the suppression of electron clouds by laser structuring the inner copper walls of the Large Hadron Collider (LHC) beam tubes was developed, fulfilling the technical constraints and surface property requirements. For this purpose, fundamental dependencies between the laser processing parameters and the surface properties such as the modification depth, the surface chemical composition, the particle redeposition, and finally the SEY were investigated on a laboratory scale. A dedicated setup able to perform the modification treatment *in situ*, directly in the beam pipe hosted by the LHC magnet, was commissioned and the operation parameters were optimized. The device consists of a picosecond laser source, a beam coupling system, a 15 m long hollow-core fiber, and a robot that travels inside the beam tube. Treatment at low accumulated laser fluence in nitrogen flux resulted in "optimal surface properties", and specifically, a low modification depth ( $\approx 15 \mu\text{m}$ ), low particle redeposition, a  $\text{Cu}_2\text{O}$ -dominated surface and a SEY maximum of 1.4 after cleaning, which reduces to 1 upon electron irradiation at both room and cryogenic temperatures. A selective longitudinal scan scheme was developed to process the 10 m long beam pipes installed in the cryogenic magnet assemblies of the LHC with the highest effectiveness. A 3.1 m long laser-processed vacuum chamber was installed in the LHC to validate the method with respect to particle detachment.





## Abstract (german)

Die Bildung von Elektronenwolken durch die Multiplikation von Sekundärelektronen im Strahlrohr von Teilchenbeschleunigern kann während des Betriebs zu einer verringerten Leistung führen. Durch Ultrakurzpuls-Laserstrukturierung kann die Sekundärelektronenemission einer Oberfläche effizient reduziert werden. Im Rahmen dieser Arbeit wurde eine Lösung zur Unterdrückung der Elektronenvervielfachung durch Laserstrukturierung der aus Kupfer bestehenden Innenwände der Strahlrohre des Large Hadron Colliders (LHC) entwickelt, die technische Einschränkungen und Anforderungen an die Oberflächeneigenschaften und Vakuumkompatibilität erfüllt. Dafür wurden fundamentale Abhängigkeiten zwischen den Laserbearbeitungsparametern und den Oberflächeneigenschaften wie z.B. der Abtragstiefe, den oberflächenchemischen Eigenschaften, der Wiederablagerung von Partikeln und letztendlich der Sekundärelektronenausbeute (SEY) im Labormaßstab untersucht. Für die Behandlung der Rohrrinnenflächen der Vakuumkammern wurde ein spezieller Aufbau verwendet, der aus einer Pikosekunden-Laserquelle, einem Strahlkopplungssystem, einer 15 m langen Hohlkernfaser und einem Roboter besteht, der sich im Inneren des Strahlrohrs bewegt. Dieses System wurde im Rahmen dieser Arbeit in Betrieb genommen und kalibriert. Eine Behandlung bei niedriger akkumulierter Fluenz in Stickstofffluss resultierte in „optimalen Oberflächeneigenschaften“, d.h. einer geringen Abtragstiefe (ca.  $15\text{ }\mu\text{m}$ ), geringer Partikelbedeckung, einer  $\text{Cu}_2\text{O}$  dominierten Oberfläche und einem SEY-Maximum von 1.4 nach der Reinigung, welches sich während der elektroneninduzierten Konditionierung zu 1 reduziert. Die 10 m langen Strahlrohre, die in den kryogen gekühlten Magnetaufbauten im LHC installiert sind, sollen mit einem Longitudinal-Scanning-Verfahren selektiv bearbeitet werden. Ein 3.1 m langes, laserbearbeitetes Strahlrohr wurde im LHC installiert, um die Methode bezüglich möglicher Partikelablösungseffekte zu prüfen und um die Laserbehandlung als Oberflächentechnologie für Teilchenbeschleunigervakuumsysteme zu validieren.



# List of publications

First-author publications:

- **Selective laser processing of particle accelerator beam screen surfaces for electron cloud mitigation**, E. Bez, A.K. Reascos Portilla, V. Petit, Konstantinos Paraschou, Lotta Mether, K. Brunner, P. Krkotić, Y. Askar, S. Calatroni, M. Taborelli, M. Himmerlich. *Submitted to RSC Appl. Interfaces*.
- **Picosecond pulsed 532 nm laser system for roughening and secondary electron yield reduction of inner surfaces of up to 15 m long tubes**, E. Bez, M. Himmerlich, A.K. Reascos Portilla, B. Beaudou, S. Wackerow, M. Rimoldi, S. Pfeiffer, M. Wiesendanger, F. Benabid, M. Taborelli, A. Abdolvand, P. Chiggiato, *Rev. Sci. Instrum.*, 94, 103007 (2023), DOI:10.1063/5.0166156. *Part of Chapters 3 and 5*.
- **Influence of wavelength and accumulated fluence at picosecond laser-induced surface roughening of copper on secondary electron yield**, E. Bez, M. Himmerlich, P. Lorenz, M. Ehrhardt, A. G. Gunn, S. Pfeiffer, M. Rimoldi, M. Taborelli, K. Zimmer, P. Chiggiato, A. Anders, *J. Appl. Phys.*, 133, 035303 (2023), DOI: 10.1063/5.0131916. *Part of Chapter 4*.
- **Laser-induced surface structuring for electron cloud mitigation in particle accelerators**, E. Bez, M. Himmerlich, A. K. Reascos Portilla, L. Baudin, P. Lorenz, K. Zimmer, M. Taborelli, A. Anders, *Proceedings of 12. Mittweidaer Lasertagung*, 079-082 (2021), DOI:10.48446/opus-12862. *Partly included in Chapter 4 (Fig 4.1b)*.

Co-author publications:

- **Cleaning of laser-induced periodic surface structures on copper by gentle wet chemical processing**, P. Lorenz, M. Ehrhardt, A. Lotnyk, J. Griebel, K. Zimmer, J. Zajadacz, M. Himmerlich, E. Bez, M. Taborelli, S. Rosenow, R. Tepper, A. M. Breul, *Appl. Surf. Sci.*, 679, 161115 (2025), DOI: 10.1016/j.apsusc.2024.161115.
- **Pulse duration dependence of infrared laser-induced secondary electron yield reduction of copper surfaces**, P. Lorenz, E. Bez, M. Himmerlich, M. Ehrhardt, M. Taborelli, K. Zimmer, *J. Laser Micro Nanoen*, 18, 121-126 (2023), DOI:10.2961/jlmn.2023.03.2002. *Partly included in Chapter 4 (Fig. 4.15a)*.

- **Out of focus ultrafast processing of metals for reduced secondary electron yield**, R. Uren, A. Din, S. Wackerow, E. Bez, S. Pfeiffer, M. Rimoldi, M. Himmerlich, M. Taborrelli, A. Abdolvand, *Opt. Mater. Express*, 1228-1240 (2023), DOI: 10.1364/OME.484235.
- **Laser-induced periodic surface structuring for secondary electron yield reduction of copper: dependence on ambient gas and wavelength**, Jijil JJ. Nivas, M. Hu, M. Valadan, M. Salvatore, R. Fittipaldi, M. Himmerlich, E. Bez, M. Rimoldi, A. Passarelli, S. L. Oscurato, A. Vecchione, Carlo A, *Appl. Surf. Sci.*, 622, 156908 (2023), DOI: 10.1016/j.apsusc.2023.156908.
- **Secondary electron yield engineering of copper surfaces by 532 nm ultrashort laser pulses**, P. Lorenz, E. Bez, M. Himmerlich, M. Ehrhardt, M. Taborrelli, K. Zimmer, *Procedia CIRP* 111, 662-666 (2022), DOI: 10.1016/j.procir.2022.08.017.
- **Secondary electron yield engineering of copper surfaces using ultra short infrared laser pulses**, P. Lorenz, M. Himmerlich, M. Ehrhardt, E. Bez, K. Bogdanowicz, M. Taborrelli, and K. Zimmer, in *Laser-based Micro- and Nanoprocessing XVI*, Vol. 11989, 73-83 (2022), DOI: 10.1117/12.2609463.
- **A reliable monitoring and control system for vacuum surface treatments**, J. Tagg, E. Bez, M. Himmerlich, A.K. Reascos Portilla, *JACoW ICALEPCS 2022*, 492-496 (2022), DOI: 10.18429/JACoW-ICALEPCS2021-TUPV039.
- **Secondary electron yield reduction of copper after 355 nm ultrashort pulse laser ablation**, P. Lorenz, M. Himmerlich, M. Ehrhardt, E. Bez, K. Bogdanowicz, M. Taborrelli, K. Zimmer, *Lasers Manuf. Mater. Process.* 9, 135-150 (2022), DOI:10.1007/s40516-022-00167-5. *Partly included in Chapter 4 (Fig. 4.7).*

# List of abbreviations

<b>a-C</b>	amorphous carbon
<b>APA</b>	automated particle analysis
<b>BDS</b>	beam delivery system
<b>BLM</b>	beam loss monitor
<b>BS</b>	beam screen
<b>CERN</b>	European Organization for Nuclear Research
<b>COLDEX</b>	COLD bore EXperiment
<b>DC</b>	direct current
<b>DOE</b>	diffractive optical elements
<b>ECD</b>	equivalent circular diameter
<b>EDX</b>	energy dispersive x-ray spectroscopy
<b>ESD</b>	electron-stimulated desorption
<b>FE-SEM</b>	field emission scanning electron microscopy
<b>HCPCF</b>	hollow-core photonic crystal fiber
<b>HL-LHC</b>	High-Luminosity Large Hadron Collider
<b>HSFL</b>	high spatial frequency LIPSS
<b>HWP</b>	half-wave plate
<b>IC</b>	inhibited coupling
<b>IOM</b>	Leibniz Institute of Surface Engineering
<b>IR</b>	infrared
<b>LHC</b>	Large Hadron Collider
<b>LIPSS</b>	Laser Induced Periodic Surface Structures
<b>LS</b>	long shutdown
<b>LSFL</b>	low spatial frequency LIPSS

**MFD** mode field diameter  
**NEG** non-evaporable getter  
**OFE** oxygen-free electronic grade  
**OSA** optical spectrum analyzer  
**PE** primary electrons  
**PLD** pulsed laser deposition  
**PS** Proton Synchrotron  
**PSD** photo-stimulated desorption  
**RT** room temperature  
**SE** secondary electrons  
**SEM** scanning electron microscopy  
**SEY** secondary electron yield  
**SPS** Super Proton Synchrotron  
**SS** stainless steel  
**TMP** turbo molecular pump  
**TTM** two temperature model  
**TTM-MD** two temperature model molecular dynamics  
**UFO** unidentified falling object  
**UHV** ultra high vacuum  
**ULO** unidentified lying object  
**UV** ultraviolet  
**WLI** white light interferometry  
**XPS** x-ray photoelectron spectroscopy

# Contents

<b>1</b>	<b>Motivation</b>	<b>1</b>
<b>2</b>	<b>Context of the study</b>	<b>3</b>
2.1	The LHC and the high luminosity upgrade . . . . .	3
2.2	The beam vacuum system of the LHC . . . . .	5
2.3	Electron cloud in the vacuum chamber . . . . .	6
2.3.1	Introduction to SEY . . . . .	6
2.3.2	Electron cloud formation, properties and consequences . . . . .	8
2.3.3	Electron cloud mitigation via SEY reduction . . . . .	9
2.4	Ultrashort pulse laser ablation . . . . .	14
2.4.1	Gaussian beam characteristics . . . . .	14
2.4.2	Ultrashort pulse laser-matter interaction . . . . .	16
2.4.3	Laser-plasma interaction . . . . .	19
2.4.4	Consequences on the surface structure . . . . .	19
2.4.5	Applications of laser surface treatments to reduce the SEY . .	21
2.5	Requirements and challenges for laser processing the inner beam screen surfaces of the LHC . . . . .	22
2.5.1	Technical requirements . . . . .	22
2.5.2	Treatment requirements . . . . .	23
<b>3</b>	<b>Sample preparation and characterization methods</b>	<b>25</b>
3.1	Laser processing of flat surfaces . . . . .	25
3.2	Green and infrared <i>in situ</i> laser setups . . . . .	26
3.2.1	Description of the laser treatment setups . . . . .	27
3.2.2	Characterization of the setups . . . . .	33
3.3	Surface characterization methods . . . . .	40
3.3.1	Secondary electron yield (SEY) measurement . . . . .	40
3.3.2	Electron irradiation measurements (Conditioning) . . . . .	42
3.3.3	X-Ray photoelectron spectroscopy (XPS) . . . . .	42
3.3.4	Centrifugation tests . . . . .	42
3.4	Preliminary characterization of untreated copper surface . . . . .	44
3.4.1	Topography of copper . . . . .	44
3.4.2	Reflectivity of copper . . . . .	45
3.4.3	Surface chemical properties of Cu and its oxides and hydroxides	46
3.4.4	Secondary electron yield . . . . .	48
3.4.5	Conditioning . . . . .	49

<b>4</b>	<b>Fundamental dependencies of the surface properties on the laser parameters</b>	<b>51</b>
4.1	Influence of accumulated fluence and wavelength . . . . .	51
4.1.1	Structural modification . . . . .	51
4.1.2	Surface chemical properties . . . . .	57
4.1.3	Secondary Electron Yield . . . . .	59
4.1.4	Conditioning . . . . .	63
4.2	Influence of pulse duration . . . . .	65
4.3	Influence of defocusing . . . . .	68
4.4	Comparison of laser processing of Cu OFE bulk and colaminated Cu	70
4.5	Conclusions . . . . .	71
<b>5</b>	<b>Robot-assisted laser processing of curved surfaces</b>	<b>73</b>
5.1	Influence of the inert gas nozzle . . . . .	74
5.1.1	Influence of the flow speed using various nozzle designs . . . . .	74
5.1.2	Variation of the nitrogen volume flow . . . . .	77
5.1.3	Processing in air vs. with support of nitrogen flow . . . . .	78
5.2	Setting the parameter space of <i>in situ</i> processing . . . . .	81
5.2.1	Screening of processing parameters . . . . .	82
5.2.2	Particle mitigation through post-cleaning . . . . .	82
5.3	Quantification of particle detachment by centrifugal forces . . . . .	86
5.4	SEY reduction via electron irradiation (conditioning) . . . . .	91
5.4.1	Conditioning at room temperature . . . . .	91
5.4.2	Conditioning at cryogenic temperature . . . . .	92
5.5	Concluding considerations on parameter selection for the processing of beam screens . . . . .	94
<b>6</b>	<b>Large-scale treatments of beam screens</b>	<b>95</b>
6.1	Test of scan strategy on a 50 cm long beam screen (type 74) . . . . .	95
6.2	Large-scale treatment of a 2.2 m long beam screen (type 50 L) . . . . .	102
6.3	40 cm long laser-treated beam screens (type 50 A) for impedance measurement . . . . .	106
6.4	Laser-treated 3.1 m long Cu tube for beam loss measurement in the LHC108	
6.5	Conclusions . . . . .	113
<b>7</b>	<b>Conclusions and Outlook</b>	<b>115</b>
<b>A</b>	<b>Appendix</b>	<b>I</b>





# 1 Motivation

The Large Hadron Collider (LHC) of the European Organization for Nuclear Research (CERN) is currently being prepared for an upgrade to substantially increase its luminosity. It is expected that the formation of electron clouds in the machine will reach unacceptable levels, which can limit its performance. This phenomenon has been observed not only in accelerators at CERN (Proton Synchrotron (PS), Super Proton Synchrotron (SPS), LHC), but also in other machines (SuperKEKB, DaΦne). Several strategies to suppress electron clouds are used in the LHC, but there is no universal solution as each method has its own limitations. The reduction of the secondary electron yield (SEY) of the inner vacuum chamber material thereby plays a key role. Specifically, the inner copper walls of eight vacuum chambers embedded in cryogenic magnet complexes, that are up to 15 m long, require a treatment, that meets technical and surface property requirements. These magnets are installed near the interaction points 1 and 5 (indicated in Figure 2.1) and will be extracted from the machine in 2026 to perform the surface treatment. Commonly used antimultipacting treatments such as non-evaporable getter (NEG) films or amorphous carbon (a-C) coatings are efficient in SEY reduction, but are not suitable for these chambers, as specific components installed in the magnet complexes degrade the coating performance.

Laser-induced surface modification is a promising alternative to the methods mentioned above [1]. The engraving of hierarchical structures on the surface can reduce its SEY by “trapping” the secondary electrons, as it has been demonstrated on a laboratory-scale. However, laser processing the inner part of up to 15 m long tubes is a technological challenge. The light source must be guided to the inner surface and scanned along the length. For this task, a dedicated setup, composed of an ultrashort pulse laser source, an optical coupling system, a 15 m long hollow-core fiber, and a robot, has been previously designed as proof-of-principle. In addition, specific treatment requirements on the surface topography, chemical composition and the SEY must be fulfilled for the application in the LHC. A laser-processed test surface successfully mitigated electron clouds in the SPS at CERN [2] and the method is expected to meet the criteria for the treatment of the vacuum chambers installed in the magnet complexes of the LHC. The advantage of the laser processing is that it allows the exclusion of critical components by restricting the scanning to specific areas, and the surface structures can be tailored using a variety of laser processing parameter.

The existing early experimental studies confirmed the efficiency of the principle for SEY reduction and electron cloud mitigation on laboratory-scale without including all

## *1 Motivation*

constraints linked to large-scale processing, effects during accelerator ramp-up, LHC operation, and machine protection.

Various physical properties and technical limitations had to be investigated for the final implementation of laser-treating the beam screens of selected LHC magnets. Therefore, this thesis is dedicated to systematically study the influence of the most relevant laser processing parameters on the surface properties of copper. The focus is on electron emission reduction and the minimization of particle deposition during laser ablation to mitigate possible risks of particle contamination in the vacuum chamber of the accelerator as well as the characterization of all relevant material parameters. Furthermore, the limitations in optical focus adjustment for treatments of tubes with non-circular cross-sections had to be identified and the process adjusted accordingly. Moreover, laboratory-scale test needed to be transferred to the operation of a new experimental setup that allows to treat the inner surface of long tubes, including the experimental characterization of the setup. The selected processing parameters were targeted to be applied to the inner tube surface of various vacuum chamber test objects to demonstrate the scalability of the process up to several meters in length.

## 2 Context of the study

### 2.1 The LHC and the high luminosity upgrade

The LHC is the largest and most powerful particle accelerator in the world, with a circumference of 27 km. The proton beams are progressively pre-accelerated to an energy of 450 GeV before they are injected into the LHC from the SPS. The two beams consist of bunches 25 ns apart, each containing  $1.5 \times 10^{11}$  protons. These protons are accelerated to almost the speed of light by high radio-frequency electric fields. As visualized in Figure 2.1, the beams travel in opposite directions in two separate beam pipes in ultra high vacuum (UHV). Superconducting dipole magnets (8.3 T) force the beam on a circular trajectory. Quadrupole magnets collimate it and three quadrupole magnets in series (inner triplet magnets) focus the beam before the interaction points to a minimum spot size of  $17 \mu\text{m}$  (interaction points 1 and 5). The beams are then collided at an energy of 13.6 TeV [3]. In the event of beam loss or e.g. sudden loss of magnet superconductivity (magnet quench), the beam is extracted from the machine at point 6, the so-called beam dump.

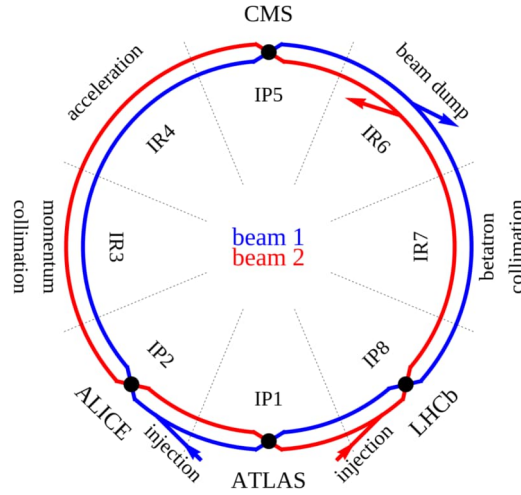


**Figure 2.1:** LHC layout: Beam injection from SPS (IR2 & IR8), radio frequency acceleration (IR4), beam collimation (IR3 & IR7), collision points at ATLAS (IR1), A Large Ion Collider Experiment (IR2), Compact Muon Solenoid (IR5) and Large Hadron Collider beauty (IR8) and beam extraction (IR6). Figure taken from Ref. [4]. The standalone magnets of interaction points 1 and 5 are foreseen for laser treatment.

## 2 Context of the study

As of 2029, the LHC is expected to operate at a higher luminosity level. Luminosity is defined as the number of potential collisions per unit area per second. Therefore, the number of protons per bunch will be increased (from  $1.5 \times 10^{11}$  to  $2.2 \times 10^{11}$  p<sup>+</sup>) and the collision cross section at the interaction points will be maximized by superconducting crab cavities that tilt the proton bunches. The objective is a peak luminosity of  $L = 5 \times 10^{34} \text{ cm}^{-2} \text{ s}^{-1}$  (instead of  $2 \times 10^{34} \text{ cm}^{-2} \text{ s}^{-1}$ ) and an increase of integrated luminosity  $\int L dt$  from  $450 \text{ fb}^{-1}$  to  $3000 \text{ fb}^{-1}$  in the decade after the upgrade [5]. Thus, rare events, such as the Higgs Boson generation, will occur more often. The main upgrade of the machine will take place in the vicinity of the ATLAS (IR1) and CMS (IR5) experiments. This includes the installation of more powerful focusing magnets and the newly designed superconducting crab cavities. Concomitantly, the detectors are being upgraded to cope with the increased number of interactions. The increase in luminosity leads to higher beam-induced heat loads caused by synchrotron radiation, impedance, or electron cloud, which can exceed cooling capacity limits of available infrastructure. The so-called electron clouds, that form in the vacuum tubes during operation of the LHC, are expected to reach unacceptable values at higher luminosity (see Sec. 2.3.3). Therefore, some of the beam pipes installed in magnet complexes (see Sec. 2.2) in cryogenic areas close to the interaction points require a surface treatment of the inner wall. The next installation and maintenance phase (long shutdown (LS) 3) will take place in the period 2026 – 2029, according to the schedule in Fig. 2.2, during which the machine is warmed up to room temperature (RT) and parts of the vacuum system are vented to atmospheric pressure. The laser treatment is foreseen to be applied *in situ* on the beam pipes of four standalone magnets (Q5) located on each side of the interaction points 1 and 5. The magnets will be brought to the surface, without extracting the beam pipes.



**Figure 2.2:** Upgrade schedule for LHC and High-Luminosity Large Hadron Collider (HL-LHC). Figure taken from Ref. [6].

## 2.2 The beam vacuum system of the LHC

The beam vacuum system of the LHC comprises cryogenic and RT sectors at a pressure of less than  $10^{-10}$  mbar [3] to reduce beam losses resulting from scattering between protons and residual gas molecules in the chamber [7]. This way, the required beam lifetime of 100 h and the minimization of background noise for the detectors is ensured. In the RT field-free sectors, the inner surfaces of the vacuum chambers are coated with TiZrV NEG films [8], providing a high pumping speed after thermal activation. The vacuum chamber in the cryogenic sectors is illustrated in Figure 2.3a. It is a “cold bore” surrounded by superconducting coils that operate at 1.9 K. A beam screen (BS), shown in Figure 2.3b, is installed in the vacuum chamber that BS shields beam-induced heat loads from the cold bore. The heat load is dissipated by the cryogenic cooling system, which is designed in a way that it recovers the superfluid He by a refrigerator. If the heat load on the BSs exceeds a critical value (at present the limit is between 185 and 280 W per half cell (three dipoles and one quadrupole)), the cryogenic cooling system would reach its operational limit and could no longer cool the magnets sufficiently. Beam-induced heat sources are (1) synchrotron radiation, (2) image current, (3) electron multipacting (Sec. 2.3), and (4) beam losses by nuclear scattering of the high-energy protons at the residual gas molecules [7].

In addition, the BS enables both cryopumping of residual gas molecules and the conduction of the image current induced by the proton beam. The complete BS is cooled to 5 – 20 K by supercritical helium circulating in two stainless steel (SS) tubes, installed on the flat parts of the BS. The principle of cryopumping is the following (Fig. 2.3c): Since the temperature of the BS is higher than that of the cold bore, the residual gas molecules (mostly  $H_2$ ) preferentially travel through the pumping slots of the BS. These holes in the BS are visible in Figure 2.3b, c, and allow the molecules to escape before they cryosorb on the cold bore (1.9 K) outside of the BS. This allows for a large cryopumping capacity.

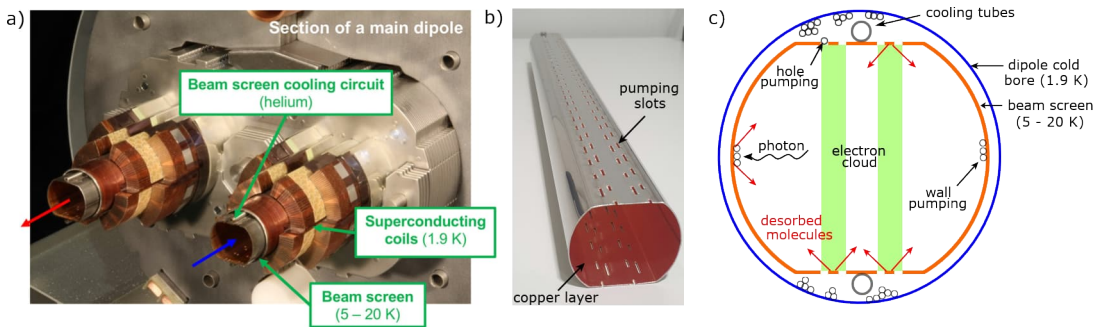


**Figure 2.3:** a) BS installed in an arc dipole magnet of the LHC. Figure taken from Ref. [9], b) Photograph of a BS (type 50 L). c) Schematic of the cryopumping principle in the vacuum pipe.

## 2 Context of the study

**Table 2.1:** Dimensions of various beam screen types at RT: Wall thickness and inner beam screen dimensions ( $ID$ ).

Beam screen	SS + Cu thickness (mm)	$ID_{\text{radial}}$ (mm)	$ID_{\text{flat}}$ (mm)
Type 50 A	1.0 + 0.075	46.35	36.75
Type 50 L	0.6 + 0.075	47.15	37.55
Type 74	0.6 + 0.075	70.65	60.95

Moreover, the BS prevents excessive dynamic pressure instabilities induced by electron-stimulated desorption (ESD) or photo-stimulated desorption (PSD) in the vacuum chamber due to physisorption of the gas molecules outside the BS. Desorbed gases from the BS wall may either be cryopumped or stick back to the BS surface (recycling). In standalone magnets, the cold bore is at 4.2 – 4.5 K at which the  $H_2$  sticking coefficient is lower. Therefore, cryosorbers made of carbon fibers [10] are installed facing the pumping slots to increase the pumping surface area.

Since the inner wall of the BS must conduct the image current induced by the proton beam, a 75  $\mu\text{m}$  thick Cu layer is laminated on the SS wall of the BS [3]. It provides high conductivity (low surface resistance) and limits the Joule heating through the induced image current following the beam on the BS walls. The BS has two opposite curved and two opposite flat parts. Its dimensions vary depending on the installation location. The aperture of the ones usually installed in the cold bore (type 50 A) of dipole magnets is as small as 36.75 mm (Tab. 2.1).

## 2.3 Electron cloud in the vacuum chamber

The electron cloud build-up in vacuum pipes during the operation of particle accelerators constitutes a major limitation of the performance of the machine. The phenomenon has been observed not only in accelerators at the CERN (PS, SPS, LHC [11, 12]), but also in other machines [13–20]. The SEY of the inner vacuum chamber material thereby plays a key role.

### 2.3.1 Introduction to SEY

When primary electrons (PE) impinge on a surface, they are either elastically reflected or interact with the solid through elastic and inelastic scattering, excitation processes and the cascade-like generation of secondary electrons (SE) [21–23]. The majority of SE is absorbed by the material, and only the ones, generated within the escape depth ( $< 20 \text{ nm}$ ), are emitted from the surface, as illustrated in Figure 2.4a. These electrons follow a cosine distribution independent of the angle of incidence  $\theta$  [24]. The energy

### 2.3 Electron cloud in the vacuum chamber

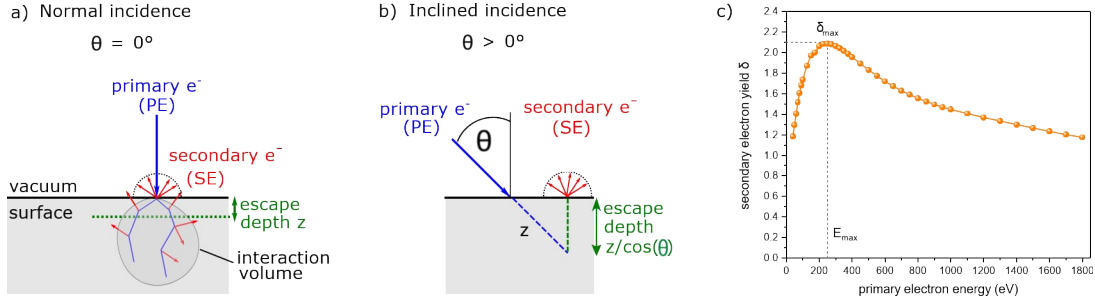


**Figure 2.4:** a) Schematic of electron interaction with the material at normal ( $\theta = 0^\circ$ ) and b) oblique incidence ( $\theta > 0^\circ$ ), c) SEY of Cu for primary electron energies between 50 and 1800 eV at normal incidence.

spectrum of SEs of a monoenergetic impinging beam contains true secondaries ( $E \leq 50$  eV), backscattered and elastically reflected electrons ( $50 \text{ eV} < E \leq E_p$ ), all referred to as SE in the following.

The total SEY  $\delta(E)$  for a given primary electron energy  $E$  is defined as the ratio between SE and PE:

$$\delta(E) = \frac{SE(E)}{PE(E)}. \quad (2.1)$$

The SEY of an air-exposed copper surface in dependence of primary electron energy is shown in Figure 2.4c. As the PE energy increases, more SE are generated. However, the average depth, at which the SE are generated, also increases. The maximum yield  $\delta_{\max}$  in the SEY spectrum is obtained when the PEs deposit a maximum energy  $E_{\max}$  within the depth from which the SE can be emitted into the vacuum. As primary electrons penetrate deeper into the material, secondary electrons cannot escape anymore, causing the SEY to decrease with increasing energy. For air-exposed copper, the maximum yield of  $\sim 2.1$  is at an energy of  $E_{\max} = 250$  eV at normal incidence and depends on surface roughness and adsorbates.

The penetration depth of the PEs decreases with the density (atomic number  $Z$ ) of the material. A larger  $Z$  implies stronger scattering of electrons closer to the surface, which generally results in a higher SEY at higher primary energy. Semiconductors or insulators typically have a higher SEY than metals due to their band gap or low work function (minimum energy required to extract an electron from the surface), which reduces the penetration depth of primary electrons [25, 26].

The SEY is dependent on the incident angle  $\theta$  of the PEs. When the PEs impinge at normal incidence  $\theta = 0^\circ$  on a smooth surface,  $\delta_{\max}$  is minimal as the PEs penetrate deep into the material. At an inclined angle  $\theta > 0^\circ$ , the PEs penetrate obliquely into the material and excite SEs closer to the surface, which are therefore more likely to escape from it. This results in a higher SEY  $\delta$ .



## 2 Context of the study

The angular dependence was empirically described [27]:

$$\delta_{\max}(\theta) = \delta_{\max}(0) \left( 1 + k_s \frac{\theta^2}{2\pi} \right), \quad (2.2)$$

where  $k_s$  depends on the surface roughness.

The SE are emitted at higher energy as they are now created closer to the surface. This results in a shift of  $\delta_{\max}$  to higher energy. Electrons in a dipole magnet field of the LHC, mainly impinge at normal incidence on the BS surface [28], because the magnetic field lines are parallel and perpendicular to the BS surface. Technical surfaces used in particle accelerator experiments were air-exposed and give a higher SEY compared to clean surfaces due to hydrocarbon adsorbates or adsorbed water molecules. In some cases the formation of an insulating oxide or hydroxide can contribute to the increase in SEY [29, 30]. These adsorbates are removed by heating [29] or irradiation with electrons [31–33].

Secondary electron emission is often used for signal amplification in various applications, including scanning electron microscopy (SEM) [34], plasma displays [35, 36], photomultipliers [37], and measurement methods in space applications [38]. Alternatively, electron emission can be suppressed by a low SEY [39]. Particle accelerator applications typically aim to reduce the SEY, for example to suppress electron clouds in the vacuum chambers.

### 2.3.2 Electron cloud formation, properties and consequences

When protons are forced into a circular orbit by a perpendicular magnetic field, they emit synchrotron radiation tangential to their direction of motion. Thus, photoelectrons can be produced when the photons impact on the chamber wall (photoelectric effect), or the protons simply ionize the residual gas molecules/atoms and thereby generate electrons. Both are considered as PE, which are then accelerated by the proton beam potential due to Coulomb attraction to several hundreds of eV. When they impinge on the vacuum chamber walls, a series of low-energy SE ( $\sim 10$  eV) are created, as shown in Figure 2.5. They are elastically reflected or absorbed by the surface, but do not have enough energy to produce new SE. Some of them survive in the vacuum chamber until the next proton bunch arrives and are again accelerated by the proton potential towards the opposite wall. If the SEY of the inner beam screen wall is less than one, there is no amplification. The process repeats over several bunch passages (25 ns in the LHC), in which the number of secondary electrons is multiplied until an equilibrium of space charge is reached and the electron cloud is formed [40, 41].

The magnetic field lines of a dipole magnet have a vertical, parallel stripe pattern. The BS is embedded in central position in the magnet. The electrons in the BS experience the Lorentz force and move in a spiral along the magnetic field lines. This is why the electron cloud distribution follows the same stripe pattern, as shown in Figure 2.6a,

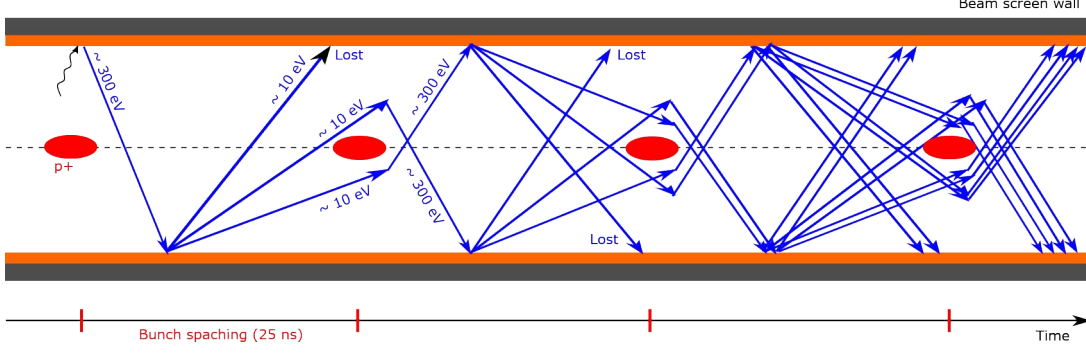


**Figure 2.5:** Schematic of electron cloud formation in the vacuum chamber during operation of the LHC.

top row. For a quadrupole magnet, it is a fourfold stripe pattern (Fig. 2.6b, top row). The gradient of the quadrupole magnet field leads to the trapping of electrons [20, 44] during which they gain energy [9] before impinging on the BS surface. For this reason, the intensity of the electron cloud is an order of magnitude higher than for a dipole magnet (Fig. 2.6, top row). The energy density of electrons impinging on the vacuum wall is highest for electron energies less than 200 eV and the majority is below 500 eV (Fig. 2.6, middle row). The electron cloud density increases with shorter bunch spacing [12, 45] or higher SEY of the surface [43]. As the electron activity produces heat loads to the cryogenic system, the heat also increases with higher SEY (Fig. 2.6, bottom row). Electron cloud is the main contributor to dynamic heat load in the cryogenic sectors [46]. The SEY threshold at which the heat load increases drastically is  $\delta_{\max} = 1.25$  for a dipole magnet and  $\delta_{\max} \approx 1.05 - 1.35$  in a quadrupole magnet for higher bunch populations (Fig. 2.6, bottom row), as envisaged for High-Luminosity Large Hadron Collider (HL-LHC). Since the intensity of the electron cloud is higher in a quadrupole than in a dipole magnet, the threshold is accordingly lower.

In addition to the heat loads in the cryogenic sectors [47], electron clouds that interact with the proton beam cause beam instabilities, losses or emittance growth [48, 49]. Moreover, perturbation to beam diagnostics [50] can occur as well as a local vacuum pressure rise of several orders of magnitudes due to ESD [49]. Since the electron cloud density is directly influenced by the beam properties, it limits the performance of the accelerator. Therefore, a solution to mitigate the electron cloud is paramount.

### 2.3.3 Electron cloud mitigation via SEY reduction

Several electron cloud mitigation strategies are used in the LHC, but there is no universal solution as each method has its own limitations. General countermeasures include a sawtooth-shaped surface on the outer BS surface in the cold arc dipoles to reduce electron generation from synchrotron radiation, or external solenoid fields [51] installed in field-free regions, whose longitudinal magnetic field forces the electrons on

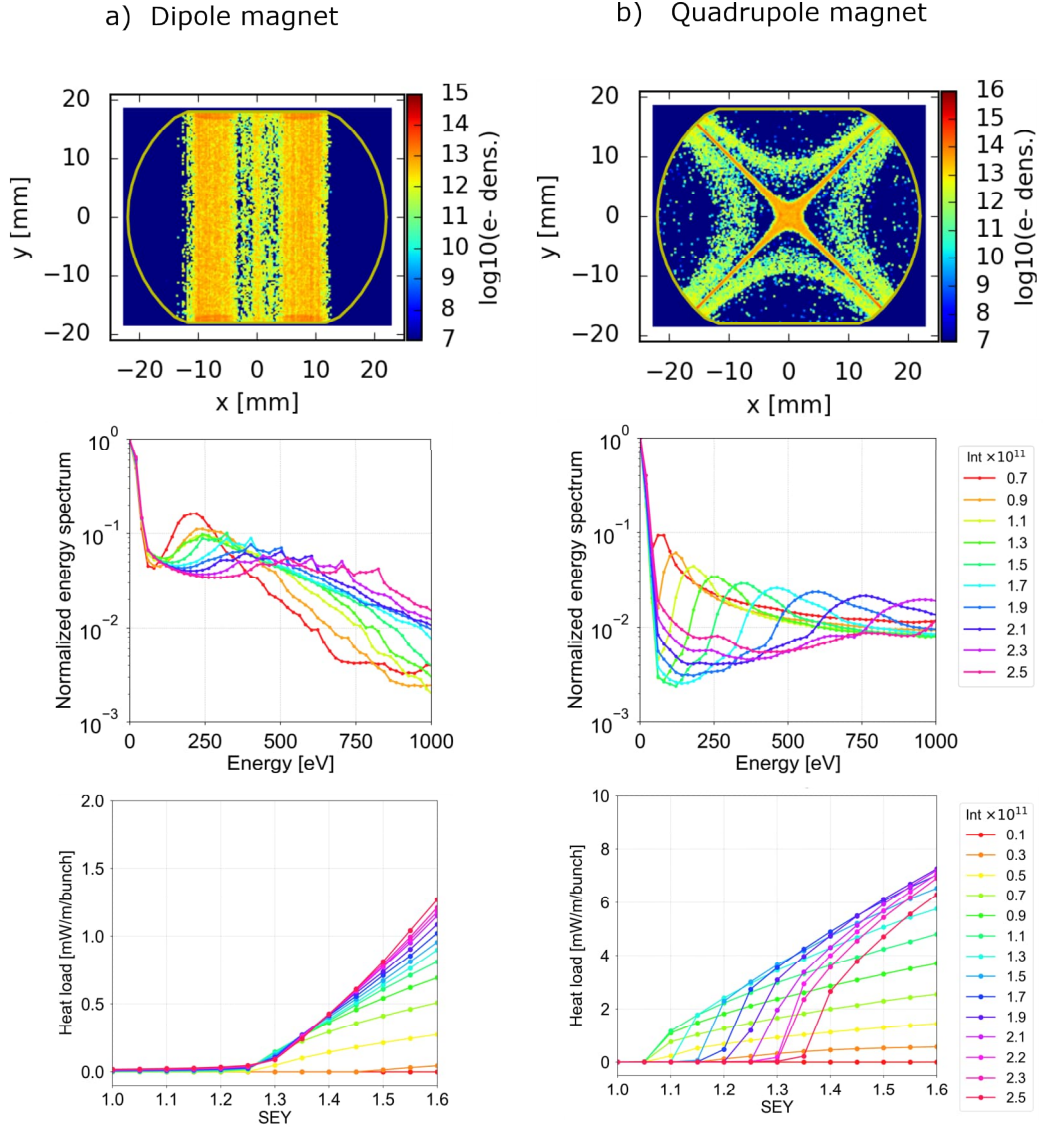


**Figure 2.6:** Electron cloud spatial distribution simulation at a collision energy of 6.5 TeV (top row). Figure taken from Ref. [42]. Energy distribution of electrons impinging on the vacuum wall (middle row), for a) dipole and b) quadrupole magnet, 25 ns bunch spacing, 7 TeV collision energy, and an assumed SEY of 1.5. Figure taken from Ref. [43]. Heat load simulation threshold as a function of SEY for 25 ns bunch spacing and 7 TeV collision energy (bottom row). Figure taken from Ref. [43].

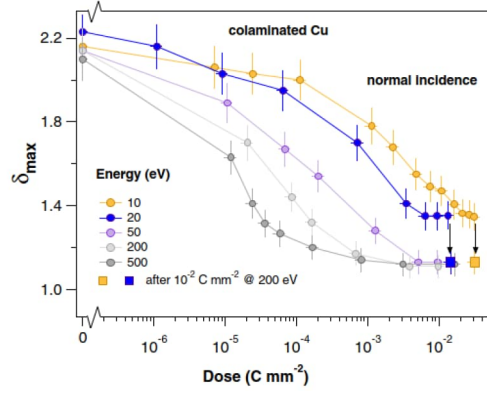


**Figure 2.7:** SEY maximum decrease upon electron irradiation of a Cu surface for varying electron energies. Figure taken with permission from Ref. [32].

circular orbits remaining confined near the wall. Other strategies are based on reducing the SEY of the inner beam screen surface. The following strategies aim to suppress SE multipacting by reducing the SEY of the inner BS surfaces.

### Beam Scrubbing

When the LHC is placed under vacuum and cooled down after a long shutdown, the copper surfaces of the BSs can be contaminated due to the adsorption of hydrocarbons and water molecules, as well as the formation of hydroxide. This contamination can increase the SEY [29]. When a surface is exposed to electrons, adsorbed molecules are partially detached by electron-stimulated desorption and chemical reactions are induced, such as the graphitization of hydrocarbon adsorbates as well as dissociation of surface hydroxides at room temperature. This cleaning of the surface is referred to as the “conditioning” effect, leading to a gradual decrease in SEY with increasing electron dose [31–33]. The SEY of Cu gradually decreases from  $\delta_{\max} \sim 2$  (Cu exposed to air) to close to 1 where it saturates, as shown in Figure 2.7. The Figure also shows that the SEY decrease is slower for lower electron energies, and results in higher values for electron energies of 10 and 20 eV. In particle accelerators, “scrubbing runs” [52–54] are performed prior to normal operation. During these runs, the beam intensity is gradually increased to condition the vacuum chamber surfaces using the electrons from the electron cloud build-up. The process is self-limited because electrons are no longer multiplied once the SEY is close to 1. In laboratory experiments, the surface is conditioned using an electron gun. Consequently, the SEY maximum can decrease below 1, depending on the material. However, the conditioning of copper has its limitation at cryogenic temperature. During run 2 of the LHC, a higher heat load was observed in some cryogenic areas that conditioned less [47] due to the transformation of copper hydroxide into CuO [55, 56]. In addition, the SEY decrease was limited to  $\delta_{\max} = 1.2$  [55].

### Surface coatings

In the 20 % of the LHC that are at room temperature, a NEG film [8] was deposited on the inner beam screen surface by magnetron sputtering using TiZrV twisted wires. After activation by 24 h thermal annealing at 180 °C in UHV, it acts as a getter pump with excellent vacuum properties [57, 58] and reaches a low SEY maximum of  $\sim 1.1$  (Fig. 2.8a). However, the BSs in the cryogenic regions are surrounded by magnetic coils and embedded in a cryostat. Therefore, a surface treatment at room temperature without thermal annealing is required. Graphite has an inherently low SEY. Therefore, amorphous carbon (a-C) [59] is coated on the inner Cu surface of these BSs by magnetron sputtering. During the fabrication process, a thin Ti layer (150 nm) is deposited onto the Cu surface to reduce the outgassing of the BS and to improve the adhesion of the a-C layer (50 nm) on top. The coating has a SEY  $\delta_{\max} \sim 1$  (Fig. 2.8b). The SEY of the coated surface decreases for a more graphitic structure (conversion of  $sp^3$  hybrids into six-fold aromatic domains of graphite), obtained at higher coating temperatures. This correlates to smaller band gaps in the electronic structure and thus higher conductivity [60, 61]. The process is well developed and electron cloud mitigation has been demonstrated in the SPS at RT [62, 63], at cryogenic temperature in the COLD bore EXperiment (COLDEX) [64], and in a test bench (vacuum pilot sector) of the LHC [65]. In addition, high surface adsorption capacity was observed in the absence of dynamic pressure instabilities [64].

Since the BSs of the cryogenic sectors are installed inside dipole or quadrupole magnet assemblies, which comprise a cryogenic cooling system and a complex vacuum system, their removal and replacement is an elaborate and time consuming operation, and in some cases, these magnets are unique. This high-risk operation must be avoided and a solution for an *in situ* treatment is required. Therefore, the carbon coating process was developed for *ex situ* treatment in the laboratory or *in situ* in the LHC tunnel.

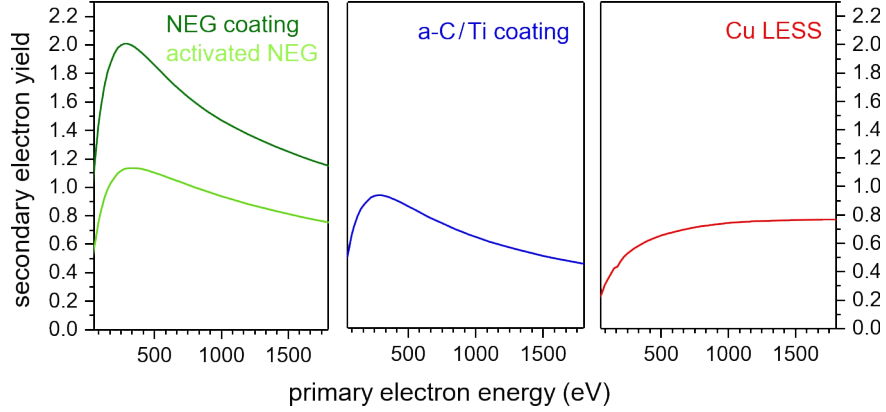


**Figure 2.8:** SEY as function of primary electron energy for antimultipacting surface treatments such as NEG film on Cu before and after thermal activation, amorphous carbon/Ti coating on Cu, and Laser Engineered Surface Structures (LESS) on copper. Data taken with permission from Ref. [66].

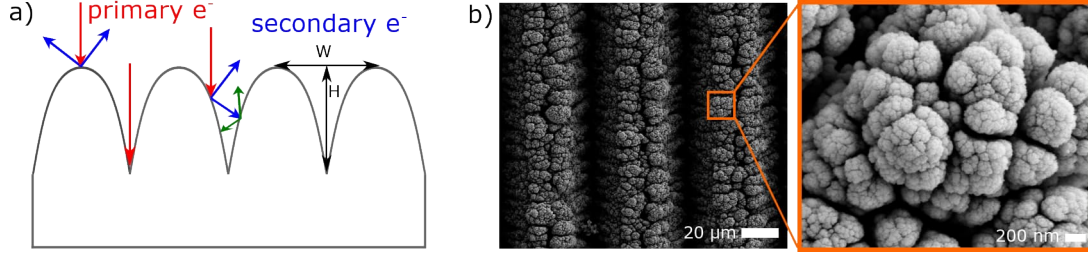


**Figure 2.9:** a) Sketch of SEY reduction at grooved surface, b) SEM images of laser-induced micro- (left) and nanostructure (right) on Cu.

However, the performance of the a-C coating in presence of the cryosorbers installed in the BS (see Sec. 2.2) is markedly reduced in terms of the resulting SEY. Magnetron sputtering can only be applied to the entire object, thus a selective treatment of the curved parts of the BS where cryosorbers are not present is not possible. For these reasons, laser-based surface modification is investigated as an alternative method to suppress electron clouds. The following section provides detailed information on the concept.

### Geometrical modification

The concept of reducing the SEY by surface roughness has been developed since the 1930s [67]. Theoretical simulations of triangular and rectangular grooved structures showed that a high aspect ratio between the height  $H$  and width  $W$  of the structures efficiently reduces the SEY [68–71]. Figure 2.9a illustrates the principle of secondary electron suppression by a microstructure. Due to the geometrically modified surface, the primary electron – perpendicular to the macroscopic surface – now hits the micro/nanostructure at an oblique angle. As discussed above (Sec. 2.3.1), the electrons are emitted in a cosine distribution. Thus, if the aspect ratio of the surface geometry is high enough, the emitted secondary electrons either repeat the same process by impinging on neighbouring structures or are absorbed by the geometry. This way, the angular dependence of  $\delta_{\text{max}}$  (Eq. (2.2)) cancels out. However, these models only focus on simple surface geometries, and do not account for nano-features on top of the grooves (visible in Fig. 2.9b). On a microscopic scale, the primary electrons impinge at an inclined angle on the surface structure. Experimentally, metallic surfaces were roughened using various techniques such as thermal oxidation [30] or electrical discharge machining [69]. The breakthrough was the generation of high absorptive [72], grooved structures using ns pulsed lasers [73–75]. Short and ultrashort pulse laser processing is an effective method to structure and functionalize surfaces. When the laser light is scanned across a surface, material is ablated, followed by an expanding plasma plume, and ejected particles from the plasma plume are partially redeposited on the surface. This process results in micrometer deep trenches decorated with particles, as shown in Figure 2.9b, that reduce the SEY to below 1 (Fig. 2.8c). Laser-induced

surface structures were then proposed for SEY reduction to mitigate electron clouds in particle accelerators [1]. A laser-treated test surface with  $\text{SEY} \leq 1$  proved the suppression of electron multipacting in the SPS at CERN [2]. In contrast to other techniques, the laser processing can be applied at atmospheric pressure, the Cu layer is directly patterned without adding other materials, and selected areas can be treated.

## 2.4 Ultrashort pulse laser ablation

This section focuses on ultrashort pulse laser ablation: the laser properties, the laser-matter interaction, the influence of laser parameters on the surface properties, and its applications including SEY reduction for electron cloud mitigation in particle accelerators.

### 2.4.1 Gaussian beam characteristics

Laser light is primarily a flux of photons described by an electromagnetic wave. It is a transverse wave where the magnetic and electric fields are located exclusively in planes perpendicular to the direction of propagation. In the fundamental transverse mode  $\text{TEM}_{00}$  of the laser resonator, the intensity distribution  $I(r, t)$  of a pulsed laser is Gaussian in its spatial  $r$  and temporal  $t$  property. It is given by [76]:

$$I(r, t) = I_0 \exp\left(\frac{-2r^2}{\omega_0^2}\right) \exp\left(-4 \ln\left(\frac{2t^2}{\tau_p^2}\right)\right), \quad (2.3)$$

with the beam waist  $\omega_0$ , the pulse duration  $\tau_p$ , the maximum intensity  $I_0 \approx \frac{2E_p}{\pi \tau_p \omega_0^2}$ , and  $E_p$  being the pulse energy. The temporal Gaussian profile is an approximation and may vary depending on the laser system used. The integration over the irradiated area  $A$  results in the power distribution of the laser pulse, which is again Gaussian in time:

$$P(t) = \int_A I(r, t) dA = P_0 \exp\left(-4 \ln\left(\frac{2t^2}{\tau_p^2}\right)\right), \quad (2.4)$$

with the peak power  $P_0 \approx \frac{E_p}{\tau_p}$ . For a pulsed laser with repetition rate  $f_{\text{rep}}$ , the time averaged laser power is defined as:

$$P = E_p \cdot f_{\text{rep}}. \quad (2.5)$$

By integrating the intensity of the Gaussian laser beam over time, the fluence  $F(r)$  is obtained:

$$F(r) = \int_{-\infty}^{+\infty} I(r, t) dt = F_0 \exp\left(\frac{-2r^2}{w_0^2}\right), \quad (2.6)$$

with the peak fluence  $F_0 = \frac{2E_p}{\pi\omega_0^2}$ .

When a single line is scanned, the number of laser pulses  $N$  on a spot is:

$$N = \frac{f_{\text{rep}} \cdot 2\omega_0}{v}. \quad (2.7)$$

Consequently, the averaged deposited energy per spot amounts to:

$$F = N \cdot \frac{F_0}{2} = \frac{2E_p f_{\text{rep}}}{v\pi\omega_0} = \frac{2P}{v\pi\omega_0}. \quad (2.8)$$

Note that this is an approximation, using an average energy density of  $F_0/2$ . As previously stated, the laser has a Gaussian distribution of intensity.

The number of laser pulses  $N_{\text{acc}}$  on a spot of a scanned area with overlapping lines at distance of  $\Delta y$  is defined as:

$$N_{\text{acc}} = \frac{f_{\text{rep}} \cdot \pi\omega_0^2}{v\Delta y}, \quad (2.9)$$

and the accumulated laser fluence  $F_{\text{acc}}$  calculates to:

$$F_{\text{acc}} = N_{\text{acc}} \cdot \frac{F_0}{2} = \frac{P}{v\Delta y}. \quad (2.10)$$

This averaged quantity cannot be generally used for comparison of effects, but it allows to follow processing trends within defined parameter limits. For the ps-laser operating at 100 kHz, it is a useful value if the scanned lines neither overlap too much nor are too far separated ( $d/2 > \Delta y > 10 \cdot 2\omega_0$ ). In the case of a stronger overlap, the line distance  $\Delta y$  should be replaced by the laser diameter.

When a Gaussian beam is focused, its beam waist  $\omega(z)$  is minimal in the focal plane  $\omega(z=0)$  and diverges along the propagation direction  $z$ :

$$\omega(z) = \omega_0 \sqrt{1 + \left(\frac{z}{z_R}\right)^2}, \quad (2.11)$$

with  $z_R$  being the Rayleigh length:

$$z_R = \frac{\pi\omega_0^2}{M^2\lambda}, \quad (2.12)$$

the laser wavelength  $\lambda$  and the beam quality factor  $M^2$ , which is  $M^2 > 1$  for a non-ideal Gaussian profile. At the Rayleigh length, the beam radius increases by a factor of  $\sqrt{2}$  and the laser intensity drops to 50 %.

Due to its wave nature, the beam is diffraction-limited and can therefore not be focused to an arbitrarily small spot. To obtain a small spot, the initial beam with a radius  $\omega_p$



## 2 Context of the study

should be expanded before being focused with a lens of focal length  $f$ . Consequently, the beam radius in the focal plane  $\omega_0$  calculates to:

$$\omega_0 = \frac{\lambda f M^2}{\pi \omega_p}. \quad (2.13)$$

For certain laser systems, the choice of  $\omega_p$  and  $f$  may be geometrically limited.

The laser radius  $\omega_0$  can be experimentally determined from the surface profiles engraved in the material using Liu's method [77]. For a Gaussian spatial beam profile, the relation between the trench width  $D$  and the laser power  $P$  can be written as:

$$D^2 = 2 \omega_0^2 \ln \left( \frac{P}{P_{th}} \right), \quad (2.14)$$

with  $P_{th}$  being the threshold laser power for material ablation. The laser radius  $\omega_0$  (defined at the width where the photon intensity is reduced to  $1/e^2$ ) can be determined from the slope  $\Delta = 2 \omega_0^2$  of a semi-logarithmic plot.

### 2.4.2 Ultrashort pulse laser-matter interaction

The ultrashort pulse laser interaction with a substrate is influenced by both the substrate (heat conduction, absorption coefficient, electron-phonon coupling) and the laser properties (pulse duration, wavelength, beam shape). The dominating ablation mechanism is determined by the deposited laser intensity and its spatial and temporal distribution. The following is a brief overview of the interaction processes involved in laser ablation such as (1) laser excitation of electronic states, (2) energy transfer and phase transitions/melting, and (3) thermal cooling/re-solidification/material removal [76, 78–81]. An overview of the process is given in Figure 2.10a. The main focus is on ultrashort (fs/ps) laser irradiation of metals, since it is used in this study.

#### 1) Laser excitation of electronic states

When a metal, featuring an electron gas, is irradiated with fs laser pulses, electrons from the conduction band near the Fermi level absorb photons when they collide with other charged particles or, in the other words, when they change momentum upon deflection in the electric field of other particles. This process is called inverse bremsstrahlung. Commonly these are interband excitations of s/p-band electrons. However, interband transitions from d-bands to s/p-bands are also probable, if the photon energy is larger than the distance between the edge of occupied states (d-band) and the Fermi level. In the case of copper, the d-band is fully occupied ( $[\text{Ar}] 3d^{10} 4s^1$ ) and with 2 eV close to the Fermi level. Inelastic scattering processes between the excited higher energetic electrons with the remaining electrons in the conduction band lead to a thermalization of the electronic system on a timescale of a few femtoseconds, approximately equal to the laser pulse duration. This results in a thermal equilibrium of conduction electrons at higher temperature, described by a new Fermi-Dirac distribution of elevated temperature.

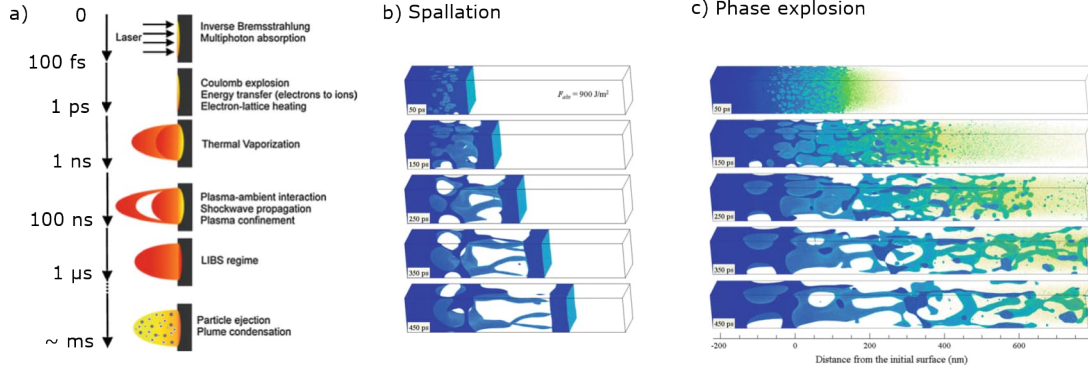


**Figure 2.10:** a) Time scales of fs laser ablation process. Figure taken from Ref. [82], two temperature model molecular dynamics (TTM-MD) simulation of metal (Al) transformation during b) laser spallation and c) phase explosion, irradiated with fs laser pulses at fluences of  $0.09 \text{ J cm}^{-2}$  and  $0.2 \text{ J cm}^{-2}$ , respectively. Figure taken with permission from Ref. [83].

In case of semiconductors and insulators, the photon absorption process is more complex. Under intense laser irradiation, free electrons are photo-excited from the valence to the conduction band via single- or multiphoton absorption that is determined by the ratio of the band gap to the photon energy and/or via tunneling ionization. After the conduction band is filled with free electrons, they absorb the laser energy by inverse bremsstrahlung, due to increased collision frequency between charged particles. Now they can gain enough energy to ionize neutral atoms in collisions. This process is called avalanche ionization. After the laser pulse, the generated free carriers are gradually or swiftly recombining to the ground or defect state depending on material type [84].

The generation of free electrons in semiconductors and insulators, excitation of d electrons in transition metals, and heating of the electrons in the conduction band cause a dynamic change of the optical material response to laser irradiation. In metals, the reflectivity is strongly reduced at relatively high laser fluences after single laser pulses [85, 86].

## 2) Energy transfer, phase transitions, and melting

The built-up thermodynamic non-equilibrium between the hot electrons (at temperature  $T_e \approx 10\,000 \text{ K}$ ) and the cold lattice of atoms and ions ( $T_l$ ) equilibrates through electron-phonon collisions on a time scale of picoseconds. The electronic heat conductivity  $k$ , the heat capacity  $c$ , and the strength of the electron-phonon coupling  $G$  determine the energy transport from the hot surface layer to the bulk of the metal, and ultimately the electron-lattice equilibrium temperature.

To describe the energy transport, the consecutive phase changes (from solid to liquid) and the resulting ablation depth, hydrodynamic or molecular dynamic (MD) simulation models are usually combined [87–94]. The basis of which is usually the description of

the thermodynamic non-equilibrium in one dimension  $z$  by the two temperature model (TTM) [95, 96]:

$$c_e \frac{\partial T_e}{\partial t} = \frac{\partial}{\partial z} \left( k_e \frac{\partial T_e}{\partial z} \right) - G (T_e - T_l) + S, \quad (2.15)$$

$$c_l \frac{\partial T_l}{\partial t} = \frac{\partial}{\partial z} \left( k_l \frac{\partial T_l}{\partial z} \right) + G (T_e - T_l), \quad (2.16)$$

with the laser source term  $S$ , which simulates the excitation of conduction band electrons. The latter includes both properties of the laser source (temporal and spatial profile) and optical properties of the material (absorption/reflectivity, optical penetration depth etc). A simplified expression for  $S$  is given by  $S = I(t)A\alpha \exp(-\alpha z)$ , with the temporal laser intensity  $I(t)$ , the surface transmissivity  $A = 1 - R$ , and the material absorption coefficient  $\alpha$  [96]. This however does not consider reflectivity changes of the material during laser irradiation, that was observed after few ps of laser irradiation [92]. More elaborated expressions for  $S$  were included elsewhere [92, 93].

### 3) Thermal cooling, re-solidification, and material removal

Two ablation regimes have been identified for fs laser ablation: spallation and phase explosion. At fluences slightly above the ablation threshold ( $0.5 \text{ J cm}^{-2} < F < 2 \text{ J cm}^{-2}$  for Cu [92, 93] using 800 nm, 120 fs and 1 kHz), the relaxation of the laser-induced compressive stresses drives heterogeneous nucleation and the growth of subsurface voids in a subcritical liquid phase, as observed in a two temperature model molecular dynamics simulation in Figure 2.10b. This process is known as spallation and occurs in the surface region of the target, resulting in minor ablation.

During phase explosion at fluences well above the threshold ( $\geq 2 \text{ J cm}^{-2}$  for Cu [92] using 800 nm, 120 fs and 1 kHz), the liquid regions in the upper part of the expanding foam structure are surrounded by vapor. The evaporation can occur faster than the electron-phonon energy transfer and is therefore non-thermal, while in the deeper regions of the target, large voids are created by a melting front. The explosive removal of hot matter triggers a strong convective cooling that limits further heat diffusion and freezes the churned melt front, resulting in the characteristic topographies of churned melt [97].

The ejected plume is a mix of vaporized atoms at the front part of the plume, followed by medium sized clusters of atoms and large droplets from the slow process of liquid decomposition (Fig. 2.10c). The large clusters or droplets from deeper regions have higher internal temperatures ( $\approx 4000 \text{ K}$  [83]) than the small clusters. The more efficient cooling of the top part of the plume can be attributed to the explosive decomposition and fast expansion of the mixture of vapor and small clusters, in contrast to the slower cooling of the larger clusters in the tail of the ablation plume. Similar observations have been made in plasma diagnostics, where the plasma plume splits into a fast component with optical emission characteristic of neutral atoms and a slow component

with blackbody-like emission, indicating the presence of hot clusters [98–101]. Phase explosion is usually characterized by a steep increase in ablation depth when the laser fluence increases [93]. It is the dominating ablation mechanism in femtosecond laser ablation at high fluences. However, both regimes can occur simultaneously within the laser spot: phase explosion at the maximum fluence of the spot and spallation in its periphery [83].

For longer pulse durations (ns), the ablation mechanism changes. The process is dominated by melting as the thermalization of both electrons and lattice occurs during the laser pulse. A thermal equilibrium exists, rendering the TTM unnecessary. Consequently, the process is no longer dominated by explosive pressure changes and high velocities [102]. These changes in laser-matter interaction result in less precision on the processed target. The structures are primarily composed of melt and exhibit a higher degree of roughness [103], rather than sharp edges [96]. Picosecond pulse durations are in an intermediate regime, leading to a combination of thermal and non-thermal effects, which also depends on the laser fluence applied [104].

### 2.4.3 Laser-plasma interaction

During the laser pulse, energy is transferred onto the surface and a plasma is ignited at a time scale of ns, as shown in Figure 2.10a. The material that is evaporated from the target forms a thin layer of very dense plasma, consisting of electrons, ions, and neutrals. The laser beam is absorbed by the plasma, causing an increase in temperature and pressure. As a result, the plasma expands into the surrounding atmosphere. The duration of the expansion depends on the laser pulse duration and can last several hundreds of ns. At sufficiently high energies, plasma splitting occurs, separating the vapor from heavier species. This is experimentally observed using fast photography and illustrated in Figure 2.11a. Plasma confinement starts as energy is dissipated by interacting with the cold surrounding. The cool down phase and particle redeposition can last several  $\mu\text{s}$  (Fig. 2.11).

The plume expands adiabatically and almost collision free in vacuum. A background gas can be used to reduce the kinetic energy of the plume species and to increase the number of chemical reactions between the plume and the gas, as well as increasing the formation of nanoclusters and nanoparticles through inelastic atomic collisions [80]. When processed in air, the particles are oxidized in the plasma phase. This can be prevented by an inert gas atmosphere.

### 2.4.4 Consequences on the surface structure

Tuning the laser parameters enables the generation of a variety of laser structures [82, 85] with defined properties, e.g. low reflectivity [72, 105, 106], high emissivity, wettability [107–109], tribology [110] or structural coloring [111–113]. The scan pattern defines

## 2 Context of the study

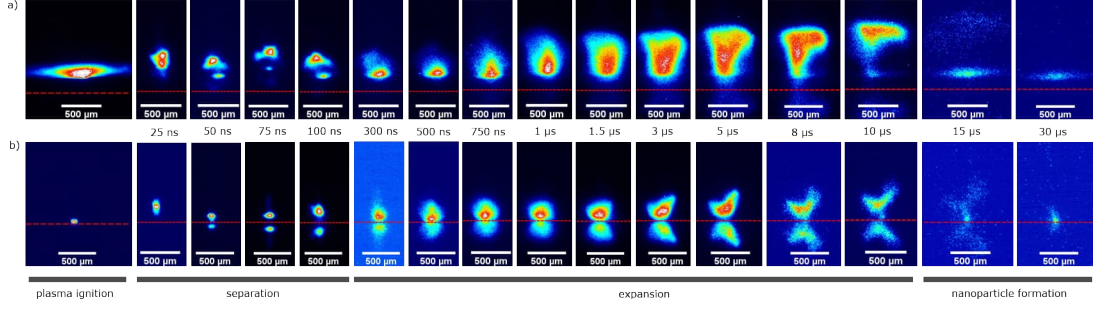


**Figure 2.11:** Fast photography of plasma expansion process of fs laser irradiated Cu at an average laser power of a) 760 and b) 112 mW, a repetition rate of 1 kHz, and scanning speed of  $1 \text{ mm s}^{-1}$ . The dashed red line indicates the sample surface. The color code refers the intensity (not normalized). Photography performed by Afaque M. Hossain.

if pyramids [72], holes [103] or grooves [2] are formed. At laser fluences close to the ablation threshold, the material transformation is dominated by spallation as discussed above (Sec. 2.4.2). In this regime, Laser Induced Periodic Surface Structures (LIPSS) are formed either via the superposition of the incident laser pulse and a plasmon wave within the irradiated substrate or via self-organization of matter [114, 115]. They are characterized by sub- $\mu\text{m}$  scale ripples, oriented either parallel or perpendicular to the laser pulse polarization. Two types of LIPSS are typically distinguished [114]: low spatial frequency LIPSS (LSFL) with a periodicity  $\Lambda$  close to the laser wavelength  $\lambda$  ( $\lambda/2 < \Lambda_{\text{LSFL}} < \lambda$ ) at normal incident laser radiation and high spatial frequency LIPSS (HSFL) ( $\Lambda_{\text{HSFL}} < \lambda/2$ ) [114].

### Ablation depth and volume

A relation between the ablation depth  $\Delta z$  and the laser power  $P$  exists [116]:

$$\Delta z = \frac{1}{\alpha_{\text{eff}}} \ln \left( \frac{P}{P_{\text{th}}} \right), \quad (2.17)$$

with the effective absorption coefficient of the material  $\alpha_{\text{eff}}$  and using the Beer-Lambert law.

In general, the crater depth or the aspect ratio of the crater increases, the more energy is deposited per surface area [117, 118]. The accumulated fluence can be increased by increasing the number of pulses  $N$ , increasing the average laser power  $P$  (pulse energy  $E$  and repetition rate  $f_{\text{rep}}$ ), or decreasing the laser radius  $\omega_0$  (Eq. (2.8)). The ablation is dependent on the material and can be influenced by absorption and heat conduction (Sec. 2.4.2). In semiconductors and insulators, the laser wavelength plays a significant role in the absorption process, which is based on multiphoton absorption. The accumulation of multiple laser pulses increases the absorptivity of the material, as

the roughening of the spot area reduces the surface reflection, resulting in a decrease of the ablation threshold due to incubation effects [119–121]. Similar effects can be achieved when processing in a pre-pulse (burst) mode, leading to an increased ablation rate [122]. A decrease in ablation efficiency is observed when the laser irradiates the surface at an oblique angle [123].

### Properties of laser-induced nanostructure

The more material is ablated, the more species collide in the plasma plume and the more particles are redeposited onto the surface. Whether particle generation is desirable or not, depends on the application. In pulsed laser deposition (PLD) for example, the ablated particles are condensed on a different substrate to grow films [124–126]. Particle deposition on the surface is greater when processed in a gas atmosphere compared to vacuum conditions. This is due to the free expansion of the plasma in vacuum and the suction of the particles [127–129]. The particle size ranges from few nm (vapor) up to several hundreds of nm ejected from deeper parts in the material [83].

### 2.4.5 Applications of laser surface treatments to reduce the SEY

The SEY of laser-treated surfaces is mainly influenced by the surface geometry, namely the micro- and nanostructures. In particular, surfaces with micrometer deep trenches of high aspect ratio decorated with cauliflower features had been studied for SEY reduction [130–132], for which a low SEY of  $\delta_{\max} = 0.7$  was achieved [131] in laboratory-scale experiments. These are generated at high average laser power ( $\sim 1$  W) and low scanning speed ( $10 \text{ mm s}^{-1}$ ) [131], resulting in a significant increase of surface roughness. The SEY decreases with higher aspect ratio between the trench height and width [69, 132]. However, laser parameters were merely changed to minimize the SEY, and no clear correlations were established between the processing parameters and the changes in surface composition and topography. The optimization efforts towards low SEY mainly focused on processing Cu with a green laser, as it was assumed that 532 nm photons ablate copper more efficiently than 1030 nm photons.

LIPSS structures were also investigated for SEY reduction [133], resulting in a maximum SEY of  $\delta_{\max} = 1.6$  [134]. These structures can be fabricated nearly particle-free, which is advantageous for use in vacuum components of particle accelerators. Cleaning of the laser-processed surfaces, such as ultrasonication, results in an increase of SEY [2, 132, 135], due to the altered surface morphology. On the other hand, similar tendencies as for untreated surfaces apply (see Sec. 2.3.3): A contaminant-free surface has a lower SEY. This was observed by thermal heating [131] or electron conditioning [1, 136]. The oxidation state plays a minor role for SEY reduction compared to the geometrical modification, as low SEY values ( $\delta_{\max} \leq 1$ ) were observed for both CuO-dominated and Cu<sub>2</sub>O-dominated surfaces [131]. Processing in a gas atmosphere minimizes surface/particle oxidation during the plasma phase as opposed to processing

in air. Using  $N_2$  resulted in  $Cu_2O$ -dominated surface instead of  $CuO$  obtained in air with a considerable lower SEY [131]. In addition, laser-processing in an inert gas atmosphere confines the plasma expansion. This leads to different particle compositions. At cryogenic temperatures, the SEY increases compared to RT due to molecules that adsorb on the cold surface [131].

## 2.5 Requirements and challenges for laser processing the inner beam screen surfaces of the LHC

### 2.5.1 Technical requirements

The surface treatment is expected to be applied in cryogenic areas of the LHC near the interaction points (IR1 and IR5) where the electron cloud density is anticipated to reach unacceptable values. These BSs are installed in superconducting magnets (Fig. 2.3a) that will be brought to the surface, without extracting the BSs from the magnets. Since the *in situ* a-C coating would damage the cryosorbers, installed on these BS, an *in situ* laser treatment of  $8 \times 10$  m BSs is envisaged.

The BS is an up to 15 m long tube with a non-circular cross section (see Fig. 2.3) and a minimal aperture of only 61 mm (see 2.1) between the flat faces. Its inner surface must be laser treated. The beam delivery from the laser source to the target surface is a technical challenge, because the laser beam must be guided over several meters and focused on the inner surface, where spatial access for the laser optics is limited due to the small aperture of the BS. This necessitates the use of optical fibers [137] or similar technologies. In addition, assuming that the light source is positioned on the longitudinal central axis, the non-circular cross section requires a laser treatment at variable focal distances, depending on the azimuth angle. Up to now, no industrial solution is available to process such an object. Considering the length of the BS, processing is likely to take several days or weeks. It is crucial that the entire system remains stable during this period, particularly the optical system, which must be in thermal equilibrium. Moreover, the surface must be uniformly treated. Therefore, a dedicated laser surface treatment setup, which meets all the mentioned requirements, has been developed. The system includes a hollow-core photonic crystal fiber for ultrashort laser pulses combined with a beam delivery system and robot-assisted beam scanning.

### 2.5.2 Treatment requirements

In the vacuum system of the LHC, the surface treatment must meet the following requirements:

- The SEY maximum should be in the range of  $\delta_{\max} \sim 1.1 - 1.3$  to not exceed the multipacting thresholds (see Sec. 2.3.3) or it should decrease close to 1 upon electron exposure during beam scrubbing (Sec. 2.3.3).
- The surface modification depth shall not exceed  $25\text{ }\mu\text{m}$  to ensure a low impedance at cryogenic operation temperature (5 - 20 K) of the colaminated  $75\text{ }\mu\text{m}$  thick Cu layer. A higher surface resistance deteriorates the proton beam quality and adds a contribution to the heat load on the cryogenic system of the surrounding cold mass of the magnet.
- A  $\text{Cu}_2\text{O}$ -dominated surface is preferable to CuO. Oxidation of a Cu surface cannot be completely suppressed as  $\text{Cu}_2\text{O}$  naturally forms in air. However, the formation of CuO should be avoided as it can lead to charging of the laser-treated surface at cryogenic temperature [131], causing an additional heat load on the cryogenic system.
- The quantity and size of redeposited particles resulting from the laser ablation process must be limited. It has not yet been measured, whether the laser-generated particles may detach randomly from the surface during LHC operation or if those at the bottom of the BS may be lifted by the proton beam.

Flying particles that cause beam losses are commonly referred to as unidentified falling objects (UFOs). Particle beam interactions become critical at a particle diameter greater than  $10\text{ }\mu\text{m}$ . For particle diameters larger than  $60\text{ }\mu\text{m}$ , detachment can cause significant damage to machine components or result in a magnet quench [138]. In such an event, the beam must be extracted from the machine. Objects that lie at the bottom of the BS are categorized as unidentified lying objects (ULOs). It is still under investigation whether they can be charged [139] and lifted by the proton beam.

In addition, the ablated material can deposit on the laser optics during processing and reduce the light intensity in the interaction zone. Therefore, surface structures with reduced particle density are of special interest.

- The time, in which all magnets need to be processed, is limited to the duration of the long shutdown 3 and its technical schedule. A reasonable processing time for one magnet is one month.





## 3 Sample preparation and characterization methods

This chapter is divided into three main parts. First, the laser setups used for processing are presented. All flat surfaces were processed using commercial laser setups at Leibniz Institute of Surface Engineering (IOM) (Leipzig, Germany). The surface properties of the flat surfaces are discussed in Chapter 4. All curved surfaces and BSs were treated using two setups built and commissioned at CERN, referred to as *in situ* setups (532 nm and 1030 nm). They are designed to treat the BSs installed in the magnet complexes of the LHC. The treatment will take place on the surface rather than underground. However, the BSs will not be extracted from the magnets. The *in situ* setups were described and characterized in more detail, as they are not standardized. The surface analysis results of curved surfaces are discussed in Chapter 5, while Chapter 6 covers the results of BSs. Second, the surface characterization methods are introduced such as SEY and conditioning measurement. In the third part, the untreated Cu surfaces were analyzed prior to the laser processing.

### 3.1 Laser processing of flat surfaces

A Nd:YVO<sub>4</sub> pulsed laser (Lumera Super Rapid) was used as photon source with fixed pulse duration ( $\tau_p = 12$  ps) and repetition rate ( $f_{\text{rep}} = 100$  kHz, unless otherwise defined). The primary (1064 nm), doubled (532 nm), and tripled (355 nm) laser frequencies were employed. The linearly polarized Gaussian beam (with a quality factor  $M^2 = 1.3$ ) was focused on the surface by a f-theta lens with focal lengths of 165 (infrared (IR) and green) and 103 mm (ultraviolet (UV)), and scanned in parallel lines with distances  $\Delta y$  of 10 and 50  $\mu\text{m}$ , as illustrated in Figure 3.1. The laser radii were determined following Liu's method [77] and were evaluated to be 13.2 (IR), 5.8 (green), and 14.6  $\mu\text{m}$  (UV), respectively. Laser processing in air was performed varying the average laser power  $P$  and the scanning speed  $v$  from 10 up to 4100 mW and from 1 to 200  $\text{mm s}^{-1}$ , respectively.

A solid-state laser (Carbide CB3-40W from Light Conversion), which replaced the previous laser, has a tunable pulse duration of 238 fs–10 ps and repetition rates of 100 kHz–2 MHz. Unless otherwise defined, a pulse length of 10 ps and a repetition rate of 100 kHz were used for all experiments. The primary (1030 nm), doubled (515 nm),

### 3 Sample preparation and characterization methods

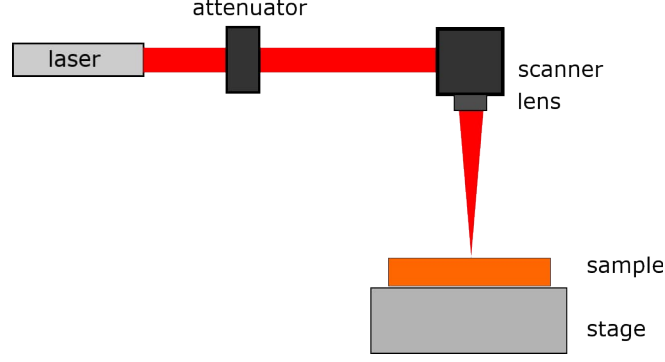


**Figure 3.1:** Schematic of ultrashort pulse laser treatment setup used for the processing of flat Cu surfaces at IOM.

and tripled (343 nm) laser frequencies were used. Identical focusing lenses were used, resulting in radii of 23.0 (IR), 13.9 (green), and 15.9  $\mu\text{m}$  (UV).

### 3.2 Green and infrared *in situ* laser setups

Since no commercial solutions are available to treat the inner surface of a 10 m long tube with a minimum cross-sectional diameter of 46 mm, the *in situ* laser setup was designed to treat such objects. The setups are described and characterized in more detail below due to the unique combination of fiber technology and robot-assisted scanning. The laser processing of small, curved samples was mainly performed on the green *in situ* setup, while the IR laser setup, was primarily used to process longer BSs and tubes. Their working principle is similar, but there are slight differences in the laser source parameters (Tab. 3.1) and the laser beam properties (diameter, Rayleigh length), which are discussed in Section 3.2.2.

**Table 3.1:** Overview of parameters of green and IR *in situ* laser setups.

Component	Parameters	Green laser setup	IR laser setup
Laser	Wavelength $\lambda$	532 nm	1030 nm
	Pulse duration $\tau_p$	12 ps	500 fs
	Repetition rate $f_{\text{rep}}$	200 kHz	500 kHz
	Maximum average laser source power $P$	25 W	20 W
	Laser diameter at laser output	5 mm	5 mm
Fiber	Mode field diameter (MFD)	26.4 $\mu\text{m}$	42 $\mu\text{m}$
	Hollow-core diameter $2R_{\text{core}}$	38 $\mu\text{m}$	60 $\mu\text{m}$
	Collimated beam diameter at output cell $2\omega_p$	1.5 mm	2.6 mm

### 3.2.1 Description of the laser treatment setups

An overview of the laser treatment setup is shown in Figs. 3.2 and 3.3. The aim is to imprint micro- and nanostructures on the Cu surface of the BS. Therefore, an ultrashort-pulse laser source (Tab. 3.1) was chosen to ablate the surface efficiently. After the laser source, a beam delivery system (BDS) was installed in which the power ( $P_{\text{BDS}}$ ) is regulated by an attenuator composed of a half-wave plate (HWP), which allows for selective rotation of the light polarization axis, and a fixed thin film polarizer to filter out any light not aligned with the polarizer axis. The laser beam diameter is focused into a 15 m long hollow-core photonic crystal fiber (HCPCF) to a mode field diameter (MFD) of:

$$\text{MFD} = 2 \sqrt{A_{\text{eff}}/\pi} = \begin{cases} 26 \mu\text{m} \text{ (green)}, \\ 42 \mu\text{m} \text{ (IR)}, \end{cases} \quad (3.1)$$

using the approximation of the effective area  $A_{\text{eff}} \hat{=} 0.482 \pi R_{\text{core}}^2$  for a core radius  $R_{\text{core}}/\lambda > 27$  as previously proposed [140].

The HCPCF guides the laser pulses to the inner surface of the BS via inhibited coupling (IC) [141]. Since an ultrashort pulse laser is used, a solid silica fiber is not appropriate due to alterations in pulse characteristics (such as spectrum broadening and pulse duration) and deterioration of the beam transmission properties (including damage and intensity losses along the fiber) [141–143]. These factors can impact the quality of the processed material due to a change in the laser-matter interaction [102].

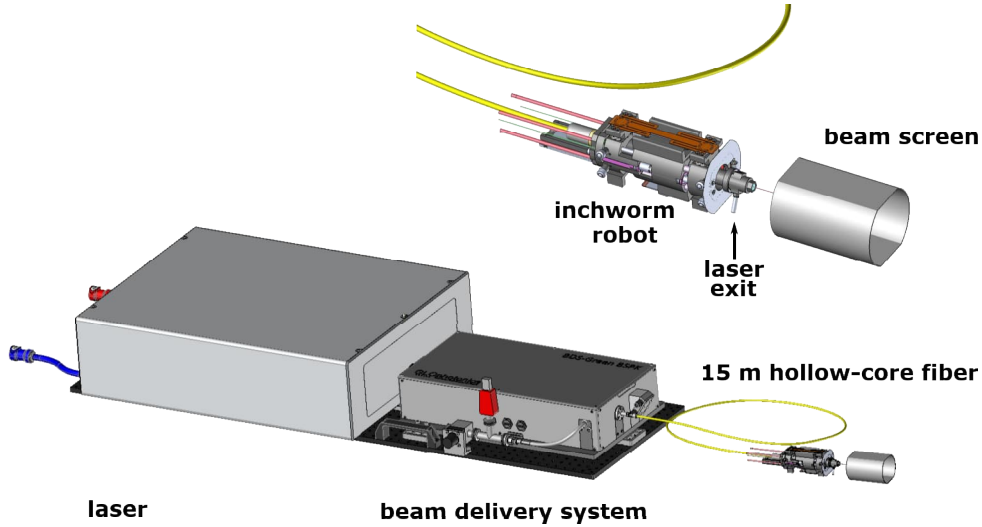


**Figure 3.2:** *In situ* laser treatment setup composed of an ultrashort pulse laser source, a beam delivery system (GLOphotronics), a 15 m hollow-core photonic crystal fiber (GLOphotronics), and an inchworm robot (Waygate Technologies Robotics) that travels inside the beam screen and irradiates the inner Cu surface. Published in Ref. [144].

### 3 Sample preparation and characterization methods

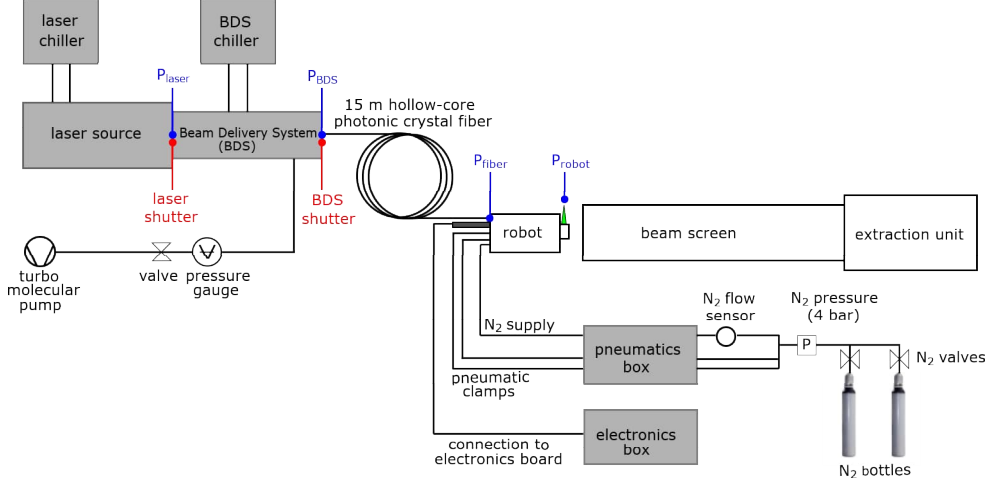


**Figure 3.3:** Detailed visual representation of the entire laser treatment system, which comprises control, monitoring, and supply components. The positions where light power is measured are highlighted in blue and the laser shutters are indicated in red. Published in Ref. [144].

The HCPCF is designed with either an 8-tube single ring (green laser) or a 7-cell (the number of capillaries taken off from the preform to make the core), 3-ring (number of cladding rings) Kagome structure (IR laser), respectively (Fig. 3.4, top row). The green fiber has a hollow-core diameter of  $2R_{\text{core}} = 38 \mu\text{m}$ , while the IR fiber has a larger diameter of  $60 \mu\text{m}$ . The geometry of the IR fiber is considered more robust and therefore preferred due to its geometry. In contrast, the green fiber features a single tubular arrangement instead, because small core diameters required for short wavelengths are difficult to fabricate. The coupling into small core diameters is impacted by thermal fluctuations that may occur during extended operation time. To address this issue, the system by water cooling of the critical components involved in light coupling. In addition, beam drifts are corrected using piezo-actuated mirrors in the in the BDS. These mirrors adjust the beam position based on feedback from two 4-quadrant photodiodes that continuously monitor beam position offsets. To maintain the the temporal and spectral shape of the pulse, the fiber is evacuated using a turbo molecular pump (TMP). The hollow-core of the green fiber is evacuated first and operated under static vacuum at a base pressure of about 2 mbar, while the IR fiber is pumped continuously to a base pressure of  $1 \times 10^{-3}$  mbar. The fiber is coiled to a bending radius of 15 cm for efficient cable management during the targeted *in situ* treatment. At the output cell of the HCPCF, the beam is first widened and then collimated to a spot diameter of  $2\omega_p = 1.5 \text{ mm}$  with  $\sim 91\%$  ellipticity (green) and  $2\omega_p = 2.6 \text{ mm}$  with  $> 98\%$  ellipticity (IR) (see Fig. 3.4, bottom row). These values were chosen to reach similar laser spot sizes for green and IR light and large Rayleigh lengths (Sec. 3.2.2). The fiber is then inserted into a robot in which the beam is focused by a plano-convex lens, then deflected by a  $45^\circ$  oriented mirror inside a motorized rotating unit and directed towards the BS surface through a hollow tube that acts as

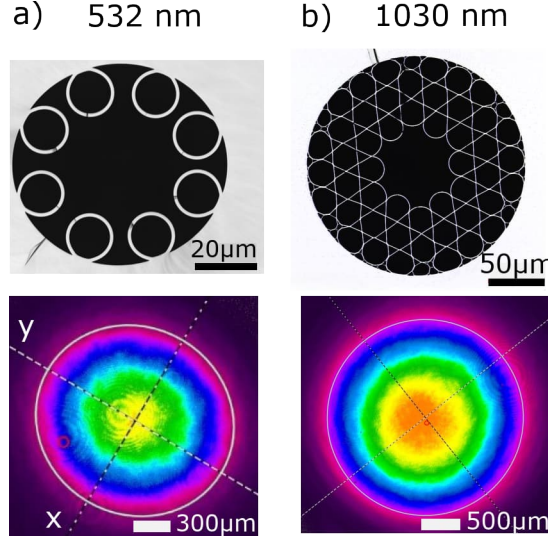


**Figure 3.4:** a) 532 nm laser setup: cross-sectional photograph of the hollow-core fiber with eight capillaries and the evacuated hollow-core (black part) and collimated laser spot profile at the fiber output cell ( $2\omega_{px} = 1.45$  mm,  $2\omega_{py} = 1.6$  mm). b) 1030 nm laser setup: cross-sectional photograph of the hollow-core fiber with 7-cell (the number of capillaries taken off from the preform to make the core), 3-ring (number of cladding ring) Kagome structure with the evacuated hollow-core (black part). Collimated laser spot profile at the fiber output cell ( $2\omega_{px} = 2.66$  mm,  $2\omega_{py} = 2.66$  mm). Left column published in Ref. [144].

nozzle for out-streaming nitrogen gas to minimize both oxidation of the Cu BS surface and contamination of the optics in the internal part of the robot. This component is visible in Figs. 3.2 and 3.5a. It rotates at defined speed to perform the treatment. The robot is designed to scan the laser beam across the surface by crawling (supported by nitrogen actuated clamps ( $\sim 4$  bar)) inside the BS, whose aperture is as small as 61 mm (Figs. 3.2 and 3.5). Moreover, it can be adapted to smaller BS geometries, such as those installed in arc dipole magnets of the LHC (BS type 50 A/50 L, see Tab. 2.1).

The gas supply for the pneumatic clamps and the nozzle flow is regulated using fast-switching valves and pressure sensors located in the pneumatics box. The flow rate is monitored by a flow meter positioned upstream of the pneumatics box and the robot is connected to an electronics box as shown in the schematic overview of the setup in Figure 3.3. During laser treatment experiments in the laboratory, the BS is placed inside a tube for safety purposes, and a vacuum-based extractor (Weller Laser Line LL 200V) generates a constant airflow to eliminate particles and dust produced during laser ablation. These particles are collected in a filter unit. The control of all equipment, including the robot, is managed through an embedded real-time industrial controller (Compact Rio) from National Instruments, paired with a customized user interface in LabVIEW. During treatments, the laser shutter remains open, while the delivery and

### 3 Sample preparation and characterization methods

synchronization of the beam is controlled by actuating the shutter in the BDS. A more detailed description of the software integration can be found elsewhere [145].

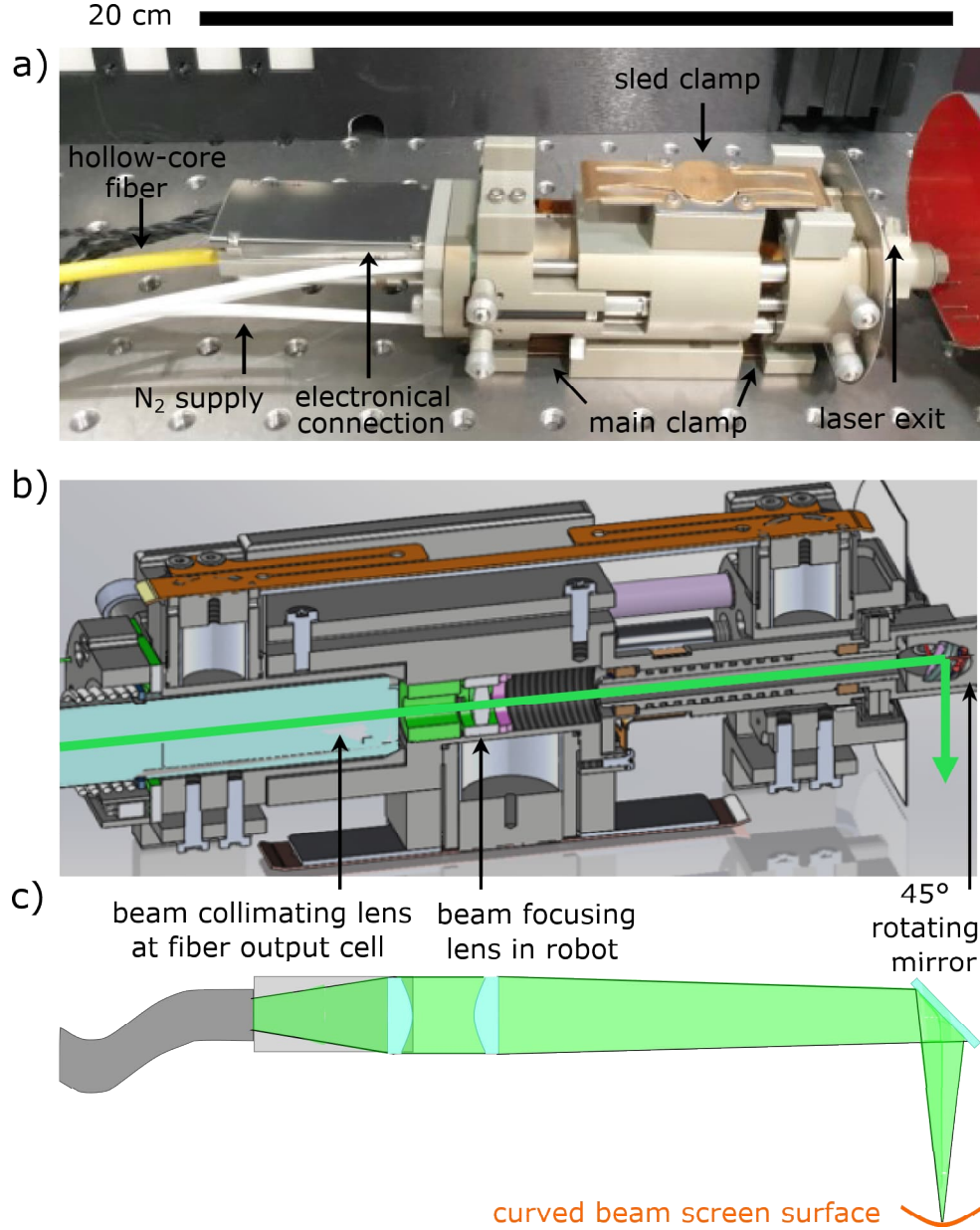


**Figure 3.5:** a) Photograph of the robot with indicated components. b) Cross-sectional 3D model visualizing the optical path of the laser light and the optical components inside the robot. c) Scheme of laser beam collimation at the fiber output cell, focusing by a plano-convex lens (with focal length  $f$ ) installed in the robot, and directing the beam via a rotating mirror onto the BS surface. Published in Ref. [144].

### Robot-assisted scanning and scan strategies

The robot (Fig. 3.5a) uses a coarse longitudinal motion to move forward in the BS between treatments and a precise longitudinal motion to move its laser scanning arm during treatments. The sled is linked to the main body through a linear rail and precise spindle (pitch 1 mm), enabling accurate control over its position along the linear axis. Pneumatic clamps on the sled and main body, powered by pressurized nitrogen ( $\sim 4$  bar), support the rough movement by alternately gripping and advancing the body/sled. The robot head, which directs the laser, rotates using intermeshing gears and a pinion. Both rotary and translational axes are driven by brushless direct current (DC) motors. A magnetic quadrature encoder converts the electronic signals into precise counts: 4 096 cts/mm on the linear axis and 32 768 cts/rev on the rotational axis. This results in an encoder resolution of  $0.24\text{ }\mu\text{m}$  (translation) and  $0.011$  degree (rotation) or  $0.62\text{ }\mu\text{m}$  on the curved beam screen surface, respectively.

The theoretical motor top speed is limited by the available voltage of 24 V. For the surface treatment, it translates into a maximum rotational scanning speed (defined along the scan line and relative to the BS surface) of  $\sim 200\text{ mm s}^{-1}$  and a maximum translational speed of  $\sim 50\text{ mm s}^{-1}$ , which corresponds to a minimum processing time of  $0.6\text{ s cm}^{-2}$  and  $2.3\text{ s cm}^{-2}$  respectively for a line distance of  $50\text{ }\mu\text{m}$ . However, the actual processing time is longer since readjusting the clamps of the robot requires approximately 10 % additional time.

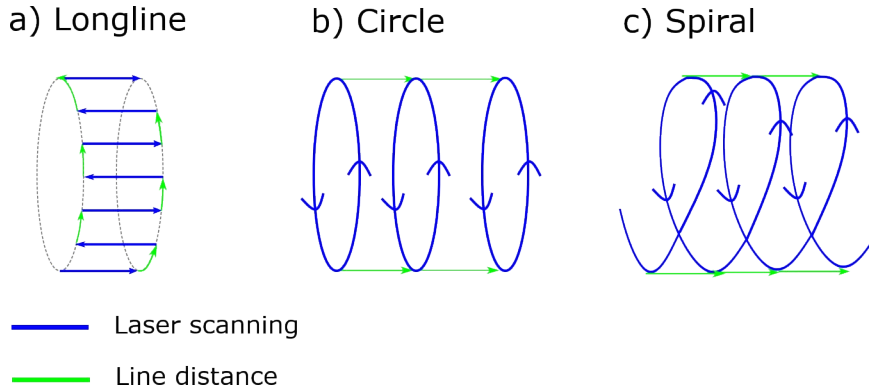


**Figure 3.6:** Implemented scan patterns that are executed by the robot. The BDS shutter is open during the line scanning (blue), and closed when moving to the next line (green) (a, b). During the spiral pattern, the shutter remains open all the time (c). The line distance (green) is defined by a rotational step for the longline movement (a), and by a linear move of the robot for circular (b) and spiral movement (c). Published in Ref. [144].

Integrating both linear and rotational motion, a variety of scanning patterns (Fig. 3.6) were developed and tested for surface processing. These patterns include: a) a longitudinal line movement (longline), where the line spacing is defined by a rotational



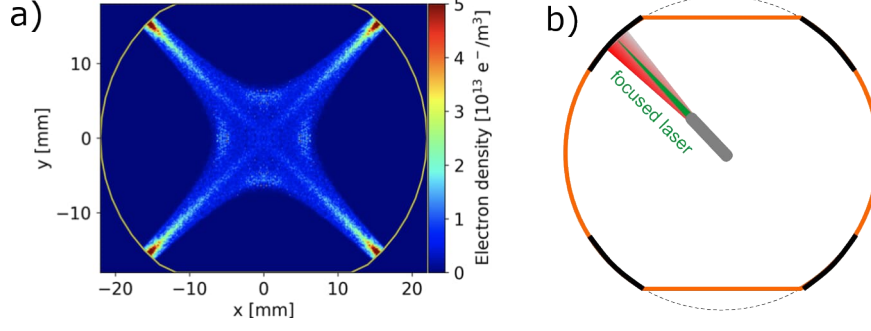


**Figure 3.7:** a) Electron cloud spatial distribution simulation [9] for quadrupole magnet. Figure extracted from Ref. [9]. b) Schematic of BS cross-section for selective treatment of a quadrupole: laser treatment of 4 corners (black), non-treated zones (orange).

move, b) a circular movement, where the laser beam is rotated azimuthally and the line distance is defined by a (fine) linear forward translation, and c) a spiral movement, which is a combination of azimuthal rotation and a continuous (fine) linear forward movement of the body whose velocity is adapted to the rotation speed, the geometry of the beam screen and the line spacing.

Since the electron cloud density in a quadrupole magnet (the ones likely to be laser-treated) is highest at the four corners of the BS (Fig. 3.7a), it is sufficient to treat only  $4 \times 7^\circ$  [146]. To ensure a margin, an angle between 15 and 20 degrees will be always treated. The selective treatment has the advantage that the cryosorbers, installed on the flat parts of some BSs, are not affected by the processing, in contrast to the case of a-C coating. Therefore, a selective treatment was implemented, in which the BDS shutter and the robot's movement are controlled to treat only selected parts of the BS of the standalone magnets of the LHC. This was implemented for the spiral and longline movement. The concerned zones are located on the curved part of the BS, which means that there is only one focal point. In summary, only a proportion of the entire inner BS surface would be treated. This reduces the processing time, impedance increase, and the risk of particles falling into the proton beam during operation. If not the entire surface is treated, it is also easier to insert a post-cleaning device into the pipe without damaging the treated surface.

### 3.2.2 Characterization of the setups

In the following, the system was set into operation to characterize the power transmission and stability, and the laser spot properties.

#### Power transmission and stability

Four points (Fig. 3.3) of the systems are relevant for monitoring the laser light power: at the laser output ( $P_{\text{laser}}$ ), at the output of the BDS before the beam injection into the fiber ( $P_{\text{BDS}}$ ), at the fiber output cell ( $P_{\text{fiber}}$ ), and at the robot head ( $P_{\text{robot}}$ ). The laser sources provide an average laser output power of up to  $P_{\text{laser}} = 25 \text{ W}$  (green) and  $20 \text{ W}$  (IR), which was restricted to  $11 \text{ W}$  for the green laser to avoid any degradation or local damage of the fiber. Since the power  $P_{\text{BDS}}$  that is injected in the HCPCF is not measured continuously, it was beforehand calibrated for different HWP angular positions. The measurement was fitted using Malus law [147], to characterize the power reduction by the combination of HWP and the linear polarizer in both systems. The results of these measurements are shown in Fig. 3.8a:

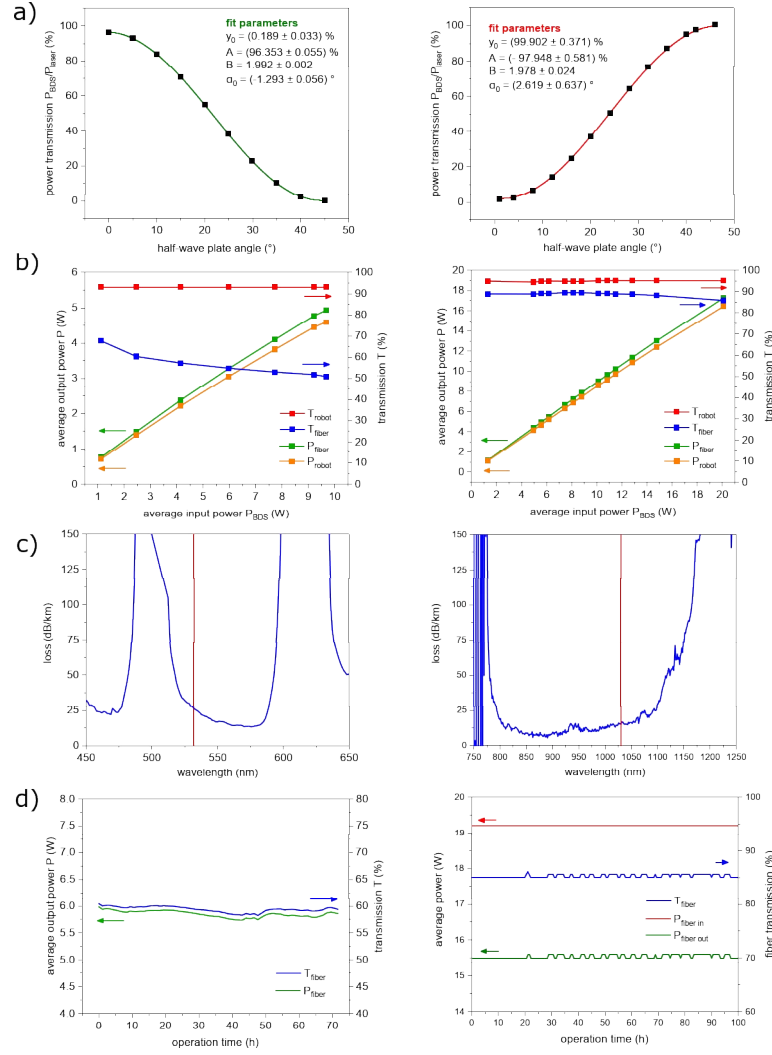
$$\frac{P_{\text{BDS}}}{P_{\text{laser}}} = y_0 + A \cdot \cos^2 \left( \frac{2\pi}{360^\circ} (B \cdot \alpha - \alpha_0) \right), \quad (3.2)$$

where  $\alpha$  corresponds to the HWP angle,  $\alpha_0$  is the alignment angle relative to the beam position;  $B$  is the periodicity of the HWP, which is close to ideally 2;  $A$  is the maximum of transmitted intensity, implying  $< 4$  losses for the green and IR (see Fig. 3.8a) due to reflections/absorption on the optical components; and  $y_0$  represents the transmitted intensity when the polarization direction behind the HWP is perpendicular (green)/parallel (IR) to the polarizer axis.

The average laser power at the fiber output  $P_{\text{fiber}}$  is not recorded permanently during processing of the BS due to the limited spatial access. It is therefore measured manually with an external thermal power sensor before and after laser processing. An overview of the measured power values is shown in Fig. 3.8b. The transmissions  $T_{\text{fiber}} = P_{\text{fiber}}/P_{\text{BDS}}$  of the fibers were determined at a bending radius of  $15 \text{ cm}$  and include the coupling efficiency into the fiber. For the green system, it amounts to  $\sim 70 \%$  ( $-1.3 \text{ dB}$ ) at low average input power ( $\sim 1 \text{ W}$ ), while it decreases to  $\sim 50 \%$  ( $-3 \text{ dB}$ ) at higher average input power ( $\sim 10 \text{ W}$ ). The transmission of the IR fiber is nearly constant at  $88 \%$  ( $-0.52 \text{ dB}$ ) for various average input powers and decreases slightly to  $85 \%$  ( $-0.64 \text{ dB}$ ) at the highest value of  $20 \text{ W}$ .

The attenuation (propagation losses) over a wide spectral range is shown in Fig. 3.8c. It was measured at GLOphotonics using a broadband source (supercontinuum from  $300 \text{ nm}$  to  $1800 \text{ nm}$ ) at low power ( $< 100 \text{ mW}$ ) to couple into the fiber, and an optical spectrum analyzer (OSA) to measure the output spectrum. The power difference was measured at both its full length and at a cut length of  $3 - 5 \text{ m}$  (cutback method) placed in a loose position of  $25 \text{ cm}$  bending radius. The attenuation of the green fiber

### 3 Sample preparation and characterization methods



### 3.2 Green and infrared *in situ* laser setups

amounted to  $25 \text{ dB km}^{-1}$  at the wavelength of 532 nm (see Fig. 3.8c), which corresponds to 0.375 dB (92 % transmission) for a length of 15 m. The attenuation of the IR fiber is  $15 \text{ dB km}^{-1}$  at 1030 nm, or 0.225 dB (95 % transmission), respectively.

Transmission losses in the setup are generally a sum of propagation losses ( $-0.375 \text{ dB}$  (green),  $-0.225 \text{ dB}$  (IR)), coupling losses at the fiber injection ( $-0.2 \text{ dB}$ ) and bending losses of  $-1.1 \text{ dB}$  (0.05 (green) and 0.02 (IR) dB/turn for a radius of curvature 11 cm), if the fiber is coiled along its full length. In sum, this results in an overall estimated loss of about 1.675 dB (green) and 0.777 dB (IR), corresponding to an estimated transmission of 68 % (green) and 83 % (IR), which roughly fits the measured transmission as discussed above. Bending losses in the green system have therefore a major impact on the transmission quality. The compromise found is to set the operating wavelength (532 nm) to the fifth quarter (wavelength-wise) of the transmission band (see Fig. 3.8c), which results in good beam quality but rather bend-sensitive transmission of the fiber. Moreover, the shorter the laser wavelength is, the smaller is the required core diameter of the fiber to reduce Rayleigh scattering at the surface roughness. The fabrication of small core diameter HCPCF remains challenging due to the difficulty in maintaining a thin, homogeneous microstructure along the fiber during the drawing process. Therefore, an infrared laser + fiber was selected for the new version of the *in situ* setup. The larger core diameter facilitates to couple the laser beam into the fiber and the transmission mode of the fiber (see Fig. 3.8c) is wider than for the green fiber, making it less sensitive to bending losses.

It has to be further noted that the 5 % losses caused by the optical components in the robot (lens, mirror, nozzle) are minor in both setups (Fig. 3.8b).

The setup was designed to perform large-scale surface treatments that can last several days or weeks. Therefore, the beam coupling must be reliable and robust to environmental variations in temperature and humidity without degrading the fiber to achieve a uniform laser treatment. A continuous measurement (at an early fiber age stage) over 70 h (green) and 100 h (IR) (Fig. 3.8d) showed a stable transmission of about 60 % and an average power at the fiber output of  $P_{\text{fiber}} = 5.9 \pm 0.1 \text{ W}$  (green) and 85 % at an average power at the fiber output of  $P_{\text{fiber}} = 16 \pm 0.1 \text{ W}$  (IR). Both setups provide power stability over long periods with marginal fluctuations of about 2 % of the nominal average laser power. However, the IR system is expected to last longer in long-term use because of its higher light transmission, which means less power loss/heat that can damage the fiber structure.

#### Laser spot characteristics at the beam screen surface

The theoretical Gaussian laser diameter  $2\omega_0$  in the focal point ( $z = 0$ ) at the BS surface increases with larger wavelength  $\lambda$ , smaller laser diameter at the fiber output cell  $2\omega_p$  and larger focal length  $f$  of the convex lens installed in the robot, according to Eq. (2.13). For the focusing, some geometrical limitations exist in the robot. To

### 3 Sample preparation and characterization methods

**Table 3.2:** Beam characteristics for various lens & beam screen configurations.

Configurations	(1)	(2)	(3)
Wavelength $\lambda$	532 nm	1030 nm	1030 nm
Laser frequency	200 kHz	500 kHz	500 kHz
Collimated beam at fiber output $2\omega_p$	1.5 mm	2.6 mm	2.6 mm
Quality factor $M^2$	1.3	$< 1.3$	$< 1.3$
Focal length $f$	90 mm	84 mm	75 mm
BS type (dimensions Tab. 2.1)	74	50 L / 50 A	50 L / 50 A
Spot diameter $2\omega_0$	52.8 $\mu\text{m}$	55.1 $\mu\text{m}$	49.2 $\mu\text{m}$
Rayleigh length $z_R$	3.2 mm	1.8 mm	1.4 mm

avoid striking internal walls, the laser diameter at the fiber output should not exceed 2.6 mm. Additionally, the available space for the lens position in the robot is limited to a maximum of 28 mm, which excludes certain focal lengths. The length of the optical path of the laser light from the fiber output cell to the BS surface depends on the type of BS to be treated. Taking all of these factors into consideration, three distinct convex lens configurations were chosen whose beam characteristics are outlined in Tab. 3.2: (1)  $f = 90$  mm for a large BS aperture (type 74) and 532 nm, (2)  $f = 84$  mm, and (3)  $f = 75$  mm for small BS diameters (type 50 L/50 A) and 1030 nm. According to Eq. (2.11), the theoretical beam waists in the focal point  $\omega(z = 0)$  are:

$$\begin{aligned}
 2\omega(z = 0 \text{ mm}) &= 2 \left( \omega_0 \sqrt{1 + \left( \frac{z\lambda M^2}{\pi\omega_0^2} \right)^2} \right) \\
 &= \begin{cases} (1) 52.8 \mu\text{m} (\lambda = 532 \text{ nm}), \\ (2) 55.1 \mu\text{m} (\lambda = 1030 \text{ nm}), \\ (3) 49.2 \mu\text{m} (\lambda = 1030 \text{ nm}). \end{cases} \quad (3.3)
 \end{aligned}$$

However, the 1030 nm beam diverges stronger as visualized in Figure 3.9a, resulting in a smaller Rayleigh length than the one for 532 nm (Tab. 3.2). At the maximum available average laser power at the robot exit of the green laser setup (5 W) and the laser frequency of 200 kHz, the peak fluence of a single pulse is  $2.3 \text{ J cm}^{-2}$  (configuration 1). Due to the higher frequency of 500 kHz used in the IR laser setup, the peak fluences at the same average laser power of 5 W are (2)  $0.8 \text{ J cm}^{-2}$  and (3)  $1.1 \text{ J cm}^{-2}$ , which is 35 % (config. 2) and 48 % (config. 3) compared to the peak fluence of the green laser, as shown in the Gaussian distribution in Figure 3.9b. To reach similar peak fluences with the IR laser, the average laser power must be increased to (2) 13.6 W or (3) 10.9 W, respectively. This corresponds to pulse energies of (2) 27.2  $\mu\text{J}$  and (3) 21.8  $\mu\text{J}$ .

### 3.2 Green and infrared *in situ* laser setups

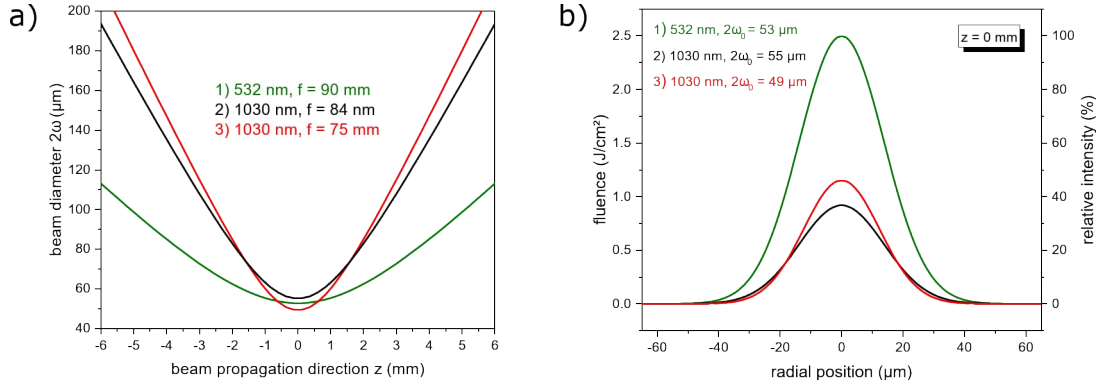


**Figure 3.9:** a) Calculated beam waist along focal axis  $z$  (according to Eq. (3.3)), b) Energy density (according to Eq. (2.6)) at  $z = 0$  of a single pulse at an average laser power of 5 W and laser frequencies of 200 kHz (532 nm) and 500 kHz (1030 nm). The full parameter settings are given in Tab. 3.2.

Since the perimeter of the BS is non-circular, the focal point is not always on the surface (Fig. 3.10a). The lens in the robot is mounted to a screw-in housing and cannot be moved during processing, i.e. no automatic focus corrections are applied. The focal point was set on the curved part of the hippodrome-shaped BS, as it is more defined and since the focal point on the flat part gradually changes. In addition, only the four corners of the curved part would need to be processed for a selective treatment. Setting the focal point on the curved part, would result in a defocused beam on the flat part, as indicated in Fig. 3.10a. The distance between the closest and the furthest part is 4.85 mm. At 4.85 mm defocus, the spot diameters increase to:

$$2\omega(z = 4.85 \text{ mm}) = \begin{cases} (1) 96.6 \mu\text{m} (\lambda = 532 \text{ nm}), \\ (2) 159.9 \mu\text{m} (\lambda = 1030 \text{ nm}), \\ (3) 175.2 \mu\text{m} (\lambda = 1030 \text{ nm}), \end{cases} \quad (3.4)$$

and the theoretical peak fluence of the Gaussian laser beam reduces to (1) 30 %, (2) 12 % and (3) 0.1 % (Eq. (2.6)). The laser beam waist  $\omega$  diverges more for larger wavelengths  $\lambda$ . This is why the intensity drop is more significant for 1030 nm, even if the laser diameters  $2\omega_0$  are comparable. At  $z = 4.85$  mm and an average laser power of 5 W, the peak fluence of the green laser (config. 1) is still above the ablation threshold of Cu ( $0.24 \text{ J cm}^{-2}$  [132] for 532 nm, 10 ps and 200 kHz), while the IR laser (config. 2) at an average laser power of 13.6 W is at the ablation threshold value ( $0.27 \text{ J cm}^{-2}$ ), and configuration 3) at an average laser power of 10.9 W is below (Fig. 3.10b), not allowing any surface modification. However, the maximum average output power of the IR *in situ* setup is 16 W at the robot exit. Thus, there is still some margin to compensate.

In conclusion, comparable energy densities in the focal point can be reached for 532 nm and 1030 nm (Fig. 3.9), but intensity losses are more significant for the IR configurations when operating out of focus.

### 3 Sample preparation and characterization methods

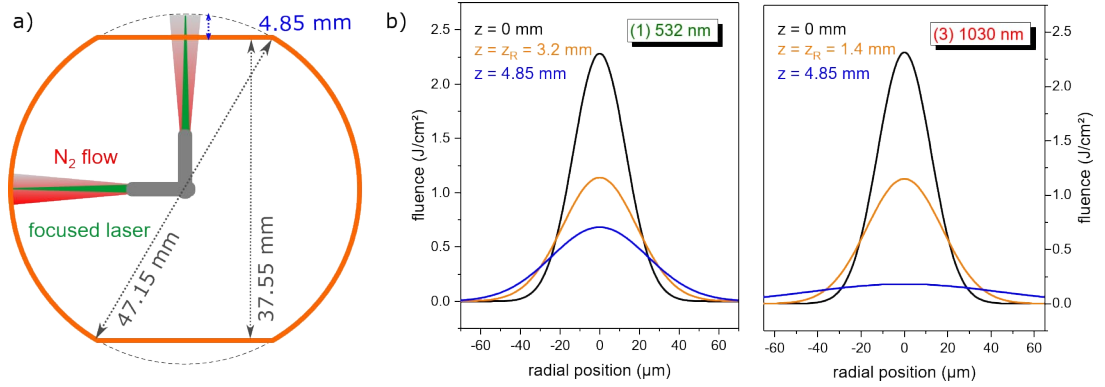


**Figure 3.10:** a) Cross-sectional illustration of the BS geometry. The gas flow through the nozzle of the robot and the focal point position are indicated. Dimensions of the BS (type 50 L) and the distance between the flat and the curved part is highlighted (in blue). Published in Ref. [144]. b) Calculated fluence distribution for an average laser power of (1) 5 W (green) and (3) 10.9 W (IR) in the focal point (black), at the Rayleigh length (orange), and at the offset between the curved and the flat part of the BS (blue).

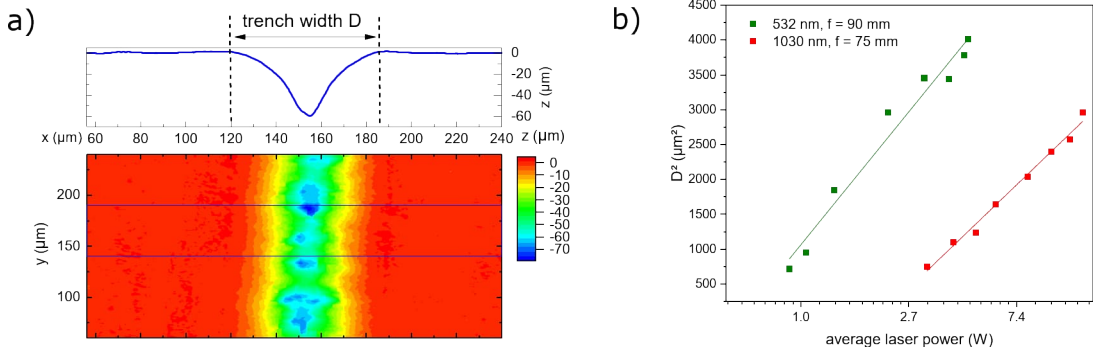


**Figure 3.11:** a) Trench width profile (averaged over blue marked range) engraved on a curved copper surface at  $P = 3.1$  W and  $v = 5$  mm s $^{-1}$  using 532 nm light. b) Laser diameter evaluation of 532 nm and 1030 nm laser using Liu's method (Eq. (2.14)). Published in Ref. [144].

The laser spot diameter was experimentally evaluated using Liu's method [77]. To do so, laser lines of various average power  $P$  were engraved on the curved surface whose spatial profile approximately reflects a Gauss function. The widths  $D$  of the trenches, where material was ablated, were measured from 3D topographies (example in Fig. 3.11a) acquired with a white light interferometer (Veeco Nt3300).

From the slopes of the semi-logarithmic plot in Fig. 3.11b, the Gaussian diameters (defined at the width where the photon intensity has fallen to  $1/e^2$ ) for 532 nm (configuration 1) and 1030 nm (configuration 3) were determined using Liu's method (Eq. (2.14)):

$$2\omega_0 = \begin{cases} (1) 61.7 \mu\text{m} (\lambda = 532 \text{ nm}), \\ (3) 54.5 \mu\text{m} (\lambda = 1030 \text{ nm}). \end{cases} \quad (3.5)$$

Deviations from the theoretical values (Tab. 3.2) may occur if the beam at the fiber output was not perfectly collimated (smaller  $\omega_p$ ) or if the lens in the robot was slightly misaligned. The ablation threshold laser powers  $P_{\text{th}}$  are 0.56 W (green laser) and 0.71 W (IR laser), extrapolated from the linear fit in Figure 3.11b. The corresponding threshold fluences are  $0.19 \text{ J cm}^{-2}$  (532 nm, 10 ps, 200 kHz) and  $0.12 \text{ J cm}^{-2}$  (1030 nm, 1 ps, 500 kHz). This is consistent with values reported in literature ( $0.24 \text{ J cm}^{-2}$  [132] for 532 nm, 10 ps and 200 kHz).

#### Scan precision

The implemented scan patterns shown in Figure 3.6 were tested for accuracy on curved copper samples. Each scan line should be separated by  $50 \pm 5 \mu\text{m}$  to generate homogeneous surface structures. For the processing tests, an average laser power of  $P = 4 \text{ W}$ , a scanning speed of a)  $v = 5 \text{ mm s}^{-1}$ , b)  $15 \text{ mm s}^{-1}$  and c)  $15 \text{ mm s}^{-1}$  and a nominal line distance of  $\Delta y = 50 \mu\text{m}$  were applied. The ultrashort laser pulses imprinted micrometer deep trenches aligned with the laser scanning direction. The samples were laterally polished and ground to obtain a cross-sectional view, which is shown in Figure 3.12. The distances between each valley of the trenches were measured with an optical microscope at 5 different points along the cross-section.

The average distances amounted to a)  $50.0 \pm 3.6 \mu\text{m}$  for longline, b)  $48.0 \pm 3.6 \mu\text{m}$  for the circle and c)  $49.3 \pm 3.0 \mu\text{m}$  for the spiral movement, which confirms the precision of the robot movement in both the translational and rotational axis. A deviation of  $\sim 3 \mu\text{m}$  for the different actuation procedures is acceptable for the intended large-scale surface roughening and could be minimized calibrating the control software settings, if required. It is worth noting that surface structures created using the longline movement are aligned parallel to the beam propagation direction in the LHC, potentially keep the surface resistance low.



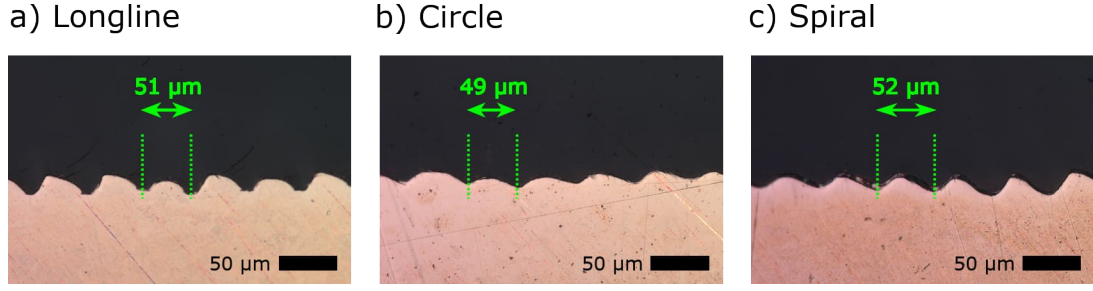


**Figure 3.12:** Cross-sectional optical microscopy images of laser-processed copper samples using a) longline, b) circular, and c) spiral movement at a nominal line distance of  $\Delta y = 50 \mu\text{m}$ , an average laser power of  $P_{\text{robot}} = 4 \text{ W}$ , and scanning speeds of a)  $5 \text{ mm s}^{-1}$ , b)  $15 \text{ mm s}^{-1}$ , c)  $15 \text{ mm s}^{-1}$ , equivalent to accumulated laser fluences of a)  $1600 \text{ J cm}^{-2}$ , b)  $530 \text{ J cm}^{-2}$ , and c)  $530 \text{ J cm}^{-2}$ . Published in Ref. [144].

### 3.3 Surface characterization methods

In the following, the most important methods used to characterize the surface properties are presented.

The topography of laser-processed surfaces was characterized by field emission scanning electron microscopy (FE-SEM) (ZEISS Sigma 500 and ZEISS Gemini Ultra 55 system), white light interferometry (white light interferometry (WLI)) (Veeco Nt3300), and cross-sectional ablation depth measurement. For the latter, the samples were embedded in a transparent resin and mechanically ground on a silicon carbide paper, and then polished using a diamond polishing paste in water based solution. Once the cross-section had been dissected, the maximum ablation depth, defined as the distance between the surface of the untreated regions and the groove valley (Fig. 3.13c), was measured using a digital optical microscope (Keyence VHX-6000).

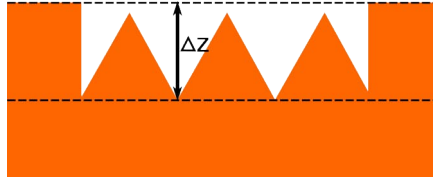


**Figure 3.13:** Definition of ablation depth  $z$  of grooved surface.

#### 3.3.1 Secondary electron yield (SEY) measurement

As introduced in the previous Chapter (Sec. 2.3.1), the SEY  $\delta$  is defined as the ratio of emitted secondary electrons ( $I_{\text{sec}}$ ) and primary impinging electrons ( $I_{\text{prim}}$ ). Two methods are commonly used to determine these two quantities: a) the sample-bias method and b) the collector-based method, both illustrated in Figure 3.14. Using

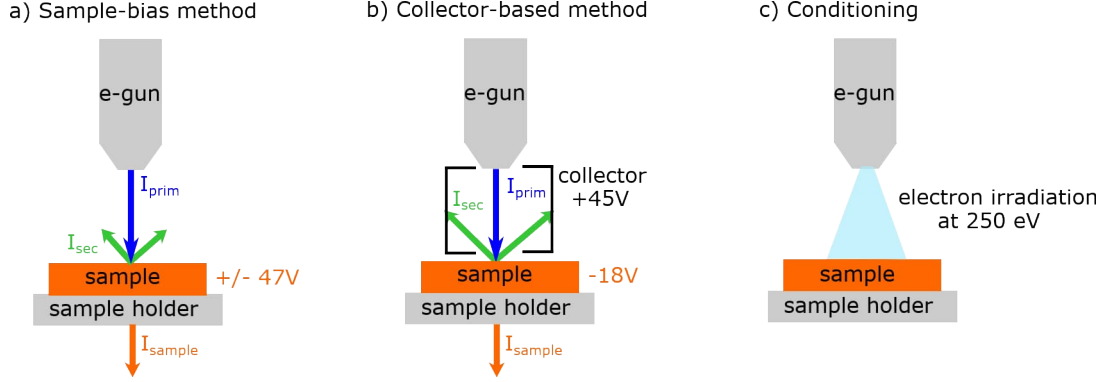


**Figure 3.14:** a) Principle of SEY measurement using a) the sample bias method, b) the collector-based method. c) Schematic of electron-irradiation experiments (conditioning).

the sample-bias method (a), the SEY is determined in two steps. First, a positive voltage is applied to the sample and the current measured at the sample  $I_{+V}$  is equal to  $I_{\text{prim}}$ . The primary electron energy is varied between 50 and 1800 eV. Second, the voltage at the sample is inverted. The current measured at the sample  $I_{-V}$  includes the primary electrons impinging on the sample and the emitted secondary electrons that are attracted by the sample. The SEY  $\delta$  is calculated:

$$\delta(E) = \frac{I_{\text{sec}}(E)}{I_{\text{prim}}(E)} = \frac{I_{+V}(E) - I_{-V}(E)}{I_{+V}(E)}. \quad (3.6)$$

The SEY of all samples was always measured using the sample-bias method in a commercial UHV system with a base pressure below  $8 \times 10^{-10}$  mbar (SPECS Surface Nano Analysis GmbH, Berlin, Germany). An electron beam of  $\sim 2$  nA ( $I_{\text{prim}}$ ) generated by a Kimball Physics ELG-2 electron gun at a distance of 2 cm from the sample was focused to a spot diameter of 1 mm on the surface. Primary electrons between energies ( $E$ ) of 50 and 1800 eV impinge at normal incidence on the surface. A sample bias of  $\pm 47.1$  V was used, and the sample current ( $I_{\text{sec}}$ ) was measured using an optical isolation amplifier with a gain of  $10^8$  V/A in combination with a 6517B electrometer (Keithley Instruments, Inc., Cleveland, USA).

The collector-based method (b) is performed in a single step. The collector, placed between the electron gun and the sample holder, is positively biased (+45 V) and the sample negatively biased (-18 V). This repels the secondary electrons to the collector. The collector current  $I_{\text{col}}$  is equal to  $I_{\text{sec}}$  and the sample current is  $I_{\text{sa}} = I_{\text{prim}} - I_{\text{sec}}$ .

$$\delta(E) = \frac{I_{\text{sec}}(E)}{I_{\text{prim}}(E)} = \frac{I_{\text{col}}(E)}{I_{\text{col}}(E) + I_{\text{sa}}(E)}. \quad (3.7)$$

This method was used in all conditioning measurements, as the system described below is a collector-based SEY setup. The relative experimental error of the SEY measurement setups amounts to 0.05.

#### 3.3.2 Electron irradiation measurements (Conditioning)

The conditioning measurements were performed in a second UHV system (base pressure of  $2 \times 10^{-10}$  mbar). It comprises two electron sources: a flood gun (FG15/40 SPECS Surface Nano Analysis GmbH, Berlin, Germany) that irradiates the surface at an electron energy of 250 eV (Fig. 3.14c) and a second electron source (Kimball Physics ELG-2 electron gun) to measure the SEY after exposure to defined doses up to  $10^{-2}$  C mm<sup>-2</sup>, using the collector-based method (Fig. 3.14b). For comparison, a much lower dose of  $1.1 \times 10^{-7}$  C mm<sup>-2</sup> is deposited on the surface during a single SEY measurement.

#### 3.3.3 X-Ray photoelectron spectroscopy (XPS)

When an electron within some material absorbs the energy of a photon and acquires more energy than its binding energy, it is ejected as a photoelectron. An unoccupied electron state (hole) in the core shell of the atom remains. If the hole is occupied again by an electron from an outer shell, the energy released can be transferred to another electron of the same atom so that it leaves the atom as an Auger electron.

The chemical properties of the surfaces were measured using x-ray photoelectron spectroscopy (XPS) in the same UHV system (SPECS) used for the standard SEY measurements. A monochromated AlK $\alpha$  x-ray source (XR50M,  $h\nu = 1486.7$  eV) is directed onto the sample surface. As a result of the x-rays interaction with the atoms both photoelectrons and Auger electrons are detected through a hemispherical electron energy analyzer with 9 channeltrons (Phoibos 150). The energy scale of the analyzer is regularly calibrated using sputter-cleaned polycrystalline Cu, Ag, and Au foils. The penetration depth of x-rays is a few microns, but the detection limit of XPS is only a few nanometers ( $\sim 10$  nm), due to the short mean free path of electrons in solids.

All surfaces studied were copper-based. Copper exists in various oxidation states such as Cu<sub>2</sub>O (naturally formed in air) or CuO (formed by heating), or mixtures including hydroxides. These compounds can be identified through the peak positions of binding energies obtained in the XPS spectra, which is discussed in Section 3.4.3.

#### 3.3.4 Centrifugation tests

As a result of the laser ablation process, particles are redeposited on the processed surface which could be loosely bound and potentially detach when a force is acting on them. During operation of the LHC, particles may fall into the proton beam and trigger beam losses. For this reason, it is important to quantify the number of detaching particles. The maximum force acting on the BS surface is during a quench, in which the magnet surrounding the BS loses its superconductivity within a few hundred milliseconds. Rapid changes in the magnetic field induce eddy currents and Lorentz

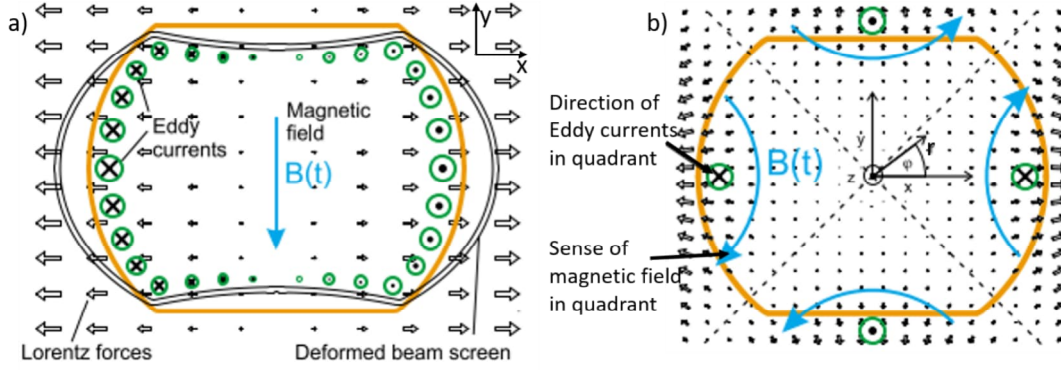


**Figure 3.15:** Sketch of eddy current, Lorentz force and deformations of the beam screen in a dipole field during a quench. b) Beam screen in a quadrupole field during quench with superposed field of Lorentz forces. Figure taken from Ref. [148].

forces in the conductive BS, as shown in Figure 3.15 for a dipole and quadrupole. The maximum force density acting on the BS surface was determined in a previous work and amounted to  $\sim 30 \text{ N mm}^{-3}$  [148]. In this study, a static force was applied on the laser-treated surfaces put in a centrifuge (Beckman Coulter Optima L-100 XP ultra-centrifuge with Beckman Coulter 70 Ti rotor, University of Geneva) to quantify detaching particles. The procedure was developed and detailed in Reference [148]. Since in the event of a magnet quench, the proton beam is anyway extracted from the accelerator, the further falling particles would be irrelevant for the beam quality. Therefore, a lower force density of  $3 \text{ N mm}^{-3}$ , 10 % of the maximum force density, was selected for this study to estimate the possible maximum number of particles released during operation of the LHC, and potentially inducing beam losses or dumps.

The centrifugal force density acting on a mass that is rotating on an axis is given by:

$$F_{\text{vol}}(r) = \rho_{\text{Cu}} r \omega^2, \quad (3.8)$$

with the density of copper  $\rho_{\text{Cu}} = 8960 \text{ kg m}^{-3}$ , the rotational speed  $\omega = 2\pi \text{ RPS}$ , and the distance  $r = 0.07615 \text{ m}$  from the axis of rotor to the sample surface.

To perform the tests, the samples were mounted in a sample holder with a carbon sticker in front of the treated surface to collect the detached particles (Fig. 3.16). The sample holder was installed in the rotor with the treated surface facing outward and at an inclined angle of  $23^\circ$  so that inertia forces act perpendicular to the macroscopic surface as visualized in Figure Fig. 3.16. The centrifuge was balanced with a counter part installed on the opposite side of the sample holder. The counter weight was balanced with water drops with a precision of  $0.0001 \text{ g}$ . The RPM was set to  $20\,000$  for the tests, which corresponds to a force density of  $3 \text{ N mm}^{-3}$ . After centrifugation, the detached particles on the carbon sticker were analyzed with automated particle analysis (APA), which is an automated particle identification and quantification algorithm integrated in the SEM operation software. In the software, the particles were considered circular in

### 3 Sample preparation and characterization methods

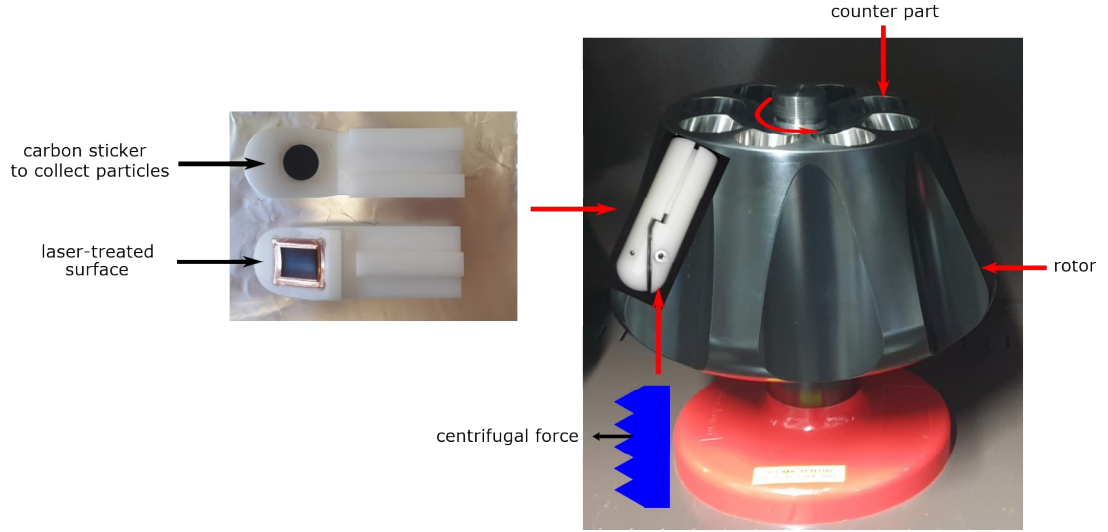


**Figure 3.16:** Centrifugation setup used for particle detachment tests. Left: Photograph of sample holder with laser-treated curved sample (bottom) and carbon sticker to collect detached particles (top). Right: Schematic of sample holder installed in the rotor, the angle of the sample with respect to the tube axis allows the sample to be placed vertically once the assembly is installed in the rotor. Schematic of centrifugal force acting on the surface topography.

projection and mainly Cu. The lower APA detection limit is  $1\text{ }\mu\text{m}$  in particle diameter.

## 3.4 Preliminary characterization of untreated copper surface

In this section, surface properties of the untreated Cu samples were characterized for flat oxygen-free electronic grade (OFE) Cu, curved OFE Cu and colaminated Cu on stainless steel (BS-type), to obtain reference measurements. All samples were cleaned at CERN using a standard procedure for UHV cleaning, comprising wet-chemical degreasing with a commercial detergent and subsequent rinsing in de-ionized water.

### 3.4.1 Topography of copper

SEM micrographs in Figure 3.17 show the topography of the untreated OFE Cu and a BS sample (laminated Cu on SS). It is apparent that the grain size of the BS sample is larger ( $30\text{--}50\text{ }\mu\text{m}$ ) than that of the OFE Cu ( $\sim 8\text{ }\mu\text{m}$ ). This can be attributed to the lamination process used to fabricate the BS, which involves cold rolling a  $150\text{ mm}$  thick OFE Cu sheet onto an austenitic stainless steel coil, which deforms the original grains. The difference in grain size may influence the ablation efficiency during laser processing, which is discussed in Section 4.4.

### 3.4 Preliminary characterization of untreated copper surface

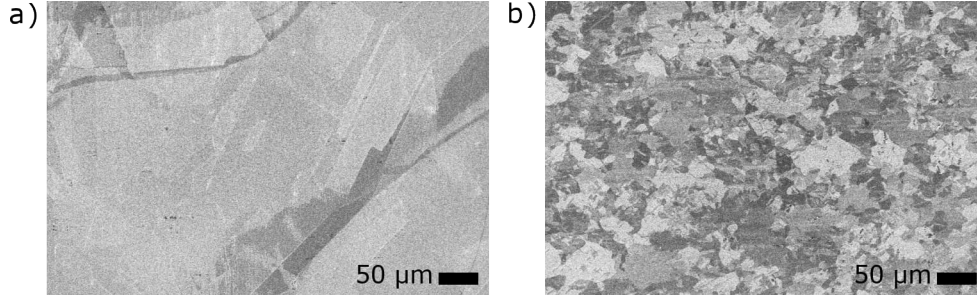


**Figure 3.17:** Topography of flat, freshly degreased a) BS-type Cu and b) OFE Cu using SEM backscattered electron detector.

#### 3.4.2 Reflectivity of copper

The ablation efficiency is influenced by the photon wavelength of the laser (UV, green or IR) and the optical properties of the material. Hence, the total and diffuse reflectivity of untreated Cu surfaces was evaluated at three distinct positions on the samples using a UV/VIS spectrometer with an integrating sphere from 250 to 850 nm. Degreased laminated Cu (BS-type) and degreased OFE Cu were measured after three months of storage. It is known from literature [149] that Cu generally reflects more than 90 % of photons in the IR ( $> 700$  nm) and less than 60 % in the visible range ( $< 550$  nm). Figure 3.18a shows that the degreased OFE Cu follows similar values as the reference Cu (data taken from Ref. [149]), while the total reflectivity of degreased BS-type Cu is about 10 % lower in the visible range and  $\sim 5$  % in the IR. The standard deviation of the three different spots on the sample surface amounted to 0.5 %. The spectra of specular and diffuse reflectance provide additional evidence (Figure 3.18b, c). The laminated Cu exhibits a lower diffuse reflectivity than OFE Cu, which matches with the larger grain size (30 - 50  $\mu\text{m}$ ) obtained on the BS sample, indicating a smoother surface. The specular reflectivity of the two samples is similar for wavelengths  $< 600$  nm and higher for the BS sample at wavelengths  $\geq 600$  nm.

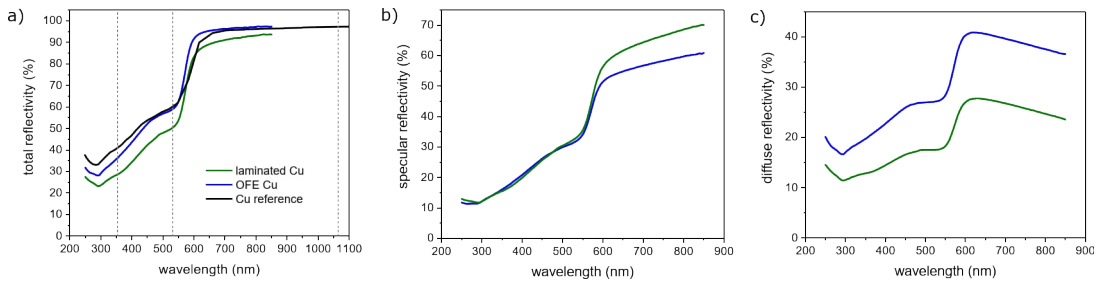


**Figure 3.18:** UV/VIS reflectivity measurement of untreated Cu: a) total, b) specular, and c) diffuse reflectivity of degreased laminated Cu and degreased OFE Cu, stored in paper after degreasing for three months, and reference values for Cu from [149]. The dashed gray lines indicate used photon wavelengths in experiments: 355 nm, 532 nm, 1064 nm.

### 3.4.3 Surface chemical properties of Cu and its oxides and hydroxides

Regardless of whether a copper surface has been recently cleaned, a layer of few nanometer of oxide  $\text{Cu}_2\text{O}$  and hydroxide  $\text{Cu}(\text{OH})_2$  spontaneously forms upon exposure to air [150, 151] or in water-based cleaning baths. Therefore, the XPS spectrum of an air-exposed Cu surface typically includes contributions of a mixture of the metallic state, oxides, and hydroxides. Figure 3.19 displays XPS spectra of freshly degreased OFE Cu (measured 1 h after cleaning), degreased OFE Cu after 17 days of storage in aluminum foil, a CuO surface, and a degreased OFE Cu stored for 7 months in humid air. The characteristics of the spectra and their elemental identification are further elaborated below. The OFE Cu that was degreased and stored in aluminum foil for 17 days is representative of the samples used for laser processing.

The freshly degreased OFE Cu surface has a main peak at a binding energy of 932.4 eV in the Cu  $2p_{3/2}$  spectrum in Figure 3.19 (blue line). Typically, it is used for elemental identification. The measured binding energy of 932.4 eV is characteristic for both metallic copper  $\text{Cu}^0$  and  $\text{Cu}^+$  oxide [152]. To distinguish between metallic copper and  $\text{Cu}_2\text{O}$ , the kinetic energy of the Auger transition is used. The Cu LMM transition occurs at a kinetic energy of 916.6 eV, compatible with  $\text{Cu}_2\text{O}$ , while the reported transition in literature for  $\text{Cu}^0$  occurs at 918.4 eV [153]. The main peak of the O 1s spectra occurs at 530.4 eV, which is assigned to  $\text{Cu}_2\text{O}$  [153]. The shoulder at higher binding energy is a mixture of adsorbed hydrocarbons ( $\text{C}_x\text{H}_y$ ) and hydroxide bonds  $\text{OH}^-$ . Most metals have a native oxide with a topmost layer of adventitious carbon that forms directly or the surface may form a hydroxide in the presence of water molecules that then adsorbs the  $\text{CO}_2$  from the air. Adventitious carbon contains different types of carbon depending on the storage time and conditions of the sample. In the C 1s spectrum of Figure 3.19, the primary peak is present at a binding energy of 284.8 eV on all surfaces shown, and is assigned to hydrocarbons (C–H, C–C). The second maximum appears at a binding energy of 288.5 eV, which corresponds to O–C=O species [152].

The spectra of CuO are represented in red in Figure 3.19. The Cu  $2p_{3/2}$  spectrum of the CuO surface has the main peak at a binding energy of 933.6 eV and a satellite feature between 940 and 945 eV. The satellite feature is characteristic for materials with an open  $d$  shell ( $3d^9$  for  $\text{Cu}^{2+}$ ) in the ground state [154]. If an ion is left in a specific excited energy state a few eV above the ground state after photoionization, the kinetic energy of the emitted photoelectron is reduced, which is observed as a “satellite” peak at a higher binding energy than the main line. The corresponding Auger line is at a kinetic energy of 917.8 eV. The O 1s spectrum has the main peak at 529.5 eV, ascribed to CuO. The shoulder around 531 eV is due to contributions of hydroxide bonds and hydrocarbon adsorbates. The generation of CuO during the laser treatment is however not desired, as it can lead to charging effects at cryogenic temperature [2].



### 3.4 Preliminary characterization of untreated copper surface

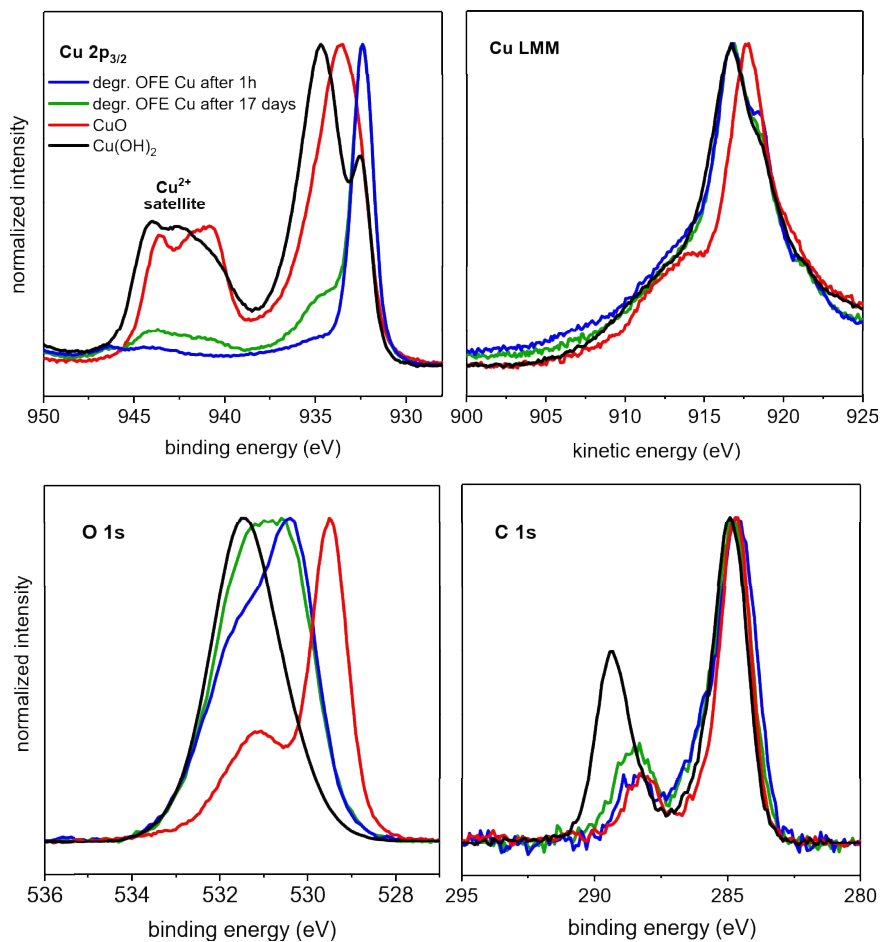


**Figure 3.19:** XPS spectra (Cu 2p<sub>3/2</sub>, Cu LMM, O 1s, C 1s) of degreased OFE Cu (after 1 h), degreased OFE Cu after 17 days of storage in aluminum foil, CuO, and degreased OFE Cu stored in humid air for 7 months (Cu(OH)<sub>2</sub>).

**Table 3.3:** Summary of specific binding (BE)/kinetic (KE) energies of the XPS spectra shown in Figure 3.19.

	BE Cu 2p <sub>3/2</sub> (eV)	BE O 1s (eV)	KE Cu LMM (eV)
OFE Cu (1 h)	932.4	530.4	916.6
OFE Cu (17 days in Al)	932.4	531.0	916.6
CuO	933.6	531.2	917.8
OFE Cu in humid air	934.7	531.5	916.7



### 3 Sample preparation and characterization methods

The OFE Cu stored in humid atmosphere (Figure 3.19, black line) has the main peak at 934.7 eV, identical to the value reported in literature for  $\text{Cu}(\text{OH})_2$  [155]. Together with the Auger transition at 916.7 eV, the modified Auger parameter – the sum of the kinetic energy of the Auger transition and the binding energy of the core level – amounts to 1851.4 eV, which confirms the presence of  $\text{Cu}(\text{OH})_2$  [155]. A second maximum is observed at 932.6 eV, which features the original oxidized character ( $\text{Cu}_2\text{O}$ ) of the surface. The satellite feature of the  $2p_{3/2}$  level is at binding energies between 942 and 945 eV. The satellite shape of  $\text{Cu}(\text{OH})_2$  has only one bump that flattens for lower binding energies, while the  $\text{CuO}$  satellite has two characteristic bumps [155]. This in combination with the Auger parameter can be used to distinguish the two species. The Auger transition of  $\text{Cu}(\text{OH})_2$  is at kinetic energy of 916.7 eV. The O 1s spectrum has a maximum at 530.8 eV, assigned to  $\text{OH}^-$ .

In the spectrum of the OFE Cu sample after 17 days of storage (Figure 3.19, green line), the Cu  $2p_{3/2}$  peak remained at a binding energy of 932.4 eV and the Auger transition at a kinetic energy of 916.6 eV, assigned to  $\text{Cu}_2\text{O}$ . However, a shoulder of the main peak in the Cu 2p spectrum developed at 934.7 eV, together with a satellite feature between 943 and 946 eV, which is assigned to a formation of copper hydroxide phases ( $\text{Cu}(\text{OH})_2$ ) at the surface. The O 1s peak is located at a binding energy of 531.0 eV, which is slightly shifted to higher binding energy, compared to the freshly cleaned OFE Cu. The shift towards the peak of OFE Cu, stored in humid atmosphere, is associated with an increase in  $\text{OH}^-$  contribution. This is compatible with the increase in  $\text{Cu}(\text{OH})_2$ , usually observed for aging, together with the increase in carbon content. In summary, the surfaces used for laser processing are primarily  $\text{Cu}_2\text{O}$  with a proportion of  $\text{Cu}(\text{OH})_2$ . The specific binding energies of the surfaces discussed above are summarized in Tab. 3.3.

#### 3.4.4 Secondary electron yield

Three types of degreased Cu samples were analyzed after storage in aluminum foil: flat OFE Cu (stored for 3 months), curved OFE Cu (stored for 3 months), and flat laminated Cu onto SS (stored for 6 months). The SEY of the samples was measured for primary electron energies ranging from 50 to 1800 eV, using the sample bias method (see Sec. 3.3). The curves in Figure 3.20 represent the average SEY of the three different locations of the sample. The SEY maxima  $\delta_{\text{max}}$  amounted to 2.1 (flat OFE Cu), 2.3 (laminated Cu), and 2.1 (curved OFE Cu) at a maximum energy of 250 eV.

The SEY maximum of a freshly cleaned Cu surface amounts to 1.8, while it is known to increase upon time and under certain storage conditions, due to the formation of hydroxide and the adsorption of hydrocarbons [29, 31, 33, 156, 157]. Given the storage time of 3 to 6 months in aluminum foil, the obtained SEY values are expected. The slightly higher SEY of the laminated Cu sample is attributed to the aging of the sample rather than the different material. This is supported by the lower values measured on a BS in Section 3.21.

### 3.4 Preliminary characterization of untreated copper surface

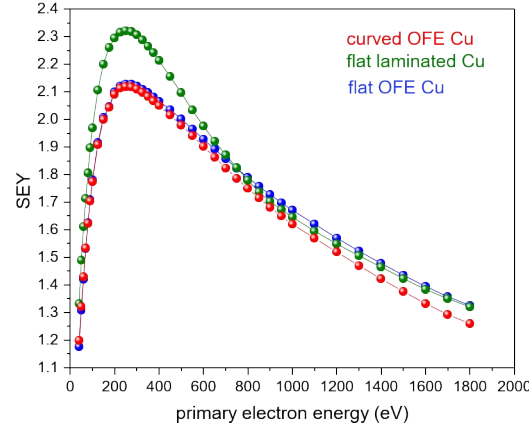


**Figure 3.20:** SEY measurement of untreated degreased Cu after storage in aluminum foil for 3 months (flat), 3 months (curved), and 6 months (laminated Cu).

#### 3.4.5 Conditioning

A comprehensive study on the conditioning of copper surfaces has been conducted previously [156], to which the reader can refer for further information. The following example briefly outlines the key aspects of conditioning a freshly degreased OFE Cu and BS-type Cu at RT. The surfaces were irradiated with 250 eV electrons up to a total dose of  $\sim 2.6 \times 10^{-2} \text{ C mm}^{-2}$  and the SEY was measured before the start of the conditioning and after each conditioning step as shown in Figure 3.21. The as received  $\delta_{\text{max}} = 2$  of the OFE Cu was higher than  $\delta_{\text{max}} = 1.8$  of the BS sample. The difference in SEY maximum is related to the aging of the samples. The SEY maximum of both samples decreased strictly monotonic, but non-linear, upon electron dose, until it saturates at electron doses of  $2 \times 10^{-2} \text{ C mm}^{-2}$ .

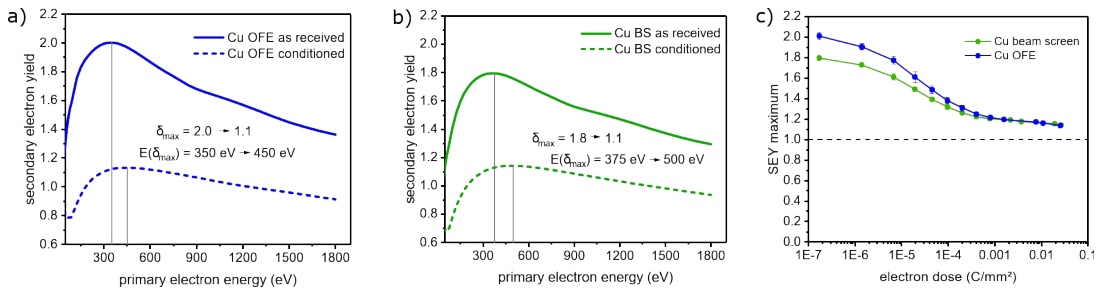


**Figure 3.21:** SEY measurement of a) Cu OFE and b) laminated Cu on stainless steel before the start of the conditioning and after a dose of a)  $2.55 \times 10^{-2} \text{ C mm}^{-2}$  and b)  $2.65 \times 10^{-2} \text{ C mm}^{-2}$ . c) SEY maximum after each conditioning step of laminated Cu and OFE Cu.

### *3 Sample preparation and characterization methods*

Both samples saturated at  $\delta_{\text{max}} = 1.1$  and the maximum energy shifted by about 100 eV (OFE Cu) and 125 eV (BS-type Cu), respectively. The decrease in SEY is ascribed to the removal of adsorbed molecules by electron-stimulated desorption as well as chemical surface reactions. Typically, surface cleaning is observed by the removal of O–C=O carbon, which is associated with the vanishing of the peak at 288.5 eV B.E. in the C 1s spectrum (see Fig. 3.19) and a peak shift in the O 1s spectra towards 530.6 eV, because of the decrease of the OH<sup>−</sup> contribution. In addition, Cu(OH)<sub>2</sub> is converted into Cu<sub>2</sub>O and the adventitious carbon layer graphitizes, usually witnessed by a shift of the C 1s peak at 285 eV towards lower binding energies. A comprehensive study on the conditioning of copper surfaces has been conducted previously [156], to which the reader can refer for further information.

## 4 Fundamental dependencies of the surface properties on the laser parameters

The present Chapter is dedicated to the understanding of the fundamental influences of the laser processing parameters on the surface properties, since the SEY of laser-treated surfaces is highly dependent on the structural modification. Various laser parameters, including the wavelength, laser power, scanning speed, line distance, pulse duration and diameter, were varied to investigate their impact on the surface structure and SEY performance by satisfying the modification depth, chemical properties, and particle coverage requirements relevant for application in the LHC (Sec. 2.5.2).

For this purpose, flat OFE Cu surfaces were processed at IOM with a commercial laser setup (12 ps, 100 kHz), where the primary laser frequency (1064 nm) can be doubled (532 nm) or tripled (355 nm). Different focal lengths are used to focus the beam on the surface, resulting in different laser diameters for each wavelength: 26.4 (IR), 11.6 (green), and 29.2  $\mu\text{m}$  (UV) (details in Sec. 3.3). On the second setup, the laser wavelengths are slightly different: 1030 nm, 515 nm and 343 nm. A pulse duration of 10 ps and a repetition rate of 100 kHz were used, unless otherwise specified. All surfaces presented in this Chapter were processed in air.

### 4.1 Influence of accumulated fluence and wavelength

#### 4.1.1 Structural modification

When ultrashort laser pulses are scanned across the surface in parallel lines at defined distances, material is removed and micrometer-deep trenches are created. Some of the ejected particles are redeposited onto the surface. At low average laser power (fluences near the ablation threshold), the laser-matter interaction is dominated by spallation, resulting in minor surface modification (Fig. 4.1e). As the average laser power increases, the energy transferred to the surface increases and ablation is driven by rapid phase transitions, explosive pressure and temperature changes, resulting in greater material ejection and trenches up to 100  $\mu\text{m}$  deep, as shown on a cross-sectional view of the laser-treated surfaces in Fig. 4.1 (left). Reducing the scanning speed also results in similar deep trenches, as the number of accumulated laser pulses per surface is increased (Fig. 4.1, right). For non-overlapping scan lines (line spacing  $\geq$  laser diameter), the trenches are well defined and separated from each other, as shown in

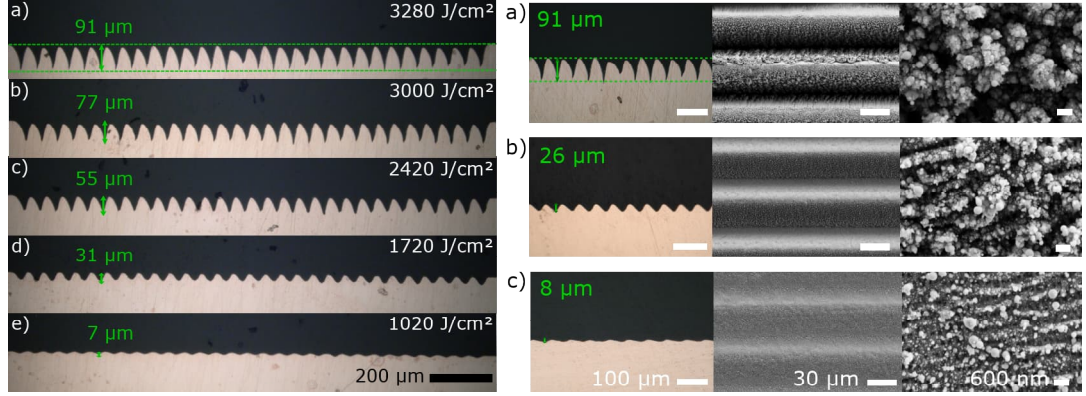


**Figure 4.1:** Surface topography of 532 nm laser-treated copper at a line distance of  $\Delta y = 50 \mu\text{m}$ . Left: cross-sections of varied average laser powers a) 1640 mW, b) 1500 mW, c) 1210 mW, d) 860 mW and e) 510 mW and constant scanning speed of  $1 \text{ mm s}^{-1}$ . Published in Ref. [158]. Right: Cross-sectional profiles and top-view SEM micrographs processed at constant average laser power (1640 mW) and various scanning speeds: a)  $1 \text{ mm s}^{-1}$  ( $F_{\text{acc}} = 3280 \text{ J cm}^{-2}$ ), b)  $5 \text{ mm s}^{-1}$  ( $F_{\text{acc}} = 656 \text{ J cm}^{-2}$ ) and c)  $20 \text{ mm s}^{-1}$  ( $F_{\text{acc}} = 164 \text{ J cm}^{-2}$ ). Published in Ref. [159]. The two dashed lines in a) indicate how the maximum ablation depth measurement from the valley of the deepest trench to the untreated region.

topview SEM photographs and on a cross-sectional view in Figure 4.2. In contrast, for overlapping lines (line spacing  $<$  laser diameter), the trenches almost disappear and only the nanostructure remains. The overlapped line scanning (line distance  $\Delta y = 10 \mu\text{m}$ ) resulted in a deeper modification depth for the same average laser power and scanning speed applied, as observed in the the cross-sectional measurement in Figure 4.2 (bottom row). This is evident, as the accumulated energy per surface area was higher. Line distances as small as  $10 \mu\text{m}$  slow down the laser processing time compared to a line distance of  $50 \mu\text{m}$ .

Three quantities (average laser power  $P$ , scanning speed  $v$ , line distance  $\Delta y$ ) are represented in the accumulated fluence  $F_{\text{acc}} = \frac{P}{v\Delta y}$ . Figure 4.3 shows that the ablation depth in general increases with increasing accumulated fluence for all laser wavelengths used (UV, green, IR). While the ablation depth is approximately the same for green and IR laser light, using the 355 nm laser mode resulted in about 50 % deeper grooves at similar fluences. It should be noted that the  $2.5 \times$  smaller focus area of the green laser produced only a small overlap of the raster-scanned lines, while UV and IR scanned lines overlapped by more than  $10 \mu\text{m}$  (Fig. 4.3). However, the laser diameter is not considered in the definition of accumulated fluence. Understanding the extent of ablation is relevant, because the modification depth must not exceed  $25 \mu\text{m}$  and the ejected volume determines the quantity of redeposited nanoparticles, which is an additional limitation for application in the LHC.

As the laser diameters were not equal in the previous test, they were equally set here to investigate the ablation volume independently. Therefore, the laser radii  $\omega_0$  in the

#### 4.1 Influence of accumulated fluence and wavelength

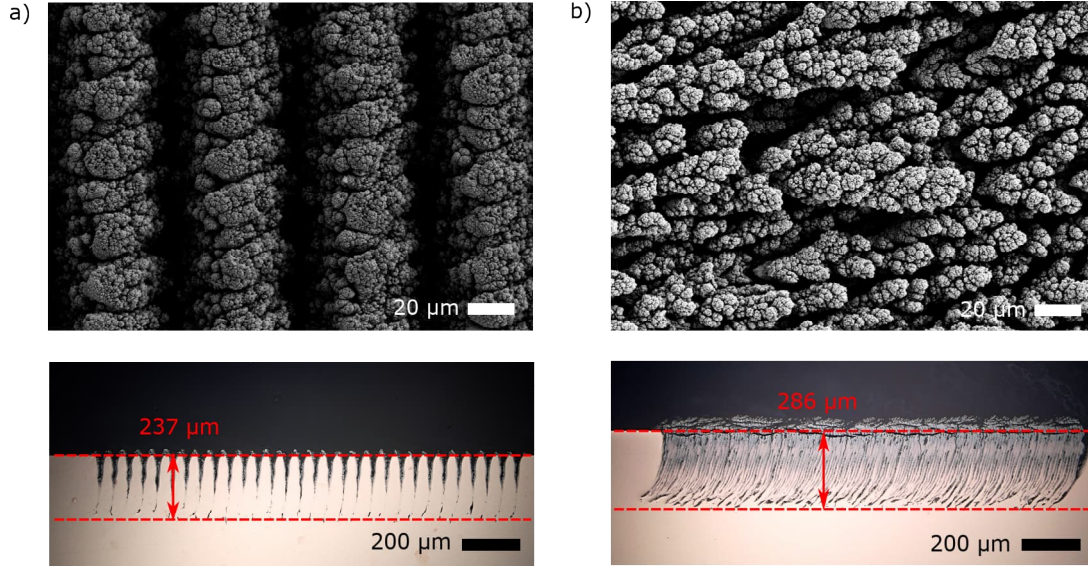


**Figure 4.2:** a) Non-overlapping ( $\Delta y = 50 \mu\text{m}$ ) and b) overlapping ( $\Delta y = 10 \mu\text{m}$ ) line scanning using an IR laser with a laser diameter of  $26 \mu\text{m}$ , a scanning speed of  $1 \text{ mm s}^{-1}$  and an average laser power of  $4.1 \text{ W}$ . SEM photographs (top row) and cross-sectional view on the surface structures and ablation depth measurement using an optical microscope (bottom row).

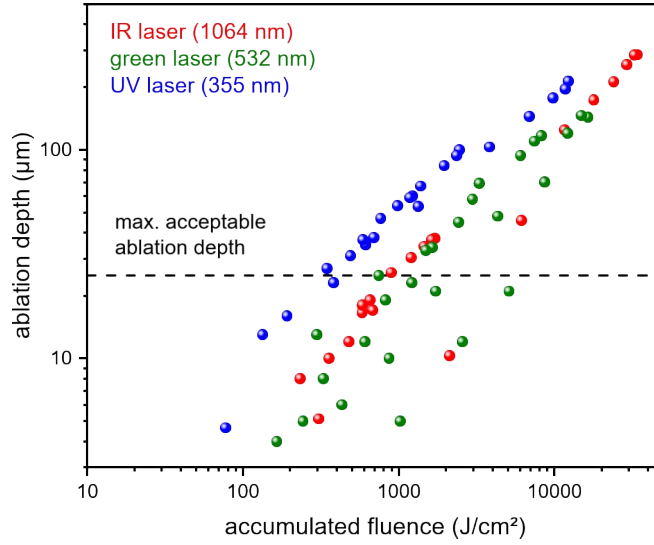


**Figure 4.3:** Measured ablation depths of micro trenches generated with 1064 nm, 532 nm, and 355 nm ps laser pulses at a line distance of  $10 \mu\text{m}$ . Plotted as a function of the accumulated fluence on a double-logarithmic scale. The corresponding plot in linear scale is shown in the Appendix (Fig. A.1). The dashed line at  $25 \mu\text{m}$  refers to the maximum acceptable ablation depth for use in the LHC. Published in Ref. [158].

#### 4 Fundamental dependencies of the surface properties on the laser parameters

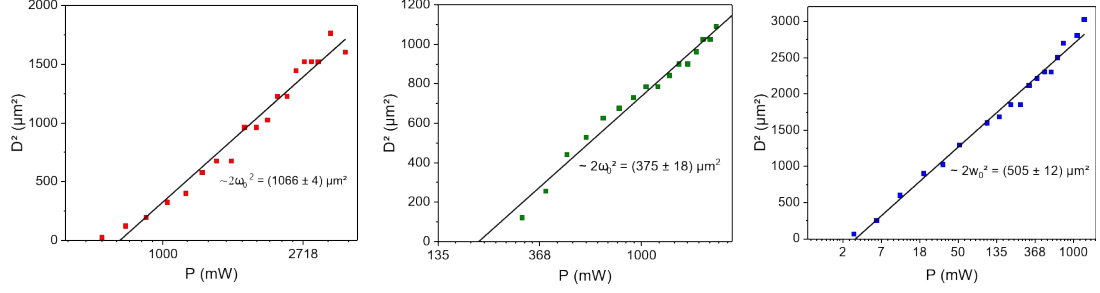


**Figure 4.4:** Linear fit for laser diameter determination in the focal plane ( $z = 0$  mm), according to Eq. (2.14) for 1030 nm (red data points), 515 nm (green data points), and 343 nm photons (blue data points).

focal point as well as the beam waists  $\omega(z)$  along the focal plane  $z$  were analyzed. Since the beam waist increases when moving out of focus, the laser diameters were adjusted to the same size by shifting the  $z$  plane, thus shifting the focal point above the sample surface. To determine the laser radii  $\omega_0$  in the focal plane ( $z = 0$  mm), single laser lines were inscribed on the Cu sample at different average laser powers  $P$  for all three wavelengths. The widths  $D$  of the lines were measured using an optical microscope and linearly fitted on a semi-logarithmic plot (Fig. 4.4), following Liu's method (Eq. (2.14)).

From the slope  $\Delta = 2\omega_0^2$  of the linear fit in Figure 4.4 the laser radii  $\omega_0$  in the focal plane ( $z = 0$  mm) amounted to:

$$\omega_0 = \begin{cases} 23.0 \mu\text{m} & (\lambda = 1030 \text{ nm}), \\ 13.7 \mu\text{m} & (\lambda = 515 \text{ nm}), \\ 15.9 \mu\text{m} & (\lambda = 343 \text{ nm}). \end{cases} \quad (4.1)$$

The determination of the beam waist followed a similar strategy. Single laser lines were inscribed on the Cu at different laser powers  $P$  and different distances  $z$  from the focal plane. The widths  $w$  of the grooves were measured using an optical microscope and were plotted against the displacement of  $z$  (see Fig. 4.5). The data points were y-shifted to  $\omega_0$  that was investigated above and fitted using the relation of the beam waist as a function of  $z$  (Eq. (2.11)). Consequently, the green and UV lasers were z-shifted to obtain equal radii of  $\omega = 23 \mu\text{m}$  (Tab. 4.1).

The ablation volume was determined by integrating the negative volume of the generated trenches of individual scanned lines from 3D profiles. Figure 4.6 shows that the UV laser ablated the most material per pulse, namely  $2.17 \pm 0.06 \mu\text{m}^3 \mu\text{J}^{-1}$ , then green  $1.17 \pm 0.03 \mu\text{m}^3 \mu\text{J}^{-1}$ , and IR marginally less than the green with  $1.11 \pm 0.02 \mu\text{m}^3 \mu\text{J}^{-1}$ . Considering the error ranges, the ablation efficiency of 1030 nm photons is almost identical to 515 nm photons. The result is comparable to the tendency obtained for the ablation depth using different diameters (see Fig. 4.3). This demonstrates that the

#### 4.1 Influence of accumulated fluence and wavelength

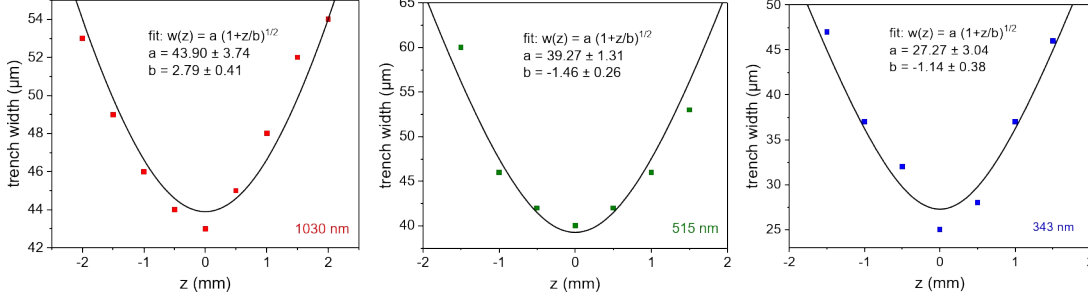


**Figure 4.5:** Measured line widths and fitted beam waists along the focal plane  $z$  according to Eq. (2.11) for 1030 nm, 515 nm, and 343 nm laser light and a pulse duration of 260 fs.

**Table 4.1:** Displacement  $z$  from the focal point ( $z = 0$  mm) for IR, green and UV laser to obtain equal radii of 23  $\mu\text{m}$  and Rayleigh lengths determined from the fits in Figure 4.5.

	1030 nm	515 nm	343 nm
$z$	0 mm	1.08 mm	0.89 mm
$z_R$	2.79 mm	1.46 mm	1.14 mm

ablation efficiency is not primarily determined by the linear reflectivity of the material, which is 60 % for green and more than 90 % for the IR wavelength at room temperature (see Fig. 3.18a). Instead, thermal diffusion within the material plays a supplementary role.

After the ablated material is explosively ejected from the surface, the nanoparticles partially redeposit on the microscopic trenches shown above (Figs. 4.1 and 4.2). The morphology of the nanostructures is strongly influenced by the applied scanning speed and the average laser power, as can be seen in Figure 4.7. For 355 nm laser pulses, different surface features were obtained and classified into four groups: (a) compact, dense cauliflower-head nanostructures ( $P \geq 400$  mW,  $v \leq 10$  mm s<sup>-1</sup>, marked red), (b) non-compact filament-shaped nanostructures ( $P \leq 140$  mW,  $v \leq 2$  mm s<sup>-1</sup>, marked green), (c) molten and resolidified spherical structures ( $v \geq 10$  mm s<sup>-1</sup>, size < 1  $\mu\text{m}$ , marked yellow), and (d) a minor modified surface ( $P \leq 760$  mW,  $v \geq 5$  mm s<sup>-1</sup>, size < 150 nm, marked blue). At high average laser power and slow scanning speed (category a), the ablation process is characterized by high temperature gradients, a high recoil pressure and explosive material removal (phase explosion), resulting in high surface roughness of the trenches. Most-likely, plasma splitting occurs in this regime, decoupling the vapor from heavier species. In the cooling phase, the high fraction of heavier nanoparticles initially redeposits and is thus covered with vapor, creating the cauliflower structures. The low scanning speed results in an additional laser tempering of the ablated material, which likely contributes to the formation of the compact nanostructure at the surface.



#### 4 Fundamental dependencies of the surface properties on the laser parameters

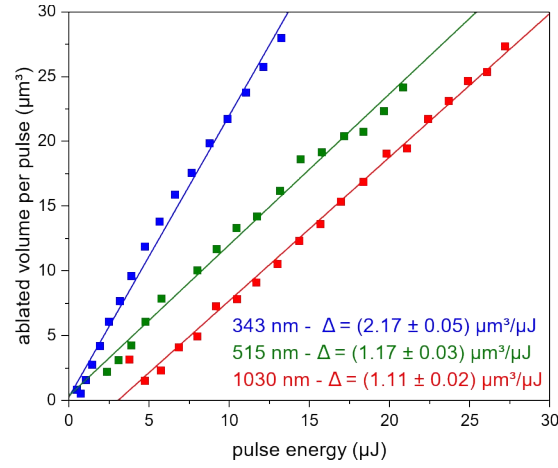


**Figure 4.6:** Ablated volume per pulse for UV, green, and IR laser at a pulse duration of 260 fs, and a laser radius of  $\omega = 23 \mu\text{m}$ . Volume measured with WLI and linearly fitted.

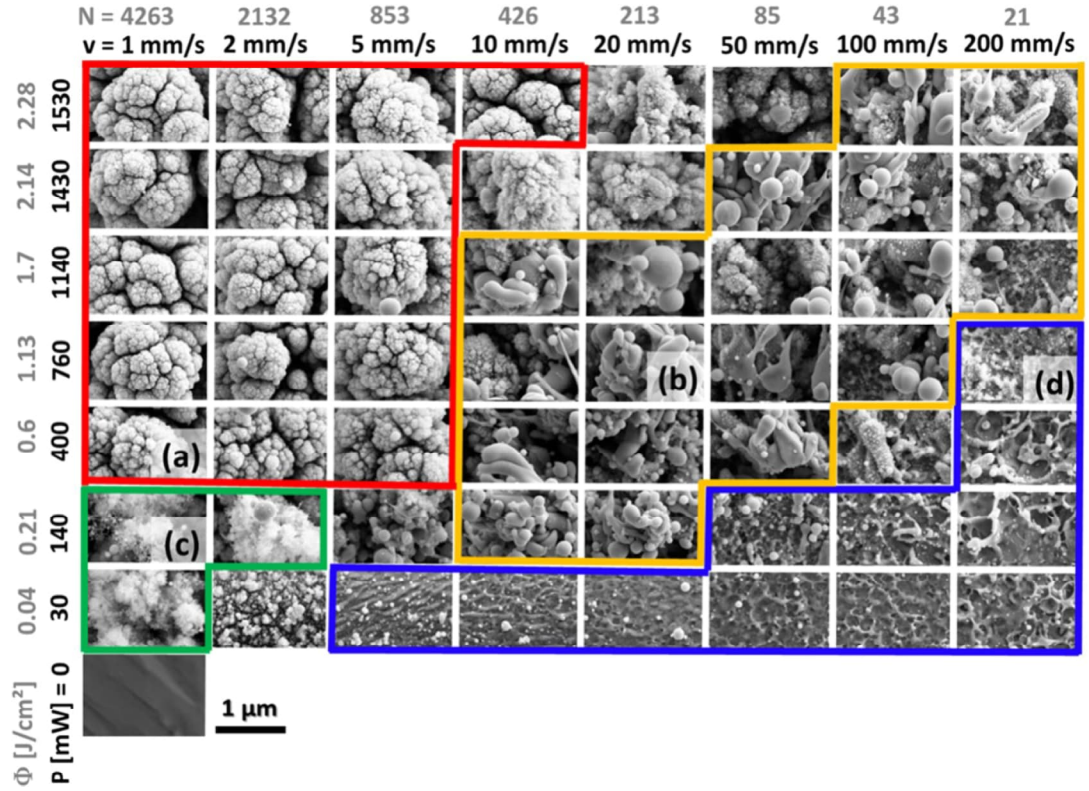


**Figure 4.7:** Array of surface morphology of 355 nm laser-treated Cu for various average laser powers  $P$  and scanning speeds  $v$ , and a line distance of  $10 \mu\text{m}$ . The calculated laser fluence  $F$  and number of laser pulses  $N$  are shown in gray. The four identified categories are highlighted in color. Published in Ref. [160].

## 4.1 Influence of accumulated fluence and wavelength

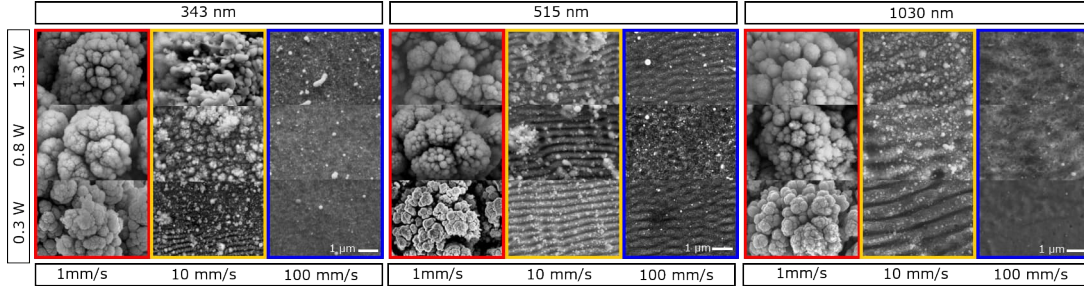


**Figure 4.8:** Array of surface morphology of 343, 515 and 1030 nm laser-treated Cu ( $\tau_p = 260$  fs,  $\Delta y = 50$   $\mu\text{m}$ ,  $\omega_0 = 23.0$   $\mu\text{m}$ ) for various average laser powers  $P$  and scanning speeds  $v$ . Equivalent color-coding as in Fig. 4.7 is used for the highlighted categories.

The closer the average laser power is to the ablation threshold, the shallower are the resulting trenches and the less material is deposited (category b). At higher scanning speeds ( $v \geq 10$   $\text{mm s}^{-1}$ , category c), melting processes mainly dominate the surface modification. The surface tension and the laser-induced temperature gradient lead to a mass flow of the liquid and results in the solidification of the micro- and nanostructures on the Cu surface after cool-down. At low average laser power and high scanning speed, only minor surface modification is observed (category d). Figure 4.8 shows SEM micrographs of UV, green and IR laser light at a radius of 23.0  $\mu\text{m}$ . On a smaller variety of scanning speed and average laser power, similar categories for all wavelengths were observed: a) compact cauliflower structures, and d) minor surface modification. Category c) exhibits molten and resolidified spherical structures for 343 nm similar to Figure 4.7, but is also dominated by LIPSS formation, especially at 515 nm. LIPSS can be generated at all wavelengths, but are not visible in the parameter settings selected for 343 nm photons.

### 4.1.2 Surface chemical properties

The process of surface transformation and plasma plume formation, along with the resulting chemical reactions, is significantly impacted by the ambient conditions during laser ablation [131, 134]. In the following tests, the laser treatment was performed in ambient air, allowing oxidation to occur. To study the influence of laser exposure on the composition of the copper surface, XPS analyses were conducted on specific samples processed at various photon wavelengths and accumulated fluences. Notably, a progressive alteration in the surface composition was observed in the Cu  $2p_{3/2}$  and Cu LMM spectra, as depicted in Figure 4.9. For fluences exceeding 2000  $\text{J cm}^{-2}$ , the binding energies of the Cu  $2p_{3/2}$  and O 1s core levels were measured at 933.7 and 529.6 eV, respectively. Furthermore, the kinetic energy associated with the Cu LMM Auger transition was identified as 917.7 eV, resulting in a modified Auger parameter of 1851.4 eV. The spectral features of copper resembled those of copper oxide (CuO),

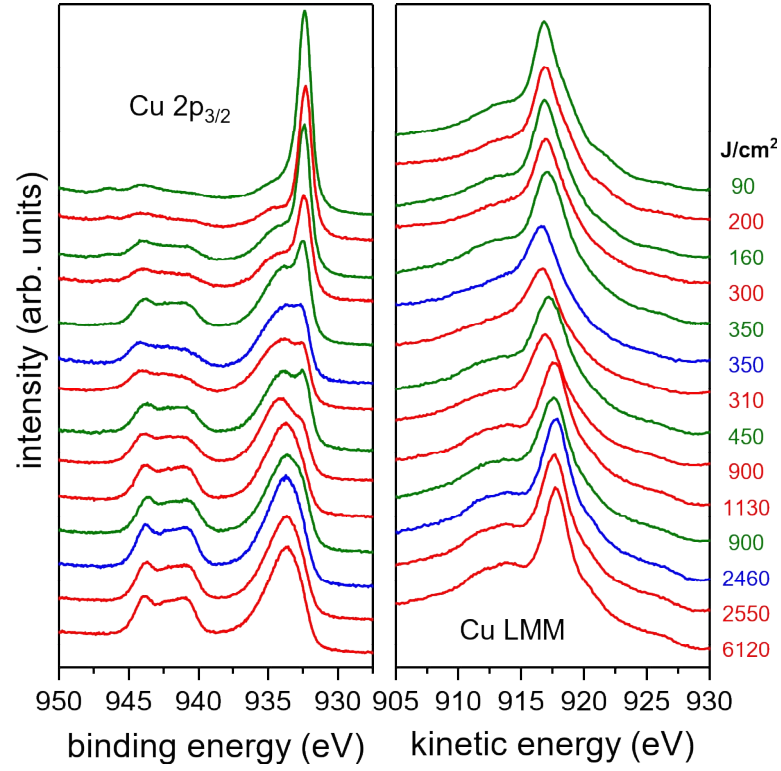


**Figure 4.9:** X-ray photoelectron spectra: Cu  $2p_{3/2}$  state and Cu LMM x-ray excited Auger emission of Cu irradiated in air, using a variety of accumulated fluences between  $90 - 6120 \text{ J cm}^{-2}$  and laser wavelengths of 1064 nm (color-coded in red), 532 nm (green), and 355 nm (blue). Published in Ref. [158].

discussed in Sec. 3.4.3. The peak energies of samples exposed to very low accumulated fluence, on the other hand, exhibited different characteristics: 932.4, 530.3, and 916.8 eV for Cu 2p<sub>3/2</sub>, O 1s and Cu LMM, respectively, with a corresponding modified Auger parameter of 1849.2 eV. Consequently, the surface is mainly composed of Cu<sub>2</sub>O. In addition, there are surface adsorbates present, including hydrocarbon species and oxygen-containing molecules, with distinct features such as a shoulder at around 531.4 – 531.5 eV in the O 1s state (shown in the Appendix Fig. A.2). These features are similar to the analyses of the untreated copper surface (Fig. 3.19, green line). In the intermediate fluence range, there is evidence of copper hydroxide surface species, detected in the Cu 2p<sub>3/2</sub> spectrum at 934.3 eV and by a slight shift of the LMM Auger line of Cu. The XPS spectra series (Fig. 4.9) clearly shows a gradual transition from predominantly pure CuO at high laser fluence, to a mixture of CuO and Cu<sub>2</sub>O in the intermediate range, and finally to a surface dominated by Cu<sub>2</sub>O at low fluences. In correlation with the changes in surface topography, this transition can be attributed to the interaction between the laser light and the material. When a metallic surface is exposed to femto- or picosecond laser pulses, the material absorbs photon energy through inverse Bremsstrahlung. This results in a thermal non-equilibrium between the heated electrons and the cold lattice. The energy transfer to the lattice begins on a picosecond timescale due to electron-phonon coupling and heat conduction. Material removal can occur through phase explosion or thermal vaporization, creating trenches in the shape of the laser beam. The interaction of the laser beam with the evaporated material generates an expanding plasma, which then interacts with the surrounding air, leading to the formation of shock waves. Following electron-ion recombination, particles and clusters are ejected from the plasma and redeposited onto the surface, forming nanostructures [80, 161]. For the experimental conditions used, high accumulated fluences ( $F_{\text{acc}} > 1000 \text{ J cm}^{-2}$ ) result in the formation of CuO nanoparticles in the plasma plume, which are most-likely oxidized due to the oxygen-containing ambient conditions. It is also possible that particles formed from the melt during laser plasma-target interactions plays an additional role, although their significance cannot be determined based on the available data.

#### 4.1.3 Secondary Electron Yield

As analyzed in Section 3.4.4, the typical primary electron energy dependence of the SEY for untreated OFE Cu, that underwent surface degreasing, exhibits a maximum SEY  $\delta_{\text{max}}$  at 250 eV between 1.8 and 2.3, variability ascribed to the “aging” and adsorbate uptake of the sample. Figure 4.10 shows  $\delta_{\text{max}}(E)$  after laser treatment at accumulated fluences ranging from 65 to 4500 J cm<sup>-2</sup> and employing the three different laser wavelengths. The data shows that the SEY decreased to 1.2 and below at a primary electron energy of 250 eV. Simultaneously, the maximum energy  $E(\delta_{\text{max}})$  shifted to higher values (between 1200 and 1800 eV), and the SEY values surpassed those of degreased copper, particularly at lower fluences and higher electron energies. The electrons with energy  $\leq 500 \text{ eV}$  [162] contribute to multipacting in the vacuum

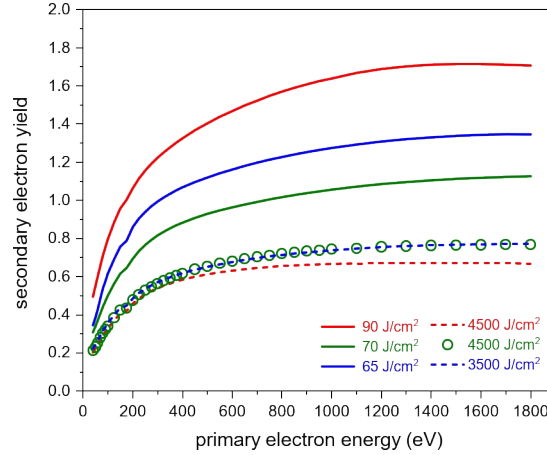


**Figure 4.10:** SEY in dependence of primary electron energy of laser-irradiated copper samples at wavelengths of 355 nm (blue), 532 nm (green), and 1064 nm (red). The used accumulated fluence is indicated in the legend and the corresponding morphologies are shown in Fig. 4.11 (right side). Published in Ref. [158].

tube of the LHC. The results presented in Figure 4.10 demonstrate that treating the surface with ultrashort pulse lasers effectively reduces the SEY by generating grooves and covering the surface with nanoparticles, as shown in Fig. 4.11 (right column). When primary electrons hit the inclined surface regions at an angle, they are scattered forward and trapped in the structures, leading to a decrease in emitted electrons.

The SEY maxima of various samples, shown in Figure 4.11, decrease as the accumulated laser fluence increases for all three laser wavelengths. There are two distinct regimes observed: for low fluences ( $< 1000 \text{ J cm}^{-2}$ ), the SEY maximum is influenced by the wavelength, with the highest value obtained for 1064 nm pulses, and changes with fluence. In the high fluence range ( $F_{\text{acc}} \geq 1000 \text{ J cm}^{-2}$ ), all three curves converge to a minimum  $\delta_{\text{max}}$  of 0.7 – the lowest value achieved in the experiments reported here. The variation in SEY with fluence is attributed to changes in the surface topography and chemical composition. Processed samples typically exhibit micro grooves (Fig. 4.1), decorated with nanoscale features. At high fluences, a layer of nanoparticles forms on the surface in a cauliflower-like pattern due to redeposition of ablated particles. Samples treated with green laser light show more spherical particles. Lower laser fluences result in shallow ablation depths and low density of surface particles (Figs. 4.7 and 4.8). At high fluences, a layer of nanoparticles forms on the surface in a cauliflower-like pattern due to redeposition of ablated particles (Fig. 4.11, right-bottom row). Samples treated with green laser light show more spherical particles. Lower laser fluences ( $F_{\text{acc}} \sim 100 \text{ J cm}^{-2}$ ) result in shallow ablation depths and low density of surface particles (Fig. 4.11, right-top row). In this regime, UV or IR laser irradiation lead to the formation of spherical structures from resolidified molten copper, while green laser light created ripples resembling LIPSS decorated with nanospheres. A detailed gradual variation of the surface morphology from low to high fluence using UV

#### 4.1 Influence of accumulated fluence and wavelength

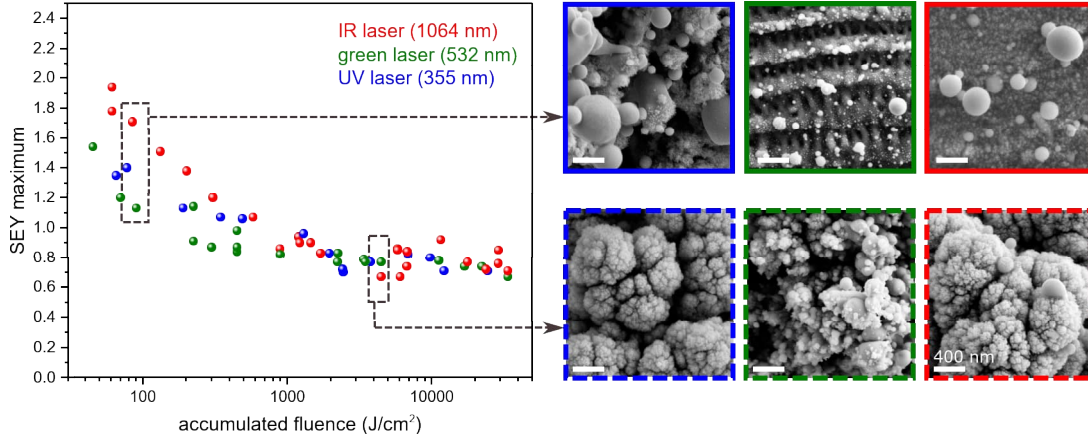


**Figure 4.11:** Left: SEY maximum in dependence of the accumulated fluence for UV (355 nm), green (532 nm), and IR (1064 nm) picosecond laser pulses. Right: scanning electron micrographs of selected samples that had been created at low (top row) and high (bottom row) accumulated laser fluence (indicated by the dashed boxes, the corresponding SEY curves are shown in Fig. 4.10). The white scale bars in the micrographs correspond to a length of 400 nm. Published in Ref. [158].

laser irradiation as an example is illustrated in Figure 4.7. and a more comprehensive comparison of the morphology of surfaces processed with different photon wavelengths and the same laser diameter is shown in Figure 4.8.

The XPS and SEY data indicate, that a saturation fluence exists. Above  $2000 \text{ J cm}^{-2}$ , the amount of CuO on the surface does not increase any further, and the SEY does not decrease any further. This phenomenon can be explained by two factors. First, at high accumulated fluence, corresponding to slow scanning speeds during processing, the number of laser pulses per unit area increases to a point where the laser pulses self-limit their effectiveness. This is because the plasma plume, created by the previous pulse, may not have fully decayed by the time the next pulse arrives, leading to a shielding effect that reduces the intensity of the laser reaching the target surface. In addition, at higher power levels, the electron density in the plasma plume increases, making it more opaque and resulting in absorption of the laser radiation through various mechanisms [163]. As a result, the ablation rate is typically limited due to plasma shielding. However, in some cases, such as the example shown, the ablation depth does not fully saturate at very high fluences, but a decrease in slope is observed (Appendix Fig. A.1). When considering the SEY trend vs. accumulated fluence (Fig. 4.11), it is clear that creating very deep trenches does not significantly reduce the SEY, as electrons do not reach these depths. Second, SEM images of samples processed at high fluence show a high concentration of nanoparticles covering the entire surface. The capacity of the surface to trap redeposited particles may be limited, causing additional particles to not adhere anymore. The effects mentioned above can help explain the existence of a minimum SEY limit for all three wavelengths and emphasize the importance of the surface nanoparticle layer in reducing SEY. It is noteworthy



that the low SEY was not obtained due to the presence of CuO. In contrast, a CuO surface without structure has a higher SEY compared to non-structured Cu<sub>2</sub>O. This indicates that CuO is not necessary to achieve a very low SEY, as processing in a nitrogen atmosphere, which inhibits the formation of CuO, also results in low values. Moreover, surfaces dominated by CuO are not ideal for use in particle accelerators, as they can cause surface charging at cryogenic temperatures and do not effectively reduce the SEY upon electron irradiation.

A gradual decrease in fluence from 1000 to 100 J cm<sup>-2</sup> results in a reduction in the density of redeposited particles on the surface. This decrease is directly observable through microscopy and can also be indirectly traced by observing the diminishing CuO-related contributions in the Cu 2p<sub>3/2</sub> XPS spectrum. As a result of this gradual change in surface properties, the SEY increases. At very low fluences, the ablation threshold of the materials becomes significant. In such cases, while the surface topography may still transform, there is neither a significant removal nor redeposition of material. The laser treatment only causes a slight modification in the surface composition, as there is a minimal amount of surface hydroxide and hydrocarbon adsorbates. In general, it is observed that at low fluences ( $F_{\text{acc}} \leq 1000 \text{ J cm}^{-2}$ ), the effectiveness of the IR laser light for surface structuring and reducing the SEY is lower. This trend is reflected in Figures 4.10 and 4.11. A higher fluence of IR light is required to achieve similar surface properties obtained with green or UV-processed surfaces, due to the higher efficiency of shorter wavelengths. The absorbance of the material partially plays a role in this behavior, with the reflectivity of a smooth copper surface being lower for longer wavelengths at RT (Sec. 3.4.2).

Considering the essential requirements for *in situ* laser processing of LHC BSs, a comparison between Figures 4.3 and 4.11 is crucial. At the maximum acceptable ablation depth of 25 µm, the accumulated fluence required is 900 J cm<sup>-2</sup> (IR), 750 J cm<sup>-2</sup> (green), and 380 J cm<sup>-2</sup> (UV). The corresponding maximum SEY values at these fluences are 0.85 (IR), 0.8 (green), and 1.0 (UV). These fluences represent the maximum values that can be applied to achieve a  $\delta_{\text{max}}$  of around 1 with an ablation depth below 25 µm. The lower limit for fluence is determined at the fluence where  $\delta_{\text{max}} = 1.0$ , namely, 650 J cm<sup>-2</sup> (IR), 130 J cm<sup>-2</sup> (green), and 380 J cm<sup>-2</sup> (UV). At these lower limits, the processing time is 95 s cm<sup>-2</sup> (UV), 32.5 s cm<sup>-2</sup> (green), and 162.5 s cm<sup>-2</sup> (IR) at an average laser power of 4 W. All three laser wavelengths meet the necessary criteria, however, the acceptable fluence range for the green laser is the widest and requires the shortest processing time. Despite the high efficiency in material removal of UV processing, it may not be ideal for preserving the copper layer on the BS surface due to its deep ablation depth. The *in situ* setup, presented in Sec. 3.2), is designed for laser processing BSs up to 15 meters in length. It includes a long optical fiber, a laser-fiber coupling system, and an inchworm robot. Technological advancements have made it possible to transmit high-power picosecond pulses through a fiber for green and, particularly, IR lasers, but such solutions are not yet available for UV light.

#### 4.1.4 Conditioning

The change in SEY, induced by electron radiation, was evaluated by exposing the surfaces to an electron beam. The measurement process plays an important role in determining and validating the surface treatment. The conditioning test aims to replicate the gradual change in surface properties induced by the electron cloud buildup in the scrubbing cycles of particle accelerators [52, 54] and their ongoing operation [65]. When an air-exposed copper surface is irradiated with electrons, molecules that are adsorbed on the surface are removed through electron-stimulated desorption and chemical reactions on the surface are induced [31, 32].

Here, the chemical transformation during conditioning at RT of a laser-processed surface ( $\lambda = 1064 \text{ nm}$ ,  $F_{\text{acc}} = 85 \text{ J cm}^{-2}$ ) was investigated and are shown in the XPS spectra of Figure 4.12. The laser-processed sample was stored in a plastic box for two months before conditioning. The XPS spectrum prior to the conditioning was dominated by  $\text{Cu}(\text{OH})_2$  as the  $\text{Cu } 2p_{3/2}$  peak is at 935 eV binding energy and a pronounced satellite feature is visible between 938 and 948 eV. The O 1s spectrum has a maximum at 531.8 eV, which is assigned to  $\text{OH}^-$  and is compatible with  $\text{Cu}(\text{OH})_2$ . The modified Auger parameter of 1850.7 eV confirms the predominant presence of  $\text{Cu}(\text{OH})_2$ . The spectra in Figure 4.12 are more dominated by hydroxide than the surfaces processed with equivalent accumulated fluences in Figure 4.9. Compared to the  $\text{AlK}\alpha$  source (XR50M,  $h\nu = 1486.7 \text{ eV}$ ) used in the other analysis, the  $\text{Mg } K\alpha$  x-ray source ( $h\nu = 1253.6 \text{ eV}$ ) used in this analysis is more sensitive to the topmost surface layer. The spectra clearly changed after the conditioning with 250 eV electrons up to a dose of  $2.6 \times 10^{-2} \text{ C mm}^{-2}$ : The  $\text{Cu } 2p_{3/2}$  peak shifted to 933.2 eV (mod. Auger parameter: 1848.9 eV), the satellite feature almost vanished, and the O 1s maximum shifted to metal oxide at 530.8 eV, all pointing to a transformation from  $\text{Cu}(\text{OH})_2$  to  $\text{Cu}_2\text{O}$ .

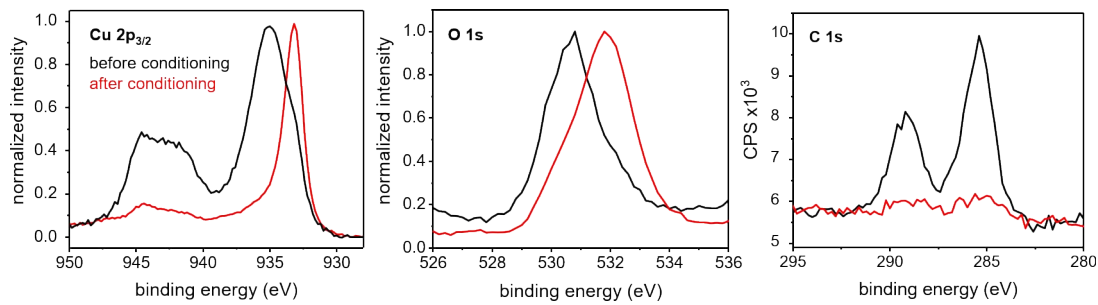


**Figure 4.12:** Chemical properties before and after conditioning up to a dose of  $2.6 \times 10^{-2} \text{ C mm}^{-2}$  of a 1064 nm laser-processed surface ( $F_{\text{acc}} = 85 \text{ J cm}^{-2}$ ). XPS spectra of Cu 2p<sub>3/2</sub>, O 1s, and C 1s. The corresponding SEY decrease is shown in Figure 4.13 (dotted red line,  $85 \text{ J cm}^{-2}$ ).



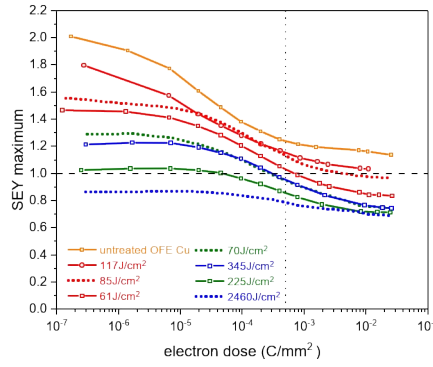


**Figure 4.13:** SEY maximum of laser-generated surface structures in dependence of electron dose during conditioning at RT with 250 eV electrons. Surface were processed with different accumulated fluences (indicated in the legend) and different wavelengths of 355 nm (blue), 532 nm (green), and 1064 nm (red color-coded). The SEY of 1 (targeted for electron cloud mitigation) is indicated by the dashed horizontal line and the dotted vertical line refers to an electron dose of  $5 \times 10^{-4} \text{ C mm}^{-2}$ . Published in Ref. [158].

In summary, both the dissociation of hydroxide and the removal of carbon adsorbates, witnessed by the decrease of carbon content in the C 1s spectrum (Fig. 4.12), result in a surface cleaning effect. The atomic composition shows that the carbon content decreased from 21.1 to 4.1 %. Concomitantly, the oxygen content decreased (50.6 to 35.5 %) and the percentage of metallic Cu increased (28.3 to 60.5 %). The observed surface changes are similar to those of an air-exposed flat Cu surface during conditioning, as explained in section 3.4.5 or studied in detail in Ref. [156]. Concomitantly, the SEY maximum of the surface decreased from 1.55 to 0.97, as shown in Figure 4.13 (dotted red line), and discussed below.

Laser-treated samples with varying initial SEY maximum values between 0.8 and 1.8 were exposed to 250 eV electrons to study their behavior as the electron dose increased gradually. The results, shown in Figure 4.13, revealed that the maximum SEY ( $\delta_{\text{max}}$ ) changed significantly up to a dose of about  $3 \times 10^{-2} \text{ C mm}^{-2}$ , indicating a conditioning effect influenced by alterations in surface properties. Generally, surfaces with lower initial  $\delta_{\text{max}}$  values exhibited a lower final value after conditioning. Samples starting with a value below 1.6 reached a final value below 1, while those with an initial SEY maximum above 1.6 remained above 1 even at high electron doses of approximately  $10^{-2} \text{ C mm}^{-2}$ . These trends suggest that the laser treatment process can be tailored to effectively mitigate electron cloud effects by balancing very low SEY with reductions in surface particle density, ablation depth, and increased processing speed. This finding allows for more versatility in choosing laser processing parameters and wavelengths, expanding the spectrum of fluence where the surface meets the SEY and ablation depth criteria. Processing at lower fluence proved to be advantageous due to the fact that the

modification depth is significantly reduced (Fig. 4.3), the surfaces show less oxidation (Fig. 4.9), and are covered by a lower amount of particles (Fig. 4.11). By taking into account the findings from electron conditioning experiments and the limitations of scrubbing campaigns, it is possible to strike a good balance for achieving satisfactory conditioning performance in accelerator applications. This can be achieved by aiming for a treatment that results in an initial maximum removal depth of 1.4–1.5, which then decreases to values below 1 at electron doses of approximately  $5 \times 10^{-4} \text{ C mm}^{-2}$ . During the ramp-up phase (scrubbing run) of the LHC, the SEY of such a surface would condition below 1, which is below the threshold values at which the heat load induced by the electron clouds becomes detrimental (see Sec. 2.3).

## 4.2 Influence of pulse duration

The influence of pulse duration on the SEY of the laser-treated surface was evaluated by varying the pulse duration from 238 fs to 10 ps using the IR laser ( $\lambda = 1030 \text{ nm}$ ,  $f_{\text{rep}} = 100 \text{ kHz}$ ,  $\omega_0 = 23.0 \mu\text{m}$ ). As the repetition rate was kept constant, the peak power  $P_0$  ranged from 180.7 MW for 238 fs to 4.3 MW for 10 ps at similar pulse energy  $E_p = 43 \mu\text{J}$ . The analysis of the ablation behavior was conducted on individual copper lines engraved at a scanning speed of  $200 \text{ mm s}^{-1}$  for pulse durations of 238 fs, 1 ps and 10 ps. Figure 4.14 illustrates the ablation depth, measured with WLI, as a function of the average laser power. It is generally observed that shorter pulse lengths lead to greater material ablation. The relation between the ablation depth  $\Delta z$  and the average laser power  $P$  was used to fit the data (Eq. 2.17). From the fit parameters, the ablation threshold power  $P_{\text{th}}(N = 23)$  and the effective absorption coefficient  $\alpha_{\text{eff}}$  were derived and listed in Table 4.2. The highest ablation threshold ( $F_{\text{th}}(N = 23) = 1.49 \text{ J cm}^{-2}$ ) was obtained for a pulse duration of 10 ps and it decreased for shorter pulses. The value is relatively high compared to the ablation threshold of Cu for green laser ( $0.24 \text{ J cm}^{-2}$  [132] for 532 nm, 10 ps and 200 kHz), but comparable values were obtained elsewhere [164] for 800 nm, 100 fs and 80 MHz on copper. The obtained absorption coefficients are two orders of magnitude higher than the value of  $6.3 \times 10^7 \text{ m}^{-1}$  reported in literature and slightly higher than in a comparable study [164]. It should be noted that the coefficients evaluated here include 23 laser pulses and the threshold fluence decreases the more pulses (higher accumulated fluence) are applied due to the incubation effect [120]. The absorption coefficient increased slightly for shorter pulses, which is consistent with the trend of the ablation threshold and the smaller slope in Figure 4.14. This behaviour is also attributed to the higher peak power that was used for shorter pulses. In the case of Cu, the electron-phonon relaxation time is approximately 10 ps, which is defined by the electron-phonon coupling constant of the material. Therefore, it takes at least 10 ps for the electron gas and the lattice to reach thermodynamic equilibrium, which is necessary for heat transfer to occur. Longer pulse durations are expected to result in more significant differences in the ablation mechanism.

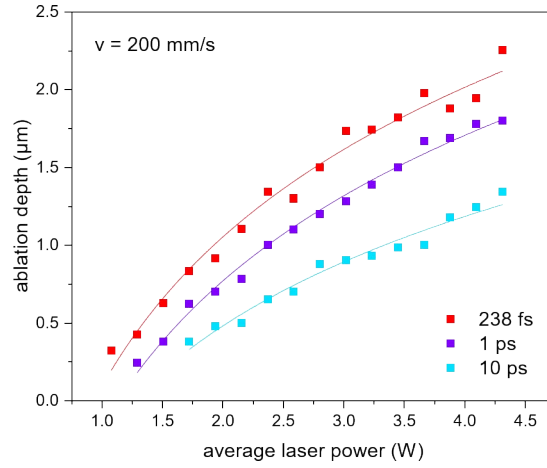


**Figure 4.14:** IR laser-irradiated Cu surfaces using various pulse durations and a constant scanning speed of  $v = 200 \text{ mm s}^{-1}$ . Ablation depth measured with WLI (squares) in dependence of the average laser power and fit according to Eq. (2.17).

**Table 4.2:** Ablation threshold and absorption coefficient of copper for  $N = 23$  infrared pulses at a repetition rate of 100 kHz obtained from the fit in Fig. 4.14.

	$\alpha_{\text{eff}}$	$P_{\text{th}}(N = 23)$	$F_{\text{th}}(N = 23)$
238 fs	$7.2 \times 10^5 \text{ m}^{-1}$	0.93 W	$1.12 \text{ J cm}^{-2}$
1 ps	$7.4 \times 10^5 \text{ m}^{-1}$	1.13 W	$1.36 \text{ J cm}^{-2}$
10 ps	$9.9 \times 10^5 \text{ m}^{-1}$	1.24 W	$1.49 \text{ J cm}^{-2}$

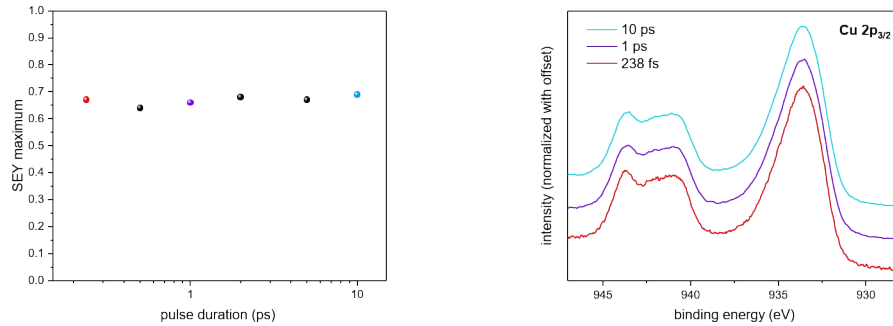


**Figure 4.15:** Left: Maximum SEY for various pulse durations between 238 fs and 10 ps. Published in Ref [165]. Right: XPS analysis of OFE Cu samples processed in air at an average laser power of 4.33 W and pulse durations of 238 fs, 1 ps and 10 ps.

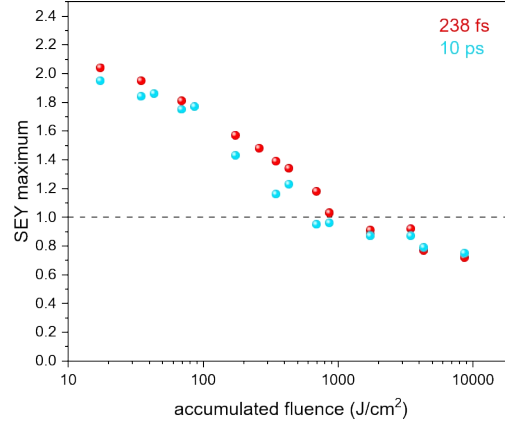


**Figure 4.16:** SEY maximum of copper surfaces processed at pulse durations of 238 fs and 10 ps. The scanning speeds were varied from 1 to 200 mm s<sup>-1</sup> for average laser powers up to 4.3 W and a line distance of 50 μm.

The laser processing at high accumulated fluence of  $F_{\text{acc}} = 4330 \text{ J cm}^{-2}$  ( $P = 4.33 \text{ W}$ ,  $v = 2 \text{ mm s}^{-1}$ ,  $\Delta y = 50 \mu\text{m}$ ) resulted in the typical cauliflower structures as obtained in the previous experiments. In the SEY measurement in Figure 4.15, values as low as  $\delta_{\text{max}} = 0.67 \pm 0.02$  were obtained for all pulse lengths used. In the previous experiments in Section 4.1, this was the lowest SEY achieved, and the SEY maximum was in the saturation regime at an accumulated fluence of  $4330 \text{ J cm}^{-2}$ . Thus, the SEY maximum does not change for shorter pulse lengths. The effect of the pulse duration on the SEY may be more significant at low accumulated fluence, as studied below. The chemical properties at this high fluence were also evaluated by XPS measurements. Figure 4.15 shows similar features in the Cu 2p<sub>3/2</sub> spectrum of surfaces processed with pulse durations of 238 fs, 1 ps, and 10 ps: The main peak at 933.6 eV and the satellite feature between 938 and 948 eV point to the presence of CuO, which matches the previous results, where the chemical composition gradually transformed from Cu<sub>2</sub>O to CuO upon increasing accumulated fluence (see Figure 4.9). On a wider parameter range, the scanning speed was varied from 1 up to 200 mm s<sup>-1</sup> and the average laser power from 0.2 up to 4.3 W at a line distance of 50 μm. The decrease of the SEY maximum upon increasing accumulated fluence obtained in Figure 4.16 is identical to the results of the IR laser in Fig. 4.11. For the surfaces processed at low accumulated fluences ( $< 1000 \text{ J cm}^{-2}$ ), ps pulses resulted in a slightly lower SEY maximum. However, the deviation is within the accuracy of the SEY measurement. Therefore, it can be concluded that the SEY in this range of pulse length and the energy per pulse is independent of the pulse duration. It is noteworthy that the SEY is similar for the applied pulse lengths, although the ps laser ablated less material. This further demonstrates that the SEY is not mainly influenced by the microstructure but also by the nanofeatures. Due to the laser-matter interaction, shorter pulses produce

less debris (less roughness) [96], which could explain the comparable SEY maxima. This is supported by SEM images in Ref. [165], where the surface morphology of Cu processed with a variety of scanning speeds and average laser powers was compared for 238 fs and 10 ps laser pulses.

### 4.3 Influence of defocusing

Defocusing may play a role in laser processing on the non-circular cross-section of the inner beam screen surface and will be analyzed in this section. To investigate the influence of defocusing on the ablation efficiency, single lines were engraved using 515 nm photons in a 1 mm thick Cu sample at various focal plane positions  $z$  ranging from +5 to -5 mm. Figure 4.17 shows the ablation depth as well as the beam waist at various focal displacements. The graph was normalized to the maximum ablation depth at  $z = 0$  mm. At a positive displacement  $z$ , the focal point was within the sample or below it. At  $-z$ , the focal point was located above the sample surface. According to Eq. (2.11) and Fig. 4.17 (black dots), the laser diameter widens as  $z$  increases. Concomitantly, the energy density per irradiated area decreases, resulting in less material removal. At the Rayleigh length of  $z = 1.5$  mm (Tab. 4.1), the ablation depth is approximately 60 % of the maximum depth that was obtained when processing in focus. At displacements of  $z = 0, -1.08, -2.24$  and  $-3.21$  mm, the beam waists amounted to 13.7, 23, 46, and 69  $\mu\text{m}$ , respectively.

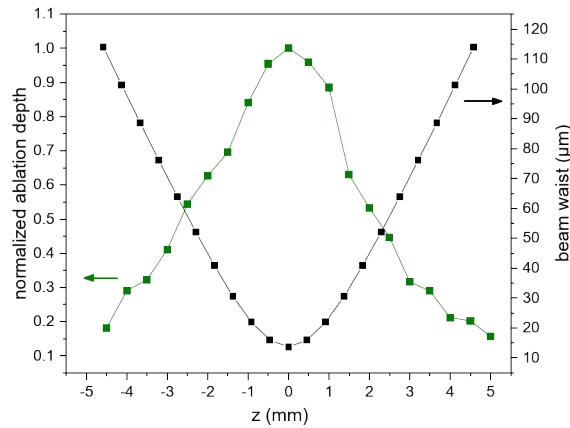


**Figure 4.17:** Normalized ablation depths along the focal plane  $z$  measured with WLI and calculated beam waist of 515 nm laser, according to the fit in Figure 4.5. The maximum ablation depth at  $z = 0$  corresponds to an ablation depth of 9.64  $\mu\text{m}$  for a scanning speed of 50  $\text{mm s}^{-1}$ , an average laser power of 2.5 W, and a pulse duration of 260 fs.

Figure 4.18 shows SEM photographs of surfaces processed at accumulated fluences of 1046 and 210 J cm<sup>-2</sup> at the four points of displacement. For green laser irradiation, the SEY maximum of a surface processed at 1046 J cm<sup>-2</sup> was in the saturation regime and approximately 0.8, and the ablation depth amounted to 30 μm. The topography is characterized by trenches of high roughness and the typical cauliflower nano-features, as visual in Figure 4.18 at  $z = 0$ . At a lower accumulated fluence of 210 J cm<sup>-2</sup>, a SEY maximum of 1.1 was obtained and a depth of  $\approx 4 \mu\text{m}$  (compare Figs. 4.11 and 4.3). The morphology is a mixture of less compact cauliflower features and LIPSS structures. Out of focus, the deposited energy is less localized, reflected in the surface structures that become more chaotic at 1046 J cm<sup>-2</sup>, the higher  $z$  is. At the maximum displacement of 3.21 mm (d), less defined and shallower trenches are observed and the surface is primarily dominated by LIPSS instead of the compact cauliflowers. According to Figure 4.17, the ablation depth reduces to 35 % of the maximum depth. This corresponds to a depth of  $\approx 10.5 \mu\text{m}$  at  $z = 3.21 \text{ mm}$ . In addition, the aspect ratio of the trench profile decreases, as the laser diameter increased. At low fluence, as shown in the right column of Figure 4.18, the defocusing resulted in shallower trenches. The LIPSS structure remained, but with almost no particles present.

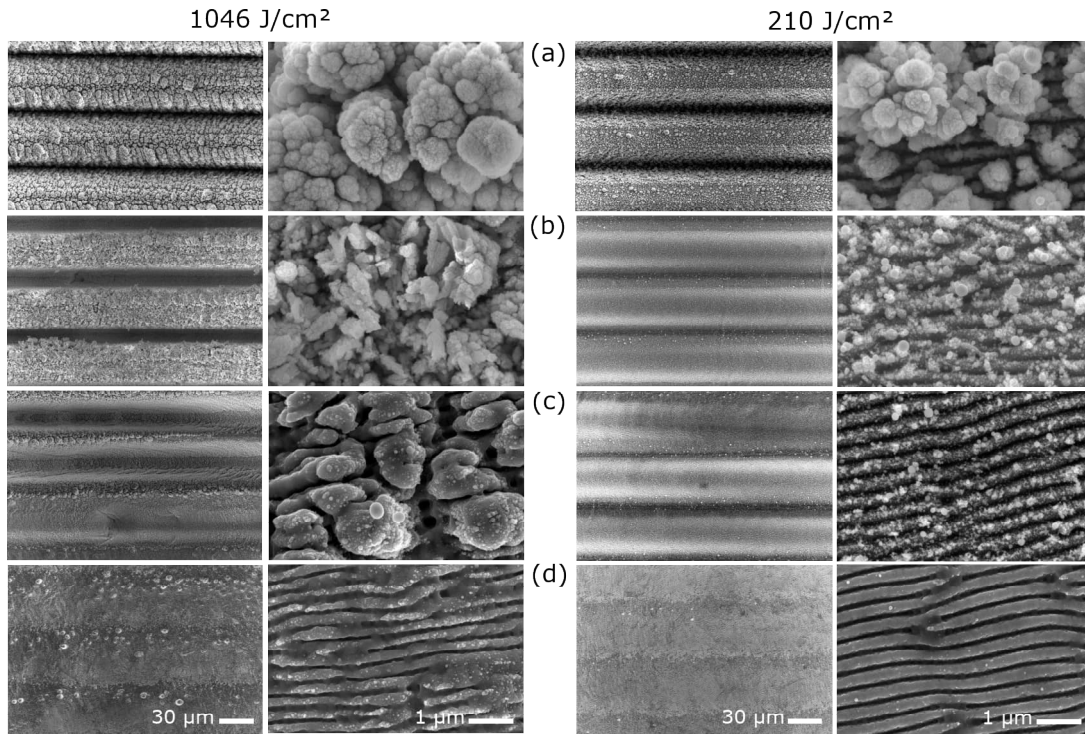


**Figure 4.18:** SEM images of surfaces processed with 515 nm photons and accumulated fluences of 1046 J cm<sup>-2</sup> (left) and 210 J cm<sup>-2</sup> (right) at various offsets  $z$  with respect to the focal plane: a)  $z = 0 \text{ mm}$ ,  $\omega_0 = 13.7 \mu\text{m}$ ; b)  $z = 1.08 \text{ mm}$ ,  $\omega_0 = 23 \mu\text{m}$ ; c)  $z = 2.24 \text{ mm}$ ,  $\omega_0 = 46 \mu\text{m}$ ; d)  $z = 3.21 \text{ mm}$ ,  $\omega_0 = 69 \mu\text{m}$ .

#### 4.4 Comparison of laser processing of Cu OFE bulk and colaminated Cu

In the above experiments, laser processing was performed on OFE copper surfaces. However, the laser treatment of the inner surface of the BS will be performed on Cu that was laminated onto stainless steel. In the preliminary analysis of the untreated surfaces, slight differences in the materials were observed. Specifically, the specular reflectivity of the colaminated Cu was higher (see Sec. 3.4.2), and the analysis of the topography revealed a larger grain size of the beam screen material (Sec. 3.4.1). Therefore, the SEY of the two processed materials is compared in the following. The surfaces were irradiated at various accumulated fluences ranging from 51 to  $10\,184\text{ J cm}^{-2}$  using an IR laser (1030 nm, 1 ps, 500 kHz). Figure 4.19 depicts the measured SEY maxima as a function of accumulated fluence. A general decrease of  $\delta_{\text{max}}$  was observed with increasing accumulated fluence. The values of the colaminated Cu were generally lower than those of OFE Cu. However, the difference in SEY of the materials was less than 0.1, which is within the experimental error of the SEY measurement. In conclusion, the material difference is negligible and does not affect the laser processing or the SEY. Therefore, the findings on the OFE copper sample can be applied to the processing of beam screen surfaces. For the sake of simplicity, the treatments on curved surfaces described in Chapter 5 were also performed on OFE Cu, before scaling up the treatment (Chapter 6).

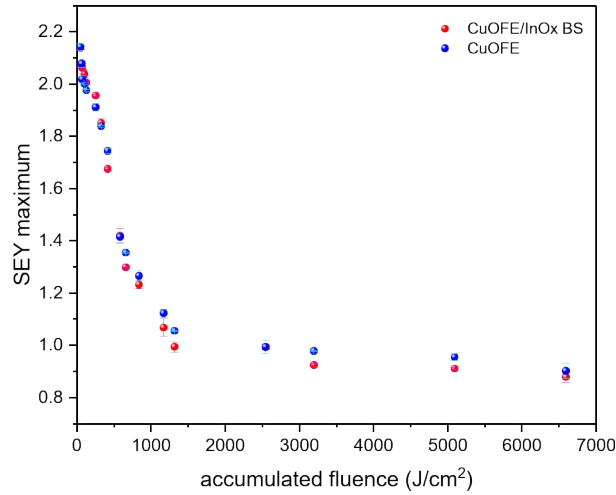


**Figure 4.19:** SEY maxima of OFE Cu and colaminated Cu on stainless steel (BS-type Cu) processed using an IR laser (1030 nm, 1 ps, 500 kHz) at various accumulated fluences. The error bars refer to the standard deviation of the averaged SEY measured at the different locations on the sample.

## 4.5 Conclusions

The influence of wavelength (covering the range from UV to IR), pulse duration, and accumulated fluence on the structuring of copper via ultrashort pulse laser irradiation at a 100 kHz repetition rate was investigated to study their effect on SEY reduction. For analysis of the surface structures, parameters such as the ablation depth, the surface morphology, the SEY, and the chemical composition were considered in relation to the average laser power, the scanning speed, and the line distance at a specific focal spot size. Independent of the laser wavelength and pulse duration, two important relations were found. First, the ablation depth showed an increase with higher laser fluence. Second, the resulting SEY maximum is reduced for increasing accumulated fluence to an ultimate limit of 0.7. When comparing the three laser wavelengths, it was observed that UV and green lasers were more effective in reducing the SEY at lower laser fluence, compared to IR laser radiation. However, above a certain fluence threshold, similar SEY values and surface morphologies were achieved.

For processing BSs up to 15 m in length, fast scanning speeds and a low surface particle density are targeted. All three laser wavelengths offer the flexibility to optimize processing parameters based on the correlation between accumulated fluence and resulting surface characteristics, directly impacting SEY. A gradual reduction in SEY was observed with increasing laser fluence, and electron conditioning proved effective for laser-structured copper samples, allowing for a trade-off between antithetical physical and technical requirements. Notably, green laser irradiation resulted in the lowest SEY at an acceptable ablation depth, while considering cost-effectiveness and system reliability, an IR laser could be a viable alternative to meet the technical requirements of transmitting high-power light pulses through long fibers.





## 5 Robot-assisted laser processing of curved surfaces

In this chapter, the laser processing was performed in the BS using the *in situ* setup, in which the laser beam is guided into the tube via a hollow-core fiber, and the beam travelling and scanning is performed by a robot (detailed description in Sec. 3.2). Laser processing in a tube, as the BS, is more complex than processing flat surfaces in an open model system: Precise optical alignment is required to couple the laser beam into the hollow-core fiber, the focal point is more difficult to align with the BS surface as the BS may deform, and the careful alignment of the optical path in the robot determines the quality of the processing. In addition, a number of factors contributing to intensity loss must be considered, ranging from the laser coupling into the hollow-core fiber to the sensitivity of the robot's optics that can get contaminated and trigger intensity losses, as detailed in Sec. 3.2. In the following, only curved OFE Cu inserts flush with the BS surface (shown in Fig. 5.1) were treated rather than the entire circumference so that only particles from the treated insert redeposit on the surface. The scaling to longer BSs and scanning strategies are discussed in the next Chapter 6. Two main aspects differ from the studies on flat surfaces. First, all model studies were conducted in air, where oxidation is not suppressed. In the *in situ* setup, a nitrogen flow through the nozzle of the robot is directed towards the interaction zone, which is indispensable to protect the optics in the robot from particle contamination and to minimize oxidation to prevent charging at cryogenic temperature. Second, particle generation in the confined space of the BS is a critical source of contamination

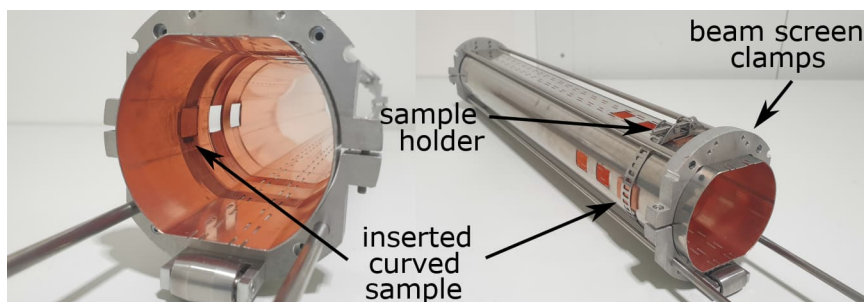


**Figure 5.1:** 50 cm BS (type 74) used as a test bench for the laser processing in this chapter. Curved OFE Cu samples were inserted in the BS holes and fixed with a metal ring so that the surface is flush with the inner BS surface. The clamps hold the BS in a fixed position.

of the optics in the robot, as opposed to processing flat surfaces in an open model system. In addition, the amount of redeposited particles on the treated surface may be higher due to the quasi-enclosed space of the tube. The fraction of loosely bound particles must be limited because they could potentially detach from the surface during operation of the LHC. This is critical as it can lead to beam losses. The more tightly bound particles form the nanostructure and are crucial to reduce the SEY.

In the following, the surface properties resulting from an *in situ* processing are presented and compared with the results on flat surfaces. Moreover, the processing parameters are optimized to achieve the treatment requirements for use in the LHC magnets, namely a maximum SEY  $\leq 1$  after conditioning, an ablation depth of less than 25  $\mu\text{m}$ , a  $\text{Cu}_2\text{O}$ -dominated surface instead of  $\text{CuO}$ , and the limitation of loosely bound particles.

## 5.1 Influence of the inert gas nozzle

In the *in situ* setup, nitrogen is supplied through a pipe connected to the robot and blown locally into the reaction zone through a nozzle, which is also where the laser beam exits. The  $\text{N}_2$  flow directed towards the surface may influence the built-up of the plasma plume, and consequently the resulting surface properties (morphology, chemical composition). In previous studies, a  $\text{CuO}$ -dominated laser-processed surface charged up upon electron exposure at cryogenic temperature, while processing in  $\text{N}_2$  atmosphere suppressed oxidation, which prevents charging [2]. Therefore, the  $\text{N}_2$  supply via the nozzle of the robot was investigated and optimized in this section to obtain  $\text{Cu}_2\text{O}$  (instead of  $\text{CuO}$ ) by varying the flow conditions (laminar/turbulent) using various nozzle designs and varying the  $\text{N}_2$  volume flow. Furthermore, the surface characteristics, such as the topography, chemical properties and SEY, of curved samples processed on the *in situ* setup in air (without additional flow through the nozzle) and in local  $\text{N}_2$  flow were compared to the model studies in air.

### 5.1.1 Influence of the flow speed using various nozzle designs

The aim is to suppress oxidation and to limit the redeposition of particles on the surface. Therefore, the speed of the flow  $v$  was changed using different nozzle designs (Fig. 5.2, top row) at a constant volume flow of  $\dot{V} = 4 \text{ L min}^{-1}$ . Three different geometries were chosen, providing either laminar or turbulent flow, distinguished by the Reynolds number of a tube:

$$Re = \frac{\rho v d}{\eta} \begin{cases} \geq 2300 & \text{turbulent flow,} \\ < 2300 & \text{laminar flow,} \end{cases} \quad (5.1)$$

with the fluid density  $\rho_{\text{N}_2} = 1.16 \text{ kg m}^{-3}$ , the tube diameter  $d$ , the dynamic viscosity of the fluid  $\eta = 1.75 \times 10^{-6} \text{ kg m}^{-1} \text{ s}^{-1}$  and the speed  $v = \frac{\dot{V}}{\pi(d/2)^2}$ .

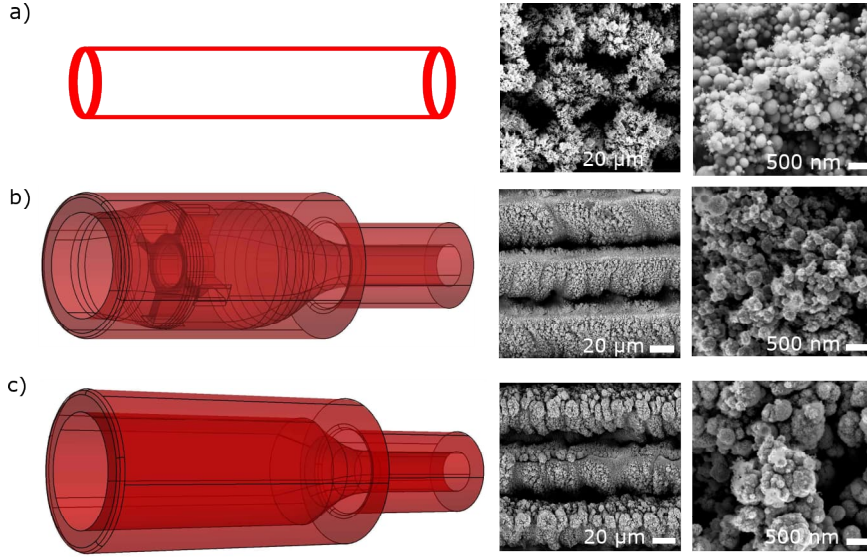


**Figure 5.2:** SEM of samples processed at an accumulated fluence of  $2000 \text{ J cm}^{-2}$  at a  $\text{N}_2$  flow rate of  $4 \text{ L min}^{-1}$  using a) a hollow thin tube (1.5 mm inner diameter) generating turbulent flow, b) a larger tube with an internal structure, and c) a hollow large tube (5 mm inner diameter) generating laminar flow. Flow speeds of a)  $38 \text{ m s}^{-1}$ , b)  $21 \text{ m s}^{-1}$ , and c)  $3 \text{ m s}^{-1}$  were applied.

The following nozzles were used (Fig. 5.2): a) a hollow thin tube with an inner diameter of  $d = 1.5 \text{ mm}$ , providing turbulent flow ( $Re = 3751$ ), b) turbulent flow ( $Re = 2813$ ) close to the critical Reynold number  $Re_{\text{crit}} = 2300$  through a larger diameter tube with an internal grid (grid opening 2 mm), and c) a hollow large tube with  $d = 5 \text{ mm}$  providing laminar flow ( $Re = 1125$ ). The grid structure of b) was designed to prevent vortices formation in a turbulent flow. The surfaces were all processed at high accumulated laser fluence of  $2000 \text{ J cm}^{-2}$ , at which  $\text{CuO}$  was formed when processing flat samples in air (see XPS measurements in Fig. 4.9).

SEM images of the treated surfaces in Fig. 5.2 indicate that the morphology is influenced by the gas supply: a) turbulent flow through the thin nozzle resulted in a random redeposition of a large number of particles, consisting of clusters of molten spheres and dust, b) the structure in the nozzle possibly created turbulences that pushed the molten spheres aside resulting in less particle coverage than using the hollow thin tube, and c) reducing the speed resulted in the absence of the molten spheres, possibly due to the low speed of  $3 \text{ m s}^{-1}$ . The morphology resembles the cauliflower structure, obtained when processing in air.

Depending on the flux regime, distinct features in the  $\text{Cu } 2p_{3/2}$  spectra and different modified Auger parameters were found in XPS analysis shown in Fig. 5.3, suggesting different oxidation states. Processing at a high flow speed of  $38 \text{ m s}^{-1}$  (a, using the thin nozzle) resulted in a  $\text{Cu } 2p_{3/2}$  peak position at  $932.5 \text{ eV B.E.}$  (modified Auger

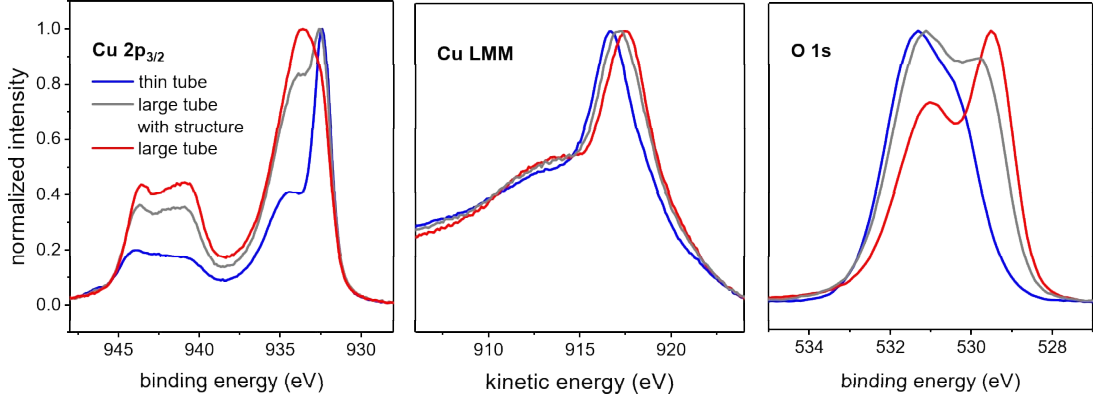


**Figure 5.3:** XPS spectra of Cu  $2p_{3/2}$ , Cu LMM Auger excitation, and O  $1s$  of laser-processed curved copper surfaces in local nitrogen flow at speeds of  $38 \text{ m s}^{-1}$  (blue),  $21 \text{ m s}^{-1}$  (gray), and  $3 \text{ m s}^{-1}$  (red), using the nozzles shown in Fig. 5.2.

parameter 1849.1 eV), at intermediate speed of  $21 \text{ m s}^{-1}$  (b, large nozzle with structure) at 932.4 eV B.E. (modified Auger parameter 1849.7 eV) and at low speed of  $3 \text{ m s}^{-1}$  (c, large nozzle) at 933.6 eV B.E. (modified Auger parameter 1851.5 eV). The satellite feature between 938 and 948 eV B.E. together with the shoulder of the main peak at 934 eV – obtained in turbulent flow – is assigned to  $\text{Cu}(\text{OH})_2$ . For the larger diameter nozzles a second bump of the satellite was observed between 938 and 942 eV B.E., which is more pronounced for the laminar flow c). The satellite feature together with the modified Auger parameter of 1851.5 eV and the O  $1s$  peak at a binding energy of 529.5 eV indicates the presence of  $\text{CuO}$  for the low flow speed of  $v = 3 \text{ m s}^{-1}$ . Exclusively the turbulent flow using the thin nozzle suppressed oxidation efficiently, resulting in  $\text{Cu}_2\text{O}$ . The processing using the large nozzle with internal structure resulted in an intermediate state of  $\text{CuO}$ ,  $\text{Cu}(\text{OH})_2$  and  $\text{Cu}_2\text{O}$ . No nitrogen incorporation was detected in any of the three samples.

Figure 5.4 shows that the SEY decreased to below 1 for primary electron energies between 50 and 1800 eV. The SEY has a maximum of  $\delta_{\text{max}} = 0.68$  at 1800 eV for turbulent flow, which increases to  $\delta_{\text{max}} = 0.87$  at 1400 eV for turbulent flow through the nozzle with structure, and  $\delta_{\text{max}} = 0.92$  at 850 eV for laminar flow, while  $E(\delta_{\text{max}})$  shifts to lower energies. The shift of the maximum energy might be related to the  $\text{Cu}(\text{OH})_2$  concentration, which was highest on this sample or more likely linked to the different surface morphology where especially the trenches in Fig. 5.2b are decorated with smaller nano-features (less roughness) and sharper trenches that reflect electrons more easily. The lowest SEY, achieved when applying a turbulent flow, can be either assigned to the high surface roughness which is no longer dominated by the microtrenches, but predominantly by the nanostructures that absorb especially low-energy electrons efficiently.

In conclusion, a more focused  $\text{N}_2$  flow through the thin nozzle increased the number of redeposited particles, but minimized surface oxidation, and allows reaching the lowest

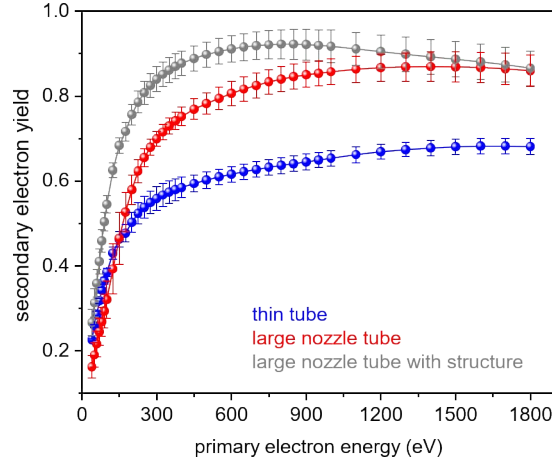


**Figure 5.4:** Secondary electron yield measurement of samples processed at an accumulated fluence of  $2000 \text{ J cm}^{-2}$  in local nitrogen flow of  $4 \text{ L min}^{-1}$  using the nozzles visualized in Fig. 5.2.

SEY, especially at primary electron energies  $< 1000 \text{ eV}$ , as opposed to laminar flow. Thus, the thin nozzle was used throughout the remaining experiments.

### 5.1.2 Variation of the nitrogen volume flow

Using the same laser parameter settings ( $F_{\text{acc}} = 2000 \text{ J cm}^{-2}$ ), the nitrogen flow was varied from  $2$  to  $5 \text{ L min}^{-1}$  using the thin nozzle tube (Fig. 5.2a) of  $1.5 \text{ mm}$  inner diameter. The corresponding Reynold numbers are  $Re = 1876$  and  $4689$ , respectively.

The XPS spectra in Fig. 5.5 point to a similar oxidation state at all flow rates with the Cu(I) peak of the Cu  $2p_{3/2}$  spectra at  $932.4 \text{ eV B.E.}$ , Cu LMM transition at  $916.7 \text{ eV K.E.}$  (modified Auger parameter:  $1849.1 \text{ eV}$ ), and O  $1s$  at  $531.3 \text{ eV B.E.}$ , which is assigned to  $\text{Cu}_2\text{O}$ . The shoulder at  $934.4 \text{ eV B.E.}$  and the flattening satellite feature between  $948$  and  $938 \text{ eV B.E.}$  indicates the presence of  $\text{Cu}(\text{OH})_2$ . Solely the flow rates  $2$  and  $5 \text{ L min}^{-1}$  incorporated nitrogen into the surface, which could explain the lower  $\text{Cu}(\text{OH})_2$  proportion (Fig. 5.5, at  $934.4 \text{ eV}$ ) and carbon content from the quantification of the XPS elemental composition (Tab. 5.1).

The most important result is the appearance of  $\text{Cu}_2\text{O}$  at all flow rates, instead of  $\text{CuO}$ . In this way, no  $\text{CuO}$  is generated even at the lowest flow rate of  $2 \text{ L min}^{-1}$ . On one hand, low flow rates increase the risk of particles entering the robot and contaminating the mirror. On the other hand, a high flow rate ( $> 5 \text{ L min}^{-1}$ ) should be avoided to reduce the  $\text{N}_2$  consumption during long-term processing. As a compromise for the application, a nitrogen flow rate of  $4 \text{ L min}^{-1}$  was used throughout the remaining experiments.

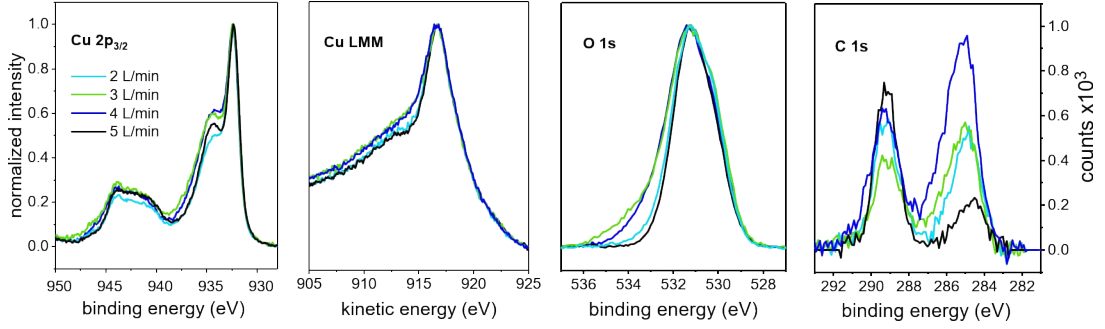


**Figure 5.5:** XPS Cu  $2p_{3/2}$  spectra, Cu LMM Auger excitation, O 1s, and C 1s state for samples processed at various nitrogen flow rates and at an accumulated fluence of  $2000 \text{ J cm}^{-2}$ .

**Table 5.1:** XPS surface composition (at. %) of samples processed at various  $\text{N}_2$  flow rates (see Fig. 5.5).

$\text{N}_2$ flow rate	C	N	O	Cu
$2 \text{ L min}^{-1}$	11.3	0.7	44.3	43.7
$3 \text{ L min}^{-1}$	14.8	-	49.1	36.2
$4 \text{ L min}^{-1}$	15.9	-	44.6	39.5
$5 \text{ L min}^{-1}$	8.4	0.3	47.3	44.0

### 5.1.3 Processing in air vs. with support of nitrogen flow

At high average laser power ( $5 \text{ W}$ ) and slow scanning speed ( $5 \text{ mm s}^{-1}$ ), corresponding to an accumulated laser fluence of  $2000 \text{ J cm}^{-2}$ , the ps laser pulses engraved micrometer deep trenches in the Cu surface that are covered with nanometer-sized structures, as shown in Figure 5.6. The laser-processing in air resulted in typical cauliflower-head nanostructures, which were previously obtained on flat surfaces without the fiber and the robot (Sec. 4.1.1) and in related studies [131, 132]. Instead, when applying the nitrogen flow ( $4 \text{ L min}^{-1}$ ) through the nozzle of the robot, the expanding plasma is confined and pushes particles expelled from the ablation zone partially back to the surface. The morphology is characterized by fine molten and re-solidified spheres of a few hundreds of nanometers in diameter (Fig. 5.6), which tend to cluster on the formed trenches and create a surface topography that is more undefined than that resulting from processing in air without nitrogen flow. These redeposited spherical clusters are loosely bound to the surface and were removed in a subsequent  $\text{CO}_2$  snow-jet cleaning. The remaining surface features reveal the cauliflower structure (Fig. 5.7), similar to the one obtained in air (Fig. 5.6). Under similar processing conditions in a flooded nitrogen chamber instead of a local nitrogen flow, the cauliflowers were also obtained in the absence of the molten spheres [131]. Consequently, the nanospheres origin from the interplay of the flow through the nozzle and the plasma plume and not from the gas. The influence of particle removal on the SEY is discussed in the next Section 5.2.2.



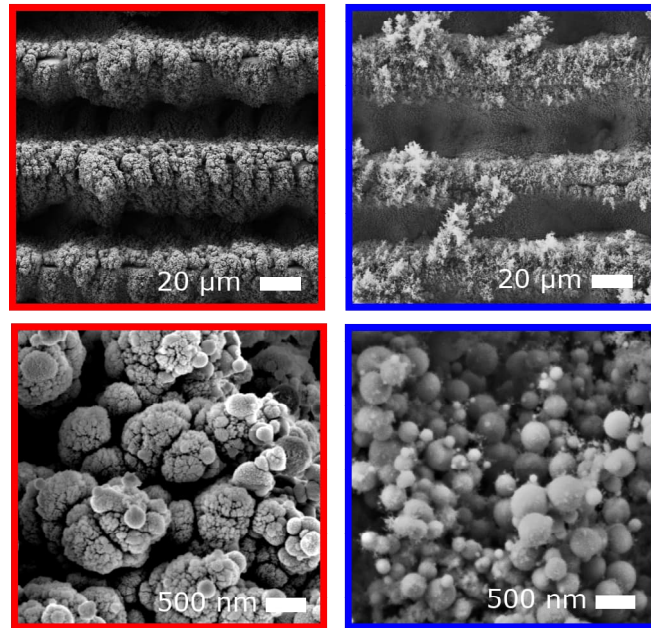


**Figure 5.6:** SEM images of micro- (top row) and nanostructures (bottom row) of laser-processed Cu in air without flow (red) and with local N<sub>2</sub> flow of 4 L min<sup>-1</sup> (blue) at an accumulated laser fluence of 2000 J cm<sup>-2</sup>. Published in Ref. [144].

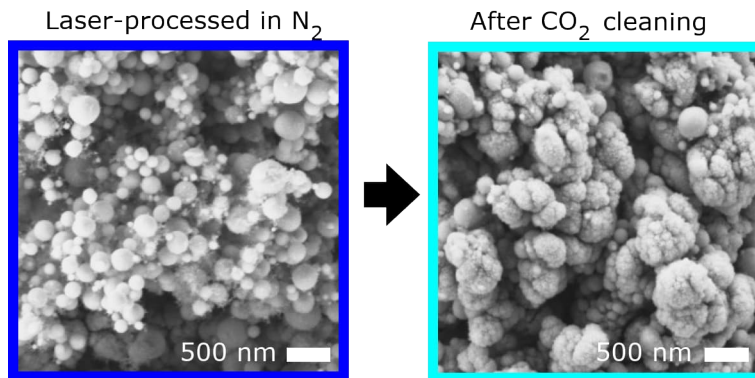


**Figure 5.7:** Morphology before and after CO<sub>2</sub> snow-jet cleaning of surface processed at 2000 J cm<sup>-2</sup>.



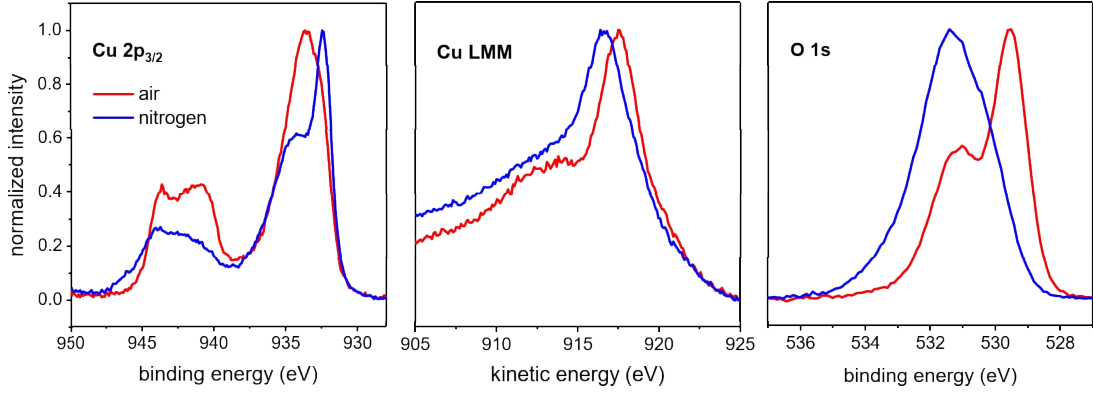


**Figure 5.8:** XPS spectra of Cu  $2p_{3/2}$  state, Cu LMM Auger excitation, and O  $1s$  state of laser-processed curved copper surfaces in air (red) and nitrogen flow of  $4 \text{ L min}^{-1}$  (blue). Published in Ref. [144].

The flow of gas through the nozzle creates a nitrogen-rich environment locally, which helps prevent particle oxidation during the plasma phase, as demonstrated by the XPS measurements in Figure 5.8. The processed surface was found to be predominantly composed of  $\text{Cu}_2\text{O}$ , as indicated by the Cu  $2p_{3/2}$  main state at a binding energy of 932.4 eV and the Cu LMM Auger transition at a kinetic energy of 916.7 eV (modified Auger parameter of 1849.1 eV). In addition, the presence of  $\text{Cu}(\text{OH})_2$  was detected from by the shoulder of the Cu  $2p_{3/2}$  state at 934.4 eV B.E. and by the shape of the Cu(II) satellite feature between 938 and 948 eV B.E. [153, 155, 166], with no detectable nitrogen on the surface. The formation of  $\text{Cu}_2\text{O}$  under nitrogen flow aligns with previous studies, conducted in nitrogen or argon atmospheres [131]. However, nitrogen was incorporated in the surface and less copper hydroxide was detected for that earlier study, which could be linked to the difference in the way the nitrogen is supplied (flow of local  $\text{N}_2$  stream vs. processing in nitrogen environment). In contrast, laser processing in air led to particle oxidation due to interactions with reactive species in the laser-induced plasma plume, resulting in a  $\text{CuO}$ -dominated surface. The Cu  $2p_{3/2}$  state is found at a binding energy of 933.7 eV, the Cu LMM Auger transition at a kinetic energy of 917.5 eV (modified Auger parameter of 1851.2 eV), and the O  $1s$  peak is at B.E. 529.5 eV, which all point to the existence of  $\text{CuO}$  [154, 155, 167]. Considering the used accumulated fluence of  $2000 \text{ J cm}^{-2}$ , the  $\text{CuO}$ -dominated surface obtained in air matches in the compositional surface transformations found on flat surfaces (Sec. 4.1.2).

Figure 5.9 compares the primary electron energy dependence of SEY (3-spot average) between 50 and 1800 eV of the two samples that had been either laser-treated in air or with the support of the nitrogen flux. A significant SEY reduction was found in the entire energy range and the SEY maximum decreased to  $0.75 \pm 0.06$  (air) and  $0.68 \pm 0.01$  (nitrogen) compared to the untreated copper surface, which had a SEY maximum of 2.1 at a primary electron energy of 250 eV (Fig. 3.20). The generated micrometer

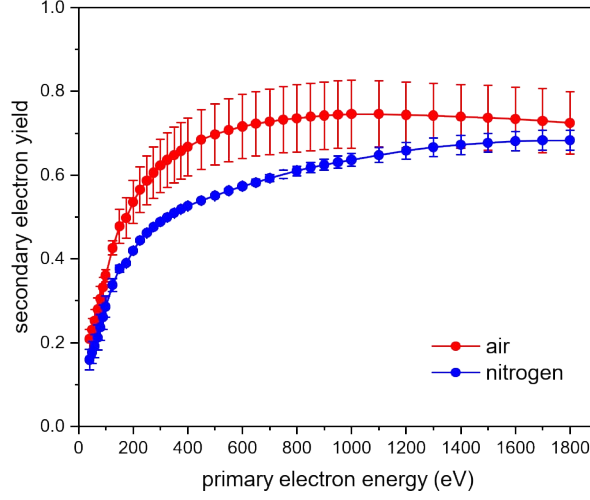


**Figure 5.9:** Secondary electron yield measurement of laser-processed copper in air (red) and local nitrogen flow (blue). Published in Ref. [144].

trenches and nanostructure efficiently absorb the low energy electrons ( $< 500\text{ eV}$ ), while a larger proportion of electrons with higher energy is backscattered from the surface, leading to a shift of the SEY maximum to higher kinetic energies. The efficient absorption at low primary electron energies is advantageous for the application since the majority of electrons, that impinge on the inner BS surface in the LHC, have kinetic energies smaller than  $500\text{ eV}$  in a dipole magnet [162]. A small difference of the SEY in dependence of primary electron energy was found for the treatments in air and in nitrogen, only slightly above the relative experimental error of 0.05 of the measurement setup. This variation is attributed to the differences in surface topography, particularly in the sub-micrometer scale (see Fig. 5.6), and the surface composition (Fig. 5.8). The SEY difference between the two laser-treated samples is generally not significant for electron cloud mitigation, as both processes lead to SEY values well below unity. Nonetheless, the addition of  $\text{N}_2$  to suppress  $\text{CuO}$  formation is beneficial to mitigate charging effects that could otherwise occur at cryogenic conditions [131].

## 5.2 Setting the parameter space of *in situ* processing

Following previous results on flat surfaces, the entire range of average laser power ( $1.5 - 5\text{ W}$ ) and scanning speed ( $5 - 200\text{ mm s}^{-1}$ ) of the green *in situ* setup is explored in the following section and processing parameters are optimized with respect to the ablation depth, SEY and particle generation.

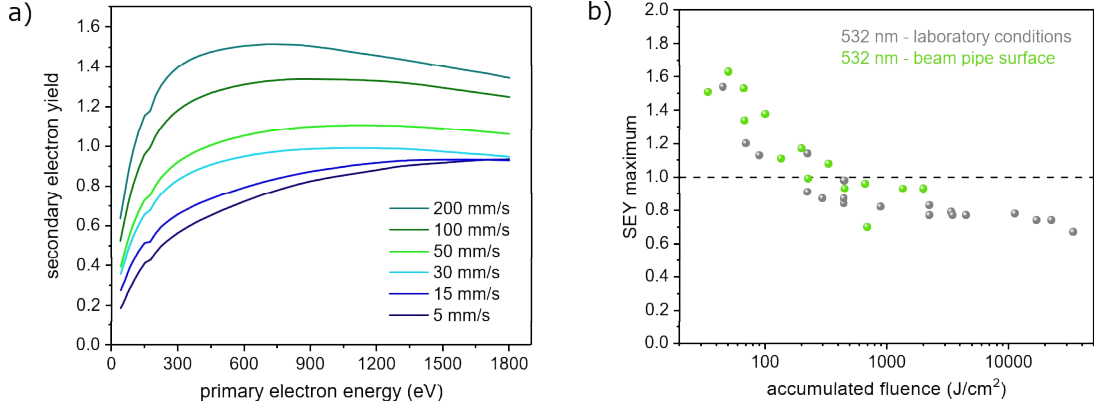


**Figure 5.10:** a) SEY measurement of curved samples processed on 532 nm *in situ* setup at an average laser power of  $P = 3.4$  W and a line distance of  $\Delta y = 50$   $\mu\text{m}$  and various scanning speeds, b) SEY maximum comparison of laboratory scale flat samples processed at IOM and curved samples processed on the *in situ* setup in dependence of accumulated fluence.

### 5.2.1 Screening of processing parameters

Increasing the scanning speed from 5 to 200  $\text{mm s}^{-1}$  resulted in an increase of SEY at all primary energies, as demonstrated in Fig. 5.10a. It is noteworthy that  $E(\delta_{\text{max}})$  shifts from 1800 eV (at 5  $\text{mm s}^{-1}$ ) to 750 eV (at 200  $\text{mm s}^{-1}$ ), as opposed to flat surfaces (Fig. 4.10), where the SEY maximum was always at high energy. Compared to the green laser at IOM (diameter: 11.6  $\mu\text{m}$ , repetition rate: 100 kHz, available average laser power:  $\sim 2.5$  W), the laser diameter of the *in situ* setup is larger (53  $\mu\text{m}$ ) and the repetition rate higher (200 kHz), which would result in lower peak fluence, which is however compensated by the higher available average laser power of 5 W. A larger laser diameter increases the width  $w$  of the grooves. Thus, at high speeds or lower accumulated fluences, where the ablation depth  $z$  is rather small ( $\sim 10$   $\mu\text{m}$ ), the aspect ratio ( $z/w$ ) decreases, making it easier for low energy electrons to be backscattered from the surface and increasing the SEY at low energies. As a function of accumulated fluence, the trend of the SEY maximum on curved surfaces matches well the one observed on flat samples using 532 nm photons (Fig. 5.10b): The SEY maximum decreases with increasing accumulated fluence and reaches an ultimate low  $\delta_{\text{max}}$  of 0.7 in the saturation regime at high accumulated fluence.

### 5.2.2 Particle mitigation through post-cleaning

In Section 5.1, processing using a dense  $\text{N}_2$  flow through a thin hollow tube minimized oxidation the most, but the surface structures were covered by clusters of molten nanospheres, which are detrimental for operation in the LHC, because detaching particles could interact with the proton beam. Therefore, a simple cleaning, which is

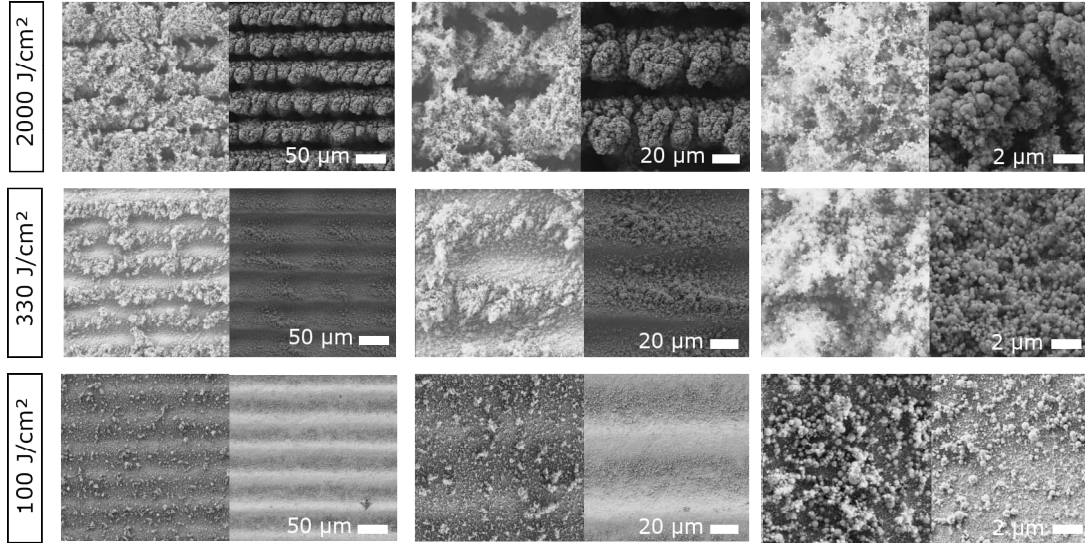


**Figure 5.11:** SEM at various magnifications of surfaces processed with the green *in situ* laser at different accumulated fluences before (left) and after post-cleaning (right columns) using a gas jet.

applicable in the BSs installed in the magnet complexes, needs to be applied to remove lightly bound particles. Conventional rinsing or ultrasonic cleaning are not suitable, because it cannot be performed *in situ*. A  $N_2$  gas jet with a flow of  $\sim 30 \text{ L min}^{-1}$  was passed over the laser-processed surfaces. This process is referred to as “post-cleaning” throughout the document. The surfaces were visibly liberated from particles after the cleaning as observed in the photographs in Figure 5.11. Clusters of vapor located on top of the trenches were mainly removed. On surfaces processed at  $2000 \text{ J cm}^{-2}$ , the cauliflower structure revealed, similar to the snow-jet cleaning (Fig. 5.7), indicating that those particles are stronger bound to the surface. However, the post-cleaning did not remove all particles; especially those in the valley of the trenches remained.

The features in the  $\text{Cu } 2p_{3/2}$  spectra in Fig. 5.12 show that the removal of particles did not change the chemical properties of the surface, neither for samples processed at low nor at high accumulated laser fluence: The main peak at B.E. 932.4 eV (modified Auger parameter 1849.2 eV) indicates the presence of  $\text{Cu}_2\text{O}$  and the shoulder at 934.4 eV as well as the flattening satellite between 948 and 938 eV remained, indicating  $\text{Cu}(\text{OH})_2$ . Compared to previous treatments in Sec. 5.1, here the nitrogen incorporation was observed in the  $\text{N } 1s$  spectra (Fig. 5.12). Perhaps the particles that were removed during post-cleaning were initially farther from the reaction zone before redepositing. The remaining surface features must have been within the reaction zone, where nitrogen gas pressure and temperature were high, which is why they remain attached.

Since the role of the nanoparticles has been shown important for efficient SEY reduction, the SEY is expected to increase after particle removal in the post-cleaning process. For surfaces treated at high accumulated laser fluence ( $F_{\text{acc}} > 1000 \text{ J cm}^{-2}$ ), the cleaning

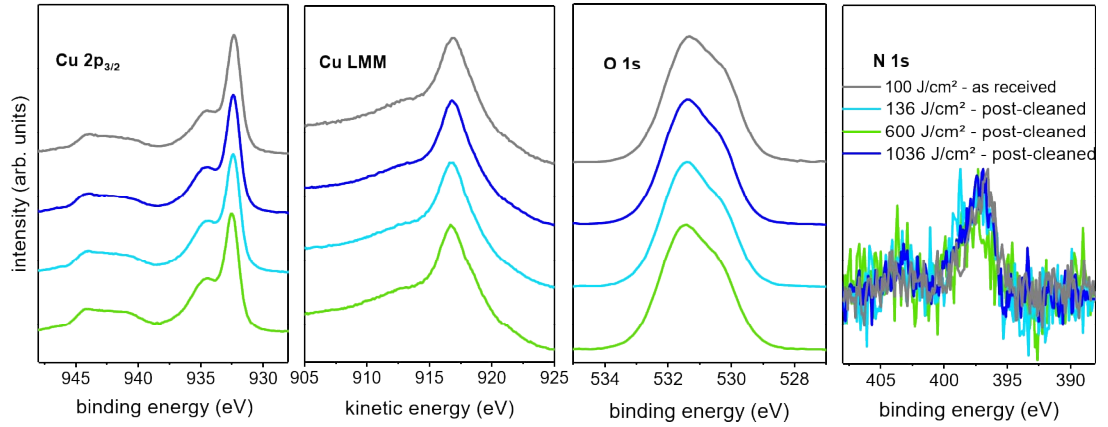


**Figure 5.12:** XPS spectra of Cu 2p<sub>3/2</sub>, Cu LMM Auger excitation, O 1s, and N 1s of as received and post-cleaned curved copper surfaces processed at various accumulated fluences.

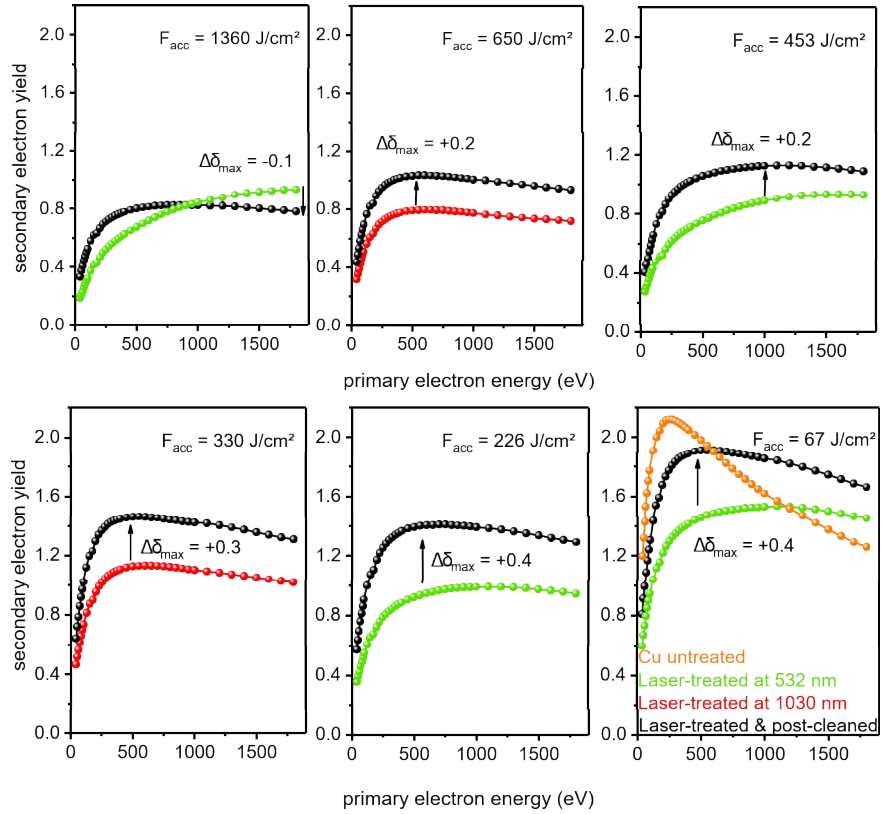


**Figure 5.13:** SEY measurement of surfaces processed at different accumulated fluences and wavelengths before and after post-cleaning using a gas jet.

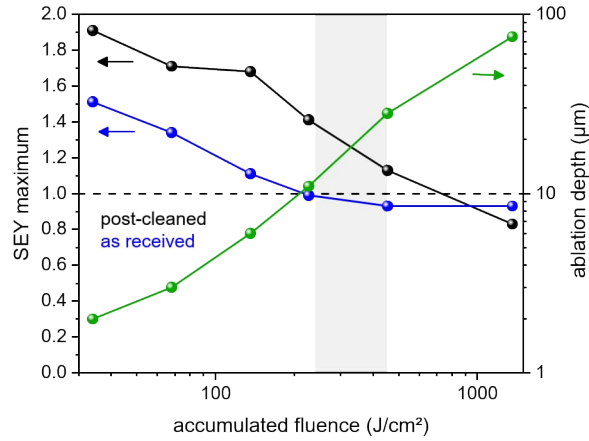


**Figure 5.14:** SEY maximum of as received and post-clean laser-treated curved samples, and ablation depth as a function of accumulated fluence for green *in situ* setup. Acceptable fluence range for installation in the LHC is shaded in gray.

had a positive effect on the SEY, as  $\delta_{\max}$  slightly decreased by 0.1 (Fig. 5.13). As observed in Fig. 5.11, the post-cleaning removed only the molten nanospheres, but not the cauliflower structures. Thus, the surface roughness remains and the cauliflowers seem more effective for SEY reduction. For intermediate fluences ( $200 < F_{\text{acc}} < 1000 \text{ J cm}^{-2}$ ),  $\delta_{\max}$  increased after removal of the majority of particles, the lower the accumulated fluence. Thus, the SEY is dominated by the microstructure, which seems to trap electrons less efficiently. For fluences below  $200 \text{ J cm}^{-2}$ , the SEY maximum is  $\delta_{\max} \geq 1.4$ . A  $\delta_{\max} = 1.5$  (Fig. 5.13,  $F_{\text{acc}} = 67 \text{ J cm}^{-2}$ ) before cleaning results in SEY values close to untreated Cu after post-cleaning and is therefore not eligible for the application. In these cases, the SEY values exceeds that of untreated Cu at high primary electron energies. The relative increase in SEY after cleaning was observed for surfaces processed with 532 nm and 1030 nm photons. The absolute SEY value using the IR laser is higher than for the green laser at similar accumulated fluences as discussed in Sec. 4.1.

The increase in SEY after cleaning must be considered when choosing the processing parameters, since it narrows the available laser parameter range where all treatment requirements are fulfilled. An overview of processing limitations for the green *in situ* setup is given in Fig. 5.14. It includes the SEY maximum of laser-treated surfaces before and after cleaning and the corresponding ablation depth as a function of accumulated fluence. As introduced earlier (Sec. 2.5.2), the max. acceptable ablation depth is  $25 \mu\text{m}$  to keep the surface resistance low and the maximum SEY should amount to  $\delta_{\max} \leq 1$  or decrease to such values upon electron exposure. In the studies on flat surfaces, it was found that a laser-processed surface with initial  $\delta_{\max} < 1.5$  satisfies this condition at an acceptable electron dose of  $5 \times 10^{-4} \text{ C mm}^{-2}$  (Fig. 4.13). This defines a final

range between 200 and 400 J cm<sup>-2</sup> (highlighted in gray in Fig. 5.14) in which SEY and ablation depth requirements are fulfilled. The lower limit set by the SEY after post-cleaning and the higher one by the ablation depth. In this range, the scanning speed and the average laser power can be adjusted to be within the accumulated fluence ranges. For instance, at the maximum available average laser power of the green laser system (5 W), speeds of speeds between 25 - 50 mm s<sup>-1</sup> can be selected to obtain accumulated fluences of 200 to 400 J cm<sup>-2</sup>.

The post-cleaning process removed the critical number of loosely bound particles. However, Figure 5.11 shows that there are still some that could detach from the surface. Therefore, particle detachment tests were performed to quantify the number of particles that could potentially interact with the proton beam once detached from the surface.

### 5.3 Quantification of particle detachment by centrifugal forces

In this section, flat (treated in air) and curved (treated in N<sub>2</sub> flow of 4 L min<sup>-1</sup>) post-cleaned Cu samples were subjected to centrifugal forces. The selected force density of 3 N mm<sup>-3</sup> is 10 % of the maximum force density acting on the BS surface when a magnet looses abruptly its superconductivity (magnet quench) [148]. In such a case, the beam is already dumped. The operation forces are less than 10 %. The curved samples were treated on an insert of the BS, whereby only the sample and not the entire circumference of the tube was treated. Thus, only particles from the treated area were deposited on the surfaces used for the tests. In addition, they were post-cleaned with a N<sub>2</sub> jet, as this revealed necessary (see previous section) to reduce the number of loose redeposited particles on the surface.

Two sets of sample series were selected that were laser-treated with different accumulated fluences and thus have different morphology and SEY values: three flat samples processed in air with  $\delta_{\max}$  ranging from 1.8 to 0.8, five curved + post-cleaned samples processed in N<sub>2</sub> (4 L min<sup>-1</sup>) with  $\delta_{\max}$  between 1.8 and 0.9, and one curved + post-cleaned sample processed in air, making the link between the two sample series. The selected surfaces and the details of processing parameters are summarized in Tables 5.2 and 5.3.

At high accumulated laser fluence (a,  $F_{\text{acc}} \geq 650 \text{ J cm}^{-2}$ ), deep grooves with cauliflower structure were generated with  $\delta_{\max} \leq 1.0$ . The cauliflower structure appears to be more compact on the samples processed in air than in N<sub>2</sub>, since in the latter some of the fine molten spheres remained on the surface after the post-cleaning. The curved sample processed with the IR laser is characterized by LIPSS on top of the grooves, and decorated with a non-negligible number of particle clusters. At intermediate fluence (b,  $100 \text{ J cm}^{-2} \leq F_{\text{acc}} < 450 \text{ J cm}^{-2}$ ), pronounced LIPSS covered with particulates emerged on the flat sample, agglomerations of molten nanospheres ( $< 1 \mu\text{m}$ ) were found mainly at the bottom of the grooves of the curved samples, resulting in  $\delta_{\max} = 1.5$  (flat), 1.4 (curved) and 1.1 (curved). Samples of this category lie within the previously defined

### 5.3 Quantification of particle detachment by centrifugal forces

range, in which the surface requirements are met (see Fig. 5.14). Surfaces with SEY maximum of 1.8 processed at low accumulated laser fluence (c,  $F_{\text{acc}} \leq 100 \text{ J cm}^{-2}$ ), were characterized by weakly pronounced LIPSS on the flat sample and shallow grooves decorated with individual molten spheres on the curved sample.

After centrifugation at  $3 \text{ N mm}^{-3}$  (see details in Sec. 3.3), the detached particles – collected on a carbon sticker – were analyzed in terms of their equivalent circular diameter (ECD) (assuming spherical particles) and the size distribution using APA. In addition, the total mass  $M$  of detached particles was calculated:

$$M = \sum_i^N V_i(\text{ECD}) \cdot \rho_{\text{Cu}} \cdot N_i, \quad (5.2)$$

with the density of copper  $\rho_{\text{Cu}} = 8.96 \text{ g cm}^{-3}$ ,  $N$  the number of detached particles per  $\text{cm}^2$  and a spherical volume  $V$  of the particles:

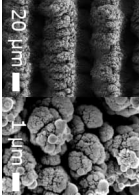
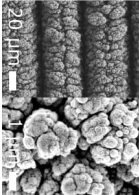
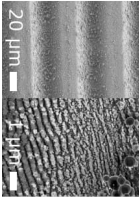
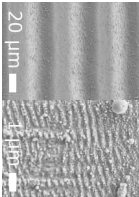
$$V = \frac{4}{3}\pi \left( \frac{\text{ECD}}{2} \right)^3. \quad (5.3)$$

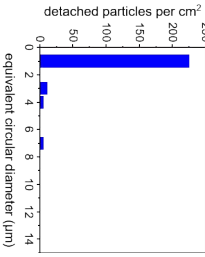
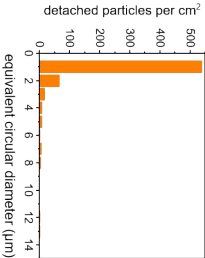
The results discussed in the following are summarized in Tabs. 5.2 and 5.3. Starting from the samples in category a) that exhibit the lowest SEY ( $\delta_{\text{max}} < 1$ ), no particles were detached from the flat sample processed in air at  $F_{\text{acc}} = 1000 \text{ J cm}^{-2}$ . The curved and post-cleaned sample treated in air globally detached 249 particles per  $\text{cm}^2$ , with an average ECD of  $1 \mu\text{m}$  (Tab. 5.2), which is also the minimum detection limit of APA. It is therefore possible that smaller particles have detached from the other flat sample, but could not be detected. The corresponding total detached mass amounted to  $0.01 \mu\text{g cm}^{-2}$ . The equivalent sample processed in local  $\text{N}_2$  flow using the robot, detached in comparison a particle number of  $146 \text{ 122 cm}^{-2}$ , corresponding to a mass of  $32.07 \mu\text{g cm}^{-2}$  (Tab. 5.3), which is significantly more than for the samples processed in air. As evaluated in Section 5.1, the redeposition of particles in local turbulent  $\text{N}_2$  flow is higher than when processing in air. The post-cleaning removed particles, but some of the molten spheres remained on the surface as observed in the SEM images in Tab. 5.3. Thus, the overall particle coverage on the curved samples is higher. In addition, the small molten spheres redeposit at the final stage of the ablation process, resulting in a longer cool-down phase and lower bond energy. The total detached mass  $M = 32.07 \mu\text{g cm}^{-2}$  fits the previous findings, where a total mass of  $\sim 50 \mu\text{g cm}^{-2}$  detached at the same force density of  $3 \text{ N mm}^{-3}$  [148]. It has to be noted that the sample in the test here was post-cleaned as opposed to previous tests. The curved sample processed with the IR laser detached less particles ( $32 \text{ 000 cm}^{-2}$ ), but the average ECD was  $3 \mu\text{m}$  compared to  $\sim 1 \mu\text{m}$  for the rest of the samples. The larger average ECD becomes evident when reviewing the SEM photograph of the surface as the structures are less compact compared to the curved sample processed with  $532 \text{ nm}$  photons. The total detached mass of  $\sim 1.2 \text{ mg cm}^{-2}$  (Tab. 5.3) was accordingly higher.



**Table 5.2:** Summary of particle detachment via centrifugation of surfaces processed in air.

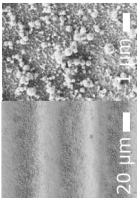
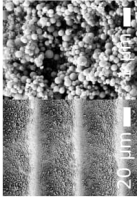
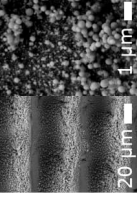
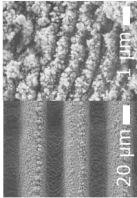
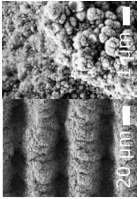
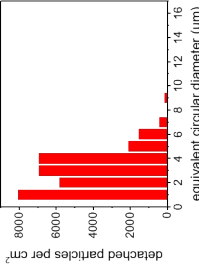
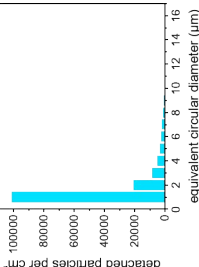
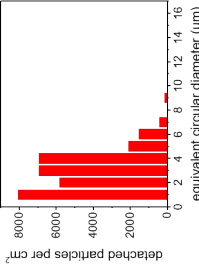
Category	c)	b)	a)	a)
Sample properties	Flat As received	Flat Post-cleaned	Flat As received	Curved Post-cleaned
Treated in	Air	Air	Air	Air
Laser wavelength	532 nm	532 nm	532 nm	532 nm
Acc. fluence $F_{acc}$	80 J cm <sup>-2</sup>	100 J cm <sup>-2</sup>	1000 J cm <sup>-2</sup>	2000 J cm <sup>-2</sup>
SEY $\delta_{max}$	1.8	1.5	0.8	0.8





Force density	3 N mm <sup>-3</sup>	3 N mm <sup>-3</sup>	3 N mm <sup>-3</sup>	3 N mm <sup>-3</sup>
Average ECD	1 μm	—	—	1 μm
Glob. detached particles $N$	644 cm <sup>-2</sup>	No detachment	No detachment	249 cm <sup>-2</sup>
Tot. detached mass $M$	0.06 μg cm <sup>-2</sup>	—	—	0.01 μg cm <sup>-2</sup>

**Table 5.3:** Summary of particle detachment via centrifugation of curved surfaces processed in  $N_2$  flow.

Category	c)		b)		a)	
						
Sample properties	Curved	Curved	Curved	Curved	Curved	
Treated in	Post-cleaned	Post-cleaned	Post-cleaned	Post-cleaned	Post-cleaned	
Laser wavelength	$N_2$ ( $4\text{ L min}^{-1}$ )	$N_2$ ( $4\text{ L min}^{-1}$ )	$N_2$ ( $4\text{ L min}^{-1}$ )	$N_2$ ( $4\text{ L min}^{-1}$ )	$N_2$ ( $4\text{ L min}^{-1}$ )	
Acc. fluence $F_{\text{acc}}$	532 nm	532 nm	532 nm	532 nm	532 nm	
SEY $\delta_{\text{max}}$	$100\text{ J cm}^{-2}$	$230\text{ J cm}^{-2}$	$450\text{ J cm}^{-2}$	$650\text{ J cm}^{-2}$	$1036\text{ J cm}^{-2}$	
	1.8	1.4	1.1	1.0	0.9	
						
Force density	$3\text{ N mm}^{-3}$	$3\text{ N mm}^{-3}$	$3\text{ N mm}^{-3}$	$3\text{ N mm}^{-3}$	$3\text{ N mm}^{-3}$	
Average ECD	—	—	—	$3\text{ }\mu\text{m}$	$1\text{ }\mu\text{m}$	
Glob. detached particles $N$	No detachment	No detachment	No detachment	$32\,000\text{ cm}^{-2}$	$146\,122\text{ cm}^{-2}$	
Tot. detached mass $M$	—	—	—	$1219\text{ }\mu\text{g cm}^{-2}$	$32.07\text{ }\mu\text{g cm}^{-2}$	

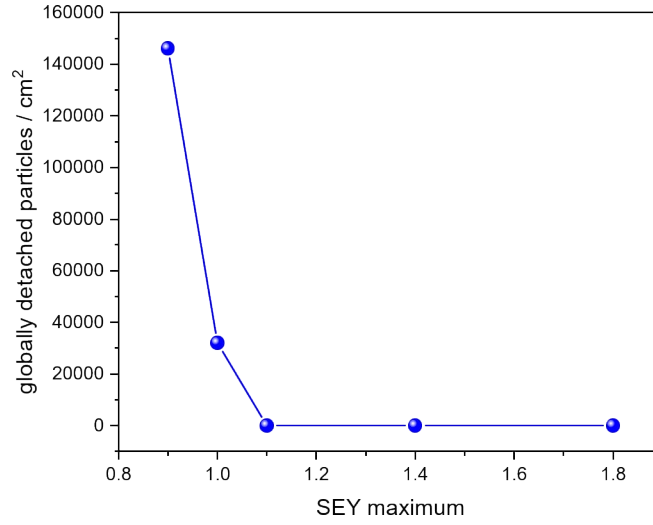


**Figure 5.15:** Globally detached particles from curved post-cleaned surfaces processed in local  $N_2$  subjected to a centrifugal force density of  $3\text{ N mm}^{-3}$  as a function of maximum SEY.

As the accumulated fluence is decreased (category b)), the SEY increases and less particles detached from the surface. The samples (flat and curved) with  $\delta_{\max} = 1.1–1.5$  did not loose any particles. It is worth mentioning that samples of category b), for which low/no detachment was observed, fulfill the treatment requirements (SEY and ablation depth). No particles were detected on the curved sample of category c) with  $\delta_{\max} = 1.8$ , but a small number of  $644\text{ cm}^{-2}$  ( $0.06\text{ }\mu\text{g cm}^{-2}$ ) detached globally with an average ECD of  $1\text{ }\mu\text{m}$  (Tab. 5.2) from the flat sample.

In summary, processing at c) low and b) intermediate fluences ablates a smaller volume and the surfaces are therefore intrinsically covered with fewer particles, which leads to marginal or no particle detachment. These surfaces are associated with  $\delta_{\max} \geq 1.0$ . In particular, the non-detachment of particles from surfaces processed at intermediate fluence with  $\delta_{\max} = 1.4$  must be emphasized, since this range is of interest for the treatment of BSs in magnets of the LHC. Solely when increasing the accumulated fluence to a)  $F_{\text{acc}} \geq 650\text{ J cm}^{-2}$ , particles detached with an average particle diameter of  $1\text{ }\mu\text{m}$  and  $3\text{ }\mu\text{m}$  for the IR sample. This trend is visualized in Figure 5.15. The majority of detached particles were  $< 15\text{ }\mu\text{m}$  in diameter, which is less than the critical diameter of  $60\text{ }\mu\text{m}$  at which the particle beam interaction can affect the operation of the LHC. The global detached masses  $M$  were  $\leq 1.2\text{ mg cm}^{-2}$ . Particles of flat surfaces processed in air seem to adhere better than on the curved samples processed in  $N_2$ , because these surfaces are free of the redeposited molten sphere clusters.

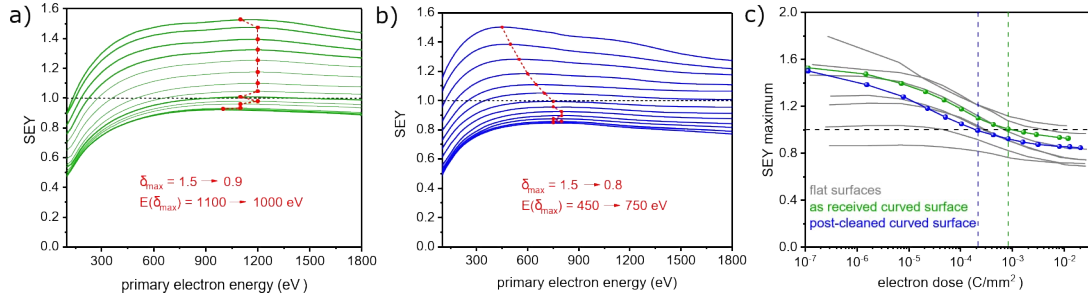


**Figure 5.16:** Electron irradiation at RT up to doses of a)  $1.8 \times 10^{-2} \text{ C mm}^{-2}$  and b)  $2.0 \times 10^{-2} \text{ C mm}^{-2}$ . SEY measurement after each conditioning step of curved laser-treated ( $\lambda = 532 \text{ nm}$ ) a) as received and b) post-cleaned samples. c) SEY maximum in dependence of electron dose on flat (according to Fig. 4.13) and curved surfaces.

## 5.4 SEY reduction via electron irradiation (conditioning)

In the model studies on flat surfaces (Fig. 4.13), an upper limit of initial  $\delta_{\text{max}} \leq 1.5$  was found up to which the SEY of laser-treated surfaces decreased upon electron exposure to values of 1 or below. Curved laser-processed (as received/post-cleaned) surfaces with initial  $\delta_{\text{max}} = 1.4 - 1.5$  were selected for conditioning at room and cryogenic temperatures, the latter because charging effects – which should be avoided for beam screen surfaces in the LHC magnets – have previously been observed at low temperatures [2]. The measurements in Section 5.4.1 were conducted at RT in the collector-based SEY setup described in Section 3.3.2. The conditionings in Section 5.4.2 were also performed on a collector-based SEY setup where the sample can be cooled to 15 K [168, 169].

### 5.4.1 Conditioning at room temperature

Two samples processed with the 532 nm *in situ* setup at a)  $F_{\text{acc}} = 200 \text{ J cm}^{-2}$  and b)  $F_{\text{acc}} = 330 \text{ J cm}^{-2}$  were selected. The latter was post-cleaning. Both SEY prior to the start of the conditioning amounted to  $\delta_{\text{max}} = 1.5$ , and the corresponding maximum energy of the as received sample is at 1100 eV, while that of the post-cleaned sample is at 450 eV. This difference is due to the removal of particles, that absorb low-energy electrons more efficiently than just the remaining grooves. Figure 5.16 shows the SEY of a) as received and b) post-cleaned samples measured at RT between 50 and 1800 eV after each electron exposure step. The SEY of the as received laser-treated sample (Fig. 5.16a) decreased to 1 at all primary electron energies at a dose of  $8.3 \times 10^{-4} \text{ C mm}^{-2}$ , and ultimately saturated at  $\delta_{\text{max}} = 0.9$ . The maximum electron energy remained between 1000 and 1200 eV at all conditioning steps. The SEY of the post-cleaned sample reached 1 at a lower electron dose of  $2.1 \times 10^{-4} \text{ C mm}^{-2}$  (Fig. 5.16c). The slope of  $\delta_{\text{max}}$  vs. electron dose is particularly steeper at low electron doses  $\leq 10^{-5} \text{ C mm}^{-2}$ .  $E(\delta_{\text{max}})$  shifted from initially low primary electron energy (450 eV) to 750 eV (Fig. 5.16b) at the

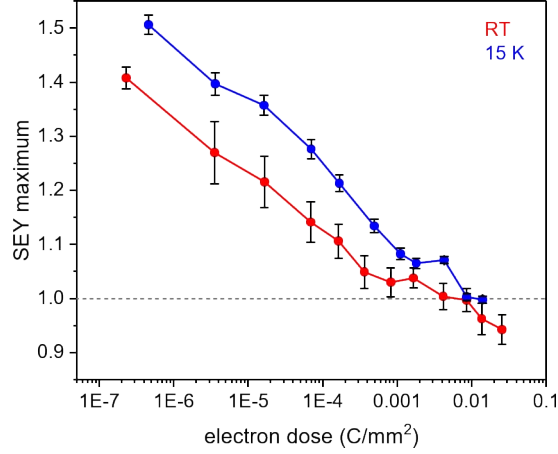


**Figure 5.17:** Surface conditioning at RT (red) and cryogenic temperature (blue) of identical curved laser-treated (1030 nm,  $F_{\text{acc}} = 385 \text{ J cm}^{-2}$ ) and post-cleaned samples. The error bars represent the standard deviation of the maximum SEY in three different locations of the samples.

ultimate  $\delta_{\text{max}} = 0.8$ . The conditioning on curved surfaces is consistent with the overall findings on flat surfaces (Fig. 5.16c, gray curves). It is noteworthy that the post-cleaned sample performs similarly to a surface with initial  $\delta_{\text{max}} = 1.2 - 1.3$ , especially at low dose. The post-cleaning has not only a positive effect on particle reduction, but also on SEY reduction upon electron irradiation.

#### 5.4.2 Conditioning at cryogenic temperature

Two equally laser-treated ( $\lambda = 1030 \text{ nm}$ ,  $F_{\text{acc}} = 385 \text{ J cm}^{-2}$ ,  $\text{N}_2$  flow =  $4 \text{ L min}^{-1}$ ) and post-cleaned, curved samples were irradiated with 250 eV electrons – one at RT and one at cryogenic temperature (15 K) – on a different experimental setup, described in detail in Refs. [168, 169]. Both samples had a maximum initial SEY of 1.4 at RT. One of the samples showed an increase in SEY by 0.1 at cryogenic temperature. This is attributed to the adsorption of residual gas molecules on the cold sample surface. As a result, more electrons are reflected at the surface adsorbates instead of penetrating into the material when the surface is irradiated with electrons. The SEY maxima of the two samples decreased upon electron dose as shown in Figure 5.17. The one at cryogenic temperature saturated at a maximum SEY value of 1 at a dose of  $1 \times 10^{-2} \text{ C mm}^{-2}$ , while the SEY at RT reached 1 at a lower dose of  $4 \times 10^{-3} \text{ C mm}^{-2}$ . No saturation of the SEY maximum was observed up to a dose of  $3 \times 10^{-2} \text{ C mm}^{-2}$ . In this measurement, the SEY of 1 was reached at higher electron doses compared to the conditionings described in Sec. 5.4.1.

Before the start of the conditioning, the chemical state of the surface was dominated by  $\text{Cu}_2\text{O}$  and  $\text{Cu}(\text{OH})_2$  (Fig. 5.18). It is noteworthy that the  $\text{Cu}(\text{OH})_2$  proportion here is

## 5.4 SEY reduction via electron irradiation (conditioning)

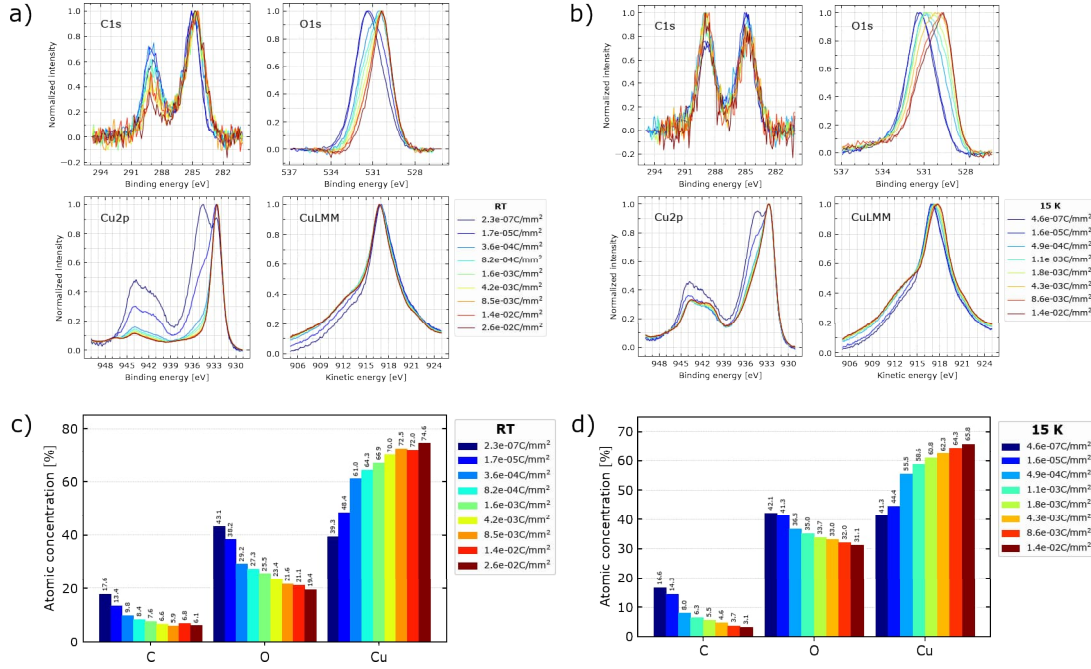


**Figure 5.18:** XPS of curved laser-treated (1030 nm,  $F_{\text{acc}} = 385 \text{ J cm}^{-2}$ ) and post-cleaned samples after each conditioning step a) at RT, and b) cryogenic temperature. Atomic concentration of the different elements at different steps of conditioning c) at RT and d) 15 K.

higher than on the reference setup used for all other XPS measurements. This is because the reference setup contains an  $\text{AlK}\alpha$  ( $h\nu = 1486.7 \text{ eV}$ ) x-ray source. The spectra shown in Fig. 5.18 were measured with a  $\text{MgK}\alpha$  source ( $h\nu = 1253.6 \text{ eV}$ ) instead, which is more sensitive to the topmost surface layer. During RT conditioning, the spectra and calculated surface stoichiometry in Fig. 5.18a indicate a reduction of  $\text{Cu}(\text{OH})_2$  to  $\text{Cu}_2\text{O}$  (no Cu 2p satellite, O 1s, and Cu LMM lines at 530.4 eV and 916.7 eV, respectively), and a reduction of the carbon content (Fig. 5.18c), as expected for RT conditioning (compare with Fig. 4.12). At cold temperature, the carbon decreased to very low values  $< 5\%$  (Fig. 5.18d), together with a conversion of  $\text{Cu}(\text{OH})_2$  into CuO (Cu 2p satellite, maximum of the O 1s and Cu LMM intensity at 529.6 eV and 917.8 eV, respectively). Thus, deoxidation is hindered at low temperature, which could also explain why the SEY reaches one at a higher dose. This conversion had already been observed on installed Cu BSs in cryogenic sectors of the LHC, where the beam-induced heat load is high [55, 56]. However, in these cases the SEY of the CuO surface saturated during RT conditioning at  $\delta_{\text{max}} = 1.2$  [55] and in conditioning at 15 K  $\delta_{\text{max}} = 1.3$  [169]. A positive aspect is that no charging effects were observed in the measurements at 15 K, which was observed elsewhere [131] for a CuO-dominated laser-treated surface with initial SEY  $< 1$ . In that case, an increase in SEY during the conditioning was observed [131], contrary to the decrease shown in Figure 5.17.

## 5.5 Concluding considerations on parameter selection for the processing of beam screens

In this chapter, the laser parameter space of mainly the green *in situ* setup was explored on curved OFE Cu samples to identify optimized processing conditions for the inner surface of BSs of the LHC. Unlike in the model studies on flat surfaces, laser processing was performed in a local N<sub>2</sub> atmosphere, which influences the laser-plasma interaction and the resulting surface morphology and chemical properties. At high accumulated laser fluence (2000 J cm<sup>-2</sup>) and turbulent N<sub>2</sub> flow, numerous fine, molten spheres redeposited in addition to the cauliflower structures that form when processing in air. Turbulent flow suppressed oxidation as opposed to laminar flow, but favored particle redeposition and clustering. Therefore, post-cleaning of the treated surfaces via a N<sub>2</sub> jet was applied as particle mitigation strategy. As a consequence, loosely bound particles were removed. However, this led to an increase in the SEY, particularly on surfaces that were processed at low accumulated fluence and especially in the low primary electron energy range. When applying centrifugal forces, a considerable number of particles detached from post-cleaned, curved samples with  $\delta_{\max} \leq 1$  processed at high acc. fluence ( $\geq 650$  J cm<sup>-2</sup>). However, the particles are small (1–2  $\mu$ m in diameter) and low in weight  $\leq 1.2$  mg cm<sup>-2</sup>. Particularly, surfaces processed at low acc. fluence ( $\sim 200$  J cm<sup>-2</sup>) and  $\delta_{\max} = 1.4 - 1.5$  did not release particles, and are therefore of interest. These surfaces have a higher SEY, that however decreased to one or below during conditioning at room and cryogenic temperature, similar to the results obtained on flat surfaces.

In the global picture of the laser parameter space (Fig. 5.14) processing at accumulated fluence of 200 – 400 J cm<sup>-2</sup> results in a surface treatment that fulfills the requirements. Finally, the laser power and scanning speed during processing can be adjusted. At the maximum average laser power (5 W) and line distance in the range of the laser diameter (50  $\mu$ m), the scanning speed can be varied between 25 and 50 mm s<sup>-1</sup>, corresponding to a minimum processing time of 80 s cm<sup>-2</sup> and 40 s cm<sup>-2</sup>, respectively. This translates into 33 or 16.5 hours per meter of the complete circumference of a 50 L type BS (see dimension in Tab. 2.1), excluding core steps for readjustment of the robot (see *in situ* setup description in Sec. 3.2.2). When scaling-up the processing of BSs, fluctuations in laser intensity can occur with longer processing times, particles may contaminate the optics in the robot, the optical fiber can be damaged at average laser powers near the limit of the setup, and mechanical components of the robot may experience wear when operating at high scanning speeds. Processing at low accumulated fluence is advantageous regarding the treatment requirements. When the accumulated fluence is reduced, the SEY is no longer in the saturation regime, but gradually increases (see Figs. 4.11 and 5.14). A SEY maximum of 1.1 (1.4 after post-cleaning) is aimed for. In this range, processing is more susceptible to intensity fluctuations due to the steep SEY increase.

## 6 Large-scale treatments of beam screens

This Chapter is devoted to applying the knowledge developed on flat (Chapter 4) and small curved surfaces (Chapter 5) to the treatment in the laboratory of real-life objects such as BSs and vacuum chambers aiming to scale up and speed up the process, and to solve practical problems that may occur during days- or weeks-long operation. The first processing was performed using the green *in situ* setup (Sec. 6.1), followed by the transition to the IR *in situ* setup, which provides higher beam stability. The treated BSs varied in size and length to achieve different objectives: defining the scan strategy (selective treatment vs. full circumference, longline vs. spiral scanning), scaling up the length of the small geometry BS (type 50 L) to 2.2 m, providing test tubes for surface impedance measurements at cryogenic temperature and finally the large-scale processing of a tube up to a length of 3.1 m for particle-beam interaction measurements in the LHC, which is one of the most critical aspects of the laser treatment and has never been tested before. The BSs in the Q5 magnets of the LHC are 10 m long and of type 50 L (small BS size, details in Tab. 2.1). During the long shutdown of the LHC in 2026, it is proposed to treat four BSs of this type with an available time of approximately six months.

### 6.1 Test of scan strategy on a 50 cm long beam screen (type 74)

Hereafter, a selective treatment (shown in Fig. 6.1) was tested on a 50 cm long BS and compared with the treatment of almost the entire circumference ( $300^\circ$ ) of the BS. The idea of the selective treatment is to process only the curved parts, where the electron cloud density is highest in quadrupole magnets during operation (Fig. 6.1a). An electron cloud simulation study showed that a selective surface treatment of about  $7^\circ$  of each corner is sufficient to reduce electron cloud multipacting in a quadrupole magnet of the LHC [146]. This way, critical parts such as cryosorbers located above the flats part of the BSs of the standalone magnets are excluded and the processing time is reduced, because only  $\sim 8\%$  of the total surface area has to be treated. In addition, different scan patterns (see Fig. 3.6) were selected, that generate microgrooves oriented either parallel or perpendicular to the BS axis, which is an aspect relevant for the surface impedance. The following schemes were applied (Fig. 6.2): a) a four corners selective treatment using the longline sequence, b) a  $300^\circ$  spiral movement, c) a four corners spiral movement, and d) a  $360^\circ$  spiral movement at higher scanning speed. A cryosorber was installed



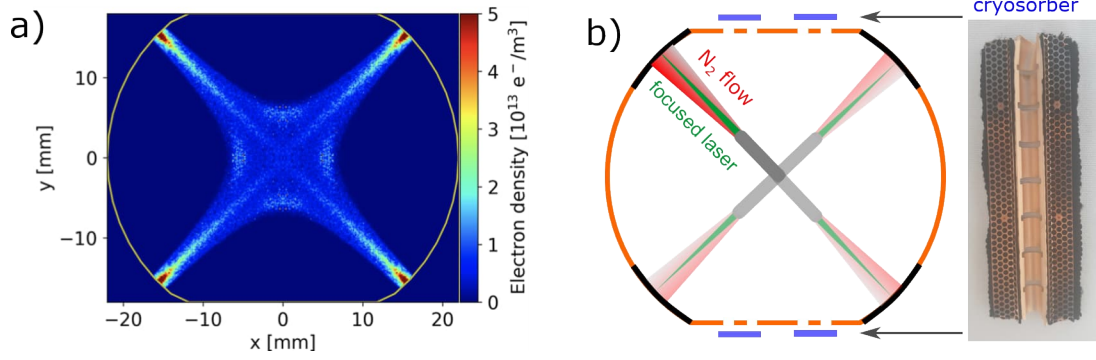


**Figure 6.1:** a) Electron cloud spatial distribution simulation. Figure extracted from Ref. [9]. b) Schematic of BS cross section for selective scanning: laser treatment of 4 corners (black), non-treated zones (orange). The cryosorbers, indicated in blue in the schematic, are excluded in the selective treatment.

on the BS in the area of 300° spiral treatment (b), as shown in Figure 6.2 (top row), to investigate whether the laser treatment could cause any damage. The treatment was performed on the green *in situ* setup at high accumulated laser fluence of  $2000 \text{ J cm}^{-2}$  ( $P = 5 \text{ W}$ ,  $v = 5 \text{ mm s}^{-1}$ ,  $\Delta y = 50 \mu\text{m}$ ) for a), b), and c), and at low fluence of  $100 \text{ J cm}^{-2}$  ( $P = 1.5 \text{ W}$ ,  $v = 30 \text{ mm s}^{-1}$ ,  $\Delta y = 50 \mu\text{m}$ ) for d). The processing parameters were selected to test the robot capability, contamination effects, damages of cryosorbers rather than to test the final processing parameters. The focus was adjusted with the curved part of the BS, as it was the main area of treatment. After the processing, the BS was cut for analysis (Fig. 6.2, top row). The dark laser-treated areas appeared homogeneous in color along the full BS length, except for two corners during the a) longline sequence. During the treatment of these corners, the fiber was not sufficiently fixed to the robot, causing it to move and the beam to hit the nozzle exit. Consequently, the beam became diluted and required realignment. This problem was identified by observing the treatment through a camera. Area d) was brighter, because of the lower applied fluence. SEM images in Fig. 6.2 (bottom row) of the treated areas a), b) and c) revealed deep microtrenches covered with redeposited nanoparticles, consistent with previous treatments on  $12 \times 15 \text{ mm}$  curved surfaces at  $2000 \text{ J cm}^{-2}$  (compare with Fig. 5.6). It is noteworthy that b) the 300° spiral treatment resulted in barely discernable trenches with higher particle coverage than the selective treatments (a and c). The nanostructures of a) - c) were dominated by agglomerations of the molten spheres, which is expected for a non-cleaned surface. Closer inspection of Figure 6.2a reveals the cauliflower structure beneath the molten spheres. In contrast, the surface treated at low fluence close to the ablation threshold (d) resembles an untreated Cu surface. At higher magnification, LIPSS formation is visible.

A cut segment of the BS (location indicated in Figure 6.3, yellow) was post-cleaned with a gas jet. This removed the molten spheres and dust on the laser-treated surface and the cauliflower structure appeared (Fig. 6.3), which was similarly observed for

## 6.1 Test of scan strategy on a 50 cm long beam screen (type 74)

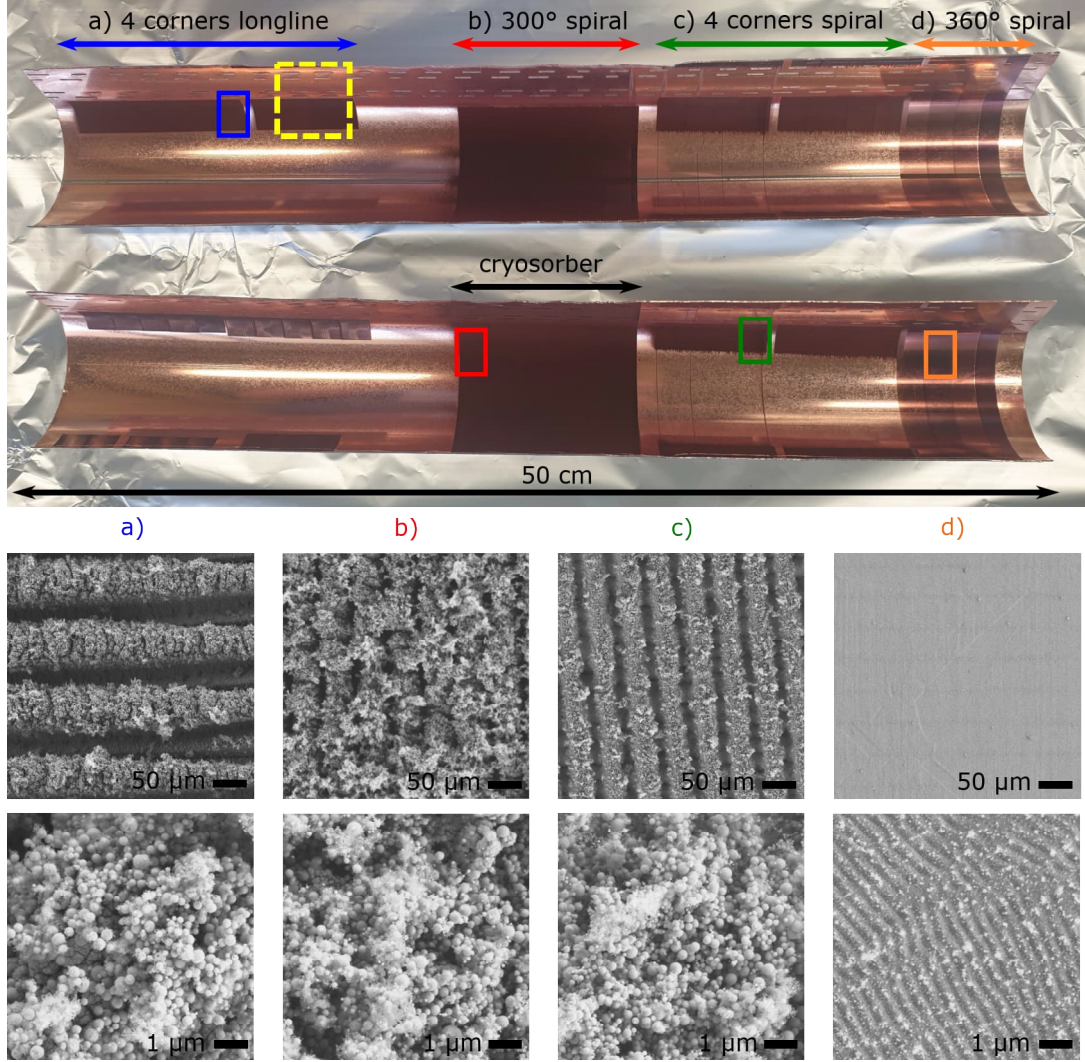


**Figure 6.2:** Photograph of 50 cm long cut BS (type 74): dark areas were laser-treated, shiny areas are the non-treated colaminated Cu (top row). SEM images of micro- (middle row) and nanostructure (bottom row) of a) four corner selective treatment ( $F_{\text{acc}} = 2000 \text{ J cm}^{-2}$ ), b) 300° spiral movement ( $F_{\text{acc}} = 2000 \text{ J cm}^{-2}$ ), c) four corners spiral movement ( $F_{\text{acc}} = 2000 \text{ J cm}^{-2}$ ), and d) a 360° spiral movement at higher scanning speed ( $F_{\text{acc}} = 100 \text{ J cm}^{-2}$ ). Yellow dashed area was used for a cleaning test (see Fig. 6.3).

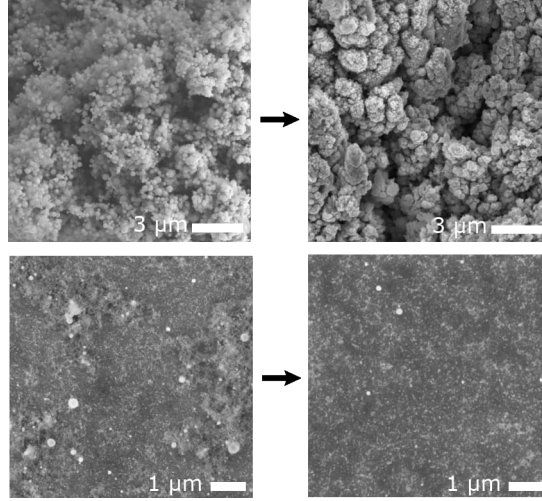


**Figure 6.3:** SEM analysis of surface morphology before (left) and after post-cleaning with a gas jet (right), defined in Sec. 5.2.2. Laser-treated BS surface with a) four corner longline selective treatment applying  $F_{acc} = 2000 \text{ J cm}^{-2}$  (top row) and untreated Cu surface (bottom row). Extracted location of the BS is indicated in yellow in Fig. 6.2.

the cleaning of small curved laser-treated surfaces (previous Chapter, Fig. 5.11). The foamy dust tends to adhere not only to the treated surface, but also to the non-treated Cu at the top flat part of the BS, as visible in the SEM photograph in Figure 6.3. It vanished after the cleaning process. This foam is loosely bound and may detach due to mechanical forces acting on the BS and interact with the beam during operation of the LHC.

During the laser treatment, the particles were extracted from the tube by a strong suction flow in the direction of the treated surface. SEM and energy dispersive x-ray spectroscopy (EDX) were used to analyze the particles that adhered to adjacent surfaces outside the BS during suction. The extracted mass consisted of foamy dust and molten spheres (Fig. 6.4a and b) that also redeposited on the treated surface. EDX was performed using a low acceleration voltage of 3000 kV to limit the analysis depth to the area of interest and to avoid any influence from the underlying substrate. This way, the electron transitions of Cu  $L_{\alpha}$ , O  $K_{\alpha}$  and C  $K_{\alpha}$  were detected in the spectra of Figure 6.4a. Both features were mainly composed of Cu (spherical particle: 94 %, dust: 86 %) and a smaller portion of oxygen and carbon. The dust contains a 7 % higher carbon concentration than the nanospheres. The size of dust agglomerations ranged from 8 to 150  $\mu\text{m}$  (Fig. 6.4c).

Finally, the cryosorber segment, placed on top of the BS during the 300° spiral sequence (indicated in Figs. 6.1 and 6.2), was analyzed. The pumping slots on the flat parts of the BS allow laser light to irradiate the component during treatment. The SEM analysis of the component after the treatment (Fig. 6.5) shows that the metal, to which the carbon fibers are attached, was laser-treated and the typical groove profile was

## 6.1 Test of scan strategy on a 50 cm long beam screen (type 74)

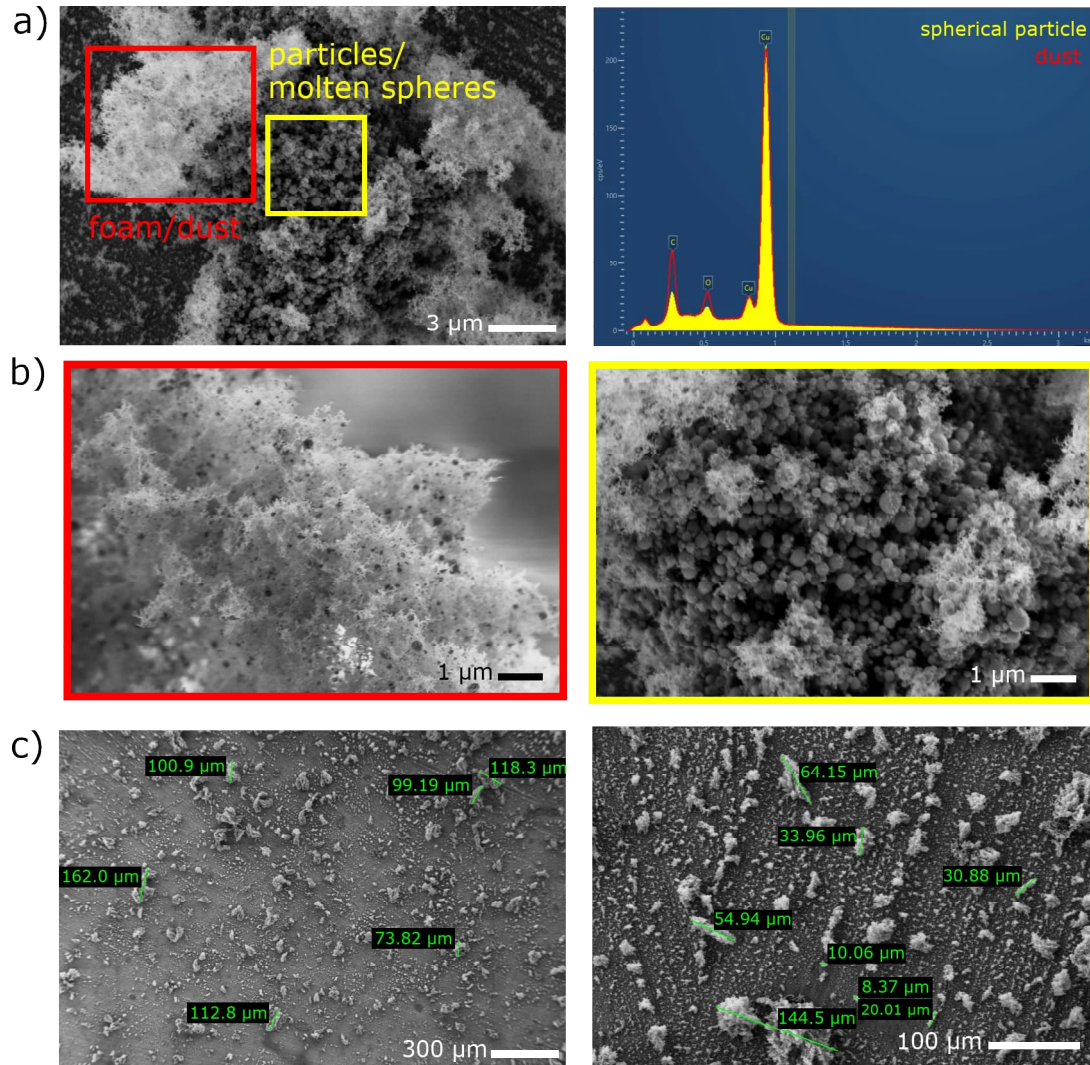


**Figure 6.4:** Analysis of particles extracted during processing by a strong suction flow during the laser treatment: a) chemical composition (EDX) of extracted particles stuck on an aluminum component outside of the BS, b) SEM images of dust (red) and molten nanospheres (yellow), c) dimension of particles that stuck to adjacent surfaces out the tube during suction.



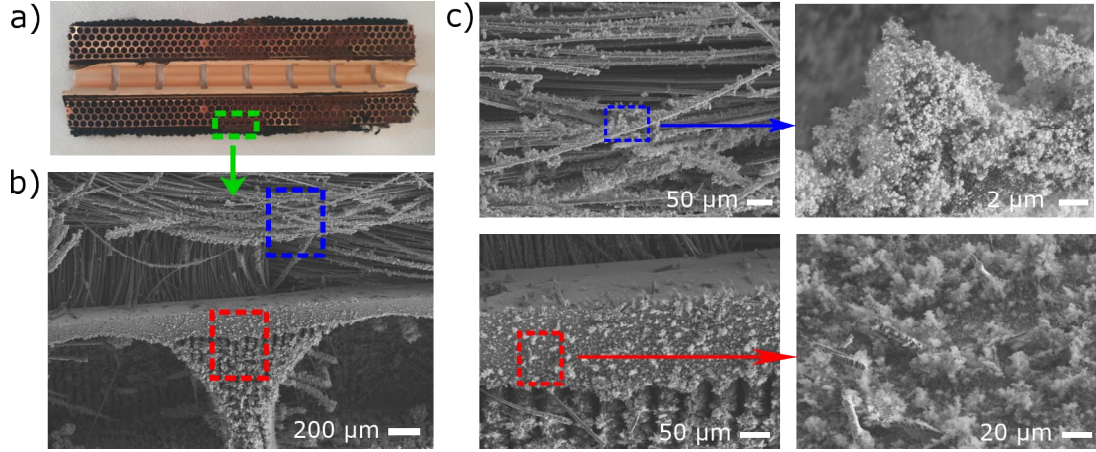


**Figure 6.5:** a) Photograph of cryosorber that was mounted on top of the flat BS during the 300° spiral treatment, b) SEM of cryosorber after the laser treatment, c) SEM of carbon fiber (blue) and Cu shield (red).

engraved (Fig. 6.5b, red zone). The fibers are decorated with nanoparticles (Fig. 6.5c, blue) and some of them were cut (Fig. 6.5, red). The laser has caused significant damage on the cryosorber and it is most likely no longer functional. This leads to a decrease in the surface area available for pumping. More importantly, the cut fibers could fall into the BS and trigger beam losses. Therefore, it is inevitable to exclude such regions from the laser processing, e.g. by selective treatment.

SEY measurements were performed on each treated area (a – d). All surface treatments at high accumulated fluence ( $2000 \text{ J cm}^{-2}$ ) resulted in a SEY below 1 (Fig. 6.6a), as expected for the processing parameter setting. The values were slightly higher (by 0.1 – 0.2) compared to those on the curved insert test samples in Chapter 5, due to the increased amount of dust remaining in the tube. The SEY maximum  $\delta_{\text{max}}$  decreased by 0.1 - 0.2 after post-cleaning the surface (Fig. 6.6b). No major differences between the SEY of a), b) and c) were observed. In addition, the SEY was  $\delta_{\text{max}} = 0.95 \pm 0.05$  and constant over the length of the treated zones, except from the area, where the fiber was misaligned in the robot. In this case, the beam was diluted, causing a loss of intensity. This resulted in a minor modification of the surface and a high SEY value of  $\delta_{\text{max}} = 1.94$ . The comparison between the flat and the curved treated surfaces unexpectedly resulted in similar SEY values at high and low accumulated fluence (Fig. 6.6c). As the flat part was expected to be 4.85 mm out of focus, the peak laser intensity should have decreased to 30 %, according to the calculation in Sec. 3.2.2. Therefore, the SEY was expected to be higher on the flat part. However, the experimental laser beam characterization on the curved part revealed a diameter slightly larger than theoretically expected (Sec. 3.2.2). Thus, the focal point was likely located between the curved and the flat parts of the BS.

### 6.1 Test of scan strategy on a 50 cm long beam screen (type 74)

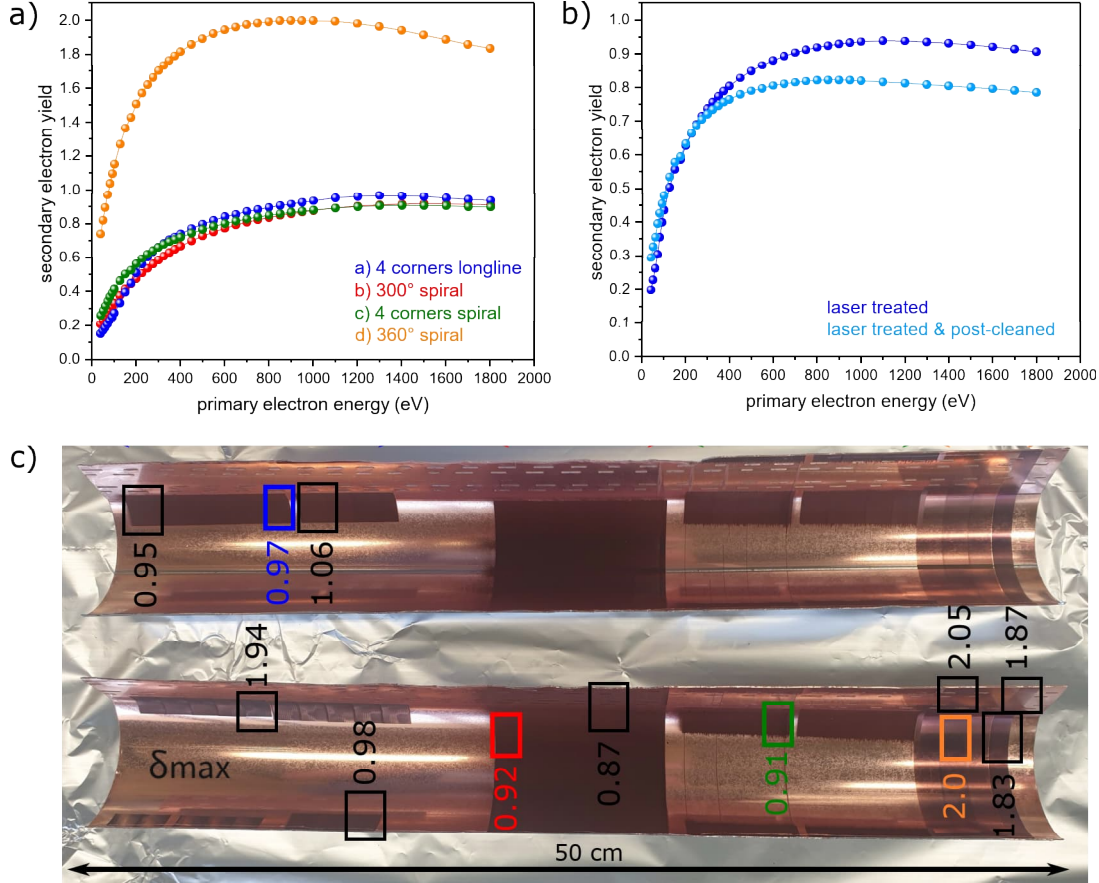


**Figure 6.6:** a) SEY measurement on the different treated areas, b) SEY measurement of laser-treated sample (longline) before and after post-cleaning, c) SEY  $\delta_{\max}$  on different treated areas along the 50 cm BS.

Finally, it is evident that intensity drifts, which occurred towards the end of the treatment (visible by distinct brown hues in the photograph shown in Fig. 6.6c) at low fluence, have a greater influence on the surface structure (see Fig. 6.2). Despite the high number of particles generated during the treatment, no degradation of optical components in the robot (lens, mirror) was observed. This is important because it ensures that the surface is treated efficiently without any intensity losses.

## 6.2 Large-scale treatment of a 2.2 m long beam screen (type 50 L)

In the following experiment, the processing was scaled up to a length of 2.2 m. For the first time, a 50 L type BS (small BS size) was treated, which is the same type installed in the Q5 magnets of the LHC. Therefore, the robot was adapted to the small size and the beam was focused on the curved BS surface to a spot size of  $54.5\text{ }\mu\text{m}$  using a convex lens of 75 mm focal length. In this configuration (see details Tab. 3.2), the theoretical Rayleigh length is only  $z_R = 1.4\text{ mm}$ , which makes the processing very sensitive to intensity losses due to defocusing. Defocusing occurs when the distance between the convex lens in the robot and the BS surface is not equal to the focal length of the lens (Fig. 3.5). This can be caused by the following scenarios:

- The lens position requires manual adjustment. Therefore, the convex lens in the robot may not be in the perfect position to match the focal point with the BS surface. Thus, it can be slightly shifted inside or outside of the BS.
- The robot is not perfectly centered in the BS. Thus, one side may be closer to the BS wall while the opposite side is further away. Ideally, the legs at the side of the robot keep it in a centered position. However, adjusting the legs of the small robot configuration on the BS surface can be challenging, resulting in a gap between the legs and the surface. To minimize this uncertainty, a modification of the robot is necessary, which involves using flexible legs supported by a spring. This is an improvement approach as a result of the present test and is currently being developed, but was not yet used in this study.
- The clamps that fix the BS shape (see Fig. 5.1) may be not equally tightened along the length of the BS.

In addition to difficulties with defocusing, processing narrow geometries presents a greater challenge. Particle generation is more significant, due to the shorter distance between the laser interaction zone and the rotating mirror, which is sensitive to contamination. Moreover, the body of the small robot is closer to the BS walls compared to the big configuration, resulting in a reduced extraction flow. Since the selective treatment proved to be beneficial (Sec. 6.1), it was applied over the entire length using the longline sequence.

The objective was to process in “optimized conditions”, in which the surface modification fulfills at best the treatment requirements (see details in Sec. 2.5.2). In the ideal case, low SEY, low ablation depth and a surface free of particles is desired. However, the laser parameters dependence on the surface properties investigated in the previous Chapter 4 are as follows: Increasing the accumulated fluence decreases the SEY, while the ablation depth and the number of loose redeposited particles increases. Thus, the compromise is to generate a surface with slightly higher SEY that conditions to below 1 after electron irradiation. The “optimized processing parameters” result in a maximum

## 6.2 Large-scale treatment of a 2.2 m long beam screen (type 50 L)

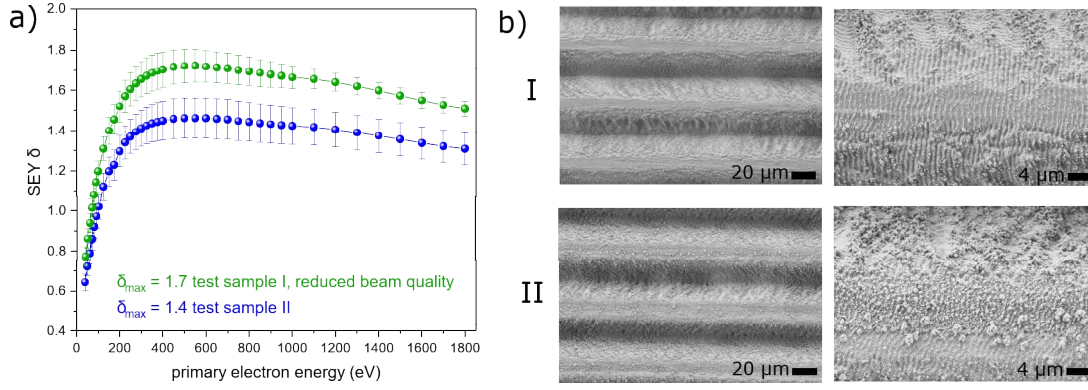


**Figure 6.7:** a) SEY measurement and b) SEM images of insert OFE Cu samples processed with the IR *in situ* setup at  $330 \text{ J cm}^{-2}$  (I) reduced beam quality due to particle contamination on the mirror in the robot and (II) high beam quality.

SEY of 1.4 after post-cleaning, which is the higher SEY acceptance limit (Chapter 5). As the IR laser was used, the parameters were adapted using the dependencies of the maximum SEY vs. accumulated fluence (Fig. 4.11) on flat surfaces. The scanning speed of  $v = 30 \text{ mm s}^{-1}$  was chosen as a compromise between avoiding degradation of the robot when operating at the maximum linear speed ( $50 \text{ mm s}^{-1}$ ) and minimizing the processing time. Therefore, an average laser power of  $5 \text{ W}$  was selected. Test on the curved OFE inserts on the BS confirmed a  $\delta_{\text{max}} = 1.1$  after the treatment and 1.4 after post-cleaning (Fig. 6.7a) with an ablation depth of  $18 \mu\text{m}$ . Using the same parameter setting, a second test sample was processed at which the beam quality was reduced due to particle contamination on the mirror. Consequently, a higher SEY of  $\delta_{\text{max}} = 1.7$  after post-cleaning was obtained. The differences in SEY are also reflected in the surface roughness. The SEM images in Figure 6.7b show that the trenches of sample (I), with higher SEY, are less pronounced ( $\sim 10 \mu\text{m}$ ) and decorated with fewer particles compared to sample (II). This finding is consistent with previous observations. The reduced beam quality decreases the energy deposited per surface area, resulting in a shallower surface modification.

The laser processing of the 2.2 m long BS was performed within 8 days (technical stops included) with an average treatment efficiency of  $56 \text{ mm per hour}$  or  $195 \text{ s cm}^{-2}$ , respectively. Technical stops included the modification of the software control that slowed down the processing time, refill of the nitrogen supply and the extraction of the robot for light intensity measurement (after 1 m and at the end of the 2.2 m) as no power measurement during processing, neither at the fiber output nor at the robot exit, is available (see Sec. 3.2). At these stages, the intensity was stable (intensity loss within 2 %), confirming the reliability of the coupling system into the fiber. Before cutting the BS into smaller pieces for subsequent surface analysis, a special cleaning tool (Fig. 6.8a) was inserted into the tube to remove redeposited particles by blowing  $\text{N}_2$ , which is likely to be used in the BSs installed in the magnets.



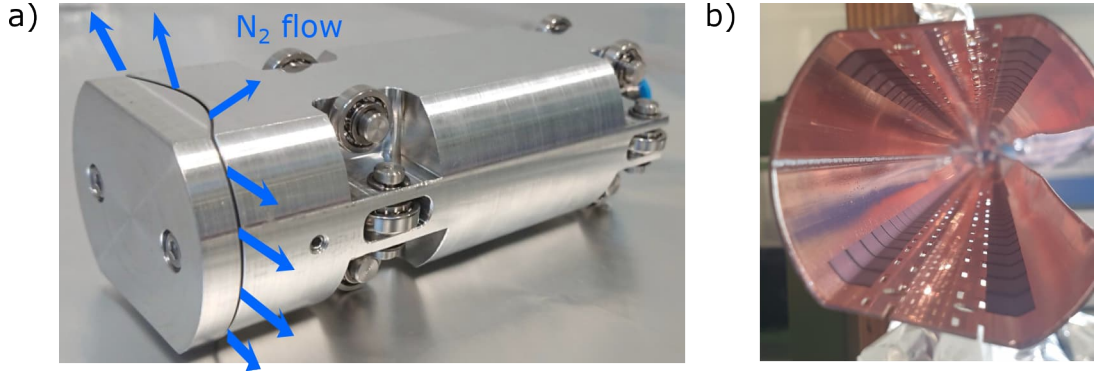


**Figure 6.8:** a) Cleaning tool, which was inserted in the BS to blow N<sub>2</sub> on the surface. N<sub>2</sub> flow indicated in blue. b) Cutting of the selectively treated BS using longline sequence.

The treated surface of the cut BS was bluish (Figs. 6.8b and 6.9a), which usually indicates the formation of LIPSS. The SEM photographs in Figure 6.9c confirmed the appearance of LIPSS, particularly on the walls of the trenches. The SEY  $\delta_{\max}$  of 1.8 – 2.0 measured along the BS length (Fig. 6.9c) was accordingly higher than targeted, but in line with what is expected for LIPSS [134]. The ablation depth of the cross-sectional surface profile in Figure 6.9d amounted to  $\sim 9\mu\text{m}$ , which is half of the one of the test sample ( $18\mu\text{m}$ ). The difference in ablation depth and SEY between the OFE test sample and the BS treatment is not assigned to the difference in material, since the SEY maximum of both surfaces was identical when comparing the laser processing of the two materials (Sec. 4.4). It is rather possible that the observed phenomenon is attributed to defocusing, given that the morphology of the treated BS was dominated by LIPSS. This was also observed when processing flat surfaces with an intentionally defocused laser beam in Sec. 4.3. It is difficult to determine the exact cause or the combined influence of defocusing factors mentioned above. Defocusing induced by the robot's position has been observed in other treatments. This resulted in a  $\delta_{\max}$  difference of approximately 0.25 for a comparable parameter setting and the robot in its small configuration. However, it is important to note that the Rayleigh length was 1.8 mm instead of 1.4 mm. Additional causes may origin from the alignment of the fiber in the robot.

The gas jet cleaning of the untreated Cu surfaces of the previous test on the type 74 BS (compare Fig. 6.3) was more effective than using the cleaning tool inside the BS (Fig. 6.8a), because in the latter the N<sub>2</sub> flow was not strong enough. Consequently many particles remained on the non-treated Cu surface, as visible in Fig. 6.9b. In addition, these particles increased the SEY of the Cu surface in the high energy range, because electrons would be scattered on the deposited dust of the non-treated zones instead of penetrating into the material. The dust agglomerations on the untreated zone of the BS may be prone to detachment. This can be critical, if those agglomerations are large in diameter and detach during operation of the LHC. In the worst case, they can

## 6.2 Large-scale treatment of a 2.2 m long beam screen (type 50 L)

damage machine components or trigger a magnet quench due to the interaction with the proton beam. Therefore, a centrifugation test was performed similar to the previous particle detachment tests (Sec. 5.3). No particles were detached during centrifugation at a force density of  $3 \text{ N mm}^{-3}$ . Nonetheless a more effective cleaning is necessary to avoid an increase of the SEY of the non-treated region.

In summary, the scale-up test provided valuable insights. It highlighted the importance of precision and the need for a margin in case of defocusing. Consequently, the convex lens of 75 mm focal length could be replaced by an 84 mm lens to increase the Rayleigh length from 1.4 to 1.8 mm. This compensates for intensity losses due to defocusing. Furthermore, the treatment provided impulses for optimizing the scale-up of processing, including the improvements to the cleaning strategy and the control system.

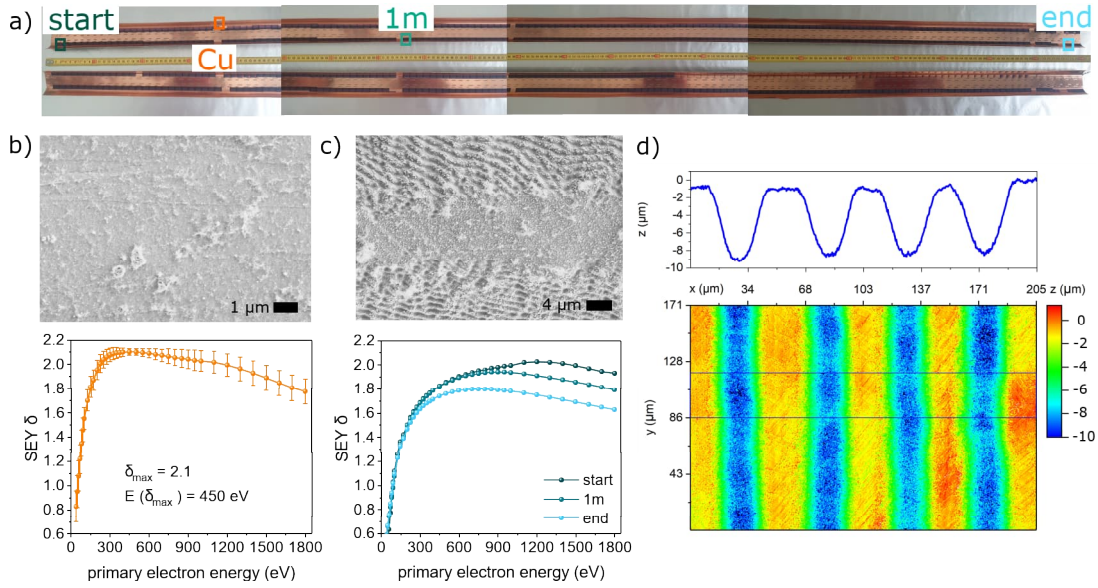


**Figure 6.9:** a) Photograph of cut 2.2m BS (type 50L) after post-cleaning. Four dark stripes represent the laser-treated parts using longline selective movement. b) Untreated Cu region with deposited particles after post-cleaning and SEY measurement. c) Laser-treated surface ( $F_{acc} = 330 \text{ J cm}^{-2}$ ) at 1 m and SEY measurement at three positions along the length of the BS after post-cleaning. d) Ablation depth measurement of the surface structure processed at  $330 \text{ J cm}^{-2}$  and 1030 nm using WLI.

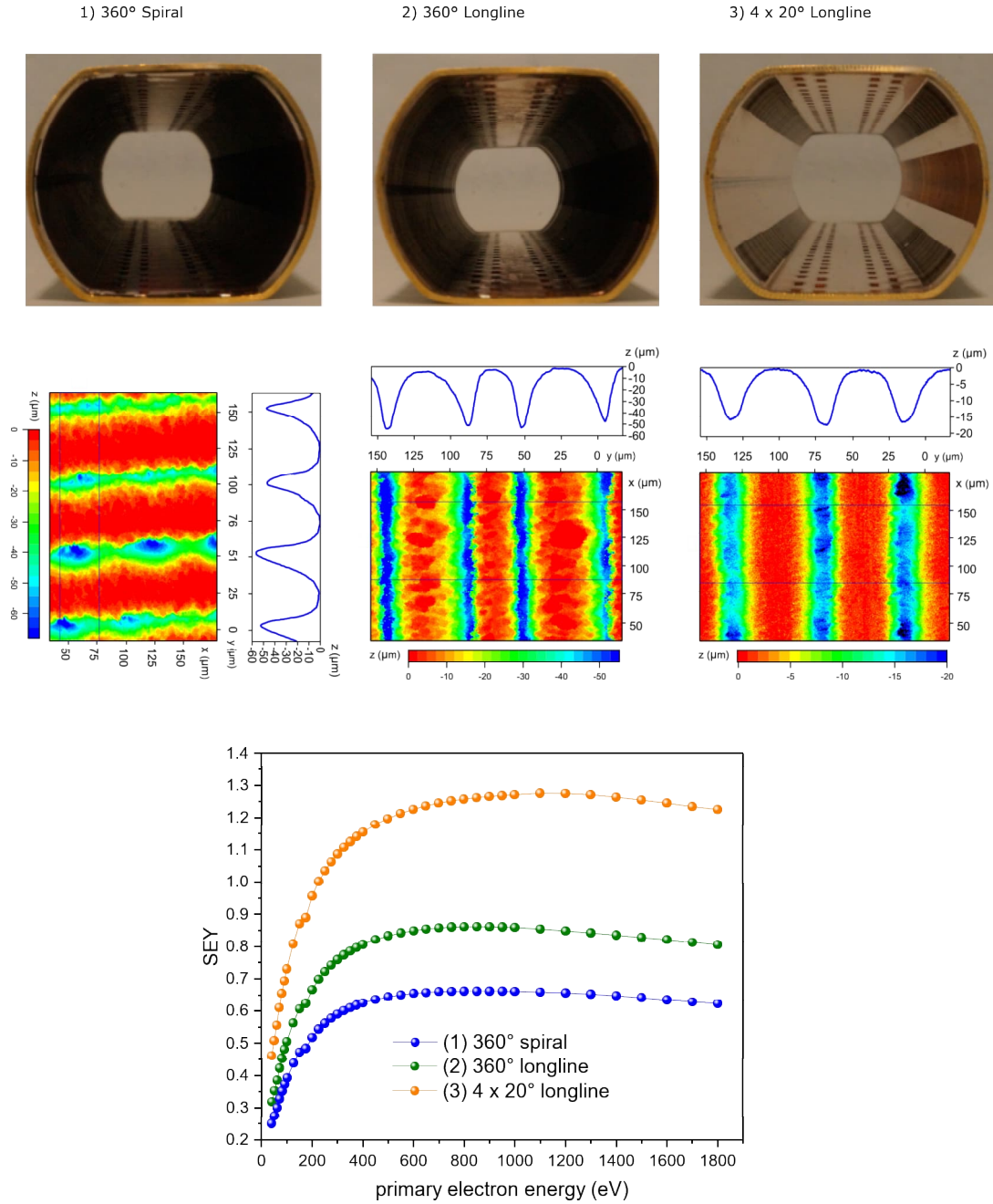
### 6.3 40 cm long laser-treated beam screens (type 50 A) for impedance measurement

The laser-induced micro groove structure increases the surface resistance compared to a smooth Cu surface [170]. A previous study on laser-treated flat surfaces has shown that grooves orientated perpendicular to the current increase the impedance more than grooves oriented parallel [171]. However, the impedance on laser-treated BSs has not yet been measured. In the following,  $3 \times 40$  cm long BSs (type 50 A) were processed using the IR *in situ* setup to measure impedance at a frequency of 400, 800 and 1200 MHz at cryogenic temperature (5 K) with the setup described in Ref. [172]. One BS was treated with the spiral movement of the robot (1) and one using the longline sequence (2). On both the complete surface was treated at a relatively high accumulated fluence of  $1133 \text{ J cm}^{-2}$  ( $P = 8.5 \text{ W}$ ,  $v = 15 \text{ mm s}^{-1}$ ,  $\Delta y = 50 \mu\text{m}$ ), intending to engrave deep grooves. The third BS (3) was selectively treated ( $4 \times 20^\circ$ ) using the longline sequence at a lower accumulated fluence of  $520 \text{ J cm}^{-2}$  ( $P = 5.2 \text{ W}$ ,  $v = 20 \text{ mm s}^{-1}$ ,  $\Delta y = 50 \mu\text{m}$ ), that complies with the “optimized processing conditions” that can be applied in the Q5 magnets of the LHC.

After each treatment, witness samples were processed on a similar BS to analyze the surface properties. The results and photographs of the treated BSs are shown in Figure 6.10. The inner surface of the BSs (1) and (2) appears darker compared to (3), because they were treated at higher accumulated fluence. Due to the geometry and design of the impedance measurement system, mainly the curved parts of the BS contribute to the measured quantity. Therefore, the laser light was focused on the curved part, while the flat area was defocused up to 4.8 mm. For this configuration, a focusing lens with  $f = 84 \text{ mm}$  was used, providing a spot diameter of  $55.1 \mu\text{m}$  with Rayleigh length  $z_R = 1.8 \text{ mm}$ . As a result, the flat parts in the photographs appear brighter, because they were barely modified due to the intensity loss caused by the defocus. The spiral treatment (1) engraved trenches that appear like holes along the trenches with a minimum depth of  $38 \pm 2 \mu\text{m}$  and a maximum of  $57 \pm 3 \mu\text{m}$ . The holes on the surface are a result of inconsistent rotational speed caused by the actuation system of the robot and its control loop. The origin is unclear. The longline treatment generated more homogeneous trenches. The ablation depth of (2) amounted to  $57 \pm 2 \mu\text{m}$ , expected for a treatment at  $1133 \text{ J cm}^{-2}$  and (3)  $15 \pm 2 \mu\text{m}$  on the BS treated at  $520 \text{ J cm}^{-2}$ . The SEY follows the fluence trend resulting in  $\delta_{\text{max}} = 0.66$  (1)  $0.86$  (2) and  $1.28$  (3) after post-cleaning.

In summary, the treated BSs (1) and (2) resulted in comparable deep trenches, which was the objective to investigate the influence of groove orientation on impedance. The slight differences are assigned to the hole structure of the grooves generated by the spiral movement. The selectively treated BS (3) is expected to have the lowest impedance due to the smaller treated area, the shallower trench depth, and the trenches that are oriented parallel to the length of the BS.

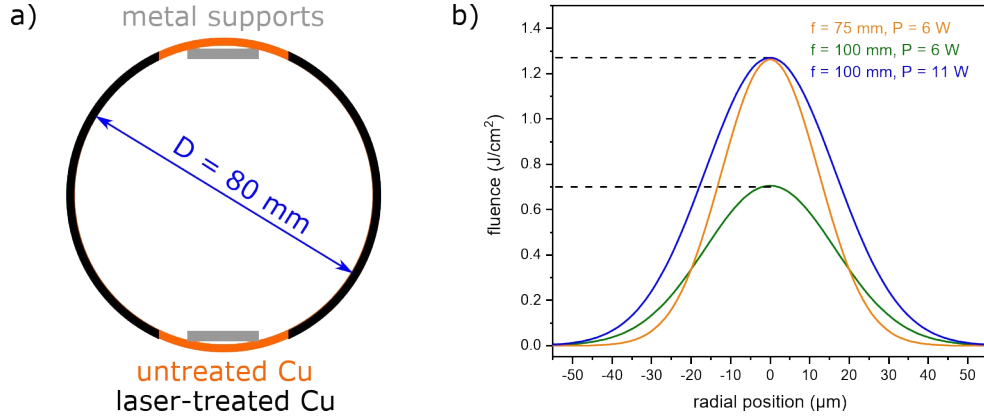
### 6.3 40 cm long laser-treated beam screens (type 50 A) for impedance measurement



**Figure 6.10:** Top row: photograph of processed BSs at (1 and 2)  $1133 \text{ J cm}^{-2}$  and (3)  $520 \text{ J cm}^{-2}$  using the  $1030 \text{ nm}$  *in situ* setup. The dark stripe in the center of the right curved part represents the sawtooth profile. Middle row: 3D profile of the surface structure of witness samples and ablation depth measurement of the cross-sectional profile using WLI. The depth profile of the spiral treatment is rotated by  $90^\circ$  compared to the others to show the orientation of the engraved microgrooves in the BS. Bottom row: SEY measurement of post-cleaned witness samples.

## 6.4 Laser-treated 3.1 m long Cu tube for beam loss measurement in the LHC

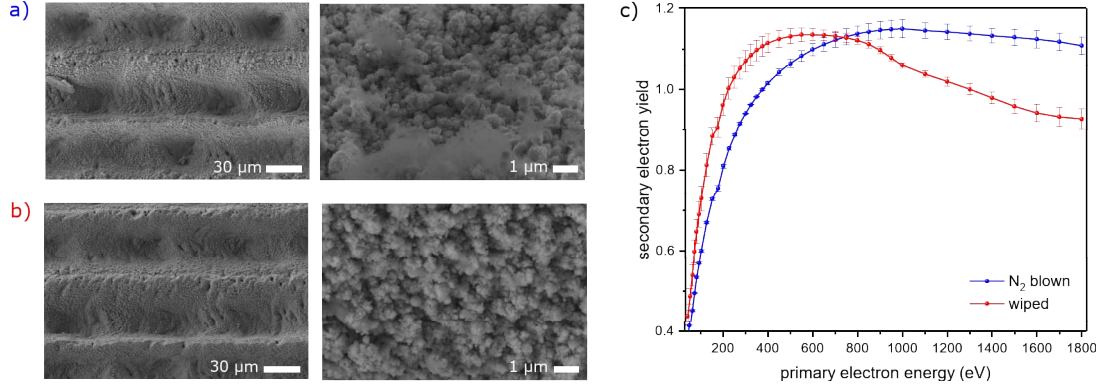
Since the presence of particles in the vacuum pipes of accelerators is considered harmful as particles could potentially detach from the surface and cause beam losses, the objective here is to install a laser-treated Cu tube in a RT long straight section of the LHC right of point 6, where beam loss monitors (BLMs) are installed to detect particle-beam interactions. The location in the RT sector was chosen because components such as cryogenic magnet complexes are far away and are not susceptible to damage in the event of harmful particle-beam interactions. For this purpose, a 3.1 m long Cu tube with a circular cross-section of 80 mm was prepared using the optimized (regarding treatment requirements) laser processing parameters. To cope with the circular cross-section of the tube, metal adapters were inserted at the top and bottom of the tube to allow activating the clamps of the robot, rendering this area unsuitable for laser treatment. Additionally, excluding the top area prevents particles from falling directly into the proton beam and is representative of the treatment to be applied in quadrupole BSs. Thus, a selective treatment of  $2 \times 110^\circ$  was applied (illustrated in Fig. 6.11a) using the longline movement. The large geometry of the tube required to use the robot in its large (type 74 BS) configuration and a convex lens with large focal length ( $f = 100$  mm) was used to focus on the inner tube surface. Consequently, the laser diameter  $2\omega_0 = 65.6 \mu\text{m}$  and the Rayleigh length  $z_R = 2.5$  mm (according to Eq. (2.12)) were larger compared to the 50 L configuration ( $2\omega_0 = 49.2 \mu\text{m}$ ,  $z_R = 1.4$  mm) used for the 2.2 m treatment in Section 6.2, where similar surface properties were targeted. As the laser diameter increases, the peak fluence decreases for the same average laser power. To achieve similar processing conditions as on the previous 50 L BS processing, the average laser power was increased to  $P = 11$  W to remain well above the ablation



**Figure 6.11:** a) Cross-sectional schematic of 3.1 m Cu tube. Zones for laser treatment ( $2 \times 110^\circ$ ) indicated in black, excluded Cu zones in orange. b) Average laser power adaption from 50 L configuration in Sec. 6.2 (using a focusing lens with focal length  $f = 75$  mm, orange) to 80 mm large configuration (focal length  $f = 100$  mm, green and blue).



#### 6.4 Laser-treated 3.1 m long Cu tube for beam loss measurement in the LHC

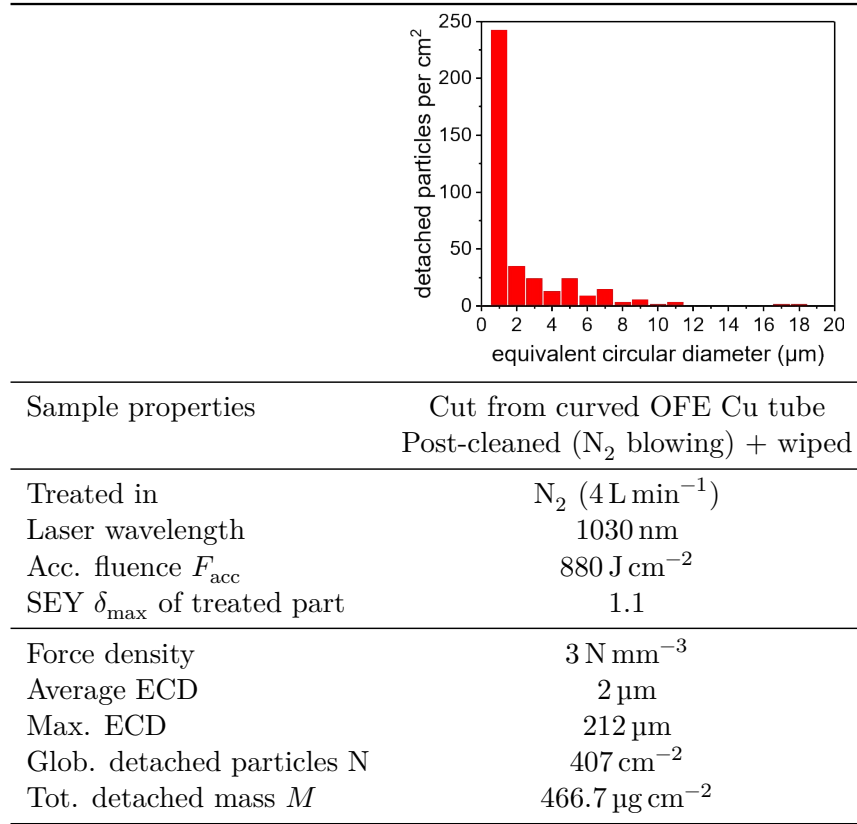


**Figure 6.12:** Surface morphology of the 3.1 m long Cu vacuum chamber processed at  $F_{\text{acc}} = 880 \text{ J cm}^{-2}$  after a) cleaning with N<sub>2</sub> blowing and b) wiping with tissue moistened in isopropanol. c) SEY measurement of laser-treated surface after N<sub>2</sub> blowing and N<sub>2</sub> blowing + wiping.

threshold, as shown in Figure 6.11b. Due to the high SEY values on the 2.2 m treated BS, the scanning speed was reduced to  $v = 25 \text{ mm s}^{-1}$  (instead of  $v = 30 \text{ mm s}^{-1}$ ).

The processing lasted a total of three weeks (including all technical stops), with an average processing speed of 20 mm per hour or  $117 \text{ s cm}^{-2}$ , respectively. Witness samples were processed on an identical shorter tube using identical processing conditions. Two of those samples were selected for surface properties analysis. Both were post-cleaned with blowing N<sub>2</sub> and one underwent an additional cleaning step, in which the surface was wiped with a tissue soaked in isopropanol. The surface morphology of both samples is depicted in Figure 6.12. The processed surfaces have the typical groove structure decorated with redeposited spherical nanoparticles. After the N<sub>2</sub> blowing, a fine foamy structure still remained on the surface, which was however removed during the wiping. The SEY of those surfaces exhibited the same  $\delta_{\text{max}} = 1.1$ . However, the maximum energy shifted from 1000 eV after N<sub>2</sub> blowing to 600 eV after the wiping, which is assigned to the removal of particles at the top of the trenches.

As a pre-particle analysis, the wiped witness sample was centrifuged under similar conditions as the particle detachment tests in Chapter (see Sec. 5.3). The results are summarized in Table 6.1. During centrifugation, a particle number of  $407 \text{ cm}^{-2}$  was released. In comparison, a surface with the same SEY did not show any detachment in the previous tests on small curved surfaces and a second surface with  $\delta_{\text{max}} = 1$  detached  $32\,000 \text{ cm}^{-2}$ , which were both not wiped. The diameter of the majority of the detached particles amounted to  $1 \mu\text{m}$ . However, a few larger clusters were detected, with diameters ranging from 20 to  $212 \mu\text{m}$ . Photographs of these large-diameter particles are shown in Figure 6.13. Some rough clusters may origin from the laser treatment (6.13a), others have a smoother shape (6.13b) and may have deposited during the cutting process of the tube, as no such particles were detected in previous centrifugation tests. The particle mass of  $466.7 \mu\text{g cm}^{-2}$  is relatively large due to the presence of

**Table 6.1:** Summary of particle detachment via centrifugation of witness sample of 3.1 m laser-treated OFE Cu vacuum chamber, where a selective treatment ( $2 \times 110^\circ$ ) was applied.

few large-diameter particles. Since the installed tube has not been cut, there are no particles resulting from the cutting process. The detachment of particles with a diameter more than 60 μm could trigger a critical particle-beam interaction event on the BLMs, at which the beam is possibly dumped.

The final laser-treated and cleaned tube is shown in Figure 6.15a. Before installation in the LHC, vacuum acceptance tests of both the laser-treated and the Cu (untreated) reference tube were conducted, in which the specific outgassing rate and mass spectra of the residual gas in the vacuum chamber were measured at RT. Typically, the vacuum chambers in the RT sectors of the LHC undergo a bake-out process to reduce outgassing and to activate the NEG coating thermally, which is applied to the majority of the RT vacuum chambers. However, neither the Cu reference nor the laser-treated tube were baked-out, since the laser-treatment is intended to be applied in magnets that operate at cryogenic temperature, and that therefore do not allow a bake-out. The mass spectra in Figure 6.14 were recorded after the chambers were evacuated for 24 h. The ion current measured by the residual gas analyzer is proportional to the partial pressure of the

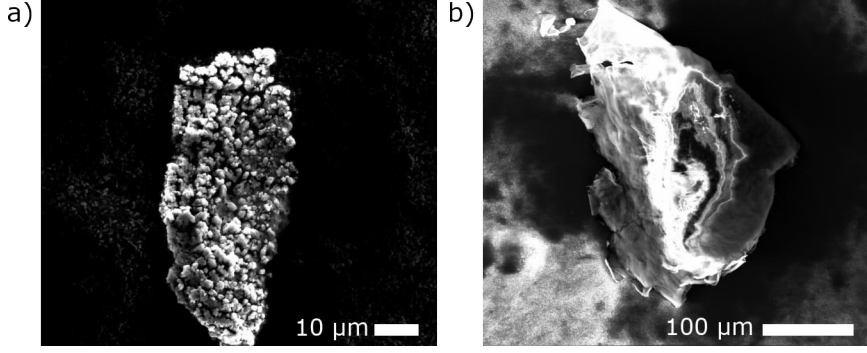
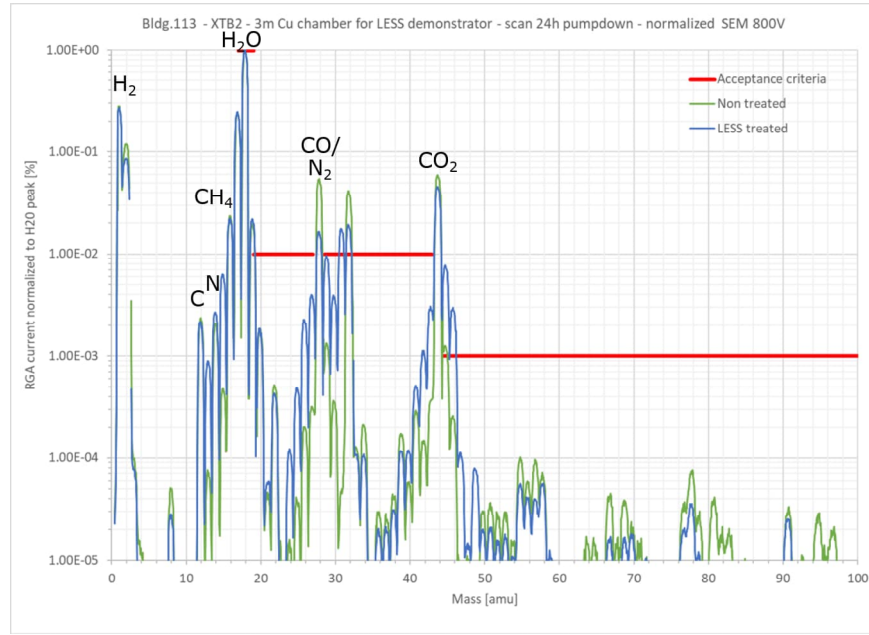


**Figure 6.13:** SEM micro graphs of detected particles after centrifugation at a force density of  $3 \text{ N mm}^3$ . The centrifuged surface was a witness sample of the 3.1 m long Cu vacuum chamber processed at  $F_{\text{acc}} = 880 \text{ J cm}^{-2}$  after wiping with tissue moistened in isopropanol. a) Particle clusters from the laser treatment, b) particles that could origin from the cutting of the tube into small samples.

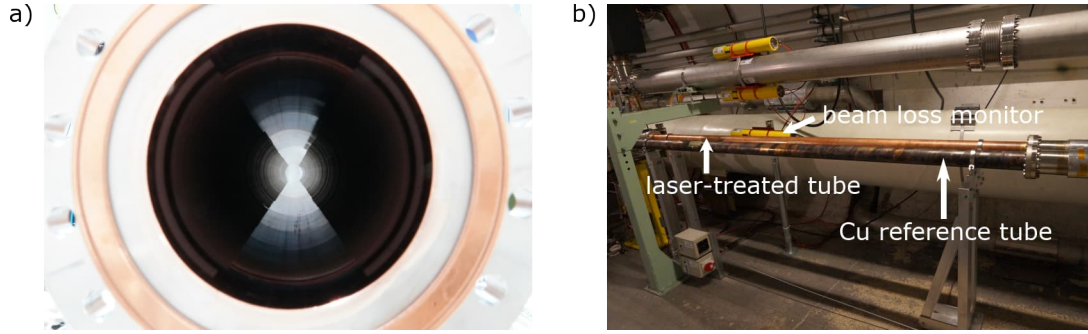
molecules. The main peaks in the spectrum correspond to hydrogen ( $m = 2$ ), carbon ( $m = 12$ ), methane ( $m = 15$ ,  $m = 16$ ), water ( $m = 18$ ), carbon monoxide/nitrogen ( $m = 28$ ) and carbon dioxide ( $m = 44$ ). As typical for an unbaked chamber, water has the highest contribution in both chambers, to which the spectra were normalized. The higher signal on masses 31, 45 and 46 are assigned to traces of ethanol  $\text{C}_2\text{H}_5\text{OH}$  ( $m_{31} - 100\%$ ,  $m_{45} - 34.4\%$ ,  $m_{29} - 23.4\%$ ) and propanol  $\text{C}_3\text{H}_7\text{OH}$  ( $m_{45} - 100\%$ ,  $m_{43} - 16.6\%$ ,  $m_{27} - 15.7\%$ ), that were used for cleaning the flanges and the inner surface, respectively. However, it is not critical for the installation in the LHC. The signal of higher masses 50 - 100, which are typically high in case of a contamination of a chamber, were below the critical threshold. The specific outgassing rate  $Q$  was measured using the throughput method [173], in which the chamber is continuously pumped and the rate  $Q = p \cdot S_{\text{eff}}/A$  is determined via the pressure decrease  $p$ , considering the fixed pumping speed  $S_{\text{eff}}$  of the system and the surface area of the chamber  $A$ . The outgassing rate of the Cu chamber was with  $2.3 \times 10^{-10} \text{ mbar L s}^{-1} \text{ cm}^{-2}$  in the expected range for an unbaked metal surface. The outgassing rate of the laser-treated chamber was  $8.7 \times 10^{-10} \text{ mbar L s}^{-1} \text{ cm}^{-2}$ . This is expected, as the effective laser-textured surface is larger, due to the roughness, than the smooth Cu surface. Thus more molecules can adsorb/desorb from the surface. The roughness factor is not included in the determination of the outgassing rate. However, a previously laser-treated vacuum chamber (unbaked), which was installed in a cryogenic sector of the SPS at CERN, exhibited a significantly higher rate of  $1 \times 10^{-8} \text{ mbar L s}^{-1} \text{ cm}^{-2}$  [64]. In this case, the SEY  $\delta_{\text{max}}$  was below 1, indicating higher roughness and a larger effective surface.

Figure 6.15b shows the tubes installed at point 6 in the LHC tunnel next to a Q5 magnet. The yellow cylinders mounted outside of the chamber represent the BLMs that protect machine components from damage and prevent quenching of the superconducting magnets by sending a beam abort signal when the measured beam loss rate exceeds the safety thresholds [3, 174]. The BLMs are ionization chambers that measure the





**Figure 6.14:** Mass spectrum of unbaked laser-treated and non-treated Cu vacuum chambers at RT after a 24 h pump down. The main peaks in the spectrum correspond to hydrogen ( $m = 2$ ), carbon ( $m = 12$ ), methane ( $m = 15$ ,  $m = 16$ ), water ( $m = 18$ ), carbon monoxide/nitrogen ( $m = 28$ ) and carbon dioxide ( $m = 44$ ). Acceptable values indicated in red. This acceptance test was performed by VSC-BVO team.



**Figure 6.15:** a) Photograph of 3.1 m laser-treated Cu tube, b) Laser-treated and untreated Cu tube with BLM installed in the LHC (point 6) for beam loss monitoring measurement.

deposited energy of secondary shower particles. The detected signal is proportional to the energy loss of the traversing particles. The BLM measurements are being performed in 2024. Of the 70 detected events, only six were clearly identified as UFOs in/around the laser-treated chamber. The UFO events occurred only at high beam intensities and mostly during the ramp-up phase of the LHC. For the largest UFO event with  $2 \times 10^5$  inelastic proton collisions, the dust particulate must have had a minimum diameter of  $4 - 6 \mu\text{m}$  [175]. These UFOs are harmless for operation of the LHC, as UFOs at other locations are significantly larger.

## 6.5 Conclusions

This Chapter described the obtained results for the scale-up from small curved surfaces to real BS treatments of various sizes and lengths. The processing parameters were adjusted for the IR laser setup, which is intended to be used for the laser treatment of the Q5 magnets due to higher beam coupling stability and less thermal drifts.

A test of various scanning strategies showed that selectively treating the four corners of the BS of a quadrupole magnet is advantageous, because a smaller surface area must be treated, reducing the the total number of generated particles in the BS. In addition, the processing time can be shortened by a factor of 4 for a selective longline treatment. When treating only the curved part of the BS, sensitive components such as the cryosorbers, which are installed on top of the flat BS, can be excluded. Furthermore, if the flat sections of the BS are excluded from treatment, the focal point remains constant on the curved section. However, agglomerations of dust particles tend to stick to the untreated Cu parts. To prevent detachment of these particles, a post-cleaning of the surface is required either with a strong gas jet or other cleaning methods compatible for application in a magnet.

## 6 Large-scale treatments of beam screens

Short segments of the smallest BS geometry (type 50 A) were laser-treated for impedance measurements with micro grooves oriented longitudinally and transversally to the BS length to study the influence of groove orientation. An additional BS was processed in "optimized processing conditions", which includes a selective treatment of the four corners, longitudinally oriented grooves and a maximum SEY of  $\sim 1.3$  after post-cleaning.

The laser processing was scaled-up to a length of 3.1 m with a total treated surface area of  $0.46 \text{ m}^2$ . For comparison, the planned four corner selective treatment ( $4 \times 20^\circ$ ) of a 10 m long 50 L BS, requires treatment of a smaller surface area of  $0.33 \text{ m}^2$ . This means, that 28 % more surface area than required was processed. For a 15 m long 50 L BS, a surface of  $0.49 \text{ m}^2$  must be treated. Thus, the large surface treatment of the 3.1 m long tube proved that the system can handle such a large surface at a high laser power without degradation of the optical system. The desired properties of the processed surface were obtained, which includes a reduced number of surface particles and  $\delta_{\text{max}} = 1.1$  after cleaning procedures. A relatively small number of particles detached in a preliminary centrifugation test at a force density of  $3 \text{ N mm}^{-3}$ . However, it also revealed that a smaller proportion of larger particle clusters (50 - 220  $\mu\text{m}$ ) may detach. For the first time, a laser-treated vacuum chamber was installed in the LHC and the BLMS detected only weak particle beam interactions that did not affect the beam stability of the LHC.

## 7 Conclusions and Outlook

In this study, an *in situ* process for electron cloud mitigation of the LHC was established via laser-induced surface ablation of the inner BS surface. The solution is in line with the technical constraints and specified surface properties, such as the modification depth and the number of generated particles. The achieved  $\text{SEY} \leq 1$  or a decrease of higher SEY to  $\leq 1$  after electron irradiation are indicators for the effectiveness in electron cloud mitigation.

Initially, in a fundamental study on flat copper surfaces, the dependencies between the processing parameters and the most relevant surface properties for the application were identified: The depth of the laser-engraved micro trenches increased upon accumulated fluence as well as the number of redeposited particles after the ablation process. When processing in ambient air, the chemical composition of the textured surface gradually transforms from  $\text{Cu}_2\text{O}$  to  $\text{CuO}$  upon accumulated fluence. Deep micro trenches and a high roughness/number of particles are beneficial for trapping secondary electrons. Therefore, the SEY decreases with increasing accumulated fluence until it saturates at a value of 0.7.

These dependencies were investigated for UV, green and IR laser light. Processing with all three laser wavelengths can satisfy the surface requirements for application in the LHC. Although UV photons are the most efficient in SEY reduction and processing time, they are not suitable for this application due to the need to guide the laser beam from the source to the inner surface of BSs up to 10 meters long. This requires hollow-core fiber technology, an automated optical coupling system, and a fiber length of more than 10 m that is not commercially available for UV laser light for the required laser power. Using the *in situ* setups (532 nm and 1030 nm), the dependencies and processing ranges found on flat surfaces were applied and validated on small curved OFE Cu surfaces, as well as on BSs and vacuum chambers of various geometries and lengths.

In view of the installation of the treated BS in the LHC, several requirements had to be met, and the treatment procedures were tuned and developed accordingly. Local  $\text{N}_2$  flow is necessary to protect the laser optics and to obtain a  $\text{Cu}_2\text{O}$ -dominated surface, but it redeposits more particles on the surface. Thus, a post-cleaning through  $\text{N}_2$  blowing was established to remove lightly bound particles from the surface, but with the disadvantage of increasing the SEY. An “optimized processing range” was identified, in which the surface properties fulfill the treatment requirements. This corresponds to processing at accumulated fluences between 200 - 400  $\text{J cm}^{-2}$  (green laser setup)

## 7 Conclusions and Outlook

and  $400 - 600 \text{ J cm}^{-2}$  (IR laser setup). Performance tests via centrifugation did not show any particle release on surfaces identified with optimized surface properties (SEY  $\sim 1.4$ , ablation depth  $10 \mu\text{m}$ ) at a force density of  $3 \text{ N mm}^{-3}$ , which is 10 % of the one acting on a BS when a magnet loses its superconductivity. In addition, the SEY of those surfaces decreased upon electron irradiation to 1.0 at both RT and cryogenic temperature.

For the large-scale processing of BSs, a selective laser treatment, in which only four corners of the BS are treated, which corresponds to 22 % of the full surface, revealed beneficial as it minimizes both the number of particles and the processing time. The IR *in situ* setup is more suitable for long-term processing (weeks/months) than the 532 nm setup due to the stable beam coupling into the fiber and reduced thermal drifts.

Ultimately, laser-treated BSs were prepared to investigate the effect of groove orientation (parallel or perpendicular to the BS length) on a deep trench depth profile of  $60 \mu\text{m}$ . Additionally, the impedance of a BS processed under “optimized conditions” using a four corner treatment, which resulted in a depth of  $15 \pm 2 \mu\text{m}$  and a SEY maximum of 1.28, will be evaluated. The processing was scaled-up to a length of 3.1 m with a processed area of  $0.46 \text{ m}^2$ , larger than the one required for a  $4 \times 20^\circ$  selective treatment of the BS (type 50 L) in a 10 m long magnet. The installation of the 3.1 m long laser-treated vacuum chamber in the LHC was completed in December 2023. In 2024, beam loss monitor signals provided important feedback on whether particles detach from the laser-treated surface and whether the interaction with the proton beam triggers beam extraction from the machine. Since the beam losses remained below critical limits, the laser treatment with the engineered surface properties is suitable for application in the LHC.

During 2024, the up-scaling to a length of 10 m is planned, for which a cable management will support the travelling of the robot. Possible improvements regarding the laser optics can be the use of a diffractive optical elements (DOE) to outbalance focusing issues. The feasibility of the post-cleaning remains to be validated on the 10 m scale. Ultimately, the treatment of  $8 \times 10 \text{ m}$  long BSs is planned during the long shutdown of the LHC in 2026. The laser treatment can also be applied to other materials and components in particle accelerators where SEY reduction is required.

# Bibliography

- [1] R. Valizadeh, O. B. Malyshev, S. Wang, S. A. Zolotovskaya, W. Allan Gillespie, and A. Abdolvand, “Low secondary electron yield engineered surface for electron cloud mitigation”, *Appl. Phys. Lett.* **105**, 231605 (2014).
- [2] S. Calatroni, E. Garcia-Tabares Valdivieso, H. Neupert, V. Nistor, A. T. Perez Fontenla, M. Taborelli, P. Chiggiato, O. Malyshev, R. Valizadeh, S. Wackerow, S. A. Zolotovskaya, W. A. Gillespie, and A. Abdolvand, “First accelerator test of vacuum components with laser-engineered surfaces for electron-cloud mitigation”, *Phys. Rev. Accel. Beams* **20**, 113201 (2017).
- [3] O. S. Brüning, P. Collier, P. Lebrun, S. Myers, R. Ostojic, J. Poole, and P. Proudlock, *LHC Design Report*, CERN Yellow Reports: Monographs (CERN, Geneva, 2004).
- [4] B. Lindstrom, P. Bélanger, L. Bortot, R. Denz, M. Mentink, E. Ravaoli, F. R. Mateos, R. Schmidt, J. Uythoven, M. Valette, A. Verweij, C. Wiesner, D. Wollmann, and M. Zerlauth, “Fast failures in the LHC and the future high luminosity LHC”, *Phys. Rev. Accel. Beams* **23**, 081001 (2020).
- [5] G. Apollinari, A. I. Béjar, O. Brüning, P. Fessia, M. Lamont, L. Rossi, and L. Taviani, *High-Luminosity Large Hadron Collider (HL-LHC): Technical Design Report V. 0.1*, CERN Yellow Reports: Monographs (CERN, Geneva, 2017).
- [6] O. Aberle, I. Béjar Alonso, O. Brüning, P. Fessia, L. Rossi, L. Taviani, and M. Zerlauth, “High-Luminosity Large Hadron Collider (HL-LHC): Technical design report”, in *Technical design report* (CERN, Geneva, 2020).
- [7] O. Gröbner, “Overview of the LHC vacuum system”, *Vacuum* **60**, 25–34 (2001).
- [8] C. Benvenuti, J. Cazeneuve, P. Chiggiato, F. Cicoira, A. Escudeiro Santana, V. Johaneck, V. Ruzinov, and J. Fraxedas, “A novel route to extreme vacua: the non-evaporable getter thin film coatings”, *Vacuum* **53**, 219–225 (1999).
- [9] G. Skripka, G. Iadarola, L. Mether, and G. Rumolo, “Non-monotonic dependence of heat loads induced by electron cloud on bunch population at the LHC”, *Eur. Phys. J. Plus* **137**, 849 (2022).
- [10] V. Anashin, R. Dostovalov, and A. Krasnov, “Summary of recent studies of cryosorbers for LHC long straight sections”, in *Proc. Part. Accel. Conf.* (2005), pp. 791–793.
- [11] G. Iadarola and G. Rumolo, “Electron cloud in the CERN accelerators (PS, SPS, LHC)”, *AIP Conf. Proc. C* **1206051**, Joint INFN-CERN-EuCARD-AccNet Workshop on Electron-Cloud Effects: ECLLOUD’12, 19–26 (2013).
- [12] G. Rumolo et al., “Electron cloud effects at the LHC and LHC injectors”, in *Proc. IPAC’17*, 8 (2017), pp. 30–36.
- [13] Y. Suetsugu, K. Shibata, T. Ishibashi, M. Shirai, S. Terui, K.-i. Kanazawa, and H. Hisamatsu, “SuperKEKB main ring vacuum system status until the end of phase-2 commissioning”, *J. Vac. Sci. Technol. A* **37**, 021602 (2019).

- [14] Y. Suetsugu, H. Fukuma, K. Ohmi, M. Tobiyama, J. Flanagan, H. Ikeda, E. Mulyani, K. Shibata, T. Ishibashi, M. Shirai, S. Terui, K. Kanazawa, and H. Hisamatsu, “Mitigating the electron cloud effect in the SuperKEKB positron ring”, *Phys. Rev. Accel. Beams* **22**, 023201 (2019).
- [15] J. Calvey, G. Dugan, W. Hartung, J. Livezey, J. Makita, and M. Palmer, “Measurement and modeling of electron cloud in a field free environment using retarding field analyzers”, *Phys. Rev. Spec. Top. Accel. Beams* **17**, 061001 (2014).
- [16] D. Alesini, A. Drago, A. Gallo, S. Guiducci, C. Milardi, A. Stella, M. Zobov, S. De Santis, T. Demma, and P. Raimondi, “DANE operation with electron-cloud-clearing electrodes”, *Phys. Rev. Lett.* **110**, 124801 (2013).
- [17] Y. Cai, M. Pivi, and M. A. Furman, “Buildup of electron cloud in the pep-ii particle accelerator in the presence of a solenoid field and with different bunch pattern”, *Phys. Rev. ST Accel. Beams* **7**, 024402 (2004).
- [18] M. Kireeff Covo, A. W. Molvik, A. Friedman, J.-L. Vay, P. A. Seidl, G. Logan, D. Baca, and J. L. Vujic, “Absolute measurement of electron-cloud density in a positively charged particle beam”, *Phys. Rev. Lett.* **97**, 054801 (2006).
- [19] M. Pivi and M. A. Furman, “Mitigation of the electron-cloud effect in the PSR and SNS proton storage rings by tailoring the bunch profile”, *Proc. Part. Acc. Conf.* **5**, 3222–3224 (2003).
- [20] R. J. Macek, A. A. Browman, J. E. Ledford, M. J. Borden, J. F. O’Hara, R. C. McCrady, L. J. Rybarczyk, T. Spickermann, T. J. Zaugg, and M. T. F. Pivi, “Electron cloud generation and trapping in a quadrupole magnet at the Los Alamos proton storage ring”, *Phys. Rev. ST Accel. Beams* **11**, 010101 (2008).
- [21] G. Gergely, “Elastic backscattering of electrons: determination of physical parameters of electron transport processes by elastic peak electron spectroscopy”, *Prog. Surf. Sci.* **71**, 31–88 (2002).
- [22] W. S. M. Werner, “Electron transport in solids for quantitative surface analysis”, *Surf. Interface Anal.* **31**, 141–176 (2001).
- [23] A. Jablonski, “Elastic scattering and quantification in AES and XPS”, *Surf. Interface Anal.* **14**, 659–685 (1989).
- [24] H. Seiler, “Secondary electron emission in the scanning electron microscope”, *J. Appl. Phys.* **54**, R1–R18 (1983).
- [25] G. F. Dionne, “Origin of secondary-electron-emission yield-curve parameters”, *J. Appl. Phys.* **46**, 3347–3351 (1975).
- [26] C. Bouchard and J. Carette, “The surface potential barrier in secondary emission from semiconductors”, *Surf. Sci.* **100**, 251–268 (1980).
- [27] J. Vaughan, “A new formula for secondary emission yield”, *IEEE Trans. Electron Devices* **36**, 1963–1967 (1989).
- [28] R. Cimino, I. R. Collins, M. A. Furman, M. Pivi, F. Ruggiero, G. Rumolo, and F. Zimmermann, “Can low-energy electrons affect high-energy physics accelerators?”, *Phys. Rev. Lett.* **93**, 014801 (2004).
- [29] N. Hilleret, C. Scheuerlein, and M. Taborelli, “The secondary-electron yield of air-exposed metal surfaces”, *Appl. Phys. A* **76**, 1085–1091 (2003).

- [30] V. Baglin, J. Bojko, O. Gröbner, B. Henrist, N. Hilleret, C. Scheuerlein, and M. Taborelli, “The secondary electron yield of technical materials and its variation with surface treatments”, in 7th Eur. Part. Accel. Conf. (2000), p. 271.
- [31] V. Petit, M. Taborelli, H. Neupert, P. Chiggiato, and M. Belhaj, “Role of the different chemical components in the conditioning process of air exposed copper surfaces”, *Phys. Rev. Accel. Beams* **22**, 083101 (2019).
- [32] R. Cimino, M. Commisso, D. R. Grosso, T. Demma, V. Baglin, R. Flammini, and R. Larciprete, “Nature of the decrease of the secondary-electron yield by electron bombardment and its energy dependence”, *Phys. Rev. Lett.* **109**, 064801 (2012).
- [33] R. Larciprete, D. R. Grosso, M. Commisso, R. Flammini, and R. Cimino, “Secondary electron yield of cu technical surfaces: dependence on electron irradiation”, *Phys. Rev. ST Accel. Beams* **16**, 011002 (2013).
- [34] D. C. Joy and C. S. Joy, “Low voltage scanning electron microscopy”, *Micron* **27**, 247–263 (1996).
- [35] T. J. Vink, A. R. Balkenende, R. G. F. A. Verbeek, H. A. M. van Hal, and S. T. de Zwart, “Materials with a high secondary-electron yield for use in plasma displays”, *Appl. Phys. Lett.* **80**, 2216–2218 (2002).
- [36] Y. M. Y. Murakami, H. M. H. Matsuzaki, H. M. H. Murakami, and N. I. N. Ikuta, “Effective secondary electron yield of a cathode for plasma display panel”, *Jpn. J. Appl. Phys.* **40**, 3382 (2001).
- [37] S. X. Tao, H. W. Chan, and H. Van der Graaf, “Secondary electron emission materials for transmission dynodes in novel photomultipliers: a review”, *Mater.* **9**, 1017 (2016).
- [38] M. Daksha, A. Derzsi, Z. Mujahid, D. Schulenberg, B. Berger, Z. Donkó, and J. Schulze, “Material dependent modeling of secondary electron emission coefficients and its effects on PIC/MCC simulation results of capacitive RF plasmas”, *Plasma Sources Sci. Technol.* **28**, 034002 (2019).
- [39] V. Nistor, L. A. González, L. Aguilera, I. Montero, L. Galán, U. Wochner, and D. Raboso, “Multipactor suppression by micro-structured gold/silver coatings for space applications”, *Appl. Surf. Sci.* **315**, 445–453 (2014).
- [40] G. Iadarola, “Electron cloud studies for CERN particle accelerators and simulation code development”, PhD thesis (Università degli Studi di Napoli Federico II, Napoli, Italy, 2014).
- [41] R. Cimino and T. Demma, “Electron cloud in accelerators”, *Int. J. Mod. Phys. A* **29**, 1430023 (2014).
- [42] P. Dijkstal, G. Iadarola, L. Mether, and G. Rumolo, “Simulation studies on the electron cloud build-up in the elements of the LHC arcs at 6.5 TeV”, Technical report: CERN-ACC-NOTE-2017-0057 (2017).
- [43] G. Skripka and G. Iadarola, “Beam-induced heat loads on the beam screens of the HL-LHC arcs”, Technical report: CERN-ACC-NOTE-2019-0041 (2019).
- [44] R. Macek, “Electron cloud generation and trapping in a quadrupole magnet at the Los Alamos PSR”, in *Proc. Part. Accel. Conf.* (2007), pp. 828–830.
- [45] G. Iadarola, B. Bradu, L. Mether, K. Paraschou, V. Petit, G. Rumolo, L. Sabato, G. Skripka, M. Taborelli, and L. Tavian, “Progress in mastering electron clouds at the Large Hadron Collider”, *Proc. IPAC’21*, 1273–1278 (2021).



- [46] G. F. B. Bradu K. Brodzinski, “How does a cryogenic system cope with e-cloud induced heat load?”, in *ECLLOUD’18 : proc. joint INFN-CERN-ARIES workshop on electron-cloud effects*, Vol. 7 (2020), pp. 73–81.
- [47] G. Iadarola, B. Bradu, P. Dijkstal, L. Methner, G. Rumolo, G. Skripka, and L. Tavian, “Overview of heat loads in the LHC”, in *ECLLOUD’18 : proc. joint INFN-CERN-ARIES workshop on electron-cloud effects*, Vol. 7 (2020), pp. 51–59.
- [48] E. Benedetto, G. Franchetti, and F. Zimmermann, “Incoherent effects of electron clouds in proton storage rings”, *Phys. Rev. Lett.* **97**, 034801 (2006).
- [49] W. Fischer, M. Blaskiewicz, J. M. Brennan, H. Huang, H.-C. Hseuh, V. Ptitsyn, T. Roser, P. Thieberger, D. Trbojevic, J. Wei, S. Y. Zhang, and U. Irso, “Electron cloud observations and cures in the Relativistic Heavy Ion Collider”, *Phys. Rev. ST Accel. Beams* **11**, 041002 (2008).
- [50] G. Rumolo, F. Ruggiero, and F. Zimmermann, “Simulation of the electron-cloud build up and its consequences on heat load, beam stability, and diagnostics”, *Phys. Rev. ST Accel. Beams* **4**, 012801 (2001).
- [51] G. Bregliozzi, V. Baglin, P. Chiggiato, P. Cruikshank, J. M. Jimenez, and G. Lanza, “Observations of electron cloud effects with the LHC vacuum system”, *Proc. IPAC’11* **110904**, 1560–1562 (2011).
- [52] O. Bruning, “Electron cloud and beam scrubbing in the LHC”, in *Proc. Part. Accel. Conf. Vol. 4* (1999), pp. 2629–2631.
- [53] G. Arduini, M. Lamont, T. Pieloni, and G. Rumolo, “Implications for operations”, *Adv. Ser. Direct. High Energy Phys.* **24**, 373–389 (2015).
- [54] Y. Suetsugu, K. Shibata, T. Ishibashi, K. Kanazawa, M. Shirai, S. Terui, and H. Hisamatsu, “First commissioning of the SuperKEKB vacuum system”, *Phys. Rev. Accel. Beams* **19**, 121001 (2016).
- [55] V. Petit, M. Taborrelli, D. A. Zanin, M. Himmerlich, H. Neupert, P. Chiggiato, and G. Iadarola, “Beam-induced surface modifications as a critical source of heat loads in the Large Hadron Collider”, *Commun. Phys.* **4**, 192 (2021).
- [56] V. Petit, P. Chiggiato, M. Himmerlich, S. Marinoni, H. Neupert, M. Taborrelli, and L. Tavian, “Origin and mitigation of the beam-induced surface modifications of the LHC beam screens”, *Proc. IPAC’22*, 780–782 (2022).
- [57] C. Benvenuti, P. Chiggiato, P. Costa Pinto, A. Escudeiro Santana, T. Hedley, A. Mongelluzzo, V. Ruzinov, and I. Wevers, “Vacuum properties of TiZrV non-evaporable getter films”, *Vacuum* **60**, 57–65 (2001).
- [58] P. Chiggiato and P. Costa Pinto, “Ti–Zr–V non-evaporable getter films: From development to large scale production for the Large Hadron Collider”, *Thin Solid Films* **515**, 382–388 (2006).
- [59] P. Costa Pinto, S. Calatroni, H. Neupert, D. Letant-Delrieux, P. Edwards, P. Chiggiato, M. Taborrelli, W. Vollenberg, C. Yin-Vallgren, J. Colaun, and S. Lucas, “Carbon coatings with low secondary electron yield”, *Vacuum* **98**, 29–36 (2013).
- [60] M. Alberti, R. Ayouchi, S. R. Bhattacharyya, N. Bundaleski, A. Moutinho, O. Teodoro, L. Aguilera, M. Taborrelli, and R. Schwarz, “Secondary electron emission yield (SEY) in amorphous and graphitic carbon films prepared by PLD”, *Phys. Status Solidi C* **9**, 1501–1503 (2012).

- [61] R. Larciprete, D. R. Grosso, A. Di Trollo, and R. Cimino, “Evolution of the secondary electron emission during the graphitization of thin C films”, *Appl. Surf. Sci.* **328**, 356–360 (2015).
- [62] C. Yin Vallgren, G. Arduini, J. Bauche, S. Calatroni, P. Chiggiato, K. Cornelis, P. C. Pinto, B. Henrist, E. Métral, H. Neupert, G. Rumolo, E. Shaposhnikova, and M. Taborelli, “Amorphous carbon coatings for the mitigation of electron cloud in the CERN Super Proton Synchrotron”, *Phys. Rev. ST Accel. Beams* **14**, 071001 (2011).
- [63] W. Vollenberg, P. Chiggiato, P. Costa Pinto, P. Cruikshank, H. Moreno, C. Pasquino, J. Perez Espinos, and M. Taborelli, “Amorphous carbon coating in SPS”, in *Proc. IPAC’21* (2021), pp. 3475–3478.
- [64] R. Salemme, V. Baglin, G. Bregliozzi, and P. Chiggiato, “Vacuum performance of amorphous carbon coating at cryogenic temperature with presence of proton beams”, in *Proc. IPAC’16* (2016), THPMY007.
- [65] E. Buratin, V. Baglin, B. Henrist, P. Chiggiato, and A. Fasoli, “Electron flux and pressure dynamic in the lhc vacuum pilot sector as a function of beam parameters and beam pipe properties”, *Phys. Rev. Accel. Beams* **23**, 114802 (2020).
- [66] M. Himmerlich, D. A. Zanin, M. Taborelli, A. R. Granadeiro Costa, P. Costa Pinto, L. Lain Amador, W. Vollenberg, A. Baris, E. Garcia-Tabares Valdivieso, A. T. Perez Fontenla, S. Wackerow, and A. Abdolvand, “Efficient combination of surface texturing and functional coating for very low secondary electron yield surfaces and rough nonevaporable getter films”, *Adv. Mater. Interfaces* **10**, 2201671 (2023).
- [67] H. Bruining, “Secondary electron emission”, *Philips Tech. Rev.* **3**, 80–86 (1938).
- [68] J. Kawata, K. Ohya, and K. Nishimura, “Simulation of secondary electron emission from rough surfaces”, *J. Nucl. Mater.* **220-222**, 997–1000 (1995).
- [69] M. Pivi, F. K. King, R. E. Kirby, T. O. Raubenheimer, G. Stupakov, and F. Le Pimpec, “Sharp reduction of the secondary electron emission yield from grooved surfaces”, *J. Appl. Phys.* **104**, 104904 (2008).
- [70] L. Wang, T. Raubenheimer, and G. Stupakov, “Suppression of secondary emission in a magnetic field using triangular and rectangular surfaces”, *Nucl. Instrum. Methods Phys. Res. A: Accelerators, Spectrometers, Detectors and Associated Equipment* **571**, 588–598 (2007).
- [71] A. Krasnov, “Molecular pumping properties of the LHC arc beam pipe and effective secondary electron emission from Cu surface with artificial roughness”, *Vacuum* **73**, 195–199 (2004).
- [72] G. Tang, A. C. Hourd, and A. Abdolvand, “Nanosecond pulsed laser blackening of copper”, *Appl. Phys. Lett.* **101**, 231902 (2012).
- [73] C. Watts, M. Gilmore, and E. Schamiloglu, “Effects of laser surface modification on secondary electron emission of copper”, *IEEE Trans. Plasma Sci.* **39**, 836–841 (2011).
- [74] G. Tang and A. Abdolvand, “Laser-assisted highly organized structuring of copper”, *Opt. Mater. Express* **1**, 1425–1432 (2011).
- [75] G. Tang and A. Abdolvand, “Structuring of titanium using a nanosecond-pulsed Nd:YVO<sub>4</sub> laser at 1064 nm”, *Int. J. Adv. Manuf. Technol.* **66**, 1769–1775 (2013).
- [76] A. Horn, “Non-linear absorption”, in *The physics of laser radiation–matter interaction: fundamentals, and selected applications in metrology* (Springer International Publishing, Cham, 2022), pp. 297–315.

- [77] J. M. Liu, “Simple technique for measurements of pulsed gaussian-beam spot sizes”, *Opt. Lett.* **7**, 196–198 (1982).
- [78] M. V. Shugaev, C. Wu, O. Armbruster, A. Naghilou, N. Brouwer, D. S. Ivanov, T. J.-Y. Derrien, N. M. Bulgakova, W. Kautek, B. Rethfeld, and L. V. Zhigilei, “Fundamentals of ultrafast laser-material interaction”, *MRS Bulletin* **41**, 960–968 (2016).
- [79] B. Rethfeld, D. S. Ivanov, M. E. Garcia, and S. I. Anisimov, “Modelling ultrafast laser ablation”, *J. Phys. D: Appl. Phys* **50**, 193001 (2017).
- [80] E. Gamaly and A. Rode, “Physics of ultra-short laser interaction with matter: from phonon excitation to ultimate transformations”, *Prog. Quantum Electron.* **37**, 215–323 (2013).
- [81] J. B. Razvan Stoian, *Ultrafast laser nanostructuring*, Vol. 239 (Springer Series in Optical Sciences, 2023).
- [82] Z. Lin and M. Hong, “Femtosecond laser precision engineering: from micron, submicron, to nanoscale”, *Ultrafast Science* **2021**, 22 (2021).
- [83] C. Wu and L. V. Zhigilei, “Microscopic mechanisms of laser spallation and ablation of metal targets from large-scale molecular dynamics simulations”, *Appl. Phys. A* **114**, 11–32 (2014).
- [84] R. Stoian, “Volume photoinscription of glasses: three-dimensional micro- and nanostructuring with ultrashort laser pulses”, *Appl. Phys. A: Mater. Sci. Process.* **126**, 438 (2020).
- [85] A. Y. Vorobyev and C. Guo, “Reflection of femtosecond laser light in multipulse ablation of metals”, *J. Appl. Phys.* **110**, 043102 (2011).
- [86] S. E. Kirkwood, Y. Y. Tsui, R. Fedosejevs, A. V. Brantov, and V. Y. Bychenkov, “Experimental and theoretical study of absorption of femtosecond laser pulses in interaction with solid copper targets”, *Phys. Rev. B* **79**, 144120 (2009).
- [87] C. Schäfer, H. M. Urbassek, and L. V. Zhigilei, “Metal ablation by picosecond laser pulses: a hybrid simulation”, *Phys. Rev. B* **66**, 115404 (2002).
- [88] J. P. Colombier, P. Combis, F. Bonneau, R. Le Harzic, and E. Audouard, “Hydrodynamic simulations of metal ablation by femtosecond laser irradiation”, *Phys. Rev. B* **71**, 165406 (2005).
- [89] J. P. Colombier, P. Combis, R. Stoian, and E. Audouard, “High shock release in ultrafast laser irradiated metals: scenario for material ejection”, *Phys. Rev. B* **75**, 104105 (2007).
- [90] Z. Lin, E. Leveugle, E. M. Bringa, and L. V. Zhigilei, “Molecular dynamics simulation of laser melting of nanocrystalline Au”, *J. Phys. Chem. C* **114**, 5686–5699 (2010).
- [91] J. Byskov-Nielsen, J.-M. Savolainen, M. S. Christensen, and P. Balling, “Ultra-short pulse laser ablation of copper, silver and tungsten: experimental data and two-temperature model simulations”, *Appl. Phys. A* **103**, 447–453 (2011).
- [92] S. Wang, Y. Ren, C. Cheng, J. Chen, and D. Tzou, “Micromachining of copper by femtosecond laser pulses”, *Appl. Surf. Sci.* **265**, 302–308 (2013).
- [93] C. Cheng, S. Wang, K. Chang, and J. Chen, “Femtosecond laser ablation of copper at high laser fluence: modeling and experimental comparison”, *Appl. Surf. Sci.* **361**, 41–48 (2016).

- [94] A. Abdelmalek, Z. Bedrane, E.-H. Amara, B. Sotillo, V. Bharadwaj, R. Ramponi, and S. M. Eaton, “Ablation of copper metal films by femtosecond laser multipulse irradiation”, *Appl. Sci.* **8**, 1826 (2018).
- [95] S. I. Anisimov, B. L. Kapeliovich, and T. L. Perel’man, “Electron emission from the metal surfaces induced by ultrashort lasers pulses”, *J. Exp. Theor. Phys.* **39**, 375–377 (1974).
- [96] B. N. Chichkov, C. Momma, S. Nolte, F. von Alvensleben, and A. Tünnermann, “Femtosecond, picosecond and nanosecond laser ablation of solids”, *Appl. Phys. A* **63**, 109–115 (1996).
- [97] D. W. Müller, T. Fox, P. G. Grützmacher, S. Suarez, and F. Mücklich, “Applying ultrashort pulsed direct laser interference patterning for functional surfaces”, *Sci. Rep.* **10**, 3647 (2020).
- [98] S. Amoroso, R. Bruzzese, X. Wang, N. N. Nedialkov, and P. A. Atanasov, “Femtosecond laser ablation of nickel in vacuum”, *J. Phys. D Appl. Phys* **40**, 331 (2007).
- [99] T. E. Itina, K. Gouriet, L. V. Zhigilei, S. Noël, J. Hermann, and M. Sentis, “Mechanisms of small clusters production by short and ultra-short laser ablation”, *Appl. Surf. Sci.* **253**, 7656–7661 (2007).
- [100] S. S. Harilal, C. V. Bindhu, M. S. Tillack, F. Najmabadi, and A. C. Gaeris, “Internal structure and expansion dynamics of laser ablation plumes into ambient gases”, *J. Appl. Phys.* **93**, 2380–2388 (2003).
- [101] S. S. Harilal, B. O’Shay, Y. Tao, and M. S. Tillack, “Ambient gas effects on the dynamics of laser-produced tin plume expansion”, *J. Appl. Phys.* **99**, 083303 (2006).
- [102] K.-H. Leitz, B. Redlingshöfer, Y. Reg, A. Otto, and M. Schmidt, “Metal ablation with short and ultrashort laser pulses”, *Phys. Procedia* **12**, 230–238 (2011).
- [103] J. Schille, L. Schneider, P. Lickschat, U. Loeschner, R. Ebert, and H. Exner, “High-pulse repetition frequency ultrashort pulse laser processing of copper”, *J. Laser Appl.* **27**, S28007 (2015).
- [104] J. Yang, Y. Zhao, N. Zhang, Y. Liang, and M. Wang, “Ablation of metallic targets by high-intensity ultrashort laser pulses”, *Phys. Rev. B* **76**, 165430 (2007).
- [105] T. Smausz, T. Csizmadia, C. Tápai, J. Kopniczky, A. Oszkó, M. Ehrhardt, P. Lorenz, K. Zimmer, A. Prager, and B. Hopp, “Study on the effect of ambient gas on nanostructure formation on metal surfaces during femtosecond laser ablation for fabrication of low-reflective surfaces”, *Appl. Surf. Sci.* **389**, 1113–1119 (2016).
- [106] P. Fan, M. Zhong, B. Bai, G. Jin, and H. Zhang, “Tuning the optical reflection property of metal surfaces via micro–nano particle structures fabricated by ultrafast laser”, *Appl. Surf. Sci.* **359**, 7–13 (2015).
- [107] A. Y. Vorobyev and C. Guo, “Direct femtosecond laser surface nano/microstructuring and its applications”, *Laser Photonics Rev.* **7**, 385–407 (2013).
- [108] C. Deng and H. Ki, “Tunable wetting surfaces with interacting cavities via femtosecond laser patterning and wet etching”, *J. Appl. Phys.* **128**, 015306 (2020).
- [109] K. Yin, Z. Wu, J. Wu, Z. Zhu, F. Zhang, and J.-A. Duan, “Solar-driven thermal-wind synergistic effect on laser-textured superhydrophilic copper foam architectures for ultrahigh efficient vapor generation”, *Appl. Phys. Lett.* **118**, 211905 (2021).

- [110] J. Schille, L. Schneider, S. Mauersberger, S. Szokup, S. Höhn, J. Pötschke, F. Reiß, E. Leidich, and U. Löschner, “High-rate laser surface texturing for advanced tribological functionality”, *Lubricants* **8**, 33 (2020).
- [111] M. S. Sidhu, P. Munjal, and K. P. Singh, “High-fidelity large area nano-patterning of silicon with femtosecond light sheet”, *Appl. Phys. A* **124**, 46 (2017).
- [112] J. Long, P. Fan, M. Zhong, H. Zhang, Y. Xie, and C. Lin, “Superhydrophobic and colorful copper surfaces fabricated by picosecond laser induced periodic nanostructures”, *Appl. Surf. Sci.* **311**, 461–467 (2014).
- [113] B. Dusser, Z. Sagan, H. Soder, N. Faure, J. Colombier, M. Jourlin, and E. Audouard, “Controlled nanostructures formation by ultra fast laser pulses for color marking”, *Opt. Express* **18**, 2913–2924 (2010).
- [114] J. Bonse, S. Höhm, S. V. Kirner, A. Rosenfeld, and J. Krüger, “Laser-induced periodic surface structures – a scientific evergreen”, *IEEE J. Sel. Top. Quantum Electron.* **23**, 9000615 (2017).
- [115] J. Bonse and S. Gräf, “Maxwell meets marangoni—a review of theories on laser-induced periodic surface structures”, *Laser Photonics Rev.* **14**, 2000215 (2020).
- [116] J. Krüger and W. Kautek, “Ultrashort pulse laser interaction with dielectrics and polymers”, in *Advances in polymer science*, Vol. 168 (2004), pp. 247–290.
- [117] H. Büttner, M. Hajri, R. Roth, and K. Wegener, “High aspect ratio microstructuring of copper surfaces by means of ultrashort pulse laser ablation”, *Procedia CIRP* **68**, 190–195 (2018).
- [118] J. Schille, L. Schneider, and U. Loeschner, “Process optimization in high-average-power ultrashort pulse laser microfabrication: how laser process parameters influence efficiency, throughput and quality”, *Appl. Phys. A* **120**, 847–855 (2015).
- [119] Y. Jee, M. F. Becker, and R. M. Walser, “Laser-induced damage on single-crystal metal surfaces”, *J. Opt. Soc. Am. B* **5**, 648–659 (1988).
- [120] F. D. Niso, C. Gaudioso, T. Sibillano, F. P. Mezzapesa, A. Ancona, and P. M. Lugarà, “Role of heat accumulation on the incubation effect in multi-shot laser ablation of stainless steel at high repetition rates”, *Opt. Express* **22**, 12200–12210 (2014).
- [121] A. Žemaitis, M. Gaidys, M. Brikas, P. Gečys, G. Račiukaitis, and M. Gedvilas, “Advanced laser scanning for highly-efficient ablation and ultrafast surface structuring: experiment and model”, *Sci. Rep.* **8**, 17376 (2018).
- [122] A. Žemaitis, P. Gečys, M. Barkauskas, G. Račiukaitis, and M. Gedvilas, “Highly-efficient laser ablation of copper by bursts of ultrashort tuneable (fs-ps) pulses”, *Sci. Rep.* **9**, 12280 (2019).
- [123] Z. Feng, H. Zhao, C. Tan, B. Chen, X. Song, and J. Feng, “Influence of laser process parameters on the characteristic of 30CrMnSiA steel substrate and adhesively bonded joints”, *Opt. Laser Technol.* **123**, 105920 (2020).
- [124] M. Rashidian Vaziri and F. Hajiesmaeilbaigi, “Optical and structural properties of copper nanostructured thin films prepared by pulsed laser deposition”, *Optik* **126**, 1348–1351 (2015).
- [125] M. Fernández-Arias, M. Boutinguiza, J. del Val, A. Riveiro, D. Rodríguez, F. Arias-González, J. Gil, and J. Pou, “Fabrication and deposition of copper and copper oxide nanoparticles by laser ablation in open air”, *Nanomater.* **10**, 300 (2020).

- [126] L. Volfová, S. Andrei Irimiciuc, S. Chertopalov, P. Hruška, J. Čížek, M. Vondráček, M. Novotný, M. Butterling, M. O. Liedke, A. Wagner, and J. Lancok, “Tailoring pulsed laser deposition fabricated copper oxide film by controlling plasma parameters”, *Appl. Surf. Sci.* **608**, 155128 (2023).
- [127] J. Sun and J. P. Longtin, “Inert gas beam delivery for ultrafast laser micromachining at ambient pressure”, *J. Appl. Phys.* **89**, 8219–8224 (2001).
- [128] T. Lehecka, A. Mostovych, and J. Thomas, “Long duration light emission from femtosecond laser-target interactions”, *Appl. Phys. A* **92**, 727–741 (2008).
- [129] A. Weck, T. H. R. Crawford, D. S. Wilkinson, H. K. Haugen, and J. S. Preston, “Laser drilling of high aspect ratio holes in copper with femtosecond, picosecond and nanosecond pulses”, *Appl. Phys. A* **90**, 537–543 (2008).
- [130] R. Valizadeh, O. Malyshev, S. Wang, T. Sian, M. Cropper, and N. Sykes, “Reduction of secondary electron yield for e-cloud mitigation by laser ablation surface engineering”, *Appl. Surf. Sci.* **404**, 370–379 (2017).
- [131] S. Calatroni, E. Garcia-Tabares Valdivieso, A. T. Perez Fontenla, M. Taborelli, H. Neupert, M. Himmerlich, P. Chiggiato, D. Bajek, S. Wackerow, and A. Abdolvand, “Optimization of the secondary electron yield of laser-structured copper surfaces at room and cryogenic temperature”, *Phys. Rev. Accel. Beams* **23**, 033101 (2020).
- [132] D. Bajek, S. Wackerow, D. A. Zanin, L. Baudin, K. Bogdanowicz, E. G.-T. Valdivieso, S. Calatroni, B. Di Girolamo, M. Sitko, M. Himmerlich, M. Taborelli, P. Chiggiato, and A. Abdolvand, “Role of surface microgeometries on electron escape probability and secondary electron yield of metal surfaces”, *Sci. Rep.* **10**, 250 (2020).
- [133] J. Nivas, M. Valadan, M. Salvatore, R. Fittipaldi, M. Himmerlich, M. Rimoldi, A. Passarelli, E. Allahyari, S. Oscurato, A. Vecchione, C. Altucci, S. Amoruso, A. Andreone, S. Calatroni, and M. Masullo, “Secondary electron yield reduction by femtosecond pulse laser-induced periodic surface structuring”, *Surf. Interfaces* **25**, 101179 (2021).
- [134] J. JJ. Nivas, M. Hu, M. Valadan, M. Salvatore, R. Fittipaldi, M. Himmerlich, E. Bez, M. Rimoldi, A. Passarelli, S. L. Oscurato, A. Vecchione, C. Altucci, S. Amoruso, A. Andreone, S. Calatroni, and M. Rosaria Masullo, “Laser-induced periodic surface structuring for secondary electron yield reduction of copper: dependence on ambient gas and wavelength”, *Appl. Surf. Sci.*, 156908 (2023).
- [135] J. Wang, Y. Gao, Z. You, J. Fan, J. Zhang, S. Wang, and Z. Xu, “The effect of ultrasonic cleaning on the secondary electron yield, surface topography, and surface chemistry of laser treated aluminum alloy”, *Mater.* **13** (2020).
- [136] Y. Wang, W. Zhang, S. Wang, W. Wei, J. Fang, B. Zhu, and Y. Wang, “Influence of primary electron incident angle and electron bombardment on the secondary electron yield of laser-treated copper”, *J. Vac. Sci. Technol. B* **39**, 034201 (2021).
- [137] B. Debord, A. Amsanpally, M. Chafer, A. Baz, M. Maurel, J. M. Blondy, E. Hugonnot, F. Scol, L. Vincetti, F. Gérôme, and F. Benabid, “Ultralow transmission loss in inhibited-coupling guiding hollow fibers”, *Optica* **4**, 209–217 (2017).
- [138] T. Baer, “Very fast losses of the circulating LHC beam, their mitigation and machine protection”, PhD thesis (University of Hamburg, Germany, 2013).

- [139] P. Bélanger, R. Baartman, G. Iadarola, A. Lechner, B. Lindstrom, R. Schmidt, and D. Wollmann, “Charging mechanisms and orbital dynamics of charged dust grains in the LHC”, *Phys. Rev. Accel. Beams* **25**, 101001 (2022).
- [140] L. Rosa, F. Melli, and L. Vincetti, “Analytical formulas for dispersion and effective area in hollow-core tube lattice fibers”, *Fibers* **9**, 58 (2021).
- [141] B. Debord, F. Amrani, L. Vincetti, F. Gérôme, and F. Benabid, “Hollow-core fiber technology: the rising of “gas photonics””, *Fibers* **7**, 16 (2019).
- [142] E. P. Ippen, C. V. Shank, and T. K. Gustafson, “Self-phase modulation of picosecond pulses in optical fibers”, *Appl. Phys. Lett.* **24**, 190–192 (2003).
- [143] R. H. Stolen and C. Lin, “Self-phase-modulation in silica optical fibers”, *Phys. Rev. A* **17**, 1448–1453 (1978).
- [144] E. Bez, M. Himmerlich, B. Beaudou, A. K. Reascos Portilla, S. Wackerow, M. Rimoldi, S. Pfeiffer, M. Wiesendanger, F. Benabid, M. Taborelli, A. Abdolvand, and P. Chiggiato, “Picosecond pulsed 532 nm laser system for roughening and secondary electron yield reduction of inner surfaces of up to 15 m long tubes”, *Rev. Sci. Instrum.* **94**, 103007 (2023).
- [145] J. Tagg, E. Bez, M. Himmerlich, and A. K. Reascos Portilla, “A reliable monitoring and control system for vacuum surface treatments”, *Proc. 18th Int. Conf. Acc. and Large Exp. Physics Control Systems* **2021**, 492–496 (2022).
- [146] K. Paraschou, L. Mether, G. Rumolo, and G. Iadarola, *E-cloud buildup studies for the Q5 quadrupoles with partially treated beam screens*, (2023)  
<https://indico.cern.ch/event/1338420/>.
- [147] E. Malus, Baudouin, and J. B. Garnery, *Theorie de la double refraction de la lumiere dans les substances cristallisees, memoire couronne par l’institut dans la seance publique du 2 janvier 1810, par e. l. malus* (Garnery, libraire, rue de Seine, Holtel Mirabeau, 1810).
- [148] L. Baudin, “Structuration de surface par laser dans l’environnement des accélérateurs de particules : relation entre topographie superficielle, adhésion des particules et compatibilité aux applications ultravide”, PhD thesis (Université Paris sciences et lettres, France, 2020).
- [149] P. B. Johnson and R. W. Christy, “Optical constants of the noble metals”, *Phys. Rev. B* **6**, 4370–4379 (1972).
- [150] S. Chawla, B. Rickett, N. Sankarraman, and J. Payer, “An x-ray photo-electron spectroscopic investigation of the air-formed film on copper”, *Corros. Sci.* **33**, 1617–1631 (1992).
- [151] T. L. Barr, “An ESCA study of the termination of the passivation of elemental metals”, *J. Phys. Chem.* **82**, 1801–1810 (1978).
- [152] J. F. Moulder, W. F. Stickle, W. M. Sobol, and K. D. Bomben, *Handbook of x-ray photoelectron spectroscopy* (Eden Prairie: Physical Electronics Division, Perkin-Elmer Corporation, 1995).
- [153] S. Poulston, P. M. Parlett, P. Stone, and M. Bowker, “Surface oxidation and reduction of CuO and Cu<sub>2</sub>O studied using XPS and XAES”, *Surf. Interface Anal.* **24**, 811–820 (1996).

- [154] J. Ghijsen, L. H. Tjeng, J. van Elp, H. Eskes, J. Westerink, G. A. Sawatzky, and M. T. Czyzyk, “Electronic structure of  $\text{Cu}_2\text{O}$  and  $\text{CuO}$ ”, *Phys. Rev. B* **38**, 11322–11330 (1988).
- [155] M. C. Biesinger, “Advanced analysis of copper x-ray photoelectron spectra”, *Surf. Interface Anal.* **49**, 1325–1334 (2017).
- [156] V. Petit, “Conditioning of surfaces in particle accelerators”, PhD thesis (Université Toulouse, France, 2020).
- [157] I. Bojko, N. Hilleret, and C. Scheuerlein, “Influence of air exposures and thermal treatments on the secondary electron yield of copper”, *J. Vac. Sci. Technol. A* **18**, 972–979 (2000).
- [158] E. Bez, M. Himmerlich, P. Lorenz, M. Ehrhardt, A. G. Gunn, S. Pfeiffer, M. Rimoldi, M. Taborelli, K. Zimmer, P. Chiggiato, and A. Anders, “Influence of wavelength and accumulated fluence at picosecond laser-induced surface roughening of copper on secondary electron yield”, *J. Appl. Phys.* **133**, 035303 (2023).
- [159] E. Bez, M. Himmerlich, A. K. R. Portilla, L. Baudin, P. Lorenz, K. Zimmer, M. Taborelli, and A. Anders, “Laser-induced surface structuring for electron cloud mitigation in particle accelerators”, in *Proc. 12. Mittweidaer Lasertagung*, 003 (2021), pp. 079–082.
- [160] P. Lorenz, M. Himmerlich, M. Ehrhardt, E. Bez, K. Bogdanowicz, M. Taborelli, and K. Zimmer, “Secondary electron yield reduction of copper after 355 nm ultrashort pulse laser ablation”, *Lasers Manuf. Mater. Process.* (2022).
- [161] D. Bäuerle, *Laser processing and chemistry* (Springer, Berlin, 2011).
- [162] R. Cimino and I. Collins, “Vacuum chamber surface electronic properties influencing electron cloud phenomena”, *Appl. Surf. Sci.* **235**, 231–235 (2004).
- [163] S. S. Harilal, J. R. Freeman, P. K. Diwakar, and A. Hassanein, “Femtosecond laser ablation: fundamentals and applications”, in *Laser-induced breakdown spectroscopy: theory and applications* (Springer Berlin Heidelberg, 2014), pp. 143–166.
- [164] R. Le Harzic, D. Breitling, M. Weikert, S. Sommer, C. Föhl, S. Valette, C. Donnet, E. Audouard, and F. Dausinger, “Pulse width and energy influence on laser micromachining of metals in a range of 100 fs to 5 ps”, *Appl. Surf. Sci.* **249**, 322–331 (2005).
- [165] P. Lorenz, E. Bez, M. Himmerlich, M. Ehrhardt, M. Taborelli, and K. Zimmer, “Pulse duration dependence of infrared laser-induced secondary electron yield reduction of copper surfaces”, *J. Micro Nano-Manuf.* **18**, 121–126 (2023).
- [166] D. Tahir and S. Tougaard, “Electronic and optical properties of Cu,  $\text{CuO}$  and  $\text{Cu}_2\text{O}$  studied by electron spectroscopy”, *J. Condens. Matter Phys.* **24**, 175002 (2012).
- [167] T. Schedel-Niedrig, T. Neisius, I. Böttger, E. Kitzelmann, G. Weinberg, D. Demuth, and R. Schlögl, “Copper (sub)oxide formation: a surface sensitive characterization of model catalysts”, *Phys. Chem. Chem. Phys.* **2**, 2407–2417 (2000).
- [168] S. Marinoni, “An ultra-high vacuum system for secondary electron yield measurements and electron-conditioning of particle accelerators materials at cryogenic temperatures: commissioning and first experiments”, MA thesis (Politecnico Milano, Italy, 2022).
- [169] E. Stranelova, “Characterisation and modification of copper surfaces for cryogenic vacuum components of particle accelerators”, MA thesis (University of chemistry and technology, Prague, Czech Republic, 2023).



## Bibliography

- [170] S. Calatroni, M. Arzeo, S. Aull, M. Himmerlich, P. Costa Pinto, W. Vollenberg, B. Di Girolamo, P. Cruikshank, P. Chiggiato, D. Bajek, S. Wackerow, and A. Abdolvand, “Cryogenic surface resistance of copper: investigation of the impact of surface treatments for secondary electron yield reduction”, *Phys. Rev. Accel. Beams* **22**, 063101 (2019).
- [171] P. Krkotić, S. Calatroni, A. Perez Fontenla, H. Neupert, M. Himmerlich, A. Abdolvand, and S. Wackerow, “RF characterisation of laser treated copper surfaces for the mitigation of electron cloud in accelerators”, in *Proc. IPAC’23*, 14 (2023), pp. 4275–4278.
- [172] K. Brunner, P. Krkotić, S. Calatroni, and D. Barna, “Shielded pair method for beam screen surface resistance measurement at cryogenic temperature”, *Instrum.* **8**, 43 (2024).
- [173] “Handbook of vacuum science and technology”, in *Handbook of vacuum science and technology*, edited by D. M. Hoffman, B. Singh, J. H. Thomas, and J. H. Thomas (Academic Press, San Diego, 1998), pp. 815–835.
- [174] E. B. Holzer et al., “Beam loss monitoring system for the LHC”, in *IEEE Nucl. Sci. Symp. Conf. Rec.* 2 (2005), pp. 1052–1056.
- [175] M. Himmerlich and A. Lechner, *Operational experience with LESS demonstrator in LHC*, (2024) <https://indico.cern.ch/event/1457133/>.



# A Appendix

The ablation depths shown on a logarithmic scale in Figure 4.3 (Chapter 4) are presented on a linear scale in Figure A.1.

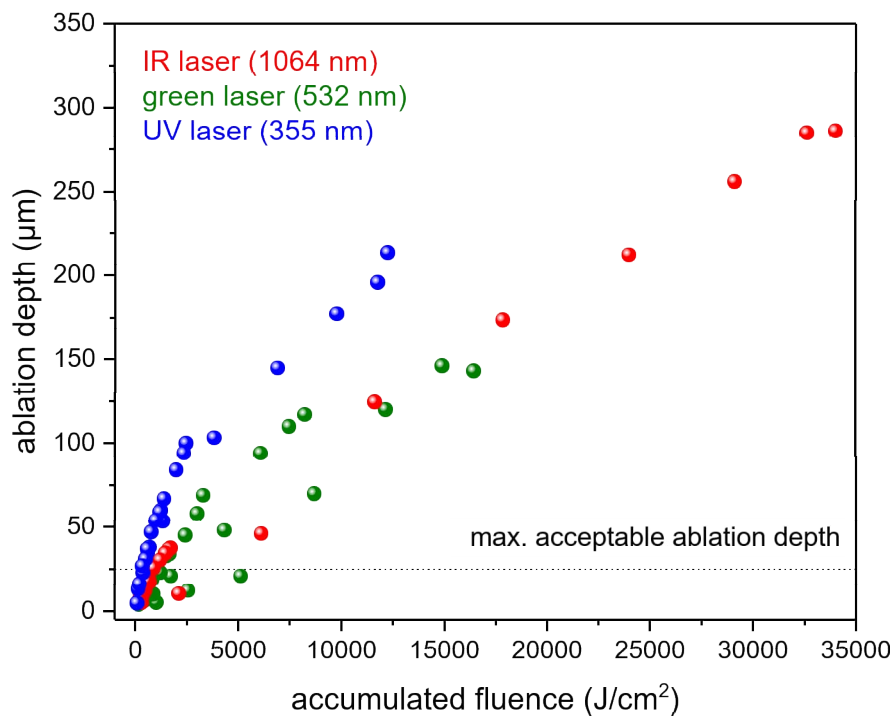


**Figure A.1:** In linear scale: measured ablation depths in dependence of accumulated fluence at a line distance of 10 μm for IR, green, and UV laser irradiation. The maximum acceptable ablation depth is indicated with the dashed line at 25 μm. Published in Ref. [158].

Figure A.2 includes the O 1s spectra of the XPS analysis performed in Chapter 4, Figure 4.9.

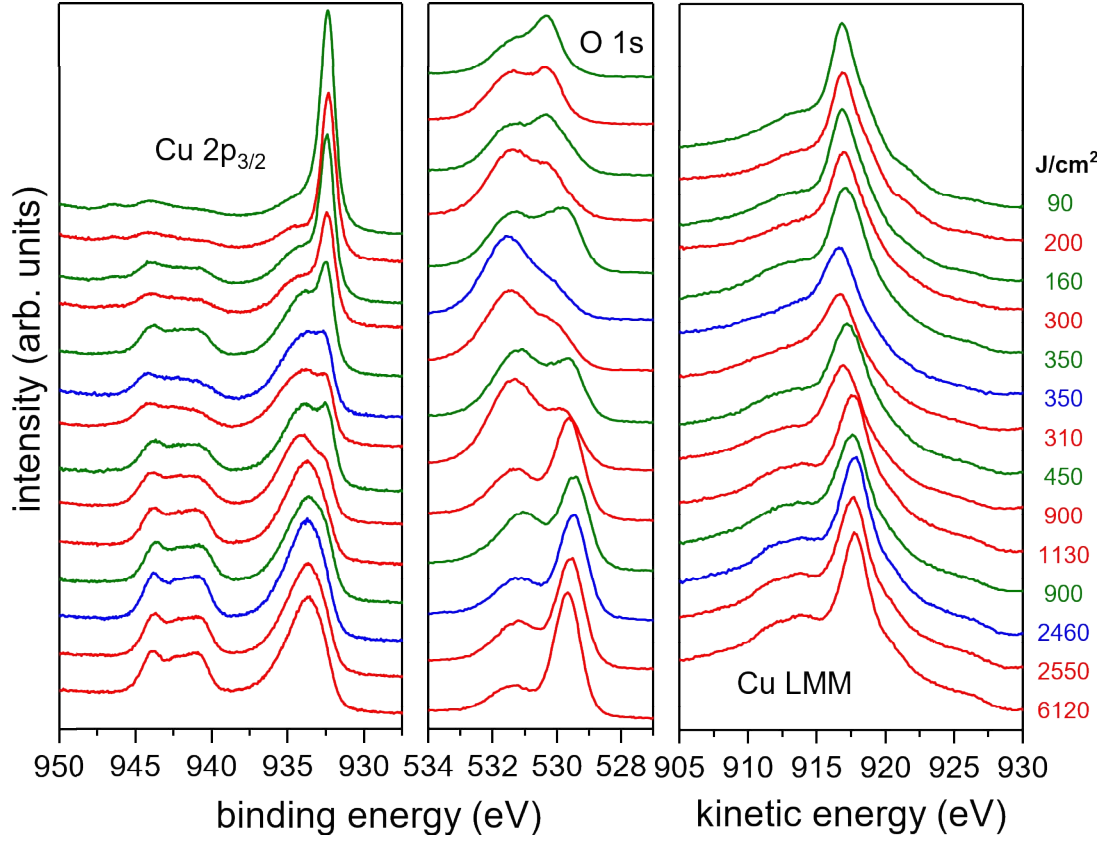


**Figure A.2:** X-ray photoelectron spectra: Cu 2p<sub>3/2</sub>, O 1s state, and Cu LMM x-ray excited Auger emission of Cu irradiated in air, using a variety of accumulated fluences between 90 – 6120 J cm<sup>-2</sup>) and laser wavelengths of 1064 nm (color-coded in red), 532 nm (green), and 355 nm (blue). Published in Ref. [158].

# List of contributions

This PhD study is part of the LESS project at CERN with the aim of developing a technical solution for the treatment of BSs in magnets. The thesis explored the material science related to the concept and developed important technical aspects and components for the optimization of the processing parameters.

Own contributions:

- Planning of experiments
- Commissioning and characterization of *in situ* setup, optical alignments, optical measurements, development and optimization of processing procedures
- Laser-processing of all samples at CERN, beam screens and vacuum chambers using *in situ* laser setups
- Testing and contributing to the optimization of LabVIEW control software
- Contribution to the laser processing of flat samples during visits at IOM in Leipzig.
- Surface analysis measurements: SEY, XPS, electron-conditioning experiments
- Data analysis and interpretation of results
- conceptualization and writing of thesis and first-author papers

External contributions:

1. Material and sample characterization (contributions from central services at CERN):
  - Surface analysis measurements: SEY, XPS, conditioning: Martino Rimoldi, Marcel Himmerlich
  - Conditioning measurement at cryogenic temperature: Valentine Petit
  - SEM imaging and Automated Particle Analysis: Stephan Pfeiffer, Yasemin Askar (Metallurgy & material analysis service at CERN)
  - EDX measurement: Ana Teresa Perez Fontenla (Metallurgy & material analysis service at CERN)
  - Preparation of cross-sections for depth measurement: Stephan Pfeiffer (Metallurgy & material analysis service at CERN)

- WLI measurements: Didier Glaude, Dominique Pugnât, Ahmed Chérif (Metrology service at CERN)
2. Developments for the hardware and control software of the experimental setup at CERN:
- Design and manufacturing of mechanical components and curved samples: Matthew James Watkins, Paul Garritty
  - Electrical connections and installation of experimental setup: Ana Karen Reascos Portilla
  - Programming of control software: Joseph Tagg, Louis Cordier–Temple
  - Technical support for beam delivery system & fiber: Benoit Beaudou (GLOphotonics)
  - Technical support for robot: Markus Wiesendanger (Waygate Technologies Robotics, Baker Hughes)
3. Other contributions:
- Collaboration with IOM: laser-processing of flat samples and partially SEM: Pierre Lorenz
  - Scientific exchange/discussions/review of manuscript: Marcel Himmerlich, Mauro Taborelli, Pierre Lorenz, Klaus Zimmer, André Anders

Collaborations:

- IOM: fundamental studies on flat surfaces
- University of Dundee: development and improvement of *in situ* laser setup
- University of Naples: LIPSS studies

Supervisors:

- Prof. Dr. André Anders (University of Leipzig, IOM)
- Dr. Marcel Himmerlich (CERN)

# Acknowledgements

- I express my gratitude to Prof. André Anders for accepting me as a doctoral student and providing valuable guidance and inspiration for my research. I am thankful for the opportunity to visit the IOM in Leipzig on two separate occasions.
- I am very grateful to my supervisor at CERN, Marcel Himmerlich, for making me part of the LESS team. I greatly appreciate his valuable guidance and support over the past few years, his extensive knowledge and his willingness to help me whenever I needed it.
- I am grateful to my colleagues of the LESS team for the great time together and for all the efforts to make the LESS project a success.
- I would like to thank Mauro Taborelli, who hosted me in his section, for his advice and discussions.
- I am grateful to the laser team at IOM – Pierre Lorenz, Martin Erhardt, and Klaus Zimmer – for sharing their expertise and welcoming me warmly in the group. I appreciate all the resources and materials they have provided.
- The support by the Wolfgang Gentner Programme of the German Federal Ministry of Education and Research (Grant No.13E18CHA) for my PhD scholarship is gratefully acknowledged.
- I want to thank all other collaborators and colleagues who made my time at CERN a unique and unforgettable experience.
- I would like to express my heartfelt gratitude to Eva Stranelova, Stefano Marinoni, and Martino Rimoldi for their presence in the most welcoming corner of the open space. I am incredibly grateful for the unforgettable moments we spent together, with laughter, coffee breaks, psychological support and refilling emergency boxes. Your company was invaluable to me.
- I am grateful for the unwavering support and encouragement from my family and friends.
- Finally, I would like to thank Peter for being there in good and bad moments, and for not letting me down.